MULTIFARIOUS METHODS for ENHANCEMENT of LUMINESCENCE in RARE EARTH ION-DOPED UPCONVERSION NANOCRYSTALS

By

Chenshuo Ma

School of Engineering

Supervisor

Prof. Candace I Lang

Adjunct Supervisor

Prof. Dayong Jin

This thesis is presented for the degree of Doctor of Philosophy

August 2017

Statement

I certify that the work in this thesis was not previously submitted for a degree nor was it submitted as part of the requirements for a degree at another university or institution other than Macquarie University, Sydney.

I also certify that this thesis is an original piece of research and was written by Chenshuo Ma. Help and assistance received the research work and the preparation of the thesis itself is appropriately acknowledged.

In addition, I certify that all information sources and literature used in its preparation are appropriately indicated and listed in this work.

Chenshuo Ma August 2017

Acknowledgements

Over the last 3 years of that I undertook the research work reported here in this thesis, there were many people who helped me and who I would like to thank. I greatly appreciate the help I received from my supervisors, Prof. Candace Lang and adjunct supervisor Prof. Dayong Jin. Prof. Candace Lang has great personal charisma, is always patient, kind, considerate and has constantly encouraged me. I would not have been able to complete this work nor my Ph.D. program without her great encouragement and support. She spent a significant amount of time polishing my manuscripts in preparation for their publication and for this thesis. I appreciate her guidance, not only for her constructive suggestions related to my projects but also for advice on furthering my research career. I appreciate Prof. Dayong Jin for giving me the opportunity to pursue my Ph.D. at Macquarie University. I am especially appreciative of his philosophical insights and helpful experience in tackling difficulties associated with this work. His high self-motivation and strategic approach have always encouraged me. He provided me with great and useful guidance during my Ph.D.

I would like to acknowledge the research teams I was lucky enough to work with and to all of these people who helped me. Dr. Deming Liu and Dr. Fan Wang provided me with great support and patient guidance to help me solve many technical challenges during my research endeavors. Thanks also to Prof. James A. Piper, Prof. Yi Qian, Dr. Yiqing Lu, Dr. Jiangbo Zhao, Mr. Zhiguang Zhou, Mr. Shihui Wen, Mr. Ming Guan and Mr. Chao Mi, who give me great help with my experiments and publications.

I would like to show my appreciations to people who give me support and help during my Ph.D. experience: Prof. Yong Liu, A/Prof. Peng Xi, Dr. Liuen Liang, Dr. Tom Lawson, Dr. Jie Lu, Dr. Xianlin Zheng, Dr. Yujia Liu, Dr. Alfonso Garcia-Bennett, Dr. Nicholas Tse, Dr. Bingyang Shi, Dr. Tao Huang, Mrs. Debra Birch, Mrs. Nicole Vella and Miss Li Wang. I would like to thank for the other good friends, Dr. Rui Feng, Mrs. Enmei Xiong, Mrs. Ran Wang, Miss Lei Zhang, Dr. Affan Baba, Mr. Yu Li, Mr. Ali Lalbakhsh and Mr. Arslan Kiyani who give me memorable experiences, always provided me with support in life and lots of fun. I also would like to thank Dr. Xusan Yang for his understanding and joy he brings to my life. Thanks for all the support they give me which play as the missing puzzle piece to accomplish my Ph.D.

I am very thankful for Macquarie University to provide me with a harmonious and positive environment for my study. I acknowledge the financial support from the China Scholarship Council and Macquarie University in making my research possible. Thanks also to the School of Engineering at Macquarie University that provided me with the great opportunity to join the tutorial team for three semesters.

I would like to give special thanks to my parents, Prof. Zhengxian Ma and Prof. Hui Li. I would have never have achieved what I set out to do without their help and love. They give me unconditional support whenever I need it in my research and in my life. At this stage, I want to say, “I am so lucky to be your daughter, and I love you.”

List of Publications

[1] **Chenshuo Ma**, Xiaoxue Xu, Fan Wang, Zhiguang Zhou, Deming Liu, Jiangbo Zhao, Ming Guan, Candace I Lang, and Dayong Jin. "Optimal Sensitizer Concentration in Single Upconversion Nanocrystals", ***Nano Letters***, 2017, 17(5): 2858-2864.

[2] **Chenshuo Ma**, Xiaoxue Xu, Fan Wang, Zhiguang Zhou, Shihui Wen, Deming Liu, Jinghua Fang, Candace I Lang, and Dayong Jin. "Probing the interior crystal quality in the development of more efficient and smaller upconversion nanoparticles", ***The Journal of Physical Chemistry Letters***, 2016, 7(16): 3252-3258.

[3] Xiaoxue Xu, Christian Clarke, **Chenshuo Ma**, Gilberto Casillas Garcia, Minakshi Das, Ming Guan, Deming Liu, Li Wang, Anton Tadich, Yi Du, Cuong Ton-That, and Dayong Jin, "Depth-profiling of Yb^{3+} sensitizer ions in $NaYF_4$ upconversion nanocrystals", ***Nanoscale***. 2017, DOI: 10.1039/C7NR01456B.

[4] Yujia Liu, Yiqing Lu, Xusan Yang, Xianlin Zheng, Shihui Wen, Fan Wang, Xavier Vidal, Jiangbo Zhao, Deming Liu, Zhiguang Zhou, **Chenshuo Ma**, Jiajia Zhou, James A. Piper, Peng Xi, and Dayong Jin. "Amplified stimulated emission in upconversion nanoparticles for super resolution nanoscopy", ***Nature***, 2017, 543: 229-233.

[5] Deming Liu, Xiaoxue Xu, Yi Du, Xian Qin, Yuhai Zhang, **Chenshuo Ma**, Shihui Wen, Wei Ren, Ewa M. Goldys, James A Piper, Shixue Dou, Xiaogang Liu, and Dayong Jin. "Three-dimensional controlled growth of monodisperse sub-50 nm heterogeneous nanocrystals", ***Nature Communications***, 2016, 7: 10254.

[6] Deming Liu, Xiaoxue Xu, Fan Wang, Jiajia Zhou, Lixin Zhang, Yiqing Lu, **Chenshuo Ma**, Ewa Goldys, Jun Lin, and Dayong Jin, "Emission Stability and Reversibility of Upconversion Nanocrystals ", ***Journal of Materials Chemistry C***. 2016, 4: 9227-9234.

Abstract

Upconversion nanocrystals (UCNCs) have become a sought-after delivery system for advanced biomedical and photonics applications since they have the unique ability to convert low energy infrared photons into high-energy visible and ultraviolet photons. In this work, the author has developed a number of approaches to the fabrication of UCNCs that are small in size and so are of much use in the field of biology and medicine. Since a long-pursued goal for UCNCs is the further enhancement of their upconversion efficiency and the generation of a stronger emission, the author also describes new procedures for the fabrication of particles that possess enhanced efficiency in their upconversion luminescence.

To achieve the two aims, the author first investigated the nature of the interior crystal quality of these particles and how to enhance it. Experiments that formed part of this work demonstrated that smaller and more efficient UCNCs can be formed with improved interior crystal quality. In parallel to this line of investigation, the author also demonstrated the importance of controlling the $NaYF_4$ transit stage from cubic phase to hexagonal phase. Following this, an efficient method for synthesizing sub-10nm UCNCs, and then fabricating a novel sandwich structure, was developed. The sandwich structure nanocrystal can realize size-tunable and doped maximum sensitizer ions. The author also found that the particles, when enclosed by an inert shell, were able to achieve minimal surface quenching as well. Finally, the author shows that a photon-avalanche-like effect plays the key role in bringing down the intensity requirement for stimulated emission depletion with high Tm^{3+} ions doped nanocrystals s. The sensitizer ions present as a radial gradient distribute from the core to the surface. This kind of UCNCs offer efficient optical switching with saturation intensity at low power and provides a large contrast to conventional fluorescent probes used for super resolution stimulated emission depletion (STED) nanoscopy.

The three major results are presented in four publications. The author presents a summary and prospect chapter at the end as well. This thesis provided several good ways to solve the key problems of size-tunable and luminescence enhancement for $UCNC_S$ applications. It profound implications for the upconversion optical property exploration and realizes further bioimaging and biomedical applications.

List of Acronyms (in alphabetic order)

C.elegans	caenorhabditis elegans
CL	cooperative luminescence
CR	cross relaxation
CS	cooperative sensitization
CT	computed tomography
EDX	energy dispersive X-ray spectroscopy
ESA	excited state absorption
ETU	energy transfer upconversion
HRTEM	high resolution transmission electron microscope
ICP-MS	inductively coupled plasma mass spectrometry
MRI	magnetic resonance imaging
NIR	near infrared
NMR	nuclear magnetic resonance
OA	oleic acid
OA^-	oleate anions
OAH	oleic acid molecular
ODE	1-octadecene
OM	oleylamine
PA	photon avalanche
PAA	poly (acylic acid)
PDMS	polydimethylsiloxane
PDT	photodynamic therapy
PEG	poly(ethylene glycol)
PEI	poly(ethylene imine)
PET	positron emission tomography
PMMA	poly (methyl methacrylate)
PVP	polyvinylpyrrolidone
QDs	quantum dots
RE	rare earth
SEM	scanning electron microscope

SET	successive energy transfer
SPAD	single photon counting avalanche diode
SPECT	single-photon emission computed tomography
SPR	surface plasma resonance
STED	super resolution stimulated emission depletion
t-BOC	*t*-butyloxycarbonyl
TEM	transmission electron microscope
TOP	tributylphosphine
UV	ultraviolet
XPS	X-ray photoelectron spectroscopy
XRD	X-ray diffraction

Contents

CHAPTER 1

INTRODUCTION

Photoluminescence refers to the emission of photons from a material. A common example of this phenomenon is the Stokes shift where excitation by the material leads to the emission of lower-energy photons, as illustrated in **Figure 1(a)**. This work, however, is concerned with the development of luminescence that is upconverted, a kind of anti-Stokes luminescence where the absorption of photons leads to emission of light from a material at a higher energy.

1.1 Background to upconversion luminescence

The emission of a high-energy photon (referred to in this work as upconversion luminescence) after the absorption of two low-energy photons is illustrated in **Figure 1.1 (b)**. Upconversion luminescence can be further divided into three different classes: excited-state-absorption (ESA), energy-transfer-upconversion (ETU) and photon-avalanche (PA).

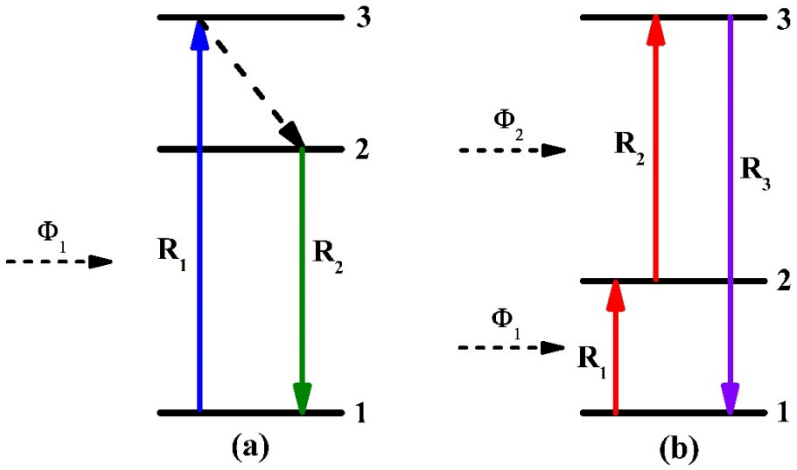

Figure 1.1 Energy transitions of photons in (a) conventional luminescence and (b) upconversion luminescence processes[1].

1.1.1 A description of excited state absorption

ESA, first proposed by Bloembergen *et al.*[2,3], sought to clarify the fundamental process of upconversion luminescence: in this model, a single ion absorbs photons over

time at its ground state and then enters a long-lived intermediate excited state. As illustrated in **Figure 1.1 (b)**, an ion absorbs photon energy by a transition from ground state 1 to excited metastable state 2; the ion subsequently absorbs another photon and transitions from state 2 to higher excited state 3. Upconversion emission occurs when the ion transitions from excited state 3 to ground state 1, i.e. emits a higher-energy photon as a result of absorbing two lower-energy photons. Alternatively, the ions may achieve a higher energy state 4 or 5, leading to absorption of 3 or 4 photons. In the ESA process, emitted photon energy from a higher energy state is larger than any single absorbed photon energy, which means that the emission photon wavelength is shorter (i.e. the emitted energy is higher) than the excitation wavelength.

1.1.2 Energy transfer upconversion

Many UCNCs achieve upconversion luminescence emission through an energy transfer process[4]. There are four different types of energy-transfer-upconversion (ETU): successive-energy-transfer (SET), cross-relaxation (CR), cooperative-sensitization (CS), and cooperative-luminescence (CL). **Figure 1.2** shows these processes. In ESA (**Fig 1.2 (a)**), energy is transferred from a sensitizer ion in the excited state to an activator ion in State 1 by energy transfer, followed by the promotion of the activator ion to metastable State 2. Final absorption occurs subsequently, resulting in promotion to excited State 3; the activator ion is thus promoted to State 3 through ESA. In SET (**Fig 1.2 (b)**), only the sensitizer ion can absorb photons from the incident light. The activator ion is promoted to metastable State 2 and again to State 3 by two energy transfer processes. In CR (**Fig 1.2 (c)**), photons from incident light are absorbed by sensitizer ions and activator ions, promoting them to State 2. Another energy transfer subsequently promotes activator ion to State 3; at the same time, the sensitizer ion reverts to ground state. CS (**Fig 1.2 (d)**) is a kind of energy transfer accumulated from two sensitizers to a single activator ion followed by promoting of the activator ion to a higher excited state. CL is similar to CS, in that they are both cooperative effects. The CL (**Fig 1.2 (e)**) process, however, is the emission of one photon from two excited ions which interacted with each other. These two ions each act as sensitizer ion and activator ion[4].

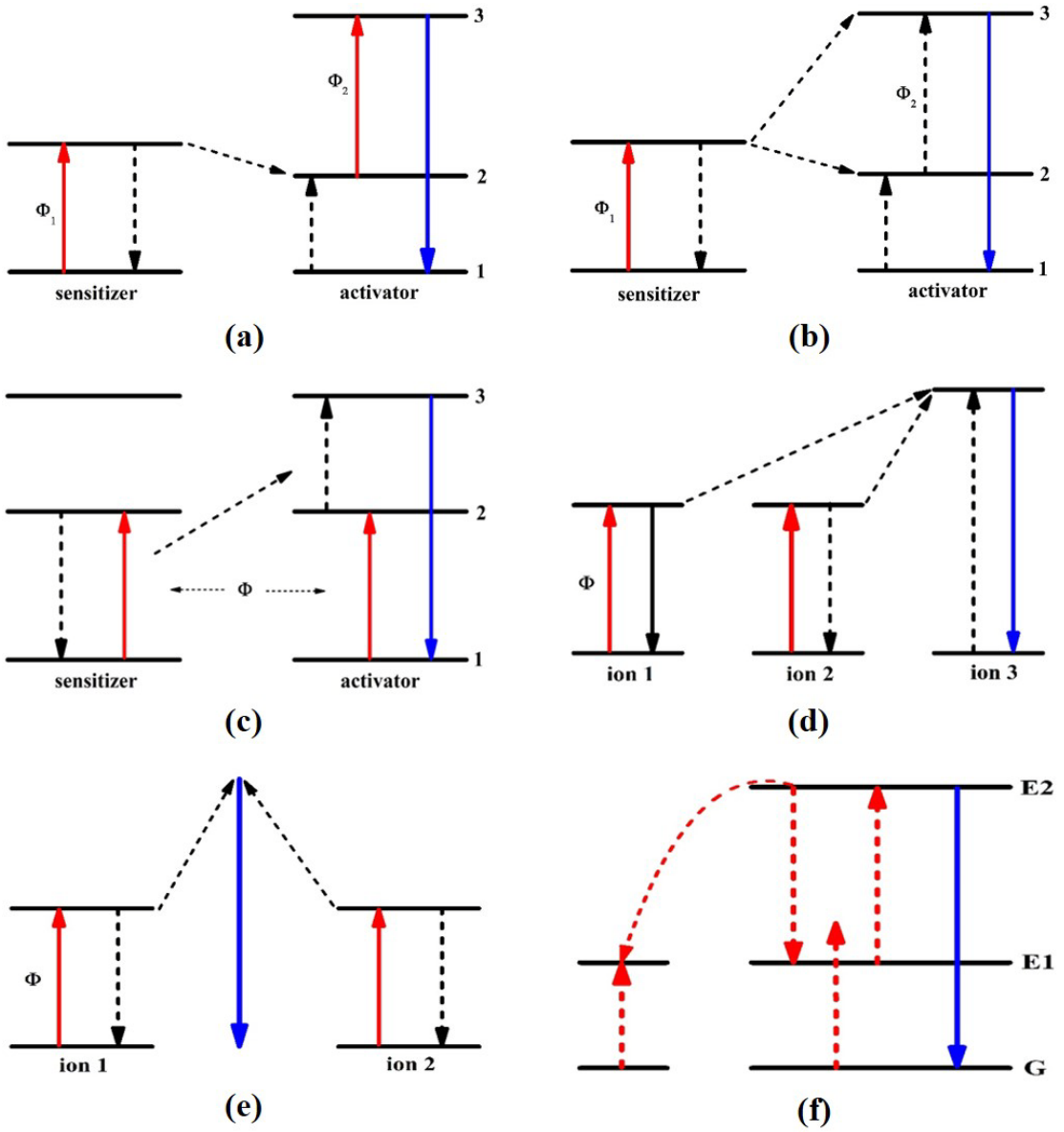

Figure 1.2 Schematic of (a) ESA and four different energy transfer modes: (b) SET; (c) CR; (d) CS; (e) CL; (f) PA[5].

1.1.3 The photon avalanche phenomena

Photon-avalanche (PA), shown in **Figure 1.2 (f)**, was first proposed by Chivian *et al.*[6]: a sensitizer ion in State G is promoted to a State E1 by ground-state-absorption (GSA) and promoted to a State E2 subsequently by ESA. Since State E1 is metastable, CR occurs between the excited ion and a ground-state ion which neighboured. ESA results in an exponential increase in the number of photons on State E2 resulting in strong upconversion luminescence.

1.2 Rare earth based upconversion materials

Auzel *et al.*[7] investigated upconversion mechanisms of rare earth based nanomaterial in the 1970s. These workers proposed upconversion mechanisms such as additional energy transition, excitation absorption, and cooperative luminescence. Typically, upconversion nanomaterials are divided into those with single dopants and those with multiple dopant materials[8–17]. The multiple dopant upconversion materials are most common since rare earth materials have an f-f forbidden transition which does not have high absorption cross section. For example, UCNCs of inorganic host materials, such as fluorides, oxides, oxysulfides, phosphates, and vanadates, are typically doped with lanthanide ions.

1.2.1 Host materials

Ideal host materials should display both low lattice phonon energy and high emission strength. Since nonradiative energy loss requires the assistance of photons which are present in the host lattice, the nonradiative loss should be minimized when choosing the host materials, while also choosing low lattice phonon energy materials. According to the efficiency of upconversion luminescence, the phonon energy level scales as follows: fluorides > oxides[18–21]. The material structure stability, however, scales as fluorides < oxides. From previous studies, a series of host materials such as $LiYF_4$[22–25], $NaYF_4$[11,26], $NaGdF_4$[27,28], $NaLuF_4$[29], $BaYF_5$[30], KY_3F_{10}[16], $BaGdF_5$[31], CaF_2[32] and SrF_2[33,34] have been proposed as good host materials which have low phonon energy.

1.2.2 Lanthanide dopants

Usually, an inorganic upconversion phosphor consists of a crystalline host, with lanthanide ions added (also referred to as doped) into it at low concentrations. In upconversion materials, the ion that emits the radiation is termed an activator and the donator of energy is termed a sensitizer. The distance between these ions and their spatial arrangement within the host is an important influence on the upconversion luminescence that results. Accordingly, processes used for the fabrication of particles with a high efficiency of upconversion luminescence allow for easy tunability to the

relationship between the host lattice, different dopant ions, and different doping concentrations

1.2.1.1 Sensitizer ions

As shown in **Figure 1.3**, the sensitizer ions are added to the host to serve as excitation sources for activator ions, which then radiate light. Yb^{3+} ions have a larger absorption area than lanthanide activators and so is often co-doped with Er^{3+}, Tm^{3+} and Ho^{3+} ions to act as a sensitizer to enhance the upconverted luminescence of a composite. A 980 nm laser can be applied as the excitation laser to match the energy of the $^2F_{7/2}$ to $^2F_{5/2}$, found in Yb^{3+} ions.

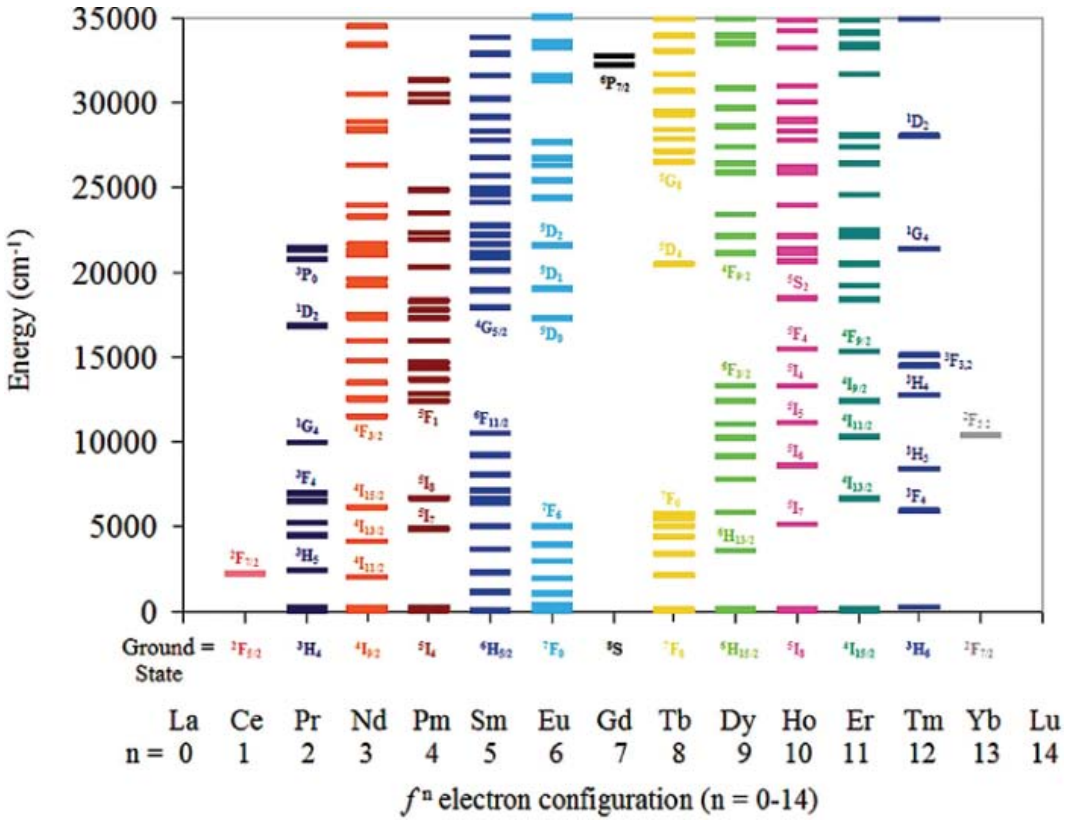

Figure 1.3 The electron configuration for lanthanide ions[1].

1.2.1.2 Activator ions

The activator is the source of luminescence for UCNCs. Most rare-earth ions (RE^{3+}) have more than one excitation level and can be successfully used as UCNCs activators. The most frequently used upconversion crystal activators are Er^{3+}, Tm^{3+} and

Ho^{3+} ions. A relatively low concentration of activator ions is usually doped to minimize the energy loss that can occur with cross relaxation[4].

1.2.3 The mechanism of upconversion emission using lanthanide doped crystals as a model

The most commonly used activators rare earth ions are Er^{3+}, Tm^{3+} and Ho^{3+} as shown in **Figure 1.4, 1.5** and **1.6** respectively. Li *et al.*[35] proposed the upconversion transition process from sensitizers to emitters for these ions, as described below.

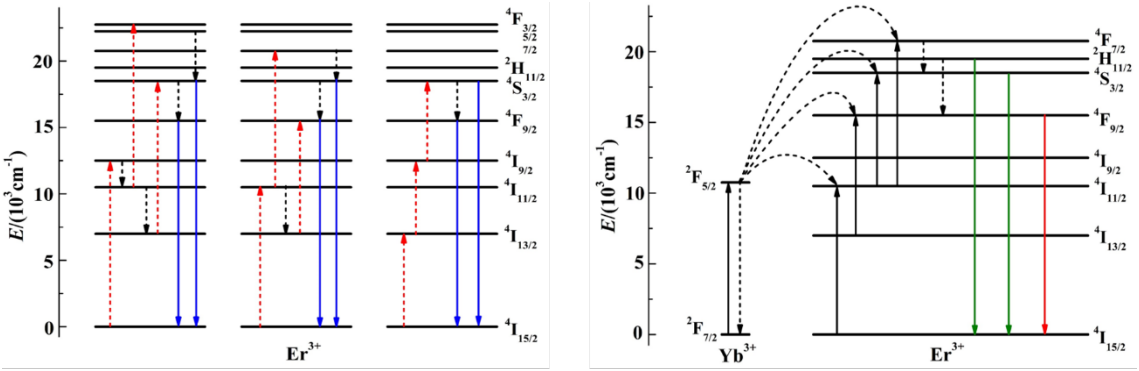

Figure 1.4 (a) Er^{3+} ions upconversion luminescence process, (b) Er^{3+}/ Yb^{3+} energy transfer process.[35]

Figure 1.4 shows the Er^{3+}, Yb^{3+} codoped upconversion luminescence process. The transition from $^2H_{11/2}$ excited states to the $^4I_{15/2}$ ground state can emit 520 nm green upconversion luminescence, and transfer from $^4S_{3/2}$ excited states to the $^4I_{15/2}$ ground state can emit 542 nm green upconversion luminescence. The transition from $^4F_{9/2}$ excited states to the $^4I_{15/2}$ ground state can emit 660 nm red upconversion luminescence. Blue emission, from $^4F_{5/2}$ excited states to the $^4I_{15/2}$ ground state can emit 450 nm luminescence, $^2P_{3/2}$ excited states to the $^4I_{11/2}$ ground state can emit 470 nm luminescence, and $^4F_{7/2}$ excited states to the $^4I_{15/2}$ ground state can emit 450 nm luminescence.

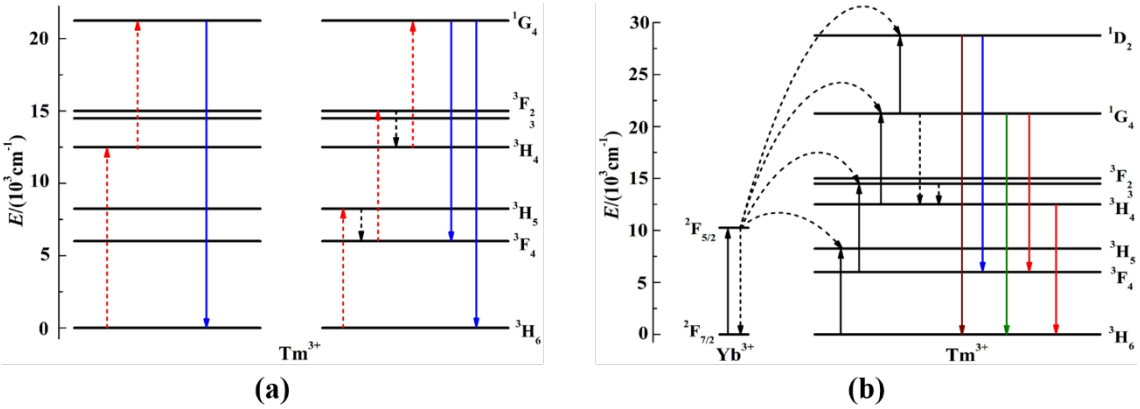

Figure 1.5 (a) Tm^{3+} ions upconversion luminescence process, (b) Tm^{3+}/ Yb^{3+} energy transfer process.[35]

Figure 1.5 shows $Tm^{3+}$and Yb^{3+} codoped upconversion luminescence processes. The transition from $^1D_2$ excited states to the $^3H_6$ ground state and $^3P_6$ excited states to the $^3F_4$ state can emit 365 nm and 345nm ultraviolet luminescence, respectively. The transition from $^3H_4$ excited states to the $^3H_6$ ground state can emit 800 nm near-infrared upconversion luminescence which is the most generally used upconversion process for Tm^{3+}.

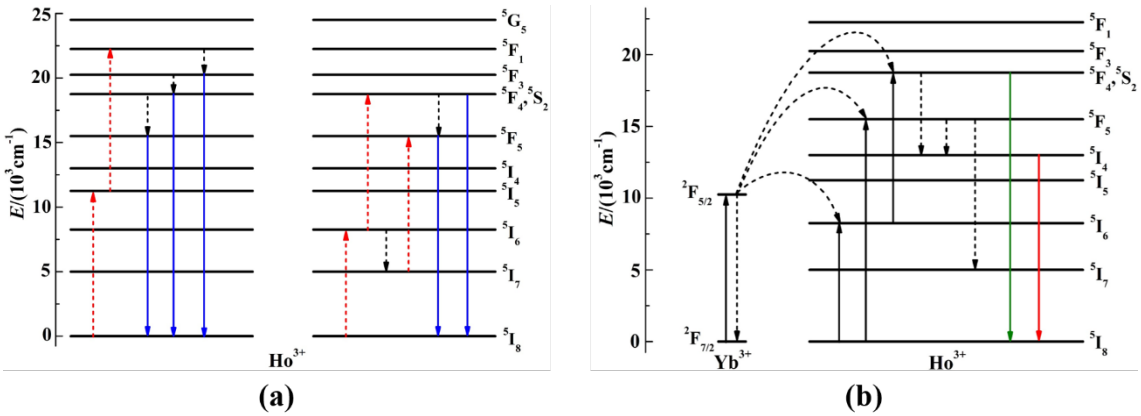

Figure 1.6 (a) Ho^{3+} ions upconversion luminescence process, (b) Ho^{3+}/ Yb^{3+} energy transfer process.[35]

Figure 1.6 shows a Ho^{3+}, Yb^{3+} codoped upconversion luminescence process. The transition from the $^4F_3$ excited states to the $^5I_8$ ground state can occur at a 486 nm blue luminescence. The transition from the $^5F_4$, $^5S_2$ excited states to the $^5I_8$ ground state can emit a 510-570 nm green luminescence. The transition from the $^5F_5$ excited states to

the $^5I_8$ ground state can emit 647 nm red luminescence. The transition from the $^5F_4$, $^5S_2$ excited states to the $^5I_7$ state can emit a 751 nm near-infrared luminescence.

In this thesis, I chose $NaYF_4$ as the host material which has low phonon energy, Tm^{3+} as the emitter ions, Yb^{3+} as the sensitizer ions, and other ions to do other specific researchers.

1.3 The outline of the thesis

The focus of the research program undertaken and described here was to increase the luminescence emission intensity of rare earth ion-doped nanocrystals under specific illumination conditions. This thesis consists of an Introduction chapter, a Literature Survey chapter, three experimental methods, results and discussion chapters based on published work, and one Conclusion chapter. The results and discussion chapters are presented in the form of four journal publications (two first author papers and two co-author papers) and comments on my input.

Chapter 3 is presented as a published, first-author paper (***The Journal of Physical Chemistry Letters***, 2016, 7(16): 3252-3258). This examines the influence of crystal defects on upconversion luminescence. Here a unique quantitative method is described for the optical characterizations of single UCNCs so that the presence of interior defects within crystals could be identified. The importance of controlling the transit stage of α-$NaYF_4$ into β-$NaYF_4$ was emphasized. UCNCs as small as 13 nm have been demonstrated by this work to exhibit high emission efficiency.

Chapter 4 is presented as a published, first-authored paper (***Nano Letters***, 2017, 17(5): 2858-2864). This focuses first on a novel method to decrease the UCNCs' size. The synthesis of a novel sandwich structure, with an active interlayer which can be doped with a maximum number of sensitizer ions, is also described. By coating with a layer of inert shell, the crystals' upconversion luminescence increases owing to a minimization of surface quenching.

Chapter 5 is presented as two co-authored papers (***Nanoscale***. 2017, 9: 7719-7726; ***Nature***, 2017, 543: 229-233). This chapter focuses on the UCNCs' uniformity detection and optical imaging applications in super-resolution nanoscopy. The sensitizer ions in the nanocrystals are shown to exhibit a radial gradient distribution in each single

UCNCs, by using synchrotron-based X-ray Photoelectron Spectroscopy (XPS) and Energy Dispersive X-ray Spectroscopy (EDX) measurements. UCNCs, highly Tm^{3+} doped with good crystal quality and small size, have good luminescence efficiency, demonstrated by low-power super-resolution stimulated emission depletion (STED) microscopy. These UCNCs offer efficient optical switching with saturation intensity at low excitation power.

Chapter 6 is a summary of the key research outcomes of my Ph.D. research, and a discussion of the future work prospects of UCNCs applications is given.

REFERENCES

(1) Chan, E. M. Combinatorial Approaches for Developing Upconverting Nanomaterials: High-Throughput Screening, Modeling, and Applications. *Chem. Soc. Rev.* **2015**, *44*, 1653–1679.

(2) Bloembergen, N. Solid State Infrared Quantum Counters. *Phys. Rev. Lett.* **1959**, *2*, 84–85.

(3) Abel, K. A.; Boyer, J.-C.; Andrei, C. M.; van Veggel, F. C. J. M. Analysis of the Shell Thickness Distribution on $NaYF_4$/$NaGdF_4$ Core/Shell Nanocrystals by EELS and EDS. *J. Phys. Chem. Lett.* **2011**, *2*, 185–189.

(4) Zhou, J.; Liu, Q.; Feng, W.; Sun, Y.; Li, F. Upconversion Luminescent Materials: Advances and Applications. *Chem. Rev.* **2015**, *115*, 395–465.

(5) Wang, F.; Liu, X. Upconversion Multicolor Fine-Tuning: Visible to near-Infrared Emission from Lanthanide-Doped $NaYF_4$ Nanoparticles. *J. Am. Chem. Soc.* **2008**, *130*, 5642–5643.

(6) Chivian, J. S.; Case, W. E.; Eden, D. D. The Photon Avalanche: A New Phenomenon in Pr^{3+}-Based Infrared Quantum Counters. *Appl. Phys. Lett.* **1979**, *35*, 124–125.

(7) Auzel, F.; Pecile, D. Comparison and Efficiency of Materials for Summation of Photons Assisted by Energy Transfer. *J. Lumin.* **1973**, *8*, 32–43.

(8) Cao, B. S.; He, Y. Y.; Zhang, L.; Dong, B. Upconversion Properties of Er^{3+}-Yb^{3+}: $NaYF_4$ Phosphors with a Wide Range of Yb^{3+} Concentration. *J. Lumin.* **2013**, *135*, 128–132.

(9) Li, C.; Liu, J.; Alonso, S.; Li, F.; Zhang, Y. Upconversion Nanoparticles for Sensitive and in-Depth Detection of Cu^{2+} Ions. *Nanoscale* **2012**, *4*, 6065.

(10) Patra, A.; Friend, C. S.; Kapoor, R.; Prasad, P. N. Upconversion in Er^{3+}: ZrO_2 Nanocrystals. *J. Phys. Chem. B* **2002**, *106*, 1909–1912.

(11) Chen, G.; Ohulchanskyy, T. Y.; Kumar, R.; Ågren, H.; Prasad, P. N. Ultrasmall Monodisperse $NaYF_4$: Yb^{3+}/Tm^{3+} Nanocrystals with Enhanced Near-Infrared to Near-Infrared Upconversion Photoluminescence. *ACS Nano* **2010**, *4*, 3163–3168.

(12) Shen, J.; Chen, G.; Ohulchanskyy, T. Y.; Kesseli, S. J.; Buchholz, S.; Li, Z.; Prasad, P. N.; Han, G. Tunable near Infrared to Ultraviolet Upconversion Luminescence Enhancement in (α-$NaYF_4$:Yb,Tm)/CaF_2 Core/shell Nanoparticles for in Situ Real-Time Recorded Biocompatible Photoactivation. *Small* **2013**, *9*, 3213–3217.

(13) Xiang, G.; Zhang, J.; Hao, Z.; Zhang, X.; Pan, G.; Luo, Y.; Lü, S.; Zhao, H. The Energy Transfer Mechanism in Pr^{3+} and Yb^{3+} Codoped β-$NaLuF_4$ Nanocrystals. *Phys. Chem. Chem. Phys.* **2014**, *16*, 9289–9293.

(14) Xu, M.; Fei, L.; Zhang, W.; Li, T.; Lu, W.; Zhang, N.; Lai, Y.; Zhang, Z.; Fang, J.; Zhang, K.; *et al.* Tailoring Anisotropic Li-Ion Transport Tunnels on Orthogonally Arranged Li-Rich Layered Oxide Nanoplates Toward High-Performance Li-Ion Batteries. *Nano Lett.* **2017**, *17*, 1670–1677.

(15) Shang, Y.; Hao, S.; Liu, J.; Tan, M.; Wang, N.; Yang, C.; Chen, G. Synthesis of Upconversion β-$NaYF_4$: Nd^{3+}/Yb^{3+}/Er^{3+} Particles with Enhanced Luminescent Intensity through Control of Morphology and Phase. *Nanomaterials* **2015**, 218–232.

(16) Mahalingam, V.; Vetrone, F.; Naccache, R.; Speghini, A.; Capobianco, J. A. Structural and Optical Investigation of Colloidal Ln^{3+}/Yb^{3+} Co-Doped KY_3F_{10} Nanocrystals. *J. Mater. Chem.* **2009**, *19*, 3149–3152.

(17) Auzel, F.; Baldacchini, G.; Laversenne, L.; Boulon, G. Radiation Trapping and Self-Quenching Analysis in Yb^{3+}, Er^{3+}, and Ho^{3+} Doped Y_2O_3. *Opt. Mater. (Amst).* **2003**, *24*, 103–109.

(18) Suzuki, H.; Nishida, Y.; Hoshino, S. Ligand-Sensitized and Up-Conversion Photoluminescence in Vacuum-Deposited Thin Films of an Infrared Electroluminescent Organic Erbium Complex. *Mol. Cryst. Liq. Cryst.* **2003**, *406*, 27–37.

(19) Aboshyan-Sorgho, L.; Besnard, C.; Pattison, P.; Kittilstved, K. R.; Aebischer, A.; Bünzli, J. C. G.; Hauser, A.; Piguet, C. Near-infrared-Visible Light Upconversion in a Molecular Trinuclear D-F-D Complex. *Angew. Chemie - Int. Ed.* **2011**, *50*, 4108–4112.

(20) Renero-Lecuna, C.; Martín-Rodríguez, R.; Valiente, R.; González, J.; Rodríguez, F.; Krämer, K. W.; Güdel, H. U. Origin of the High Upconversion Green Luminescence Efficiency in β-$NaYF_4$: 2% Er^{3+}, 20% Yb^{3+}. *Chem. Mater.* **2011**, *23*, 3442–3448.

(21) Weng, D.; Zheng, X.; Chen, X.; Li, C.; Jin, L. Synthesis, Upconversion Luminescence and Magnetic Properties of New Lanthanide-Organic Frameworks with $(4^3)_2(4^6,6^6,8^3)$

Topology. *Eur. J. Inorg. Chem.* **2007**, *2*, 3410–3415.

(22) Mahalingam, V.; Vetrone, F.; Naccache, R.; Speghini, A.; Capobianco, J. A. Colloidal Tm^{3+}/Yb^{3+}-Doped $LiYF_4$ Nanocrystals: Multiple Luminescence Spanning the UV to NIR Regions via Low-Energy Excitation. *Adv. Mater.* **2009**, *21*, 4025–4028.

(23) Mahalingam, V.; Naccache, R.; Vetrone, F.; Capobianco, J. A. Sensitized Ce^{3+} and Gd^{3+} Ultraviolet Emissions by Tm^{3+} in Colloidal $LiYF_4$ Nanocrystals. *Chem. - A Eur. J.* **2009**, *15*, 9660–9663.

(24) Chen, G.; Ohulchanskyy, T. Y.; Kachynski, A.; Ågren, H.; Prasad, P. N. Intense Visible and Near-Infrared Upconversion Photoluminescence in Colloidal $LiYF_4$: Er^{3+} Nanocrystals under Excitation at 1490 nm. *ACS Nano* **2011**, *5*, 4981–4986.

(25) Zhang, B. F.; Frigoli, M.; Angiuli, F.; Vetrone, F.; Capobianco, J. A. Photoswitching of Bis-Spiropyran Using near-Infrared Excited Upconverting Nanoparticlesw. *Chem. Commun. Chem. Commun* **2012**, *48*, 7244–7246.

(26) Yi, G. S.; Chow, G. M. Synthesis of Hexagonal-Phase $NaYF_4$: Yb, Er and $NaYF_4$: Yb,Tm Nanocrystals with Efficient up-Conversion Fluorescence. *Adv. Funct. Mater.* **2006**, *16*, 2324–2329.

(27) Vetrone, F.; Naccache, R.; Mahalingam, V.; Morgan, C. G.; Capobianco, J. A. The Active-Core/active-Shell Approach: A Strategy to Enhance the Upconversion Luminescence in Lanthanide-Doped Nanoparticles. *Adv. Funct. Mater.* **2009**, *19*, 2924–2929.

(28) Naccache, R.; Vetrone, F.; Mahalingam, V.; Cuccia, L. a; Capobianco, J. a. Controlled Synthesis and Water Dispersibility of Hexagonal Phase $NaGdF_4$: Ho^{3+}/Yb^{3+} Nanoparticles. *Chem. Mater.* **2009**, *21*, 717–723.

(29) Liu, Q.; Sun, Y.; Yang, T.; Feng, W.; Li, C.; Li, F. Sub-10nm Hexagonal Lanthanide-Doped $NaLuF_4$ Upconversion Nanocyrstals for Sensitive Bioimaging in Vivo. *J. Am. Chem. Soc.* **2011**, 17122–17125.

(30) Vetrone, F.; Mahalingam, V.; Capobianco, J. A. Near-Infrared-to-Blue Upconversion in Colloidal $BaYF_5$: Tm^{3+}, Yb^{3+} Nanocrystals. *Chem. Mater.* **2009**, *21*, 1847–1851.

(31) Yang, D.; Li, C.; Li, G.; Shang, M.; Kang, X.; Lin, J. Colloidal Synthesis and Remarkable Enhancement of the Upconversion Luminescence of $BaGdF_5$: Yb^{3+}/Er^{3+}

Nanoparticles by Active-Shell Modification. *J. Mater. Chem.* **2011**, *21*, 5923.

(32) Dong, N. N.; Pedroni, M.; Piccinelli, F.; Conti, G.; Sbarbati, A.; Ramírez-Hernández, J. E.; Maestro, L. M.; Iglesias-De La Cruz, M. C.; Sanz-Rodriguez, F.; Juarranz, A.; *et al.* NIR-to-NIR Two-Photon Excited CaF_2: Tm^{3+},Yb^{3+} Nanoparticles: Multifunctional Nanoprobes for Highly Penetrating Fluorescence Bio-Imaging. *ACS Nano* **2011**, *5*, 8665–8671.

(33) Huang, X. Enhancement of near-Infrared to near-Infrared Upconversion Luminescence in Sub-10-nm Ultra-Small LaF_3: Yb^{3+}/Tm^{3+} Nanoparticles through Lanthanide Doping. *Opt. Lett.* **2015**, *40*, 5231.

(34) Quintanilla, M.; Cantarelli, I.; Pedroni, M.; Speghini, A.; Vetrone, F. Intense Ultraviolet Upconversion in Water Dispersible SrF_2: Tm^{3+}, Yb^{3+} Nanoparticles: Effect of the Environment on Light Emissions. *J. Mater. Chem. C* **2015**, *Advance*, DOI: 10.1039/c4tc02791d.

(35) Li, X.; Zhang, F.; Zhao, D. Lab on Upconversion Nanoparticles: Optical Properties and Applications Engineering via Designed Nanostructure. *Chem. Soc. Rev.* **2015**, *44*, 1346–1378.

CHAPTER 2

LITERATURE SURVEY

2.1 Upconversion nanomaterials' applications

2.1.1 Optical applications for UCNCs

Upconversion nanomaterials convert near infrared (NIR) light into visible light. Upconversion nanomaterials hence can be used as lighting sources and in display devices, and for anti-counterfeiting and fingerprint analysis.

2.1.1.1 Upconversion nanomaterials for lighting

Bulk scale upconversion materials play an increasingly important role in lighting, such as lanthanide ion doped transparent glass[1], films[2–4], and polymers[5].

For most common silica-based glass, high transparency and high mechanical stability are advantageous. A new method for combining lanthanide ions with glasses was reported by Suzuki *et al*[6]. They proposed a flux coating method for coating $NaYF_4$: Ln^{3+} (Ln^{3+}=Yb^{3+}, Er^{3+} and Tm^{3+}) nanocrystals onto glass, which provided a new route for constructing upconversion layers in functional devices more directly.

A sol-gel method has often been used for the production of inorganic thin films containing lanthanide UCNCs. For example, Sivakumar *et al.*[7] proposed a SiO_2 thin film incorporating LaF_3 nanocrystals, to realize NIR to red and green upconversion emission[8].

Polymers such as polymethyl methacrylate (PMMA) and polydimethylsiloxane (PDMS), have been used as optical displays materials in recent years[6]. This kind of upconversion nanocomposites are stable, can be easily synthesized by an *in-situ* polymerization route and do not need any further postdeposition heating, as shown in **Figure 2.1 (a)** and **(b)**.

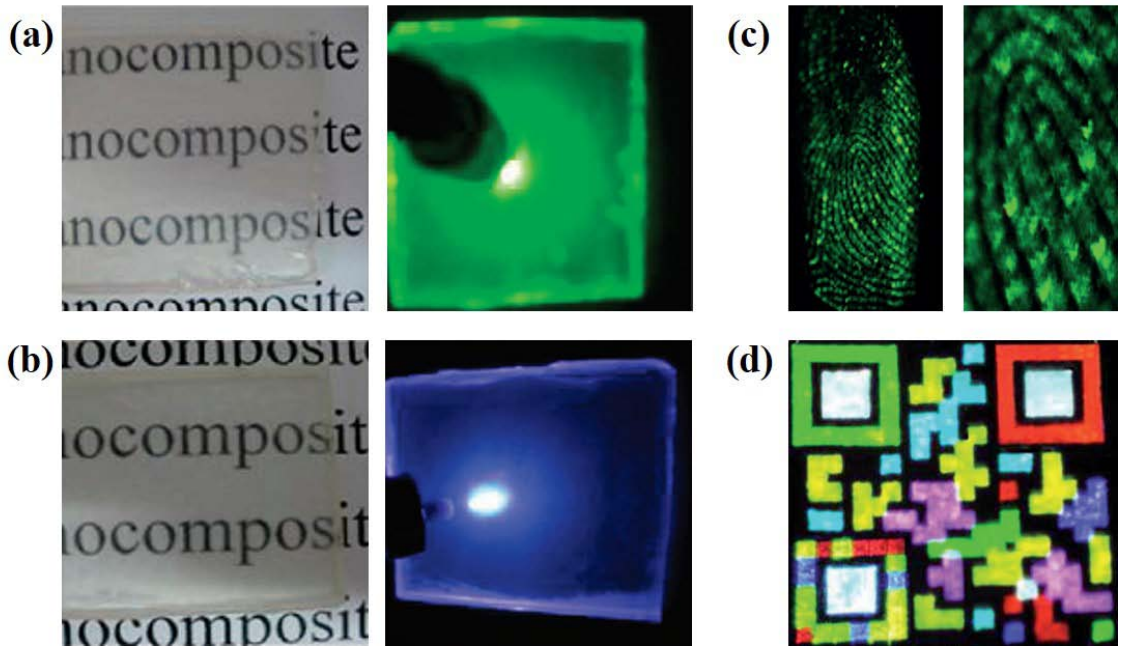

Figure 2.1 Examples of UCNCs used for imaging: photographs of the β-$NaYF_4$: Er^{3+}/PMMA (a) and β-$NaYF_4$: Tm^{3+}/PMMA (b) under 980 nm laser excitation[5]; (c) fingermark through the use of UCNCs[9]; (d) Multicolour barcode red-green-blue (RGB) printing by using UCNCs[10].

2.1.1.2 UCNCs use in colour display devices and its use as anti-counterfeiting technology

Another anticounterfeiting application is fingerprint detection[17–19].For example, Ma *et al.* proposed to use $NaYF_4$[12] and YVO_4[13] nanocrystals for fingermark detection, because it shows good sensitivity and selectivity.

2.1.2 UCNCs use as an energy source

Upconversion materials can be used as a second excitation source because of their high upconverted photon energy. This has been developed in solar cells, reaction catalysts and data storage[15–20].

2.1.2.1 UCNCs applied to solar technology

Solar cells cannot fully utilize energy from sunlight because of spectral mismatch, especially in the lower energy range of NIR. Upconversion nanomaterials can improve

the efficiency of absorption by solar cells because they can convert this lower energy to higher energy. Recently, upconversion materials have been reported which, combined with silicon solar cells, are used in solar power applications[21–23]. The efficiency enhancement of solar cells by UCNCs remains small owing to the relatively low upconversion efficiency. For example, Gibart *et al.*[22] reported 2.5 % enhancement in efficiency from a Ti-sapphire NIR laser under 891 nm, and Shalav *et al.*[21] obtained the same effect of 2.5 % under 1523 nm laser by using $NaYF_4$ UCNCs.

Another kind of novel solar cells using upconversion nanomaterials, dye-sensitized solar cells[24,25], was proposed recently, but the photocurrent density increase not obvious as well. For example, Chen *et al.*[25] proposed a film to introduce UCNCs into a conventional dye-sensitized solar cell, which achieved only 0.47 mW output under a 1W, 980 nm excitation laser. Hence, upconversion nanomaterials for solar cell applications still have several challenges to overcome[23].

2.1.2.2 UCNCs for use in photocatalysis

Semiconductor photocatalysis plays an important technical role in environmental remediation and solar energy conversion. UCNCs can serve as a light converter, providing a transfer of photons from NIR to ultraviolet (UV) and/or visible emissions. The most commonly used composite photocatalysts are UCNCs with TiO_2, excited under 980 nm laser, because TiO_2 is non-toxic, low cost, and chemically stable[26,27]. Other types of composite photocatalyst materials have been proposed such as CaF_2: $Ln^{3+}/BiVO_4$ (Ln^{3+}=Yb^{3+}/ Tm^{3+}/ Ho^{3+})[28] and g-C_3N_4/$NaYF_4$: Tm^{3+} [29], which can be activated under both visible light and NIR light by simulated sunlight.

2.1.2.3 UCNCs for data storage

Upconversion emission signals can be read by confocal imaging, and can thus be used in an optical memory system for rewriting or re-reading. For example, Zhang *et al.*[19] proposed a kind of re-writing using UCNCs with diarylethenes, which combine diarylethenes' reversible photoisomerization properties with upconversion nanomaterials' NIR readout window. An important topic currently for data storage is photoswitchable nanomaterials, using two types of lanthanide UCNCs for two-photon fluorescence microscopy[15], as shown in **Figure 2.2**.

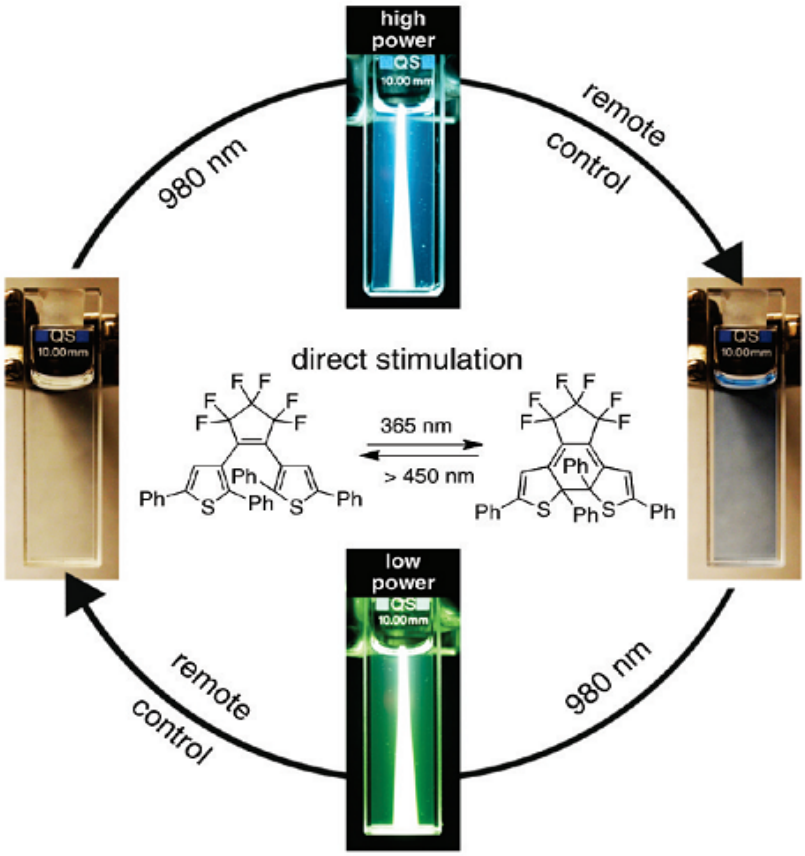

Figure 2.2 Bidirectional photoswitching of a Tetrahydrofuran (THF) solution of dithienylethenen, dispersed with Tm^{3+}/Er^{3+} codoped core-shell-shell nanocrystals, by varying NIR light[15].

2.1.3 Biosafety and bioimaging applications of UCNCs

UCNCs have several advantages for bio-applications such as detection in an auto-fluorescence free environment[30], narrowband luminescence, non-blinking and long luminescence lifetimes[31]. At the same time, a number of *in vivo* toxicity studies have been reported[32–38].

2.1.3.1 Toxicity studies of UCNCs in biological systems

Most studies of upconversion nanomaterials' toxicity have been reported in cell cultures and small animals[39]. For example, Xing *et al.*[40] reported that $NaYbF_4$ has no damaging or toxic effects on organs as a result of lengthy testing *in vivo*. Gd^{3+} based UCNCs can be used in magnetic resonance imaging (MRI) and their toxicity has been widely studied[41–43]. For example, Yang *et al.*[35] proposed Sm^{3+} doped $Gd(OH)_3$

nanorods as an MRI contrast agent: no adverse effect was reported in mice, in long-term studies (150 days) by injection of up to 100 mg/kg of $Gd(OH)_3$ nanorods.

Bio-functionalization or bio-conjugation upconversion nanomaterials, such as poly(ethylene glycol) (PEG)[44,45], poly(ethylene imine) (PEI)[38,46], SiO_2[47], poly(acrylic acid) (PAA)[48], are reported to exhibit little or no toxicological effects; and are accordingly safe for bio-applications. Many studies have accordingly focused on the toxicity or safety of modified UCNCs. For Caenorhabditis elegans (*C. elegans*), typically, Chen *et al.*[49] reported that no significant harmful effect on *C. elegans* was observed after treatment with 1 mg/mL $NaYF_4$ coated with PEI was observed after 3 hours. They also showed that it has no toxicological effect when there is a difference in size and shape or surface ligands of nanocrystals on *C. elegans* and their progeny. For zebrafish, Wang *et al.*[50] reported that LaF_3 coated with SiO_2 nanocrystals has no toxicological effects after injection of up to 100 μg/mL into zebrafish. Jang *et al.*[37] reported no changes in zebrafish when injected with $NaYF_4$ lanthanide doped nanocrystals, which showed 10 times lower toxicity than quantum dots (QDs) by comparison to the control group (Nanodot HE-series).

In a typical mouse study, Cheng *et al.*[51] reported that $NaYF_4$ nanocrystals coated with PAA resulted in no organ damage or lesion occurrence in mice after injection with 20 mg/kg. Chatterjee *et al.*[38] proposed the $NaYF_4$ nanocrystals coated with PEI accumulated and reduced in the lungs within 24 hours and were undetectable after 7 days in mice. For determination of long-term of toxicity, Xiong *et al.*[34] tested toxicity in mice after injection with $NaYF_4$ coated with PAA nanocrystals, for 24 hours, two weeks and four months. The results showed no apparent symptoms of health deterioration.

2.1.3.2 The use of UCNCs for *in vitro* and *vivo* bioimaging

Several kinds of small molecule-modified UCNCs have been selected as bioimaging probe candidates[52]. For example, SiO_2[53–55] coated UCNCs are commonly used for imaging of living cells. Lanthanide nanocrystals coated with PEG[56–58], PEI[59], PAA[59], polyvinylpyrrolidone (PVP)[60] and 3-mercaptopropionic acid[47] are also used as cell imaging labels. Among these surface modifications, surface charge can change the cell uptake significantly. Jin *et al.*[61] proposed that positively charged polymer modified

nanocrystal displayed greatly enhanced cellular uptake compared with negatively charged nanocrystals.

The upconversion luminescence bioimaging of living cells can be realized at the single crystal level since the crystals have no autofluorescence. For example, Zhang *et al.*[62] used confocal microscopy to analyze UCNCs individually (**Figure 2.3 (a, b)**), and Shan *et al.*[63] proposed visible emission at single nanocrystal-level cell imaging, by using PAA modified $NaYF_4$ nanocrystals, as shown in **Figure 2.3 (c)**.

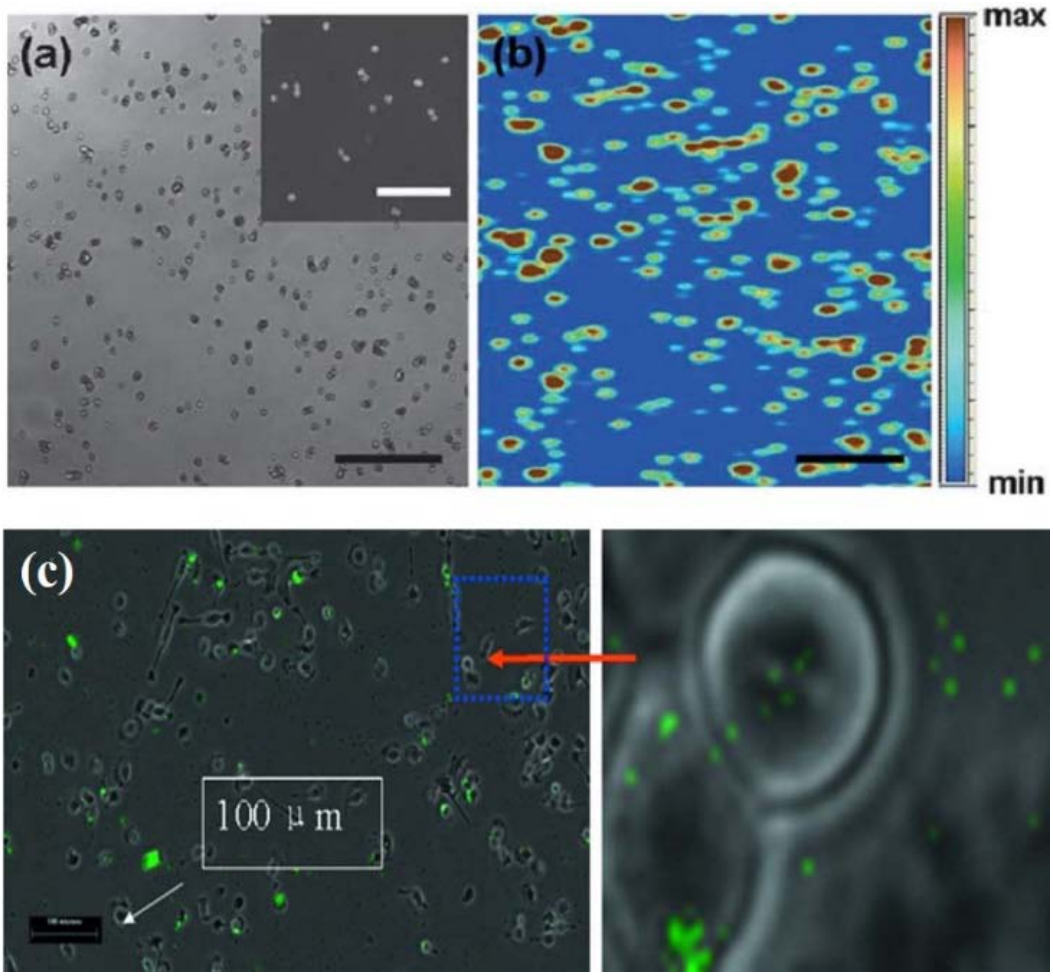

Figure 2.3 (a) Reflection image of $NaYbF_4$ nanocrystals on a glass substrate; (b) Confocal photoluminescence image of the crystals showed in (a)[62], Scale bar is 25 mm and 5mm for the (a) inset; (c) NIR imaging of $NaYF_4$: Er^{3+} nanocrystals incubating with cells[63].

In addition to cells, *C. elegans* has developed to an important model in biomedical applications. Lim *et al.*[36] first proposed $NaYF_4$ UCNCs imaging in *C. elegans* (shown in **Figure 2.4 (a-c)**); several other researchers reported that higher crystal concentration,

smaller crystal size and longer incubation times result in brighter and longer imaging time in *C. elegans* bodies[33,49]. Two other widely-used models are the Lymphatic and Vascular systems. Lymphatic imaging can be created by UCNCs without extra postprocessing[64,48]. Vascular imaging has been reported in mice through a tail vein injection (shown in **Figure 2.4 (d-e)**)[65]. An optical sectioning depth of 100 μm can be obtained by using 800 nm upconversion emission of mice brain blood vessels. For small animals, whole-body upconversion imaging of nude mice[66,67] and rabbit[68] have been proposed.

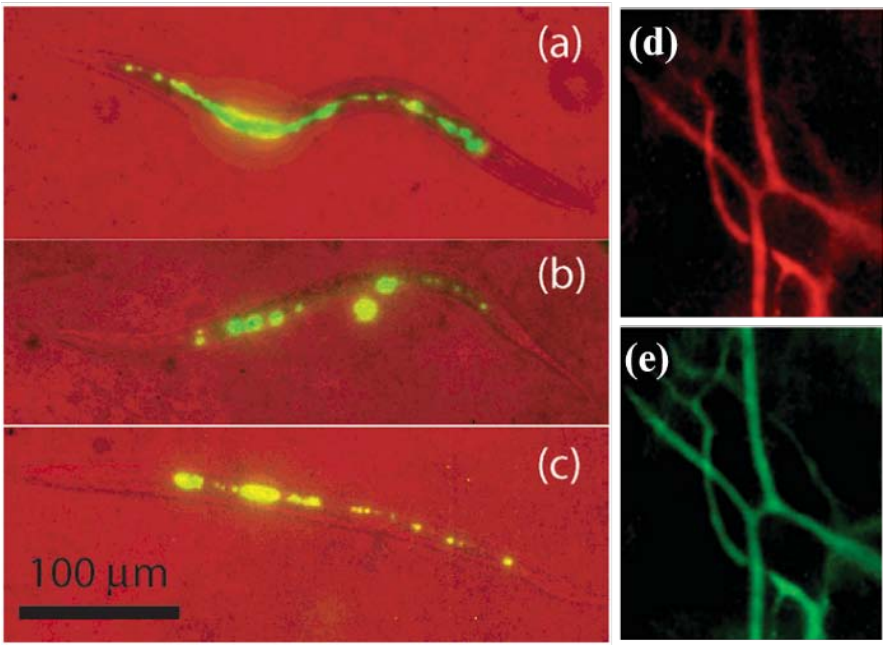

Figure 2.4 (a-c): Two-photon images, under 980 nm excitation, of *C. elegans* after different periods of food deprivation: (a) 0 hour, (b) 4 hours, (c) 24 hours[36]; (d-e): Optical imaging of blood vessels with Y_2O_3 UCNCs under (d) 980 nm excitation and (e) 737 nm excitation[65].

2.1.3.3 UCNCs used as a luminary in tracking and targeting

Single nanocrystal tracking can help researchers to better understand the route of drug delivery, cellular dynamics, and transport phenomena[69,70]. Some tracking applications have been proposed by using QDs[71] and carbon nanotubes[71]. Currently, UCNCs are reported to be used as tracking tools for cells. For example, Idris *et al.*[72] reported tracking in myoblast cells over 4 hours by using SiO_2 coated $NaYF_4$

nanocrystals. Xiang *et al*. demonstrated tracking processes in a tumor for 7 days[53] and from the liver to the lung by using oligo-arginine modified $NaYF_4$ nanocrystals[54].

Tumor diagnosis and therapy by tumor-targeted imaging[73] is another application of upconversion nanomaterials. Usually, upconversion targeted imaging by using UCNCs conjugated with folic acid[74,75], antibodies[76–78] and peptide[79,80]. For example, Liu *et al*.[81] reported that folic acid modified $NaYF_4$ nanocrystals could target a tumor in a bearing athymic nude mice for more than 24 hours after being injected into HeLa. Wang *et al*.[77] proposed SiO_2 modified $NaYF_4$ nanocrystals conjugated with anti-Her2 antibodies for targeting SK-BR-3 cells. Kumar *et al*. used anti-claudin 4 and anti-mesothelin modified $NaYF_4$ nanocrystals for delivery to cancer cells *in vivo*[78].

2.1.4 The use of UCNCs as sensors

Upconversion nanomaterials can be used as luminescent probes for several kinds of the detector such as nanothermometers[82], pH sensors[83], small molecules[84–86] and DNA/RNA[87]. Some workers have proposed that lanthanide ions are temperature sensitive and can be developed as nanothermometers. For example, Wang *et at*[88]. found that ZnO: Er^{3+} nanocrystals have thermal sensitivity and exhibit temperature-dependent upconversion luminescence phenomena. Similar temperature sensitivity phenomena have been observed in liquids and cells[89]. Nanocrystals such as $NaYF_4$[90,91], CaF_2[92], $Yb_2Ti_2O_7$[67] and Y_2O_3[93] have been reported as good candidates for nanothermometers, but none have been directly applied *in vivo* yet. UCNCs are also potentially useful as pH sensors. For example, Sun *et al*.[94] reported that $NaYF_4$ nanorods' upconversion emission intensity can be affected by pH from 6 to 10, within 30 seconds. Zhang *et al*.[83] reported that $NaYF_4$ assembled Au nanocrystals' emission wavelength can be changed by changing the pH value: 619 nm emission under pH 3 can change to 523 nm by changing pH to 11. This results from the Au nanocrystals' assembling and disassembling under different pH values.

Generally, the biomedical applications of upconversion have been widely researched in X-ray computed-tomography (CT) imaging[95–97], positron-emission-tomography (PET) imaging[98], single-photon emission computed tomography (SPECT) imaging[99–101] and photodynamic therapy (PDT)[74,75].

2.2 The fabrication and tunability of nanocrystals

Several methods for synthesis of UCNCs are available, such as high-temperature solid state methods, sol-gel methods, co-precipitation methods, hydrothermal methods, thermal decomposition methods, combustion methods, and ionic liquids-based methods. Some methods are for bulk materials and some are for solvent materials. In these approaches, controlling the outcome of nanocrystal fabrication has developed rapidly and enabled the tuning of nanocrystals to a specific size, shape and with specific surface properties necessary for their various applications. Some of these methods are described below in more detail.

2.2.1 The coprecipitation approach to UCNCs fabrication

Coprecipitation of particles is a common method used for the synthesis of nanocrystals that are lanthanide-doped. Compared to other approaches, it can be carried out with low-cost equipment. Veggel *et al.*[102] used this method to synthesize LaF_3 nanocrystals. Yi *et al.*[55] first reported using this method to synthesize $NaYF_4$ UCNCs. With the development of this method, Heer *et al.*[82] produced transparent and soluble *β*-phase $NaYF_4$ UCNCs by using a relatively low temperature. Li and Zhang[103] synthesized $NaYF_4$: Yb^{3+}, Er^{3+}/Tm^{3+} which does not need excessive amounts of fluoride reactants at high temperatures, thus decreasing volatile fluorinate: as a result, the nanocrystals' morphology is much more homogeneous. Nanocrystals synthesized by coprecipitation are shown in **Figure 2.5**.

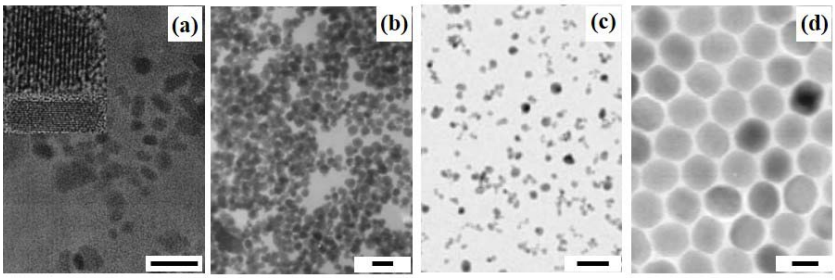

Figure 2.5 Transmission electron microscope (TEM) images of UCNCs. (a) LaF_3 nanocrystals prepared by Veggel *et al.*[102] (b) $NaYF_4$ nanocrystals prepared by Yi *et al.*[55] (c) $NaYF_4$ nanocrystals prepared by Heer *et al.*[82] (d) NaYF4: Yb^{3+}, Er^{3+}/Tm^{3+} nanocrystals prepared by Li and Zhang[103]. Scale bar: (a) and (d) are 20 nm, (b) and (c) are 100 nm.

2.2.2 Thermal decomposition procedures for making UCNCs

This is used to decompose one substance to two constituents on heating. It typically requires the use of an organic compound as a solvent. Zhang *et al.*[104] first reported a synthesis of triangular LaF_3 nanoplates by using this method. Mai *et al.*[105] subsequently reported the synthesis of high quality, monodispersed cubic phase $NaREF_4$ (RE = Pr^{3+} to Lu^{3+}, Y^{3+}) by using acetate precursors. This process also allowed the synthesis of UCNCs of either α or β phase $NaYF_4$. Mai *et al.* found that β-$NaYF_4$ can be formed from α-$NaYF_4$ by an Ostwald ripening process[106]. Ehlert *et al.*[107] synthesized a series of rare earth ions codoped with $NaYbF_4$ nanocrystals; Du *et al.*[108] synthesized a series of metal ions codoped with $NaMF_3$ (M = Mn^{2+}, Ni^{2+}, Co^{2+}, Mg^{2+}) nanocrystals and $LiMAlF_6$ (M = Ca^{2+}, Sr^{2+}) nanocrystals, also by using this method. Shan *et al.*[109] reported that tributylphosphine oxide could be used as the single solvent instead of oleic acid (OA)/1-octadecene (ODE) solvent or OA/ODE/oleylamine (OM) solvent. Chen *et al.*[110] synthesized $NaYF_4$ nanocrystals by using RE-oleate precursors. Nanocrystals synthesized by thermal decomposition are shown in **Figure 2.6**.

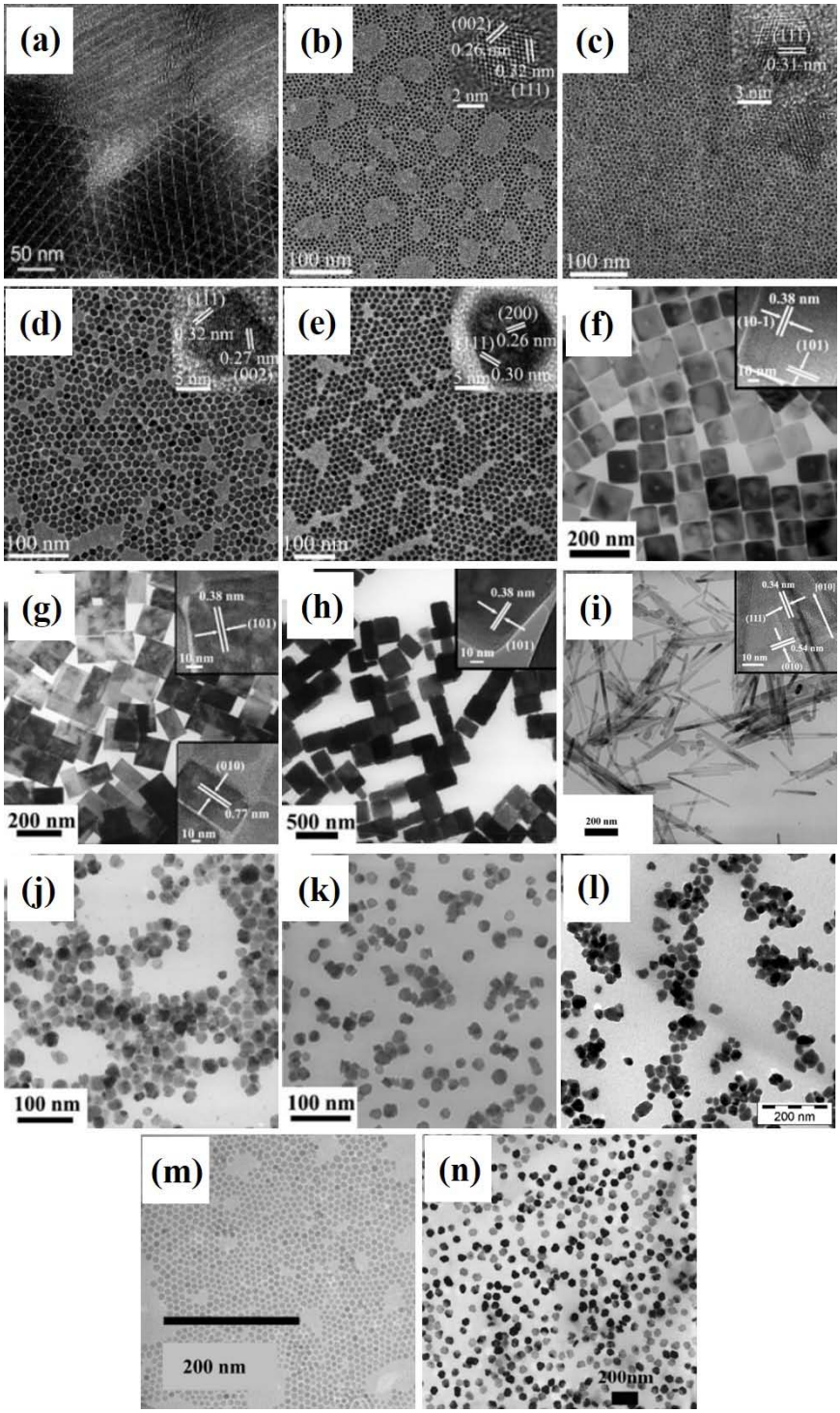

Figure 2.6 TEM images of UCNCs: (a) LaF_3 nanoplates prepared by Zhang *et al.*[104]; (b-e) $NaREF_4$ (ER= Nd^{3+}, Eu^{3+}, Y^{3+} and Yb^{3+}) nanocrystals prepared by Mai *et al.*[105] by using acetate precursors; (f-i) $NaMF_3$ (M= Mn^{2+}, Ni^{2+}, Co^{2+}, Mg^{2+}) nanocrystals, (j) $LiCaAlF_6$ nanocrystals and (k) $LiSrAlF_6$ nanocrystals prepared by Du *et al.*[108]; (l) $NaYbF_4$ nanocrystals prepared by Ehlert *et al.*[107]; (m) $NaYF_4$ nanocrystals prepared by Shan *et al.*[111] in TOPO at 360 ˚C; (n) $NaYF_4$ nanocrystals prepared by Chen *et al.*[110].

2.2.3 Hydrothermal methods for making UCNCs

Hydrothermal synthesis methods use high temperatures and high pressures. Unlike the thermal decomposition method, hydrothermal methods can use water based systems and can be synthesized in inorganic materials. In this way, various morphologies of UCNCs can be synthesized and controlled. Classical work using this method has been reported by Liang *et al.*[112], who prepared $NaHoF_4$ and $NaSmF_4$; and Zeng *et al.*[113], who prepared $NaYF_4$ nanocrystals dispersed in acetic acid and ethanol. Nanocrystals fabricated by hydrothermal methods can be synthesized in morphologies such as nanorods, nanotubes, nanodisks and flower shape nanocrystals[114] as shown in **Figure 2.7**.

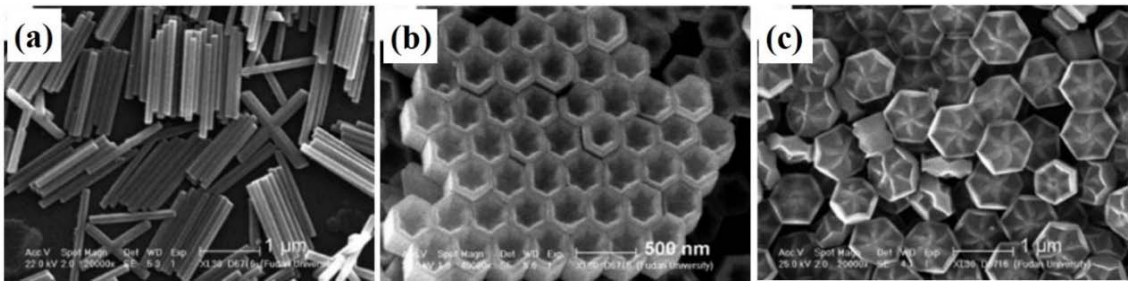

Figure 2.7 Scanning electron microscope (SEM) images of $NaYF_4$ nanocrystals with various morphologies: (a) nanorods, (b) nanotubes and (c) flower-patterned nanocrystals, prepared by Zhang *et al.*[114].

2.2.4 Sol-gel methods for making UCNCs

Sol-gel methods are widely used in oxide and fluoride nanocrystals. In this method, nanocrystals comprised of sol and agglomerate are added to another kind of gel which can form a large molecule. The crystal forms by subsequently removing the solvents from the gel by calcination. Patra *et al.* synthesized ZrO_2[115], TiO_2 and $BaTiO_3$[116] by using titanium isopropoxide and barium acetate sol precursors. Other upconversion materials such as $Gd_3Ga_5O_{12}$[117] and $Lu_3Ga_5O_{12}$[118] also can also be synthesized by this method. As shown in **Figure 2.8**, the morphologies and sizes of these nanocrystals are not easily controllable and the crystals are likely to aggregate.

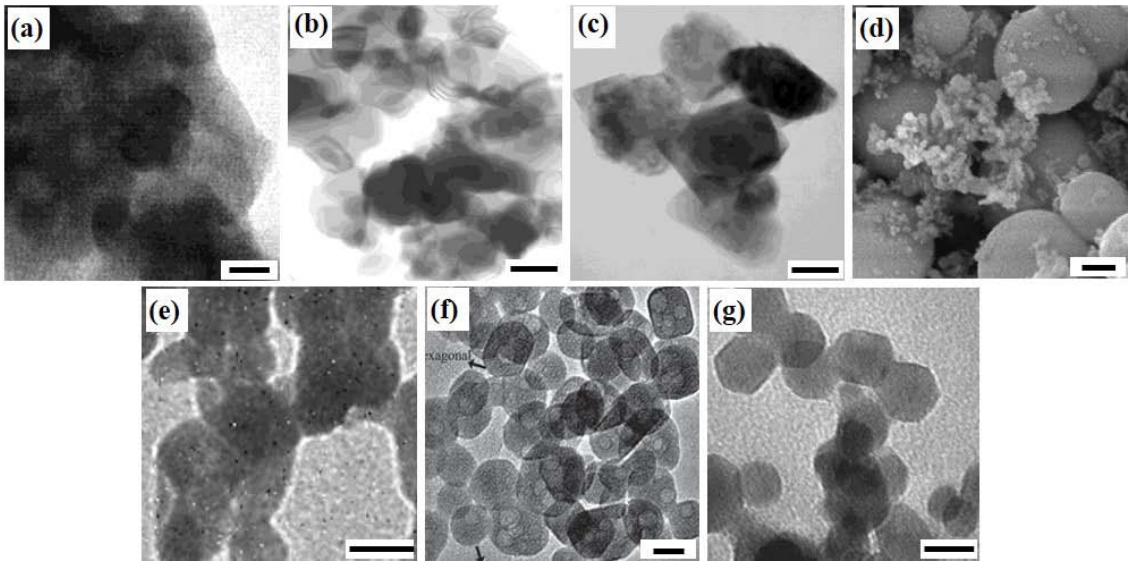

Figure 2.8 TEM images of (a) ZrO_2 (b) TiO_2 and (c) $BaTiO_3$ nanocrystals prepared by Patra *et al.*[115,116]; (d) SEM image of $Gd_3Ga_5O_{12}$ nanocrystals prepared by Daldosso *et al.*[117]; (e) TEM image of $Lu_3Ga_5O_{12}$ nanocrystals prepared by Mahalingam *et al.*[118] prepared by Sol-gel method; (f) $NaYF_4$ nanocrystals prepared by Liu *et al.*[119] using the ionothermal method; (g) Y_2O_3 nanocrystals prepared by Ju *et al.*[120] using a flame synthesis method. Scale bar: (a) 20 nm, (b) 200 nm, (c) 40 nm, (d) 500 nm and (e-g) 25 nm.

2.2.5 Other methods for making UCNCs

A new method which is more environment-friendly, the ionothermal method, has been proposed by Liu *et al.*[119]. This method can synthesize water-soluble pure $NaYF_4$ nanocrystals, as shown in **Figure 2.8 (f)**. The advantage of this method is that the synthesis process requires only a low vapor pressure and is nonflammable; the disadvantage is that the morphology of the synthesized nanocrystals is not easily controllable and there is a broad size distribution.

Combustion synthesis is a rapid synthesis method using exothermic reactions at a relatively low temperature. The combustion method can be used for the synthesis of upconversion phosphor powder such as $Gd_3Ga_5O_{12}$[121], $Er_3Al_5O_{12}$[122], Y_2O_3[123] and Gd_2O_3[124]; the last mentioned is shown in **Figure 2.8 (g)**. Another method which is widely used for the synthesis of upconversion phosphor powder is flame synthesis. Flame synthesis is a similar process which is faster and lower in cost. Flame synthesis has been reported by Ju *et al.* for the preparation of Y_2O_3[120], La_2O_3 and Ga_2O_3[125].

The new synthesis methods described above are quicker, more convenient and lower in cost than traditional synthesis methods, but the nanocrystal quality is not as good. Crystal size and morphology is typically non-homogeneous; crystal aggregation occurs readily. As a result, these new methods are commonly used only to synthesize powder samples.

2.3 The mechanism of nanocrystals nucleation and growth

2.3.1 Classical nucleation

In classical nucleation theory, nucleation can occur by homogeneous nucleation or heterogeneous nucleation. Homogeneous nucleation occurs in the pure material; heterogeneous nucleation relies on nucleation at impurities. Only homogeneous nucleation is described here. The free energy curve for nucleation shown in **Figure 2.9**.

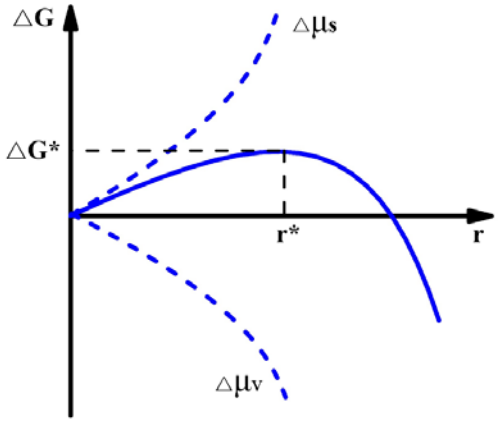

Figure 2.9 Free energy curve for nucleation[95].

Nanocrystal nucleation occurs owing to a reduction in Gibbs free energy[96], defined by:

$$\Delta G = \Delta\mu_V + \Delta\mu_S \tag{2.1}$$

Where $\Delta\mu_V$ is the change in volume energy and $\Delta\mu_S$ is the change in surface energy. They can be defined as:

$$\Delta\mu_V = \frac{4}{3}\pi r^3 \Delta G_v \tag{2.2}$$

$$\Delta\mu_S = 4\pi r^2 \sigma \tag{2.3}$$

Where r is the radius, σ is the surface energy per unit area

As **Figure 2.9** shows, when r is small, the surface energy will dominate the reaction which means that ΔG will become more positive as r increases. When r is bigger than a critical size r^*, the volume energy will dominate the reaction which means that ΔG will decrease as r increases. At the point $r = r^*$, $\Delta G = \Delta G^*$ is At the maximum. Deriving the critical size, r^*:

$$\frac{d\Delta G}{dr} = 4\pi r^2 \cdot \Delta G_V + 8\pi r \cdot \sigma = 0 \tag{2.4}$$

$$r^* = -\frac{2\sigma}{\Delta G_V} \tag{2.5}$$

Therefore, when $r < r^*$, the nucleus will dissolve into the solution. Nuclei smaller than r^* are called embryos. When $r > r^*$, ΔG decreases, i.e. the system's Gibbs free energy decreases. The nucleus with $r > r^*$ is therefore stable and can continue to grow. If the nucleus $r = r^*$, it can be dissolved or grow bigger, depending on whether extra energy is available. The nucleation process must thus overcome the energy barrier ΔG^* to form a stable nucleus. This critical energy ΔG^* can be defined with **Equation 2.1** and **2.5**:

$$\Delta G^* = \frac{4}{3}\pi\left(-\frac{2\sigma}{\Delta G_V}\right)^2 \cdot \Delta G_V + 4\pi\left(-\frac{2\sigma}{\Delta G_V}\right)^2 \cdot \sigma = \frac{1}{3}(4\pi r^{*2} \cdot \sigma) \tag{2.6}$$

From **Equation 2.6**, it can be seen that the nucleus reaches the critical energy when the nucleation energy reaches 1/3 of the surface energy.

Every unit volume of changing Gibbs free energy depends on the solution concentration.

$$\Delta G_V = -\frac{kT}{\partial} l_n \frac{C}{C_0} \tag{2.7}$$

Where ∂ is the atomic volume, C is the solute concentration, C_0 is the equilibrium concentration. This equation shows that nucleation occurs spontaneously when $C > C_0$.

The mechanism of crystal nucleation and growth was proposed by LaMer and Dinegar in 1950[97]. Commonly, this is divided into 3 stages, as **Figure 2.10** shows.

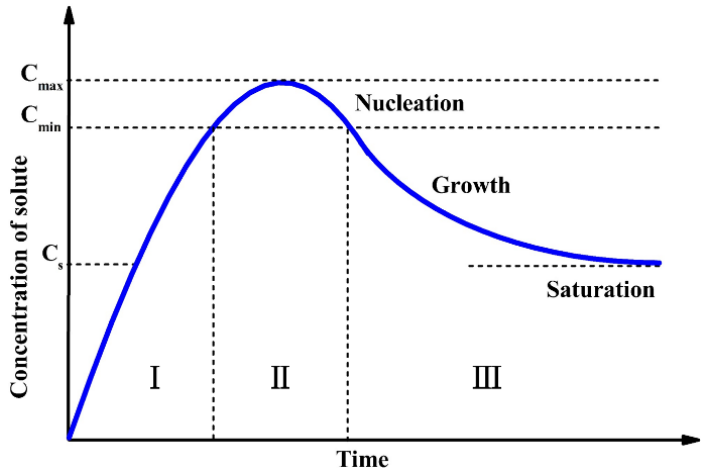

Figure 2.10 LaMer diagram schematic[97].

In Stage Ⅰ, the concentration of solute increases rapidly, but no nucleation occurs. Nucleation occurs when time increases (and the solute concentration increases). In Stage II, the solute becomes supersaturated and the nucleus forms. In Stage Ⅲ, growth occurs. With the solute concentration and supersaturation decreased, the volume Gibbs free energy will be reduced and no more nuclei formed.

2.3.2 Crystal nucleation and growth explained

The Au nanocrystal synthesis process proposed by Polte *et al.*[126] represents the classical nucleation and growth process, as shown in **Figure 2.11**. First, the initial Au salt forms nucleation crystals which are less than 2 nm in diameter. Second, the nucleation crystals grow by aggregation to about 3 nm, i.e. reach the critical radius, and further grow to about 6 nm by Ostwald ripening[127]. Finally, the crystals grow to about 8 nm by precipitation from the supersaturated solution.

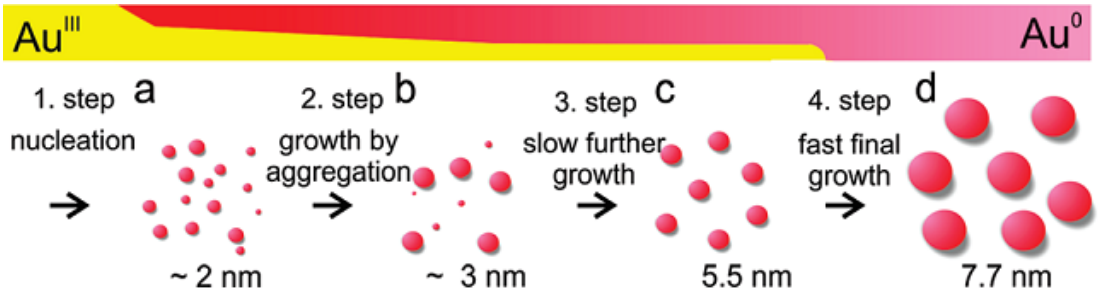

Figure 2.11 Schematic of gold nanocrystal formation and growth process[126].

The Ostwald ripening mechanism mentioned above was first proposed in 1897 by Ostwald[98]. The theory of Ostwald ripening is, small nanocrystals are more likely to dissolve into a solution, whereas large nanocrystals are likely to grow bigger by using the salt from the dissolved small crystals. The precondition for this phenomenon is that the two kinds of crystals should have a large size difference since the volume Gibbs free energy should be significantly different[128]. Gao *et al.*[129] proposed that the $NaYF_4$: 30% Mn^{2+}, 1% Er^{3+} bundle-shaped microtube synthesis is based on the Ostwald ripening process. Similarly, Johnson *et al.*[130] proposed that homogeneous $NaYF_4$ nanocrystals can be fabricated with layer-by-layer epitaxial growth, based on Ostwald ripening, as shown in **Figure 2.12**.

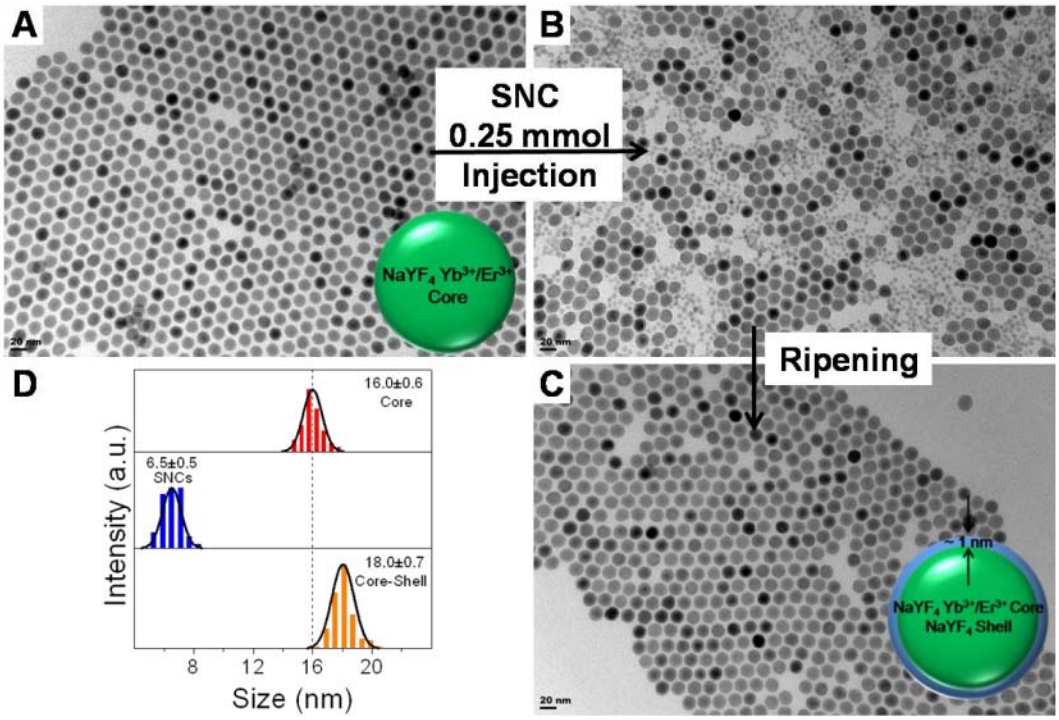

Figure 2.12 Schematic of $NaYF_4$: 15% Yb^{3+}, 2% Er^{3+} nanocrystal grow process via Ostwald ripening[130]. (A) $NaYF_4$ core nanocrystals, (B) after injection of α-$NaYF_4$ shell nanocrystals, (C) after self-focusing $NaYF_4$ core-shell nanocrystals and (D) size distribution of the core and core-shell nanocrystals.

2.3.3 The nucleation of $NaYF_4$ nanocrystals

For $NaYF_4$ nanocrystals, two different phases can be synthesized: a cubic (α) phase and a hexagonal (β) phase. The α-$NaYF_4$ phase is metastable at a high temperature and the β-$NaYF_4$ is thermodynamically stable at high temperature. In

$NaYF_4$ the change from α to β is thus thermodynamically governed when it is heated to 298 °C. As reported by Suter *et al*, **Figure 2.13** shows $NaYF_4$ changing from α to β phase as it is heated to this temperature.[131]

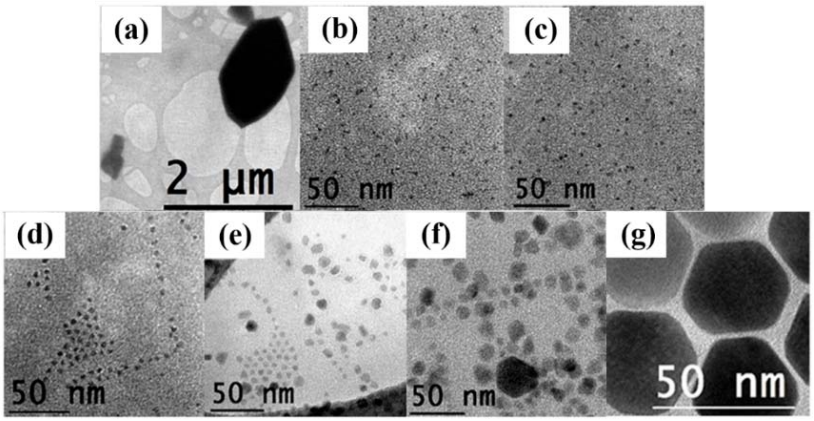

Figure 2.13 TEM images of β-$NaYF_4$ during the synthesis process, at different temperatures: (a) T = 179 °C; (b) T = 245 °C; (c) T = 298 °C for 33 min; (d) T = 298 °C for 77 min; (e) T = 298 °C for 94 min; (f) T = 298 °C for 124 min; (g) T = 298 °C for 140 min[131].

The $NaYF_4$'s crystals' growth mechanism differs from the classical mechanism model because of the α-β phase change it undergoes as it is heated and this is shown in **Figure 2.14**.

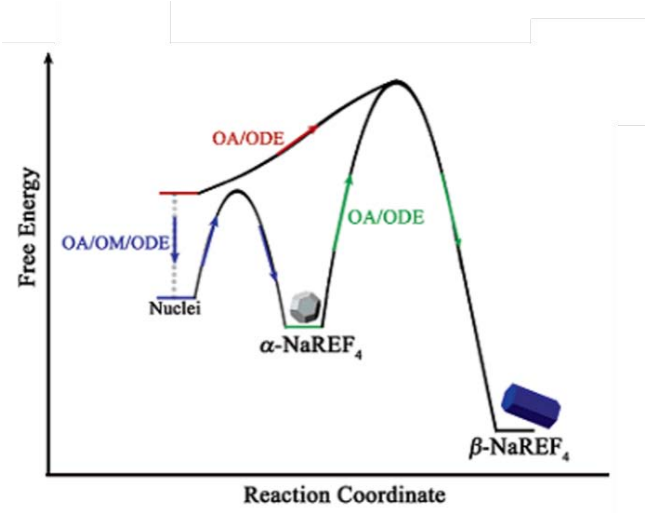

Figure 2.14 A schematic of the free energy as a function of the reaction coordinate for $NaYF_4$ nanocrystals is shown[105].

The α-$NaYF_4$ nanocrystals' nucleation energy barrier is lower than α-β $NaYF_4$, hence the synthesis of β $NaYF_4$ requires the input of additional energy.

2.4 Nanocrystals with different phase, morphology, and size

2.4.1 Different phases in $NaYF_4$ nanocrystals

UCNCs' phase can change not only with temperature change but also with changes in the ratio of dopant ions or changes in the reaction solution.

Mao *et al.*[132] proposed that different Li^+ and Na^+ dopant ratios can change $Li_xNa_{1-x}YF_4$ nanocrystals from the hexagonal phase to the tetragonal phase, as shown in **Figure 2.15 (g)**. With greater Li^+ doping, the phase was reported to change from hexagonal phase (<30% Li^+) to tetragonal phase (>70% Li^+). Mao *et al.*[132] proposed two reasons for this phase change. (1) The alkalinity of the solution is weakened by doping with LiOH since NaOH's alkalinity is stronger than LiOH. The growth of *β* $NaYF_4$ occurs along the [0001] facets through selective adsorption. (2) The ionic radius of Li^+ is smaller than that of Na^+ so that on the addition of further Li^+, the octahedron is enclosed by lower energy planes (111), which means it can easily form the tetragonal phase.

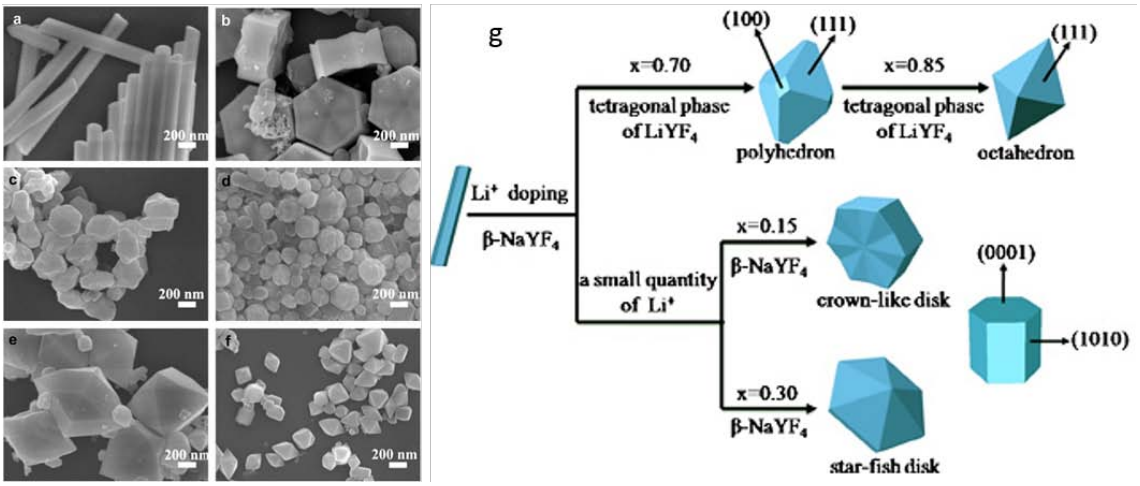

Figure 2.15 (a)-(f), SEM images of $Li_xNa_{1-X}YF_4$ nanocrystals: (a) x = 0; (b) x = 0.15; (c) x = 0.30; (d) x = 0.50; (e) x = 0.70; (f) x = 0.85. (g) schematic of the formation process of different morphologies of synthesized $Li_xNa_{1-X}YF_4$ nanocrystals[132].

Shan *et al.*[133] proposed that a different oleic acid (OA) to tributylphosphine (TOP) ratio can change the $NaYF_4$ nanocrystals' phase from cubic phase to hexagonal phase, as shown in **Figure 2.16**. Increased TOP is seen in **Figure 2.16 (f)** to cause the phase to

change from α-$NaYF_4$ to β-$NaYF_4$. Shan *et al.*[133] reported that the OA can react with TOP at high temperature, allowing the formation of a ligand with different coordination properties. This can reduce the phase transfer energy barrier, and hence favor formation of the hexagonal phase.

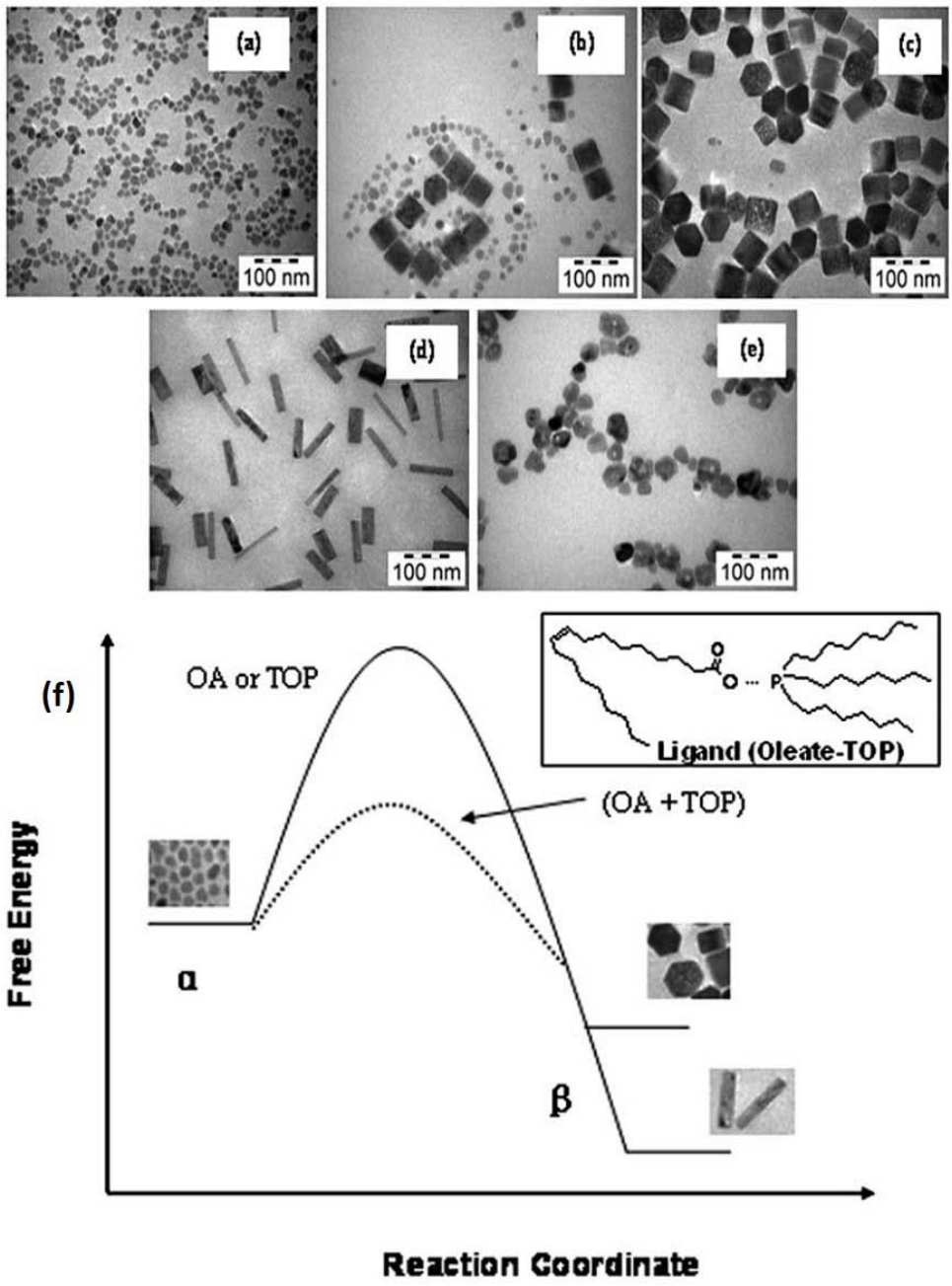

Figure 2.16 (a)-(e), TEM images of $NaYF_4$ with different OA/TOP solution ratios: (a) TOP=0; (b) OA/TOP=4:1; (c) OA/TOP=1:1; (d) OA/TOP=1:4; (e) OA=0. (f) Schematic of synthesis of $NaYF_4$ shows (f) as a function of the TOP reaction coordinate in OA/ODE[133].

2.4.2 Different morphologies of nanocrystals

The morphology of nanocrystals can change as a result of the dopant concentration of different rare materials such as Nd^{3+}, Yb^{3+}, Er^{3+} doped material[134,135] as shown in **Figure 2.17**, different ratios of solvent[136] and different pH values[135].

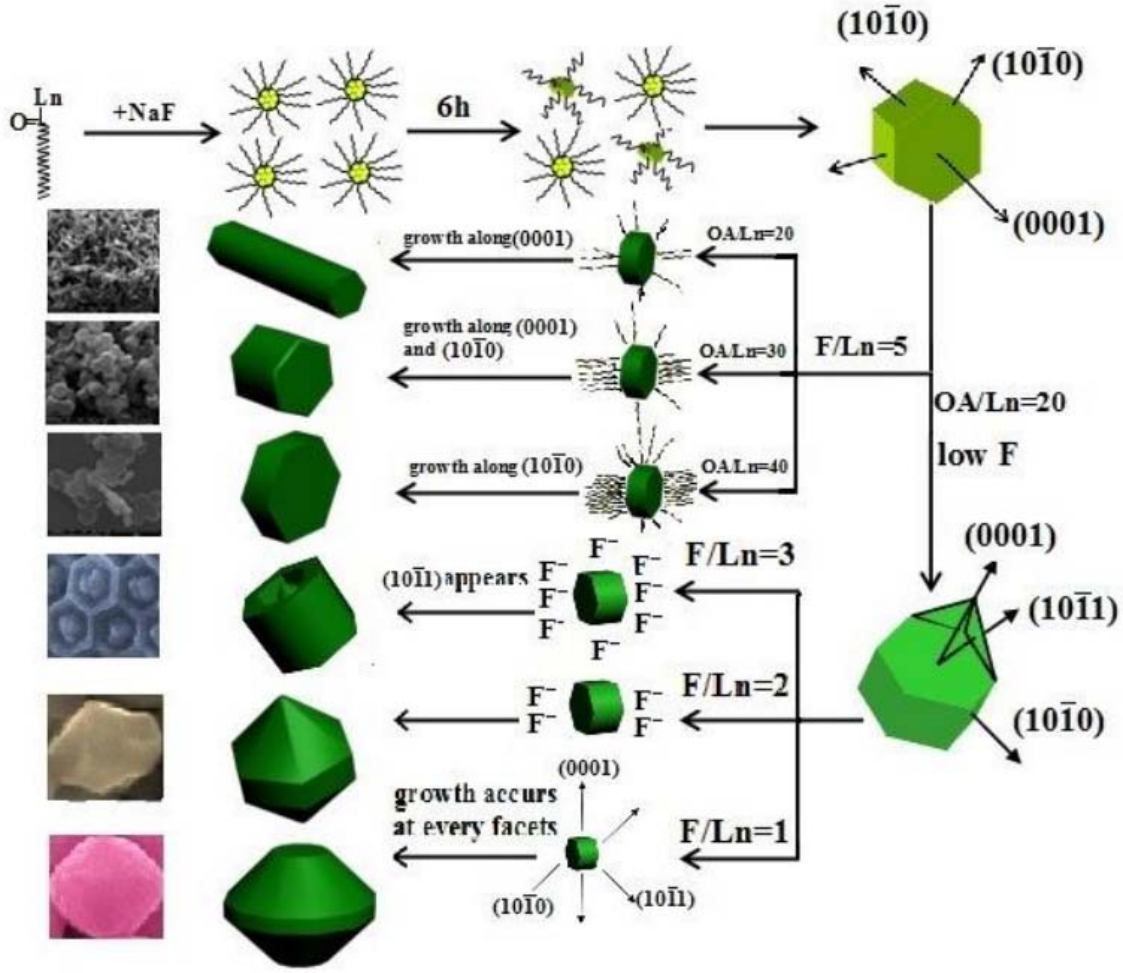

Figure 2.17 Schematic of the formation mechanism of different morphologies of $NaYF_4$ nanocrystals through different ratios of OA/Ln^{3+} and F^-/Ln^{3+} [134].

Shang *et al.*[134] proposed that increasing the ratio of F^-/Ln^{3+} can gradually change the nanocrystals' growth towards a longitudinal direction since the high F^-/Ln^{3+} ratio can let top and end surface become smoothly and higher crystallization. And the OA amount changing can influence the growth rate of facets of (0001) and (10$\bar{1}$1), which will change the directions of nanocrystals' growth.

Na *et al.*[136] proposed that different OA/ODE ratios can change nanocrystals' morphology since a large amount of OA reduces opportunities for the monomers to

attach to the nucleus, as shown in **Figure 2.18**. OA preferentially adsorbs onto the crystallographic planes $(10\bar{1}0)$ and $(01\bar{1}0)$, leading to the longitudinal growth of nanocrystals when the OA amount is high.

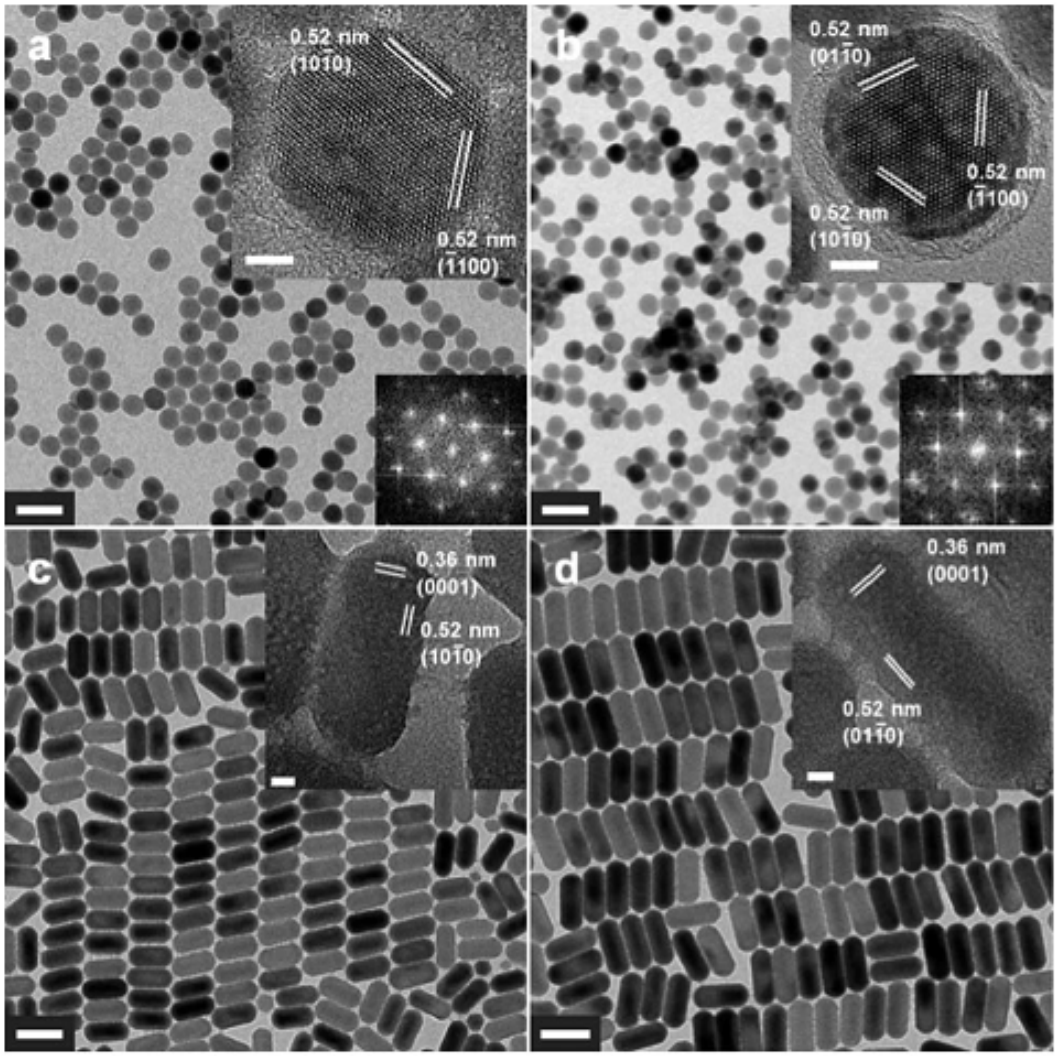

Figure 2.18 TEM and HRTEM (insert) images of β-$NaYF_4$ nanocrystals synthesized with different OA/ODE ratio: (a) =2:19, (b) =6:15; (c) =15:6, (d) =19:2. The scale bar is 50 nm[136].

Ding *et al.*[135] proposed using trisodium citrate (Na_3Cit) to synthesize β-$NaYF_4$ nanocrystals since Na_3Cit plays a role as a chelating agent that slows the nucleation of β-$NaYF_4$ nanocrystals and also selectively adsorbs to the top and bottom {0001} planes and this lowers their surface energy, as shown in **Figure 2.19**. The addition of more Na_3Cit dopant will induce the nanocrystals to grow in the [0001] direction. Ding *et al.*[135] also found that the pH value of the reaction solution influences nanocrystal

morphology; Cit^{3-} ions will combine with H^{+} ions at a low pH and this decreases the ability of Cit^{3-} ions and Y^{3+} ions to form a complex. The capping ability of Cit^{3-} allows the nanocrystal to grow faster from the {0001} plane in the [0001] direction than in the transverse direction.

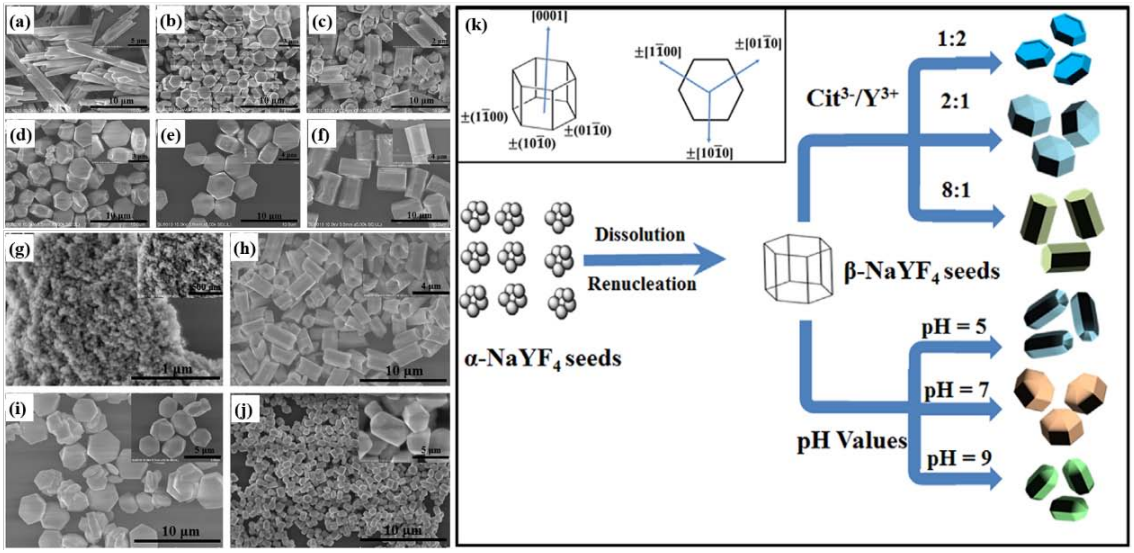

Figure 2.19 (a)-(f): SEM images of β-$NaYF_4$ nanocrystals synthesized at different ratios of Cit^{3-}/Y^{3+} is shown; (a) without Cit^{3-} ; (b) 0.5:1; (c) 1:1; (d) 2:1; (e) 4:1; (f) 8:1. (g)-(j): SEM images of β-$NaYF_4$ nanocrystals synthesized at different pH values is shown: (g) pH=3; (h) pH=5; (i) pH=7; (j) pH=9. (k) A schematic of the synthesis of different morphologies of β-$NaYF_4$ nanocrystals under various experimental conditions is given[135].

2.4.3 The fabrication of different sized nanocrystals

UCNCs can be synthesized in a wide size range, from a few nanometres[137–139] to several hundred nanometres[140,141]. The size can be influenced by several factors such as the amount of dopant ions[142,143], temperature[144], and solvent ratio[145].

Kang *et al.*[143] reported that the $NaLuF_4$ nanocrystal size decreased when Y^{3+} doping concentration increased, as can be seen in **Figure 2.20**. They point out that the smaller ionic radius of the Lu^{3+} ions has a lower electron charge density than the larger ionic radius (Y^{3+} ions[146]. Lower electron charge density on the nanocrystal surface accelerates the diffusion of the negatively charged F^{-} ions to the surface. This changes how the nanocrystals are formed and leads to an increase in their size. In contrast,

doping with Y^{3+} ions, which have a higher electron charge density, decreases the final size of the $NaLuF_4$ particles.

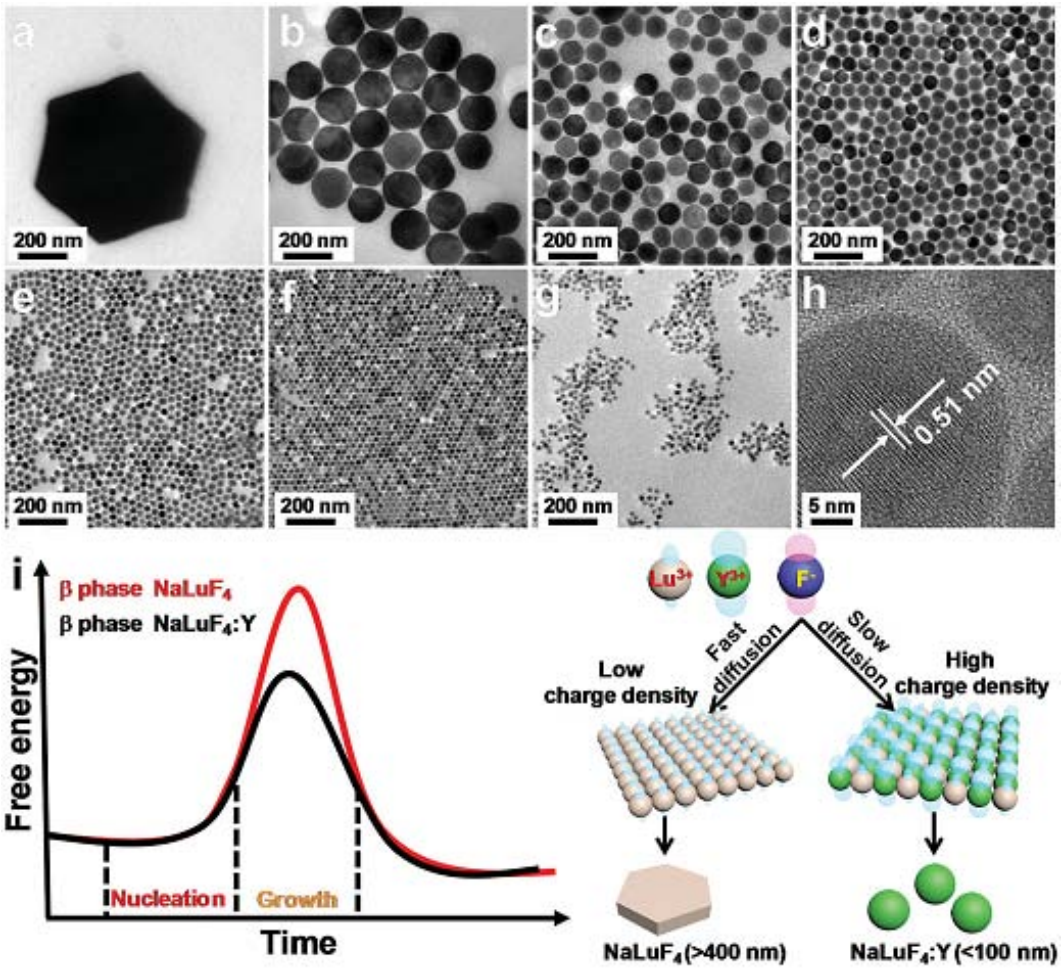

Figure 2.20 (a)-(h), TEM images of $NaLuF_4$ nanocrystals with different amounts of Y^{3+} ion dopant: (a) = 0%, (b) = 10%, (c) = 20%, (d) = 30%, (e) = 40%, (f) = 60%, (g) = 20%. (h): High resolution transmission electron microscope (HRTEM) image of (e). (i): Growth of Y^{3+} ion doped nanocrystals[143].

A similar trend in the dependence of size on doping was proposed by Lei *et al.*[142] and Damasco *et al.*[147], who doped Ca^{2+} ions into $NaGdF_4$ nanocrystals and Gd^{3+} ions into $NaYbF_4$ nanocrystals, respectively. This is shown in **Figure 2.21**. A similar explanation was also proposed by Wang *et al.*[11]: different ionic radius ions have different electron charge density. Smaller ionic radius ions have lower electron charge density, which increases the diffusion of negatively charged ions (F^-) onto the surface. Subsequently, this forms larger nanocrystals (and *vice versa*).

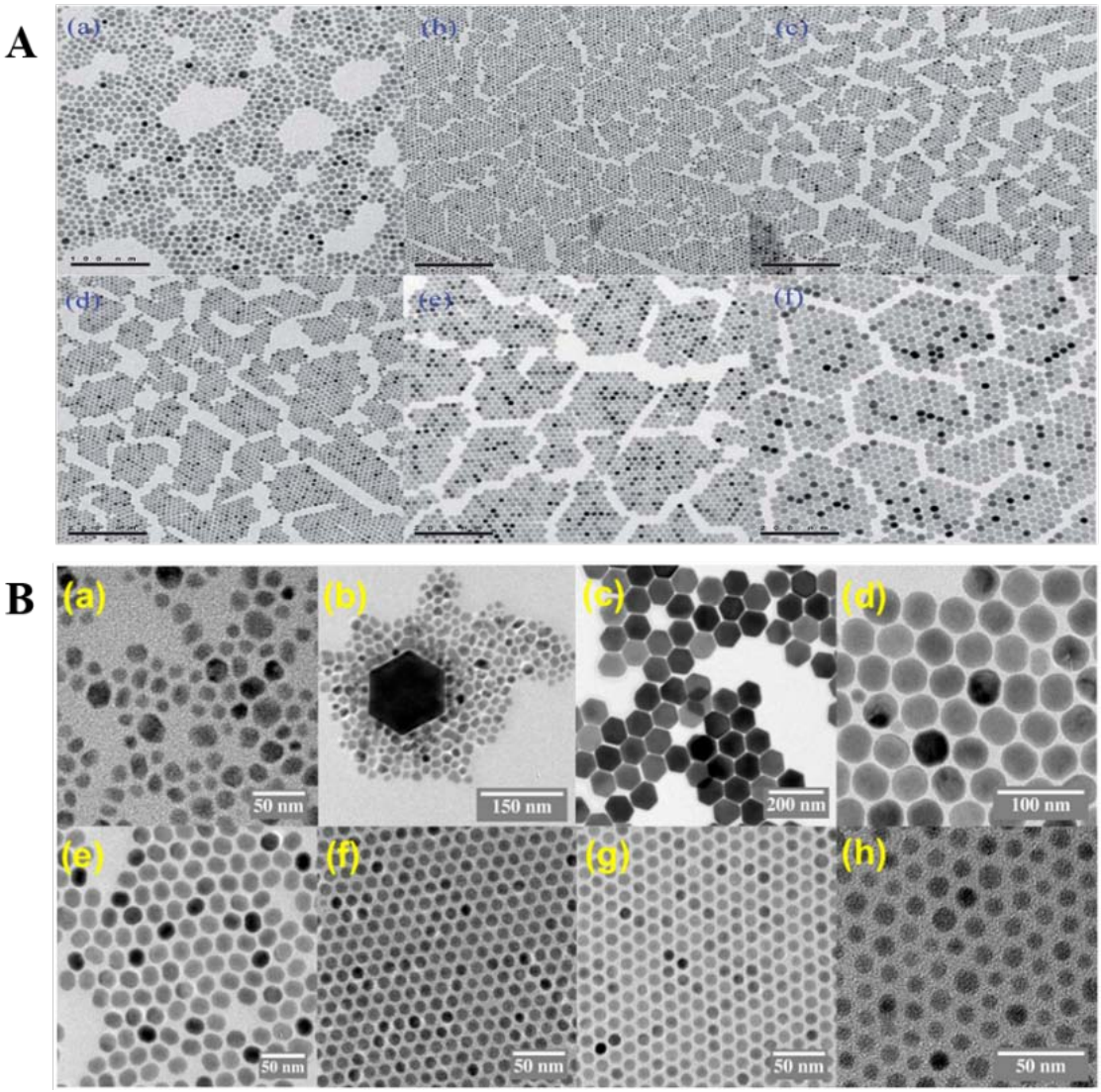

Figure 2.21 A: TEM images of $NaGdF_4$ nanocrystals with x % Ca^{2+} doping: (a) x = 0, (b) x = 10, (c) x = 20, (d) x = 25, (e) x = 30, (f) x = 40[142]. B: TEM images of $NaYbF_4$ nanocrystals with y % Gd^{3+} doping: (a) y = 0, (b) y = 7, (c) y = 10, (d) y = 20, (e) y = 30, (f) y = 40, (g) y = 50, (h) y = 70 [147].

Ostrowski *et al.*[145] proposed tuning nanocrystals size by using a different amount of OM solvent, as shown in **Figure 2.22**. These researchers used a nuclear magnetic resonance (NMR) study to show that different surfactants have different affinities for the surfaces of nanocrystals doped with rare earth cations.

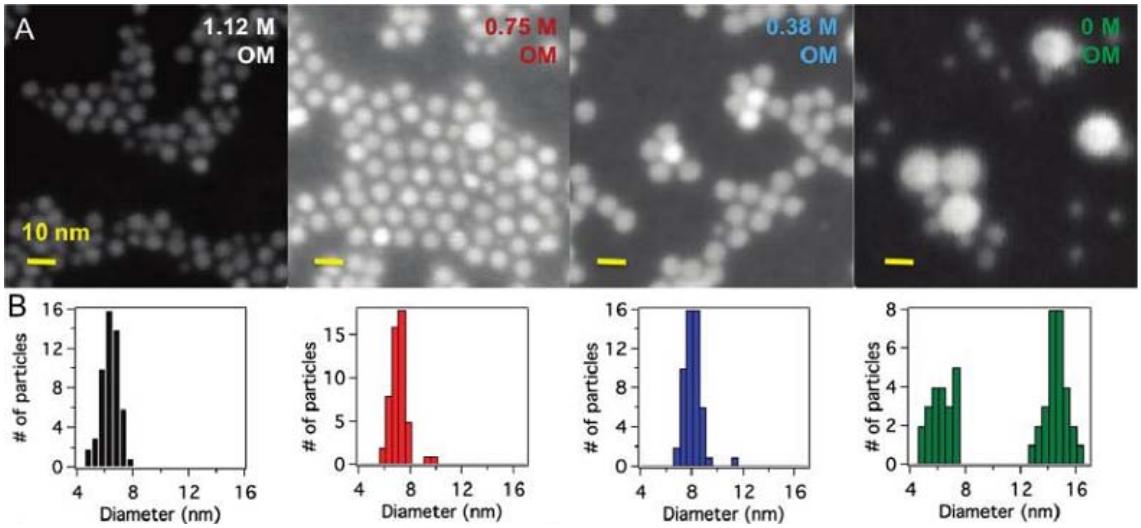

Figure 2.22 (A) Scanning transmission electron microscopy (STEM) images of β-$NaYF_4$ nanocrystals with OM concentration of 1.12 M, 0.75M, 0.38 M and without OM; (B) their corresponding size distribution (B)[145].

2.5 Growth method for extending crystals

Researchers have proposed a variety of methods to synthesize nanocrystals with various morphologies and sizes as described in the previous section. Most of these are one-pot production methods. Currently, research efforts are directed towards control of nanocrystals' morphologies and sizes, and towards growth in specific directions for particular applications and functionalities, by creating core-shell structures. In these, growth may occur either in specific directions or homogeneously.

2.5.1 The one-pot temperature increase method

The one pot, temperature increase method is a kind of seed-mediated shell growth method, first proposed by Mai *et al.*[148] and refined by Qian *et al.*[149], as shown in **Figure 2.23**. The advantage of this method is that synthesis is relatively simple.

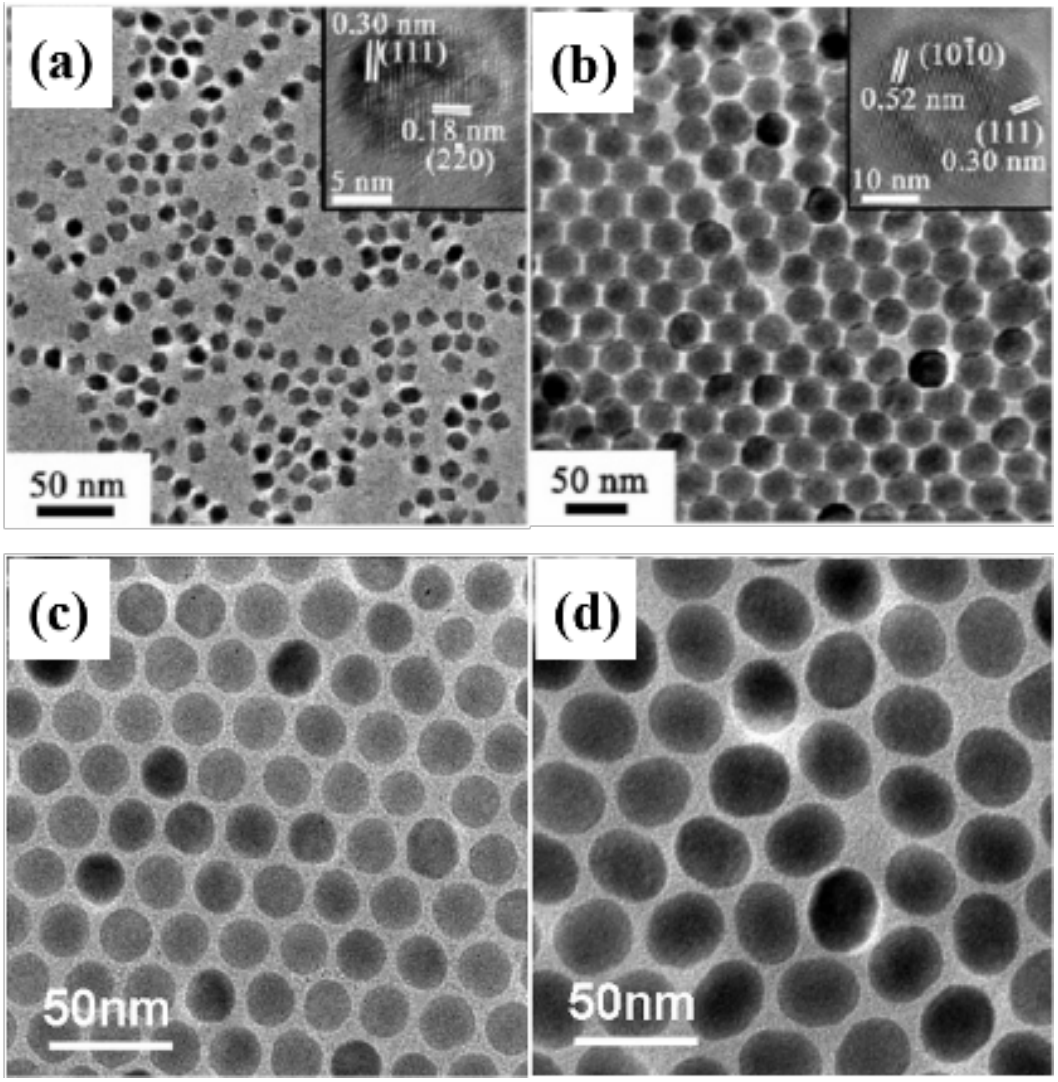

Figure 2.23 TEM images of (a) α-$NaYF_4$ core and (b) β-$NaYF_4$ core-shell nanocrystals[11]; (c) β-$NaYF_4$: Yb^{3+}, Tm^{3+} core and (d) β-$NaYF_4$: Yb^{3+}, Tm^{3+}@ β-$NaYF_4$: Yb^{3+}, Er^{3+} core-shell nanocrystals[148].

The heat up method developed more completely[151] and became the most commonly used method to synthesize core-shell structures. The disadvantage is that core-shell nanocrystals fabricated by this method are not homogeneous when the shell is thicker than about 5 nm[150], as shown in **Figure 2.24**. When this is the case, the crystals prefer anisotropic growth which, due to the different orientations of surface facets, have different binding strength with surfactants, which leads to crystal growth along preferred directions[152].

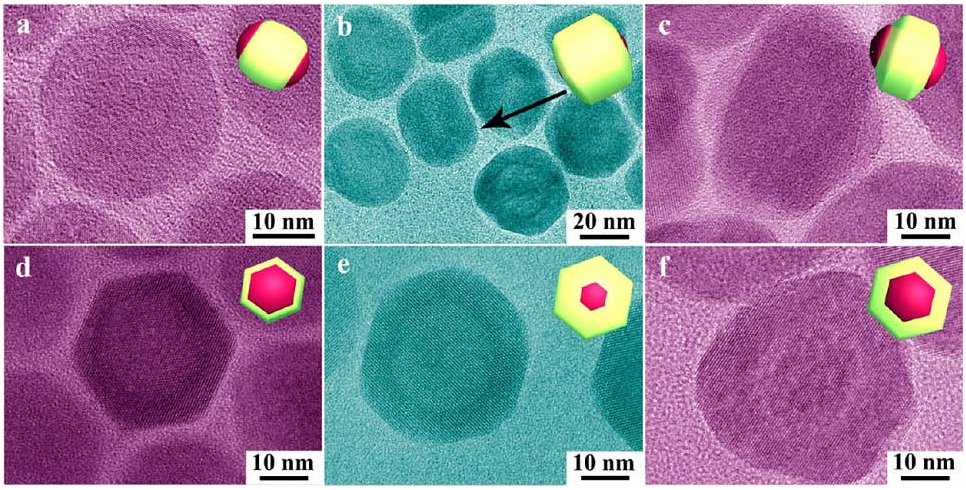

Figure 2.24 TEM images of $NaYF_4$ @ $NaGdF_4$ nanocrystals with different shell thickness: 4 nm (a and d); 8 nm (b and e); 10 nm (c and f)[150].

2.5.2 The hot injection method

The hot-injection method was developed in order to improve control of nanocrystal growth[153]. Using this method, nanocrystals can be synthesized with more homogeneous shells, and the shell thickness can be controlled within a relatively large range. For example, successive shells of around 1 nm have been reported by Johnson *et al.*[130], as shown in **Figure 2.25**. Shells of up to 8 nm have been reported by Li *et al.*[154], as shown in **Figure 2.26**.

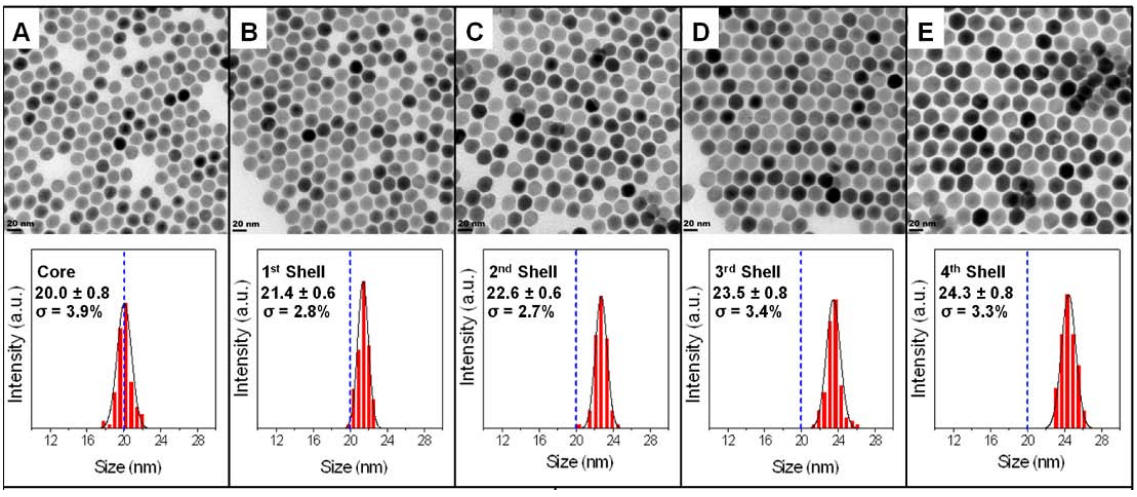

Figure 2.25 TEM images and size distribution of $NaYF_4$ core-shell nanocrystals with different size after shell growth are given: A = 20 nm; B = 21.4 nm; C = 22.6 nm; D = 23.5 nm; E = 24.3 nm[130]. The scale bar represents 20 nm.

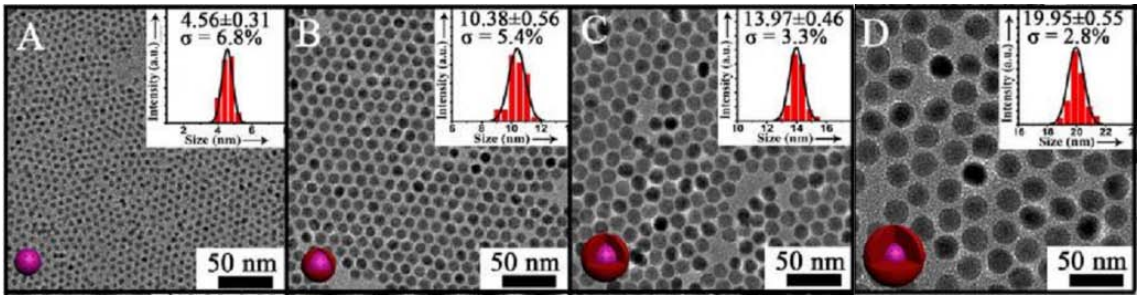

Figure 2.26 TEM images and size distribution of $NaGdF_4$ core-shell nanocrystals at different sizes is given: A = 4.56 nm; B = 10.38 nm; C = 13.97 nm; D = 19.95 nm[154].

Another advantage of this method is that nanocrystals can be synthesized with different functional layers of shells. For example, Wen *et al.*[155] proposed four different layers of shells on upconversion nanorods to realize the efficient transfer of visible upconversion luminescence, as shown in **Figure 2.27**. Wang *et al.*[156] proposed three different layers of shells on sub-15 nm upconversion spherical nanocrystals to realize the efficient transfer of upconversion luminescence, as shown in **Figure 2.28**. When using the hot-injection method, the shell precursor could be a salt solution[150] or *α*-$NaYF_4$ nanocrystals[130]. The disadvantage of this method is that the procedure is more complex than the heat up method since the shell precursors should be prepared in advance.

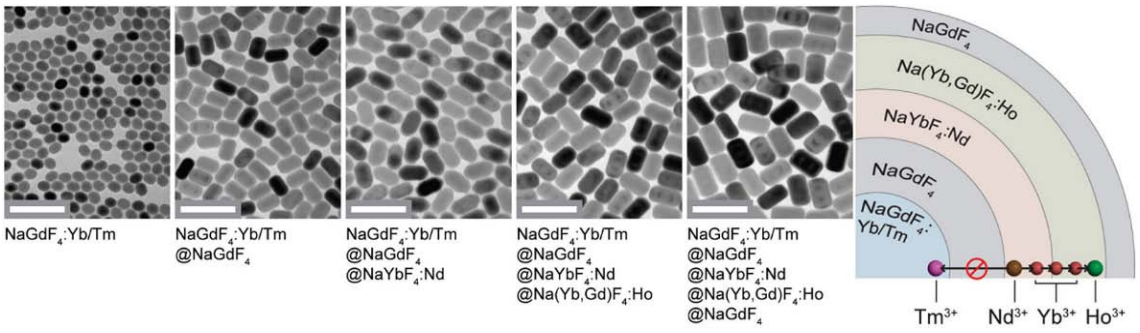

Figure 2.27 TEM images of nanocrystals obtained at different synthesis stages and the proposed upconversion energy of the multi-shelled nanocrystals[155].

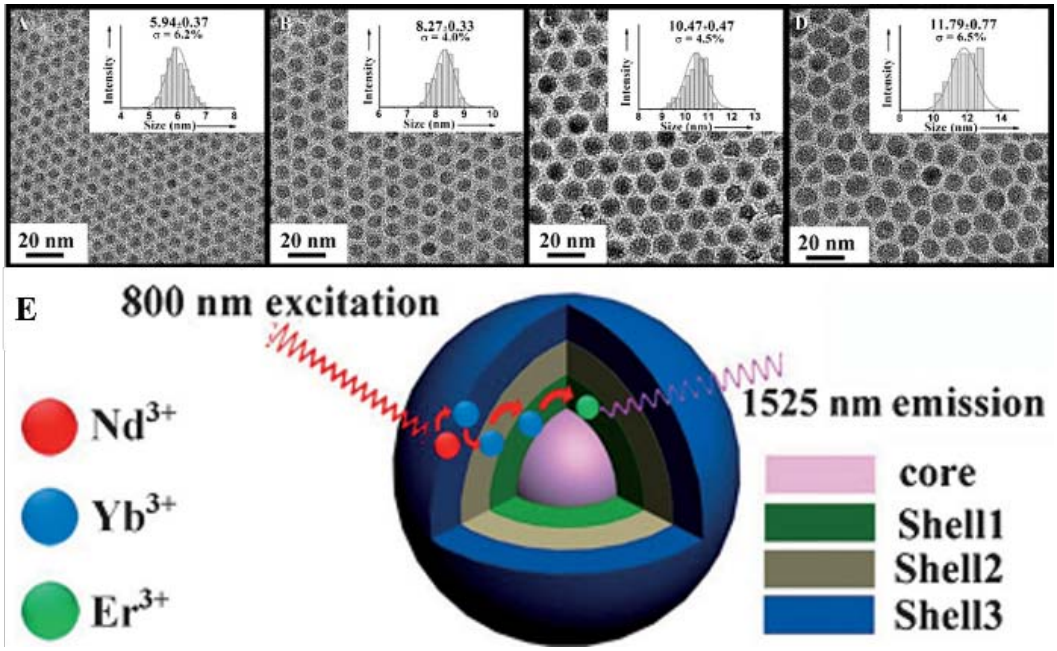

Figure 2.28 TEM images of nanocrystals abstained at different synthesis stages and the proposed upconversion energy in the multi-shelled nanocrystals[156].

2.5.3 Achieving longitudinal growth

For $NaYF_4$ nanocrystals, growth is commonly considered in two orthogonal directions since the stable crystal is a hexagonal phase. The [100] direction is always named as the longitudinal direction. Longitudinal growth can be produced by both the heat up method and the hot injection method.

For example, Wen *et al.*[155] observed longitudinal growth in $NaYbF_4$@$NaGdF_4$ nanocrystals with the heat-up method. They proposed that the $NaGdF_4$ shell procedure prefers (100) planes when grown from the $NaYbF_4$ core, as **Figure 2.29** shows. Liu *et al.*[157] reported $NaYF_4$ nanorods synthesized by the hot injection method, and this is shown in **Figure 2.29**.

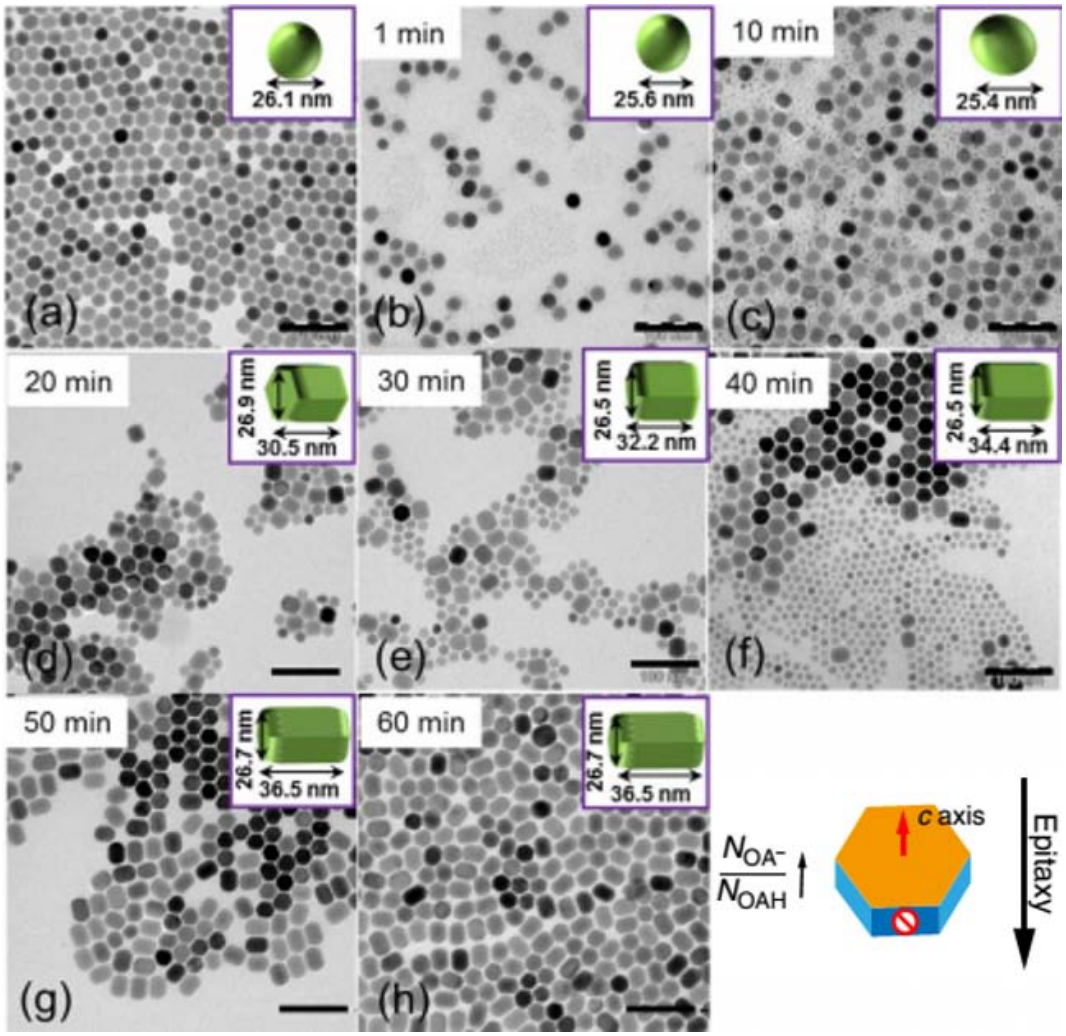

Figure 2.29 TEM images of the processing of longitudinal growth $NaYF_4$ nanorods with different hot-injection shell amount[157].

2.5.4 Achieving transverse growth

The other dominant growth direction for hexagonal phase nanocrystals is the [110] direction which is always named as transverse growth. As with longitudinal growth, transverse growth can be produced by both heat up and hot injection methods. For example, Zhang *et al.*[158] proposed transverse growth of $NaYF_4$@$NaGdF_4$ nanocrystals synthesized by the heat-up method. This is the first report providing direct evidence of core-shell nanostructure imaging using cryo-TEM microscopy. During the epitaxial growth of the $NaGdF_4$ shells, surface defects of the nanocrystals were gradually passivated by homogeneous shell deposition, and this is shown in **Figure 2.30**.

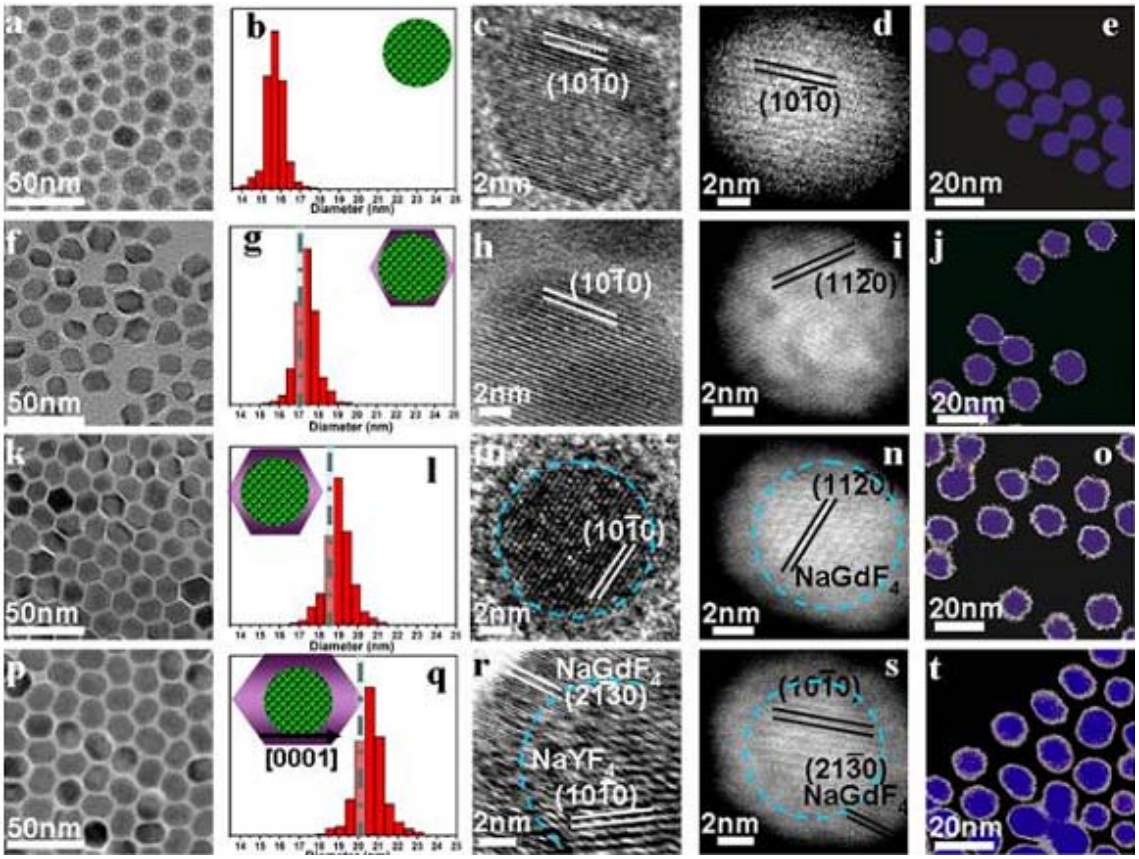

Figure 2.30 Cryo-TEM images and histograms of the $NaYF_4$ crystals (a-d) with different $NaGdF_4$ shell thickness, (f)-(i): thickness is 0.86 nm; (k)-(n): thickness is 1.64 nm; (p)-(s): thickness is 2.40 nm. (e, j, o, t) shows the composite color map of different elements, blue indicates yttrium atoms and yellow indicates gadolinium atoms[158].

In another example, Liu *et al.*[157] reported the synthesis of $NaYF_4$@$NaGdF_4$ nanoplates synthesized by the hot injection method. They believed the major cause of transverse growth is the specific adsorption of OA on nanocrystals faces. The OA etches the deposited shell at high temperature. The OA preferentially adsorbed on the {0001} faces, causing the <0001> direction growth to slow down. This then means that further nanocrystal growth is predominantly in the transverse direction, shown in **Figure 2.31**.

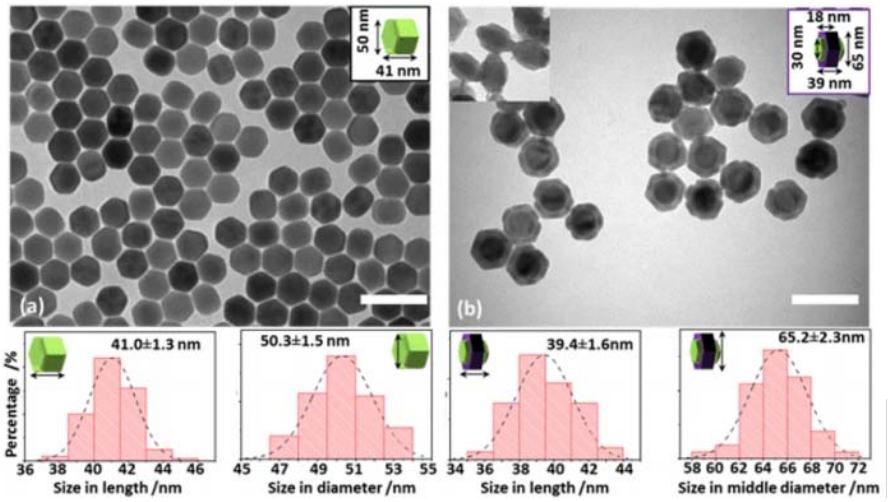

Figure 2.31 TEM images and size distribution of the processing of transverse growth $NaYF_4$@$NaGdF_4$ nanplates[157].

2.5.5 The hybrid growth approach

The hybrid growth of core-shell structures is a novel method that can combine different materials of different compositions and structures. In other words, two or more materials which have different properties and functions can be synthesized together and play more effective roles.

The hybrid core-shell nanostructure has been researched in a variety of areas such as metals and semiconductors (e.g. Au-CdSe[159], Au-PbS[160]), alloys and semiconductors (e.g. FePt-CdSe, FePt-CdS[161], Au_2Cd-CdSe[162]) and metallic oxides and metals (e.g. Fe_3O_4-Ag[153,163]). These hybrid core-shell structures are formed by fusing the two kinds of nanocrystals at a matched facet, subsequent nucleation, and further growth onto the second component on the core nanocrystals[164].

For the synthesis of hybrid UCNCs, two kinds of materials combining an upconversion property with another function, are widely used in optoelectronic sensing[165], enhanced upconversion luminescence[166,167], near-infrared light sensing by phototransistors[168] and magnetism[169], as shown in **Figure 2.32**. The hybrid structure of metal and UCNCs often depends on small crystal lattice mismatch. If the core and shell have a large crystalline mismatch, an intermediate material is applied to link them.

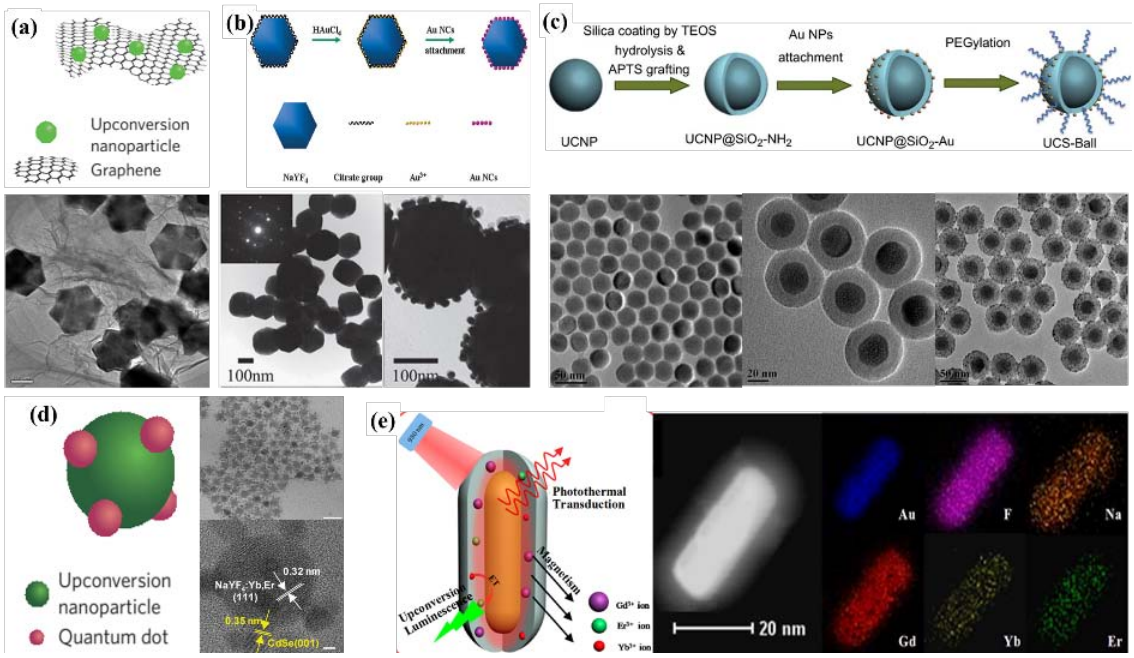

Figure 2.32 Hybrid UCNCs for different applications: (a) $NaYF_4$ with graphene nanosheets for optoelectronic sensing[164,165]; (b) $NaYF_4$ with Au nanocrystals for enhanced upconversion luminescence[166]; (c) $NaGdF_4$@SiO_2@Au nanocrystals for enhanced upconversion luminescence[167]; (d) $NaYF_4$ with quantum dot nanocrystals used by near-infrared light sensing[164,168]; (e) $NaGdF_4$ with Au nanocrystals for enhanced magnetic properties[169].

2.6 Approaches to increasing upconversion luminescence

Since upconversion luminescence is an anti-stokes phenomenon, the emission is not as easy as the more common downconversion luminescence; and its efficiency is not as high. How to enhance the upconversion luminescence, i.e. increase the upconversion efficiency, has been widely studied. Selected methods for increasing upconversion luminescence are presented here.

2.6.1 Enhancement of the luminescence by phase transition

Many researchers have studied methods to enhance upconversion luminescence in α-$NaYF_4$[106] or β-$NaYF_4$[113,170] nanocrystals individually. The upconversion efficiency of these two phases is different; John *et al.*[131] and Som *et al.*[171] reported that the upconversion luminescence increased rapidly on changing from α phase to β phase, as shown in **Figure 2.33**.

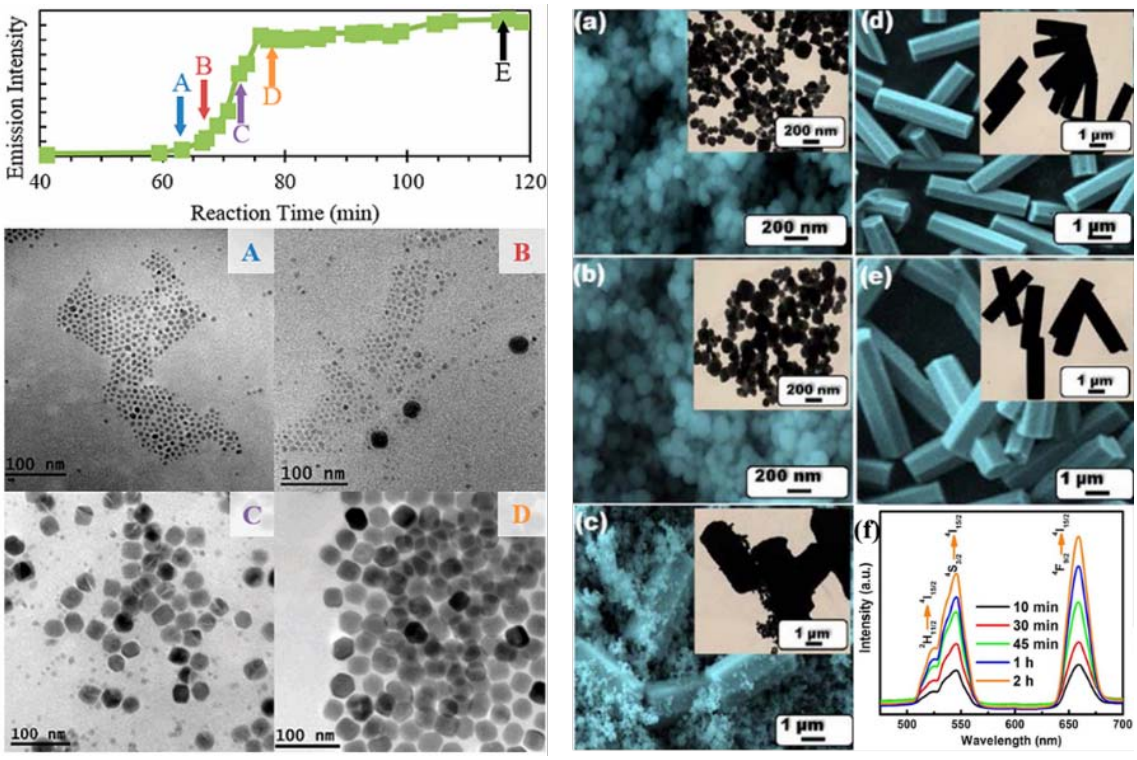

Figure 2.33 Upconversion emission intensity change as a result of phase transition[131,171].

2.6.2 Core-shell structure enhancement to the efficiency of upconversion luminescence

There are two main factors for the low luminescence seen in UCNPs: Firstly emission can be quenched by high-energy oscillation in defects that occur at a nanocrystal's surface. Secondly, the interior excitation energy of an ion can be transferred to the nanocrystal surface through adjacent ions via non-radiative cross relaxation (as described in Chapter 1, 1.2)[172].

Lezhnina *et al.*[173] first proposed core-shell structure nanocrystals in 2006, reporting that the shell can effectively protect the nanocrystal's surface, to enhance upconversion luminescence by avoiding surface defects. Subsequently, Yi *et al.*[60] reported that $NaYF_4$: Yb^{3+}, Er^{3+}(Tm^{3+})@$NaYF_4$ core-shell structure can enhance the luminescence of naked core nanocrystals, by 7 times (Er^{3+} doped) and 29 times (Tm^{3+} doped). Since then, a core-shell structure has become the most popular and efficient way to enhance upconversion luminescence, since it is the most direct way to decrease the surface defects. A large variety of core-shell structures have been reported, including $NaYF_4$ @ $NaGdF_4$[174,175], YOF @ YOF[176], $NaYF_4$ @ $NaYF_4$[82,177], $NaGdF_4$

@ $NaGdF_4$[137–139], $NaGdF_4$ @ $NaYF_4$,[154,174] CeF_3 @ LaF_3[209], $NaYF_4$ @ $NaYbF_4$[150], $NaGdF_4$ @ $NaYbF_4$[141], $NaGdF_4$ @ $NaYF_4$ @ $NaYbF_4$[141], CaF_2 @ $NaYF_4$[179], $NaGdF_4$ @ $NaYbF_4$ @ $NaGdF_4$[155], and $NaYF_4$ @ CaF_2[180].

Research by Zhang *et al.*[158] in 2012 presents direct images of the core-shell structure by cryo-transmission electron microscopy, instead of indirect evidence from measuring nanocrystal size. They showed that the shell thickness has an influence on upconversion luminescence, which increases linearly with increasing shell thickness as shown in **Figure 2.34**.

(a)

	Doses per layer/mmolar	Particle radius/nm	Volume ratio of shell/core
0	0	7.85	0
1	0.139	8.21	0.144
2	0.151	8.57	0.301
3	0.165	8.93	0.472
4	0.178	9.29	0.657
5	0.193	9.65	0.858
6	0.208	10.01	1.073

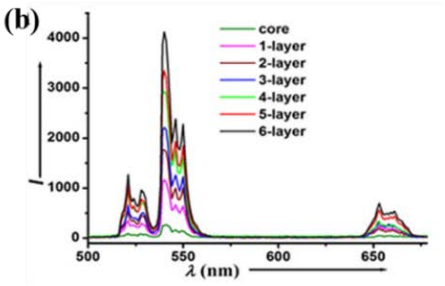

Figure 2.34 (a): Calculation for the $NaGdF_4$ shell grown from 1st to 6th layer is provided. (b): Upconversion luminescence spectra for $NaYF_4$: 20 % Yb, 2 % Er @ $NaGdF_4$ nanocrystals with different layer of $NaGdF_4$ shell[158] is shown.

This phenomenon, of a linear increase in upconversion luminescence, was also reported by Johnson *et al.*[130] (in $NaYF_4$: Yb^{3+}, Er^{3+} @ $NaYF_4$ nanocrystals synthesized by the heat up method) and Li *et al.*[154] (in $NaGdF_4$: Yb^{3+}, Er^{3+} @ $NaYF_4$ nanocrystals by one-pot hot injection method) as shown in **Figure 2.35**.

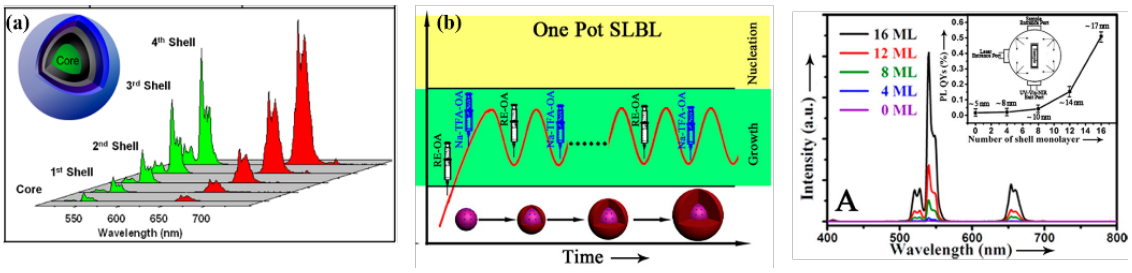

Figure 2.35 (a): Upconversion emission spectra of core-shell nanocrystals using different shell layer[130] are shown; (b): schematics are given of the one-pot synthesis of core-shell nanocrystals that use different shell layers to create different emission spectra[154].

2.6.3 Size and morphology dependent upconversion luminescence

The most common reason given for size-dependent upconversion in nanocrystals is their surface defects. Smaller nanocrystals have a larger surface to volume ratio than larger nanocrystals; this is generally accepted to be the reason that nanocrystals have lower emission intensities than bulk materials[181,182]. Another reason for the Influence of nanocrystal size on the emission of nanocrystals is that small nanocrystals restrict photon relaxation because of the phonon confinement effect, which leads to low phonon energy pathways are unavailable[175].

Nanocrystal morphology also plays an important role in luminescence intensity. UCNCs can be synthesized by a variety of morphologies, such as nanorods and nanoplates[134-136,157], nanotubes[183], nanaowires[184], spherical nanocrystals[144,145,185], unformed nanocrystals[181], nanostars[186], dumbbell nanocrystals[187], and octahedra[134]. Most of the reports elsewhere indicate that the influence of morphology on upconversion intensity arises from changes in the ratio of particle surface area to its volume. A large surface area usually has more surface defects, and this then decreases the intensity of its emission. As reported, several morphologies, such as micro rods and rod-shaped nanocrystals, have a much smaller surface area compared to other shapes, as shown in **Figure 2.36**.

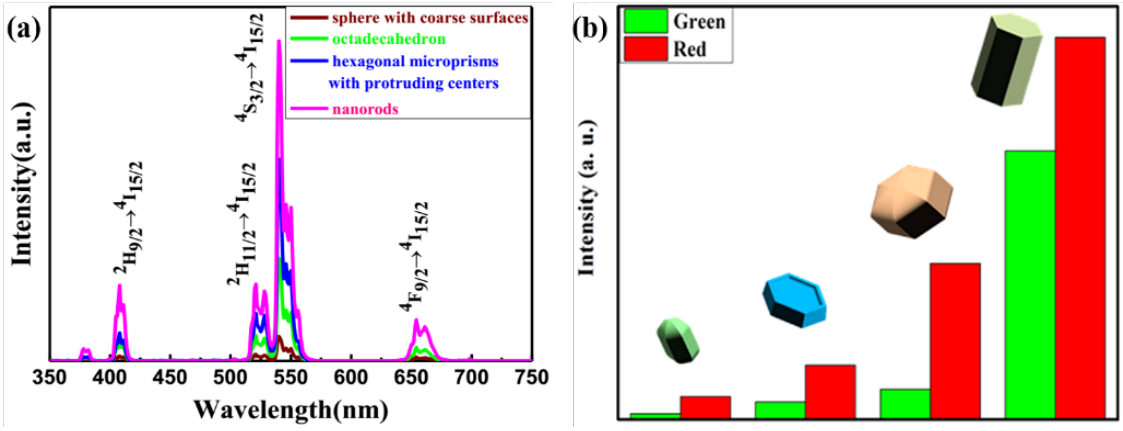

Figure 2.36 Upconversion luminescence spectra of $NaYF_4$ nanocrystals with various morphologies excited by (a): 808 nm laser[134]; and (b): 980 nm laser[135].

2.6.4 Concentration-dependent upconversion luminescence

Rare earth ions doped into nanocrystals can be activator ions or sensitizer ions[188,189]. Yb^{3+} is the most used sensitizer ion for transfer of energy from a 980 nm excitation laser; the usual Yb^{3+} (dopant) concentration is 20 %. Researchers have traditionally used this concentration of Yb^{3+} ions because too great a concentration of Yb^{3+} results in quenching of luminescence[190,191]. More recently however, scientists have found that Yb^{3+} can be doped at concentrations greater than 50 % when using high excitation power[192]. Chen *et al.*[193] reported that the near-infrared (NIR) to NIR upconversion luminescence increased about 8.6 times by increasing Yb^{3+} from 20 % to 100 % with codoped with Tm^{3+}. Hao *et al.*[194] reported that Pr^{3+} ions can be enhanced by Yb^{3+} ions, increasing by 3.4 times when Yb^{3+} increased from 10 % to 70 %, as shown in **Figure 2.37**.

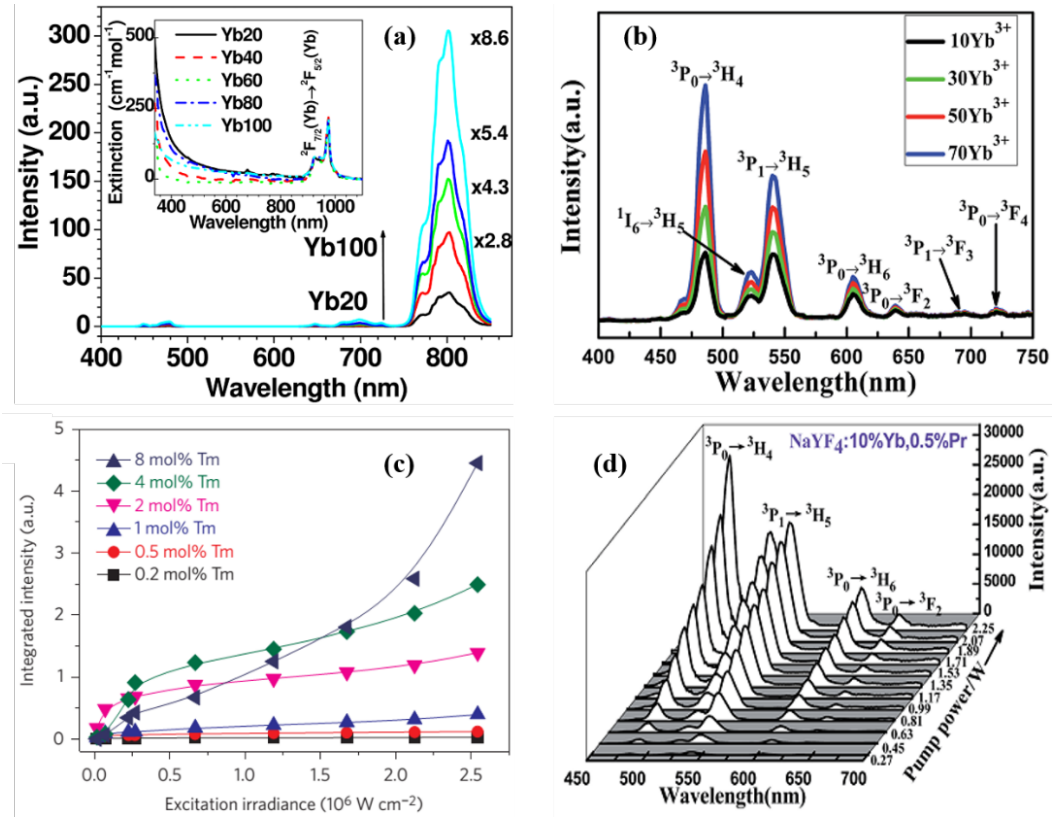

Figure 2.37 UCNCs luminescence of (a) $NaYF_4$: 2% Tm^{3+} with Yb^{3+} concentration from 20% to 100%[193], (b) $NaYF_4$: 0.5% Pr^{3+} with Yb^{3+} concentration from 10% to 70%[194], (c) $NaYF_4$: 20% Yb^{3+} with Tm^{3+} concentration from 0.2% to 8% with different excitation irradiance until 2.5×10^6 W/cm^2 [69], (d) $NaYF_4$: 10% Yb^{3+}, 0.5% Pr^{3+} with pump power from 0.27 mW to 2.25 mW[194].

For activator ions, the upconversion luminescence can be enhanced by increasing the activator concentration, but concentration quenching has also been observed[192–196]. The most common explanation of this is the decrease in distance between activator ions when dopant concentration is increased, which enhances the probability of cross-relaxation and leads to more energy loss. Similarly, the activator ion dopant concentration can be increased by enhancing excitation power[194] or by novel nanostructure[197]. For example, Zhao *et al.*[69] proposed that the Tm^{3+} dopant concentration can be enhanced to 8% by using a suspended-core fiber with relatively high excitation irradiance of 2.5×10^{6} $W\cdot cm^{-2}$. Hao *et al.*[194] proposed that Pr^{3+} ions' luminescence can be linearly enhanced by a power increase from 0.27 W to 2.25 W.

2.6.5 Surface plasma resonance (SPR) enhancement to upconversion luminescence

A novel method, SPR enhancement, can be used to increase upconversion luminescence. The most frequently used metal nanocrystals for SPR are gold and silver at present[198–204]. Researchers have found that for metal and UCNCs, the upconversion luminescence is not always enhanced but is sometimes quenched. This is the result of different distances between the luminescent material and the metal surface. If the UCNCs is brought into contact with the metal surface, the luminescence will be quenched. Control of the distance between the metallic surface and luminescent nanocrystals such as organic dyes[199], quantum dots[205], organic molecules[206] and silica[203,205] have accordingly become a hot topic in recent years. Schietinger *et al.*[198] proposed that single $NaYF_4$: Yb^{3+}/Er^{3+} nanocrystals can be enhanced 3.2 times by Au. Zhang *et al.*[203] proposed that the average photoluminescence can be enhanced 4 times by Ag SPR enhancement. Saboktakin *et al.*[200] proposed that the upconversion luminescence can be enhanced with a 3 D metal-oxide-UCNCs trilateral structure, as shown in **Figure 2.38**. With different oxide layers, Au and Ag nanocrystals can enhance the luminescence 5.2 and 45 times, respectively. Au nanohole arrays can enhance the upconversion luminescence up to 35 times[204]. Overall, the SPR enhancement of upconversion luminescence is still in infancy; much more research is needed in this area.

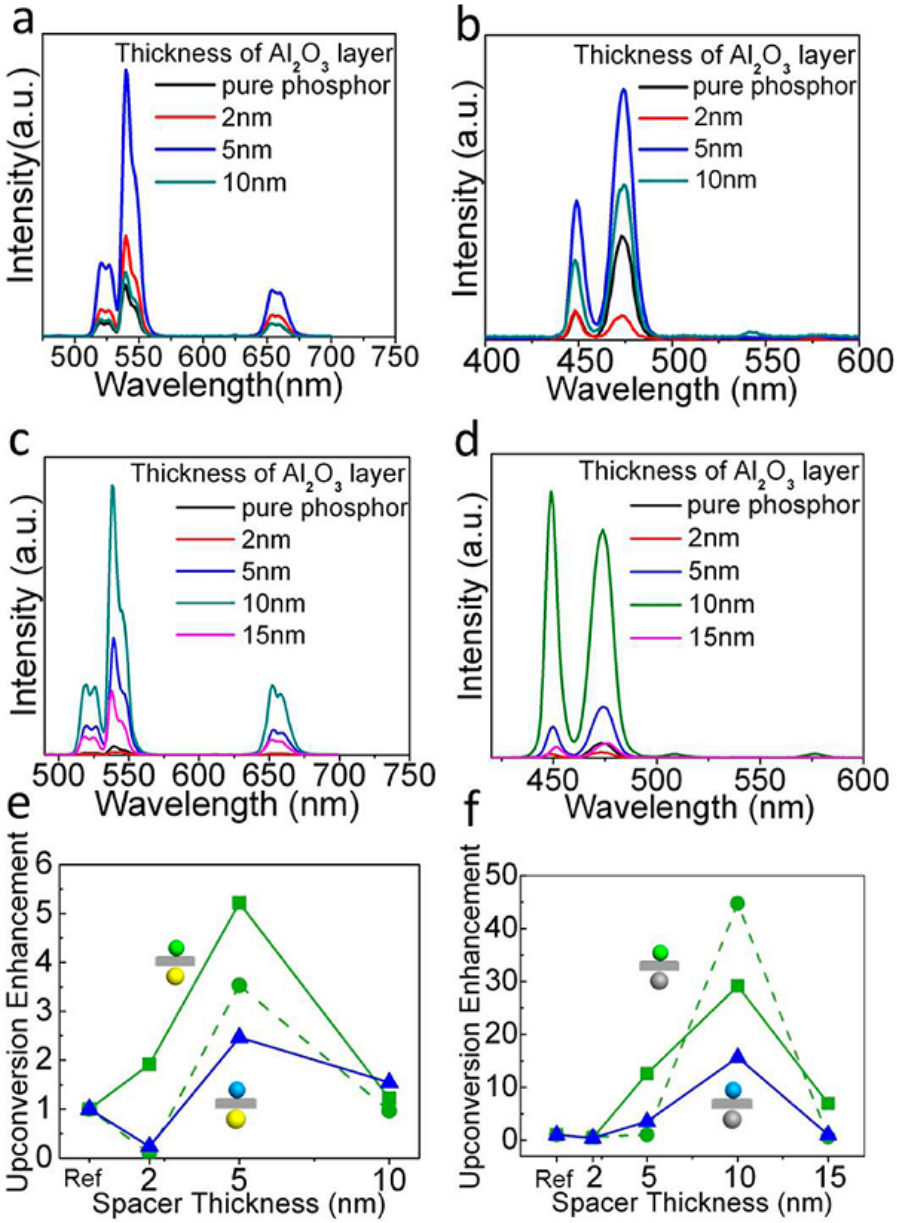

Figure 2.38 Upconversion luminescence of 3D metal-oxide-UCNCs with different thickness of Al_2O_3 layer[200]: (a) Au-Al_2O_3-$NaYF_4$: Yb^{3+}, Er^{3+}; (b) Au-Al_2O_3-$NaYF_4$: Yb^{3+}, Tm^{3+}; (c) Ag-Al_2O_3-$NaYF_4$: Yb^{3+}, Er^{3+}; (d) Ag-Al_2O_3-$NaYF_4$: Yb^{3+}, Tm^{3+}; (e) Au nanocrystals and (f) Ag nanocrystals, the green solid lines and green dashed lines correspond to the 540 nm and 650 nm emission band in $NaYF_4$: Yb^{3+}, Er^{3+}, respectively. The blue solid lines correspond to the 475 nm emission band in $NaYF_4$: Yb^{3+}, Tm^{3+}.

2.6.6 Energy migration and interactions in UCNCs

The basic model of energy migration upconversion was established several decades ago[207]. This process occurs between two neighboring ions and is usually named the "short-range energy migration model"[208]. Recently, a new energy migration process has been widely reported which partially or completely separates the donor and acceptor ions in space. This kind of novel energy migration can have brighter upconversion luminescence than the traditional energy migration forms which are commonly used by the core-shell structure. Wang *et al.*[84] named this kind of energy migration process the "long-range energy migration model" in 2011. They designed a core-shell structure for energy migration with four types: type Ⅰ for sensitizers (Yb^{3+}), type Ⅱ for accumulators (Tm^{3+}), type Ⅲ for migrators (Gd^{3+}), and type Ⅳ for activators (X^{3+} = Eu^{3+}, Tb^{3+}, Sm^{3+}, Dy^{3+}), as shown in **Figure 2.39**.

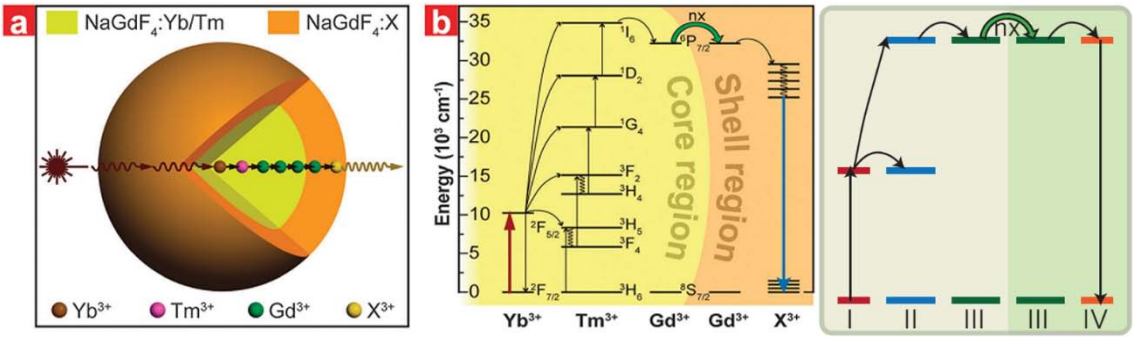

Figure 2.39 (a) Schematic diagram showing the design of nanocrystals for the energy migration upconversion process; (b) The proposed energy migration upconversion process mechanism and a scheme doped with four types of rare earth ions[209].

Without the Gd^{3+} layer to bridge between sensitizer and activator, the X^{3+} (X^{3+}=Eu^{3+}, Tb^{3+}, Sm^{3+}, Dy^{3+}) cannot emit because of the probable multiphonon emission and cross relaxation. When $NaGdF_4$ is chosen as the bridge between them, the $^6P_{7/2}$ energy state which belongs to Gd^{3+} can transfer the energy to X^{3+} and minimize energy loss to realize the X^{3+} emission. Su *et al.*[85] further coated a layer of inert $NaYF_4$ shell outside of this type of core-shell energy migration structure and enhanced the upconversion luminescence more efficiently.

Researchers subsequently found that Yb^{3+} ions have similar properties to Gd^{3+} when acting as the energy migration bridge[84,208]. Nd^{3+} ions have been found to be good

sensitizer ions by energy migration. For example, Zhong *et al.*[86] designed the energy migration of a core-shell-shell structure which can transfer energy from activator ions X^{3+} (X^{3+} = Er^{3+}, Tm^{3+}, Ho^{3+}) to sensitizer Nd^{3+} ions, as shown in **Figure 2.40 (a, b)**. Wen *et al.*[155] designed a similar structure which can transfer energy from activator ions Y^{3+} (Y^{3+} = Tb^{3+}, Eu^{3+}, Dy^{3+}) to sensitizer Nd^{3+} ions, as shown in **Figure 2.40 (c)**.

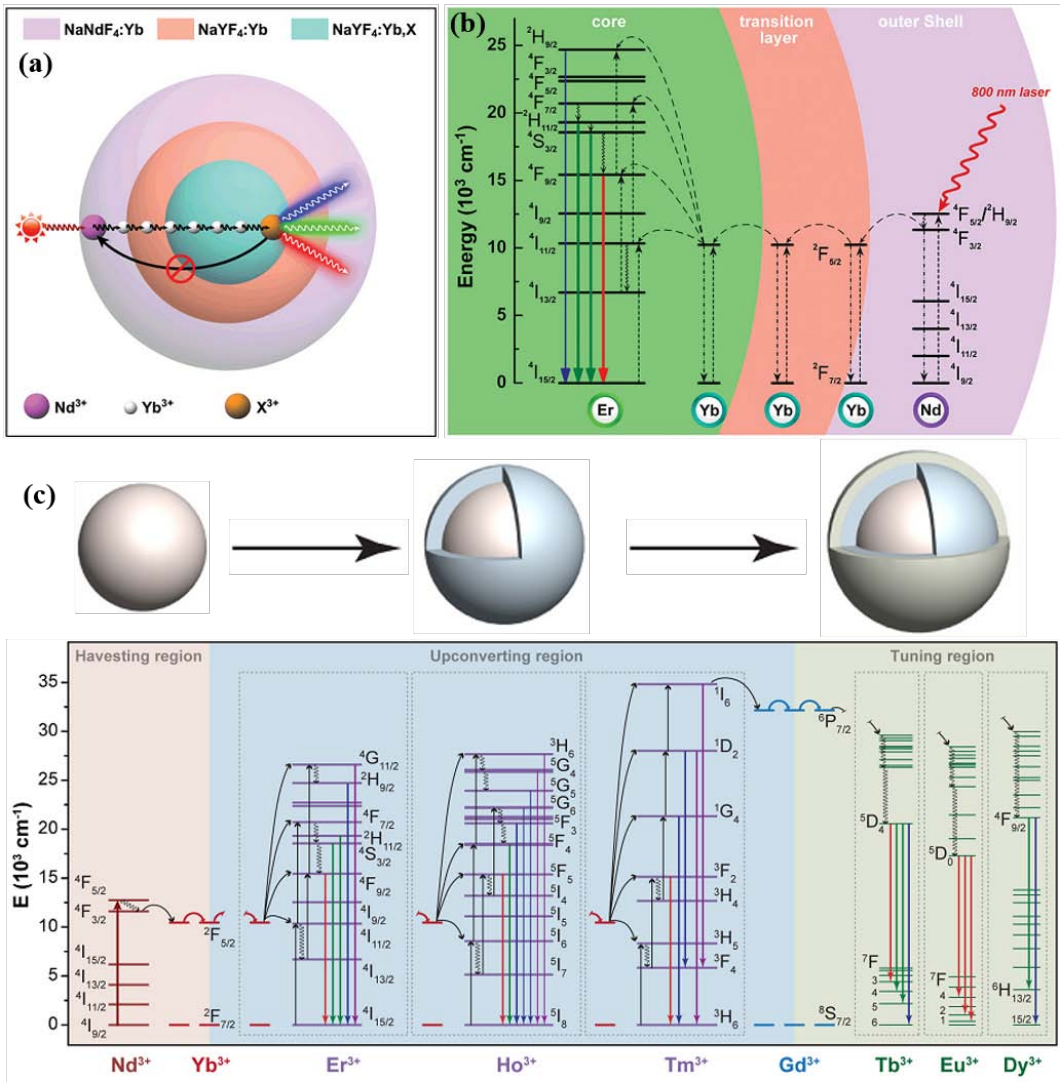

Figure 2.40 (a) Schematic diagram of core-shell-shell structure UCNCs; (b) The proposed energy migration process under 800 nm excitation[86]; (c) The proposed energy migration process in core-shell-shell nanocrystals[155].

REFERENCES

(1) Liu, C.; Gao, Z.; Zeng, J.; Hou, Y.; Fang, F.; Li, Y.; Qiao, R.; Shen, L.; Lei, H.; Yang, W.; *et al.* Magnetic/Upconversion Fluorescent Dual-Modal Molecular Probes for Imaging Tiny Tumors in Vivo. *ACS Nano* **2013**, *7*, 7227–7240.

(2) Keivanidis, P. E.; Baluschev, S.; Miteva, T.; Nelles, G.; Scherf, U.; Yasuda, A.; Wegner, G. Up-Conversion Photoluminescence in Polyfluorene Doped with Metal(II)-Octaethyl Porphyrins. *Adv. Mater.* **2003**, *15*, 2095–2098.

(3) Mezyk, J.; Tubino, R.; Monguzzi, A.; Mech, A.; Meinardi, F. Effect of an External Magnetic Field on the up-Conversion Photoluminescence of Organic Films: The Role of Disorder in Triplet-Triplet Annihilation. *Phys. Rev. Lett.* **2009**, *102*, 1–4.

(4) Liu, J.; Liu, Y.; Liu, Q.; Li, C.; Sun, L.; Li, F. Iridium(III) Complex-Coated Nanosystem for Ratiometric Upconversion Luminescence Bioimaging of Cyanide Anions. *J. Am. Chem. Soc.* **2011**, *133*, 15276–15279.

(5) Chai, R.; Lian, H.; Hou, Z.; Zhang, C.; Peng, C.; Lin, J. Preparation and Characterization of Upconversion Luminescent $NaYF_4$: Yb^{3+}, Er^{3+}(Tm^{3+})/PMMA Bulk Transparent Nanocomposites through in Situ Photopolymerization. *J. Phys. Chem. C* **2010**, *114*, 610–616.

(6) Suzuki, S.; Teshima, K.; Wakabayashi, T.; Nishikiori, H.; Ishizaki, T.; Oishi, S. Novel Fabrication of NIR-Vis Upconversion $NaYF_4$: Ln (Ln = Yb, Er, Tm) Crystal Layers by a Flux Coating Method. *J. Mater. Chem.* **2011**, *21*, 13847–13852.

(7) Sivakumar, S.; Van Veggel, F. C. J. M.; Raudsepp, M. Bright White Light through up-Conversion of a Single NIR Source from Sol-Gel-Derived Thin Film Made with Ln^{3+}-Doped LaF_3 Nanoparticles. *J. Am. Chem. Soc.* **2005**, *127*, 12464–12465.

(8) Lin, C.; Berry, M. T.; Anderson, R.; Smith, S.; May, P. S. Highly Luminescent NIR-to-Visible Upconversion Thin Films and Monoliths Requiring No High-Temperature Treatment. *Chem. Mater.* **2009**, *21*, 3406–3413.

(9) Wang, J.; Wei, T.; Li, X.; Zhang, B.; Wang, J.; Huang, C.; Yuan, Q. Near-Infrared-Light-Mediated Imaging of Latent Fingerprints Based on Molecular Recognition. *Angew. Chemie-Int. Ed.* **2014**, *53*, 1616–1620.

(10) Meruga, J. M.; Baride, A.; Cross, W.; Kellar, J. J.; May, P. S. Red-Green-Blue Printing Using Luminescence-Upconversion Inks. *J. Mater. Chem. C* **2014**, *2*, 2221–2227.

(11) Wang, F.; Han, Y.; Lim, C. S.; Lu, Y.; Wang, J.; Xu, J.; Chen, H.; Zhang, C.; Hong, M.; Liu, X. Simultaneous Phase and Size Control of Upconversion Nanocrystals through Lanthanide Doping. *Nature* **2010**, *463*, 1061–1065.

(12) Ma, R.; Bullock, E.; Maynard, P.; Reedy, B.; Shimmon, R.; Lennard, C.; Roux, C.; McDonagh, A. Fingermark Detection on Non-Porous and Semi-Porous Surfaces Using $NaYF_4$: Er,Yb up-Converter Particles. *Forensic Sci. Int.* **2011**, *207*, 145–149.

(13) Ma, R.; Shimmon, R.; McDonagh, A.; Maynard, P.; Lennard, C.; Roux, C. Fingermark Detection on Non-Porous and Semi-Porous Surfaces Using YVO_4: Er,Yb Luminescent Upconverting Particles. *Forensic Sci. Int.* **2012**, *217*, e22–e25.

(14) Liu, Y.; Ai, K.; Lu, L. Designing Lanthanide-Doped Nanocrystals with Both up- and down-Conversion Luminescence for Anti-Counterfeiting. *Nanoscale* **2011**, *3*, 4804-4810.

(15) Boyer, J. C.; Carling, C. J.; Gates, B. D.; Branda, N. R. Two-Way Photoswitching Using One Type of near-Infrared Light, Upconverting Nanoparticles, and Changing Only the Light Intensity. *J. Am. Chem. Soc.* **2010**, *132*, 15766–15772.

(16) Ishow, E.; Brosseau, A.; Clavier, G.; Nakatani, K.; Pansu, R. B.; Vachon, J. J.; Tauc, P.; Chauvat, D.; Mendonça, C. R.; Piovesan, E. Two-Photon Fluorescent Holographic Rewritable Micropatterning. *J. Am. Chem. Soc.* **2007**, *129*, 8970–8971.

(17) Corredor, C. C.; Huang, Z. L.; Belfield, K. D. Two-Photon 3D Optical Data Storage via Fluorescence Modulation of an Efficient Fluorene Dye by a Photochromic Diarylethene. *Adv. Mater.* **2006**, *18*, 2910–2914.

(18) Lim, S. J.; Seo, J.; Park, S. Y. Photochromic Switching of Excited-State Intramolecular Proton-Transfer (ESIPT) Fluorescence: A Unique Route to High-Contrast Memory Switching and Nondestructive Readout. *J. Am. Chem. Soc.* **2006**, *128*, 14542–14547.

(19) Zhang, C.; Ou, H. P.; Liao, L. Y.; Feng, W.; Sun, W.; Li, Z. X.; Xu, C. H.; Fang, C. J.; Sun, L. D.; Zhang, Y. W.; *et al.* Luminescence Modulation of Ordered Upconversion Nanopatterns by a Photochromic Diarylethene: Rewritable Optical Storage with Nondestructive Readout. *Adv. Mater.* **2010**, *22*, 633–637.

(20) Yuan, W.; Sun, L.; Tang, H.; Wen, Y.; Jiang, G.; Huang, W.; Jiang, L.; Song, Y.; Tian, H.; Zhu, D. A Novel Thermally Stable Spironaphthoxazine and Its Application in Rewritable High Density Optical Data Storage. *Adv. Mater.* **2005**, *17*, 156–160.

(21) Shalav, A.; Richards, B. S.; Trupke, T.; Krämer, K. W.; Güdel, H. U. Application of $NaYF_4$: Er^{3+} up-Converting Phosphors for Enhanced near-Infrared Silicon Solar Cell Response. *Appl. Phys. Lett.* **2005**, *86*, 1–4.

(22) Gibart, P.; Auzel, F.; Guillaume, J.; Zahraman, K. Below Band-Gap IR Response of Substrate-Free GaAs Solar Cells Using Two-Photon Up- Conversion. *Jpn. J. Appl. Phys.* **1996**, *35*, 4401–4402.

(23) de Wild, J.; Meijerink, A.; Rath, J. K.; van Sark, W. G. J. H. M.; Schropp, R. E. I. Upconverter Solar Cells: Materials and Applications. *Energy Environ. Sci.* **2011**, *4*, 4835-4848.

(24) Shan, G. Bin; Demopoulos, G. P. Near-Infrared Sunlight Harvesting in Dye-Sensitized Solar Cells via the Insertion of an Upconverter-TiO_2 Nanocomposite Layer. *Adv. Mater.* **2010**, *22*, 4373–4377.

(25) Chen, Z.; Zhang, L.; Sun, Y.; Hu, J.; Wang, D. 980-nm Laser-Driven Photovoltaic Cells Based on Rare-Earth Up-Converting Phosphors for Biomedical Applications. *Adv. Funct. Mater.* **2009**, *19*, 3815–3820.

(26) Fujishima, A.; Rao, T. N.; Tryk, D. A. TiO_2 Photocatalysts and Diamond Electrodes. *Electrochim. Acta* **2000**, *45*, 4683–4690.

(27) FUJISHIMA, A.; HONDA, K. Electrochemical Photolysis of Water at a Semiconductor Electrode. *Nature* **1972**, *238*, 37–38.

(28) Huang, S.; Zhu, N.; Lou, Z.; Gu, L.; Miao, C.; Yuan, H.; Shan, A. Near-Infrared Photocatalysts of $BiVO_4/CaF_2$: Er^{3+}, Tm^{3+}, Yb^{3+} with Enhanced Upconversion Properties. *Nanoscale* **2014**, *6*, 1362–1368.

(29) Cheng, E.; Yin, W.; Bai, S.; Qiao, R.; Zhong, Y.; Li, Z. Synthesis of vis/NIR-Driven Hybrid Photocatalysts by Electrostatic Assembly of $NaYF_4$: Yb, Tm Nanocrystals on G-C_3N_4 Nanosheets. *Mater. Lett.* **2015**, *146*, 87–90.

(30) Xu, C. T.; Svensson, N.; Axelsson, J.; Svenmarker, P.; Somesfalean, G.; Chen, G.; Liang, H.; Liu, H.; Zhang, Z.; Andersson-Engels, S. Autofluorescence Insensitive

Imaging Using Upconverting Nanocrystals in Scattering Media. *Appl. Phys. Lett.* **2008**, *93*, 1–4.

(31) Lu, Y.; Zhao, J.; Zhang, R.; Liu, Y.; Liu, D.; Goldys, E. M.; Yang, X.; Xi, P.; Sunna, A.; Lu, J.; *et al.* Tunable Lifetime Multiplexing Using Luminescent Nanocrystals. *Nat. Photonics* **2013**, *8*, 32–36.

(32) Sun, Y.; Yu, M.; Liang, S.; Zhang, Y.; Li, C.; Mou, T.; Yang, W.; Zhang, X.; Li, B.; Huang, C.; *et al.* Fluorine-18 Labeled Rare-Earth Nanoparticles for Positron Emission Tomography (PET) Imaging of Sentinel Lymph Node. *Biomaterials* **2011**, *32*, 2999–3007.

(33) Zhou, J. C.; Yang, Z. L.; Dong, W.; Tang, R. J.; Sun, L. D.; Yan, C. H. Bioimaging and Toxicity Assessments of near-Infrared Upconversion Luminescent $NaYF_4$: Yb, Tm Nanocrystals. *Biomaterials* **2011**, *32*, 9059–9067.

(34) Xiong, L.; Yang, T.; Yang, Y.; Xu, C.; Li, F. Long-Term in Vivo Biodistribution Imaging and Toxicity of Polyacrylic Acid-Coated Upconversion Nanophosphors. *Biomaterials* **2010**, *31*, 7078–7085.

(35) Yang, Y.; Sun, Y.; Liu, Y.; Peng, J.; Wu, Y.; Zhang, Y.; Feng, W.; Li, F. Long-Term in Vivo Biodistribution and Toxicity of $Gd(OH)_3$ Nanorods. *Biomaterials* **2013**, *34*, 508–515.

(36) Lim, S. F.; Riehn, R.; Ryu, W. S.; Khanarian, N.; Tung, C. K.; Tank, D.; Austin, R. H. In Vivo and Scanning Electron Microscopy Imaging of Upconverting Nanophosphors in Caenorhabditis Elegans. *Nano Lett.* **2006**, *6*, 169–174.

(37) Jang, G. H.; Hwang, M. P.; Kim, S. Y.; Jang, H. S.; Lee, K. H. A Systematic in-Vivo Toxicity Evaluation of Nanophosphor Particles via Zebrafish Models. *Biomaterials* **2014**, *35*, 440–449.

(38) Chatterjee, D. K.; Rufaihah, A. J.; Zhang, Y. Upconversion Fluorescence Imaging of Cells and Small Animals Using Lanthanide Doped Nanocrystals. *Biomaterials* **2008**, *29*, 937–943.

(39) Liu, Z.; Pu, F.; Huang, S.; Yuan, Q.; Ren, J.; Qu, X. Long-Circulating Gd_2O_3: Yb^{3+}, Er^{3+} up-Conversion Nanoprobes as High-Performance Contrast Agents for Multi-Modality Imaging. *Biomaterials* **2013**, *34*, 1712–1721.

(40) Xing, H.; Bu, W.; Ren, Q.; Zheng, X.; Li, M.; Zhang, S.; Qu, H.; Wang, Z.; Hua, Y.; Zhao, K.; *et al.* A $NaYbF_4$: Tm^{3+} Nanoprobe for CT and NIR-to-NIR Fluorescent Bimodal Imaging. *Biomaterials* **2012**, *33*, 5384–5393.

(41) Cheng, Z.; Thorek, D. L. J.; Tsourkas, A. Porous Polymersomes with Encapsulated Gd-Labeled Dendrimers as Highly Efficient MRI Contrast Agents. *Adv. Funct. Mater.* **2009**, *19*, 3753–3759.

(42) Di Corato, R.; Gazeau, F.; Le Visage, C.; Fayol, D.; Levitz, P.; Lux, F.; Letourneur, D.; Luciani, N.; Tillement, O.; Wilhelm, C. High-Resolution Cellular MRI: Gadolinium and Iron Oxide Nanoparticles for in-Depth Dual-Cell Imaging of Engineered Tissue Constructs. *ACS Nano* **2013**, *7*, 7500–7512.

(43) Zhou, J.; Lu, Z.; Shan, G.; Wang, S.; Liao, Y. Gadolinium Complex and Phosphorescent Probe-Modified $NaDyF_4$ Nanorods for T_1- and T_2-Weighted MRI/CT/phosphorescence Multimodality Imaging. *Biomaterials* **2014**, *35*, 368–377.

(44) Qian, H. S.; Guo, H. C.; Ho, P. C. L.; Mahendran, R.; Zhang, Y. Mesoporous-Silica-Coated up-Conversion Fluorescent Nanoparticles for Photodynamic Therapy. *Small* **2009**, *5*, 2285–2290.

(45) Li, Z.; Zhang, Y.; Jiang, S. Multicolor Core/shell-Structured Upconversion Fluorescent Nanoparticles. *Adv. Mater.* **2008**, *20*, 4765–4769.

(46) Wong, H.-T.; Tsang, M.-K.; Chan, C.-F.; Wong, K.-L.; Fei, B.; Hao, J. In Vitro Cell Imaging Using Multifunctional Small Sized $KGdF_4$: Yb^{3+}, Er^{3+} Upconverting Nanoparticles Synthesized by a One-Pot Solvothermal Process. *Nanoscale* **2013**, *5*, 3465.

(47) Nyk, M.; Kumar, R.; Ohulchanskyy, T. Y.; Bergey, E. J.; Prasad, P. N. High Contrast in Vitro and in Vivo Photoluminescence Bioimaging Using Near Infrared to Near Infrared Up-Conversion in Tm^{3+} and Yb^{3+} Doped Fluoride Nanophosphors. *Nano Lett.* **2008**, *8*, 3834–3838.

(48) Cao, T.; Yang, Y.; Gao, Y.; Zhou, J.; Li, Z.; Li, F. High-Quality Water-Soluble and Surface-Functionalized Upconversion Nanocrystals as Luminescent Probes for Bioimaging. *Biomaterials* **2011**, *32*, 2959–2968.

(49) Chen, J.; Guo, C.; Wang, M.; Huang, L.; Wang, L.; Mi, C.; Li, J.; Fang, X.; Mao, C.; Xu, S. Controllable Synthesis of $NaYF_4$: Yb, Er Upconversion Nanophosphors and Their

Application to in Vivo Imaging of Caenorhabditis Elegans. *J. Mater. Chem.* **2011**, *21*, 2632.

(50) Wang, K.; Ma, J.; He, M.; Gao, G.; Xu, H.; Sang, J.; Wang, Y.; Zhao, B.; Cui, D. Toxicity Assessments of near-Infrared Upconversion Luminescent LaF_3: Yb, Er in Early Development of Zebrafish Embryos. *Theranostics* **2013**, *3*, 258–266.

(51) Cheng, L.; Yang, K.; Shao, M.; Lu, X.; Liu, Z. And Toxicology Study of Functionalized Upconversion Nanoparticles in Mice P Reliminary C ommuniCation. **2011**, 1327–1340.

(52) Yu, M.; Li, F.; Chen, Z.; Hu, H.; Zhan, C.; Yang, H.; Huang, C. Laser Scanning up-Conversion Luminescence Microscopy for Imaging Cells Labeled with Rare-Earth Nanophosphors. *Anal. Chem.* **2009**, *81*, 930–935.

(53) Idris, N. M.; Li, Z.; Ye, L.; Wei Sim, E. K.; Mahendran, R.; Ho, P. C. L.; Zhang, Y. Tracking Transplanted Cells in Live Animal Using Upconversion Fluorescent Nanoparticles. *Biomaterials* **2009**, *30*, 5104–5113.

(54) Xiang, J.; Xu, L.; Gong, H.; Zhu, W.; Wang, C.; Xu, J.; Feng, L.; Cheng, L.; Peng, R.; Liu, Z. Antigen-Loaded Upconversion Nanoparticles for Dendritic Cell Stimulation, Tracking, and Vaccination in Dendritic Cell-Based Immunotherapy. *ACS Nano* **2015**, *9*, 6401–6411.

(55) Yi, G.; Lu, H.; Zhao, S.; Ge, Y.; Yang, W.; Chen, D.; Guo, L. H. Synthesis, Characterization, and Biological Application of Size-Controlled Nanocrystalline $NaYF_4$: Yb, Er Infrared-to-Visible up-Conversion Phosphors. *Nano Lett.* **2004**, *4*, 2191–2196.

(56) Zako, T.; Nagata, H.; Terada, N.; Utsumi, A.; Sakono, M.; Yohda, M.; Ueda, H.; Soga, K.; Maeda, M. Cyclic RGD Peptide-Labeled Upconversion Nanophosphors for Tumor Cell-Targeted Imaging. *Biochem. Biophys. Res. Commun.* **2009**, *381*, 54–58.

(57) Hu, H.; Yu, M.; Li, F.; Chen, Z.; Gao, X.; Xiong, L.; Huang, C. Facile Epoxidation Strategy for Producing Amphiphilic up-Converting Rare-Earth Nanophosphors as Biological Labels. *Chem. Mater.* **2008**, *20*, 7003–7009.

(58) Boyer, J. C.; Manseau, M. P.; Murray, J. I.; Van Veggel, F. C. J. M. Surface Modification of Upconverting $NaYF_4$ Nanoparticles with PEG-Phosphate Ligands for NIR (800 nm) Biolabeling within the Biological Window. *Langmuir* **2010**, *26*, 1157–1164.

(59) Naccache, R.; Vetrone, F.; Mahalingam, V.; Cuccia, L. a; Capobianco, J. a. Controlled Synthesis and Water Dispersibility of Hexagonal Phase $NaGdF_4$: Ho^{3+}/Yb^{3+} Nanoparticles. *Chem. Mater.* **2009**, *21*, 717–723.

(60) Yi, G.; Chow, G. Core/Shell/Shell Nanoparticles with Significant Enhancement of Upconversion Fluorescence. *Chem. Mater.* **2007**, *19*, 341–343.

(61) Jin, J.; Gu, Y.; Man, C. W.; Cheng, J.; Xu, Z.; Zhang, Y.; Wang, H.; Lee, V. H.; Cheng, S. H.; Wong, W. Polymer-Coated $NaYF_4$: Yb^{3+}, Er^{3+} Upconversion Nanoparticles for Charge-Dependent Cellular Imaging. *ACS Nano* **2011**, *5*, 7838–7847.

(62) Zhang, H.; Li, Y.; Lin, Y.; Huang, Y.; Duan, X. Composition Tuning the Upconversion Emission in $NaYF_4$: Yb/Tm Hexaplate Nanocrystals. *Nanoscale* **2011**, *3*, 963-966.

(63) Shan, J.; Chen, J.; Meng, J.; Collins, J.; Soboyejo, W.; Friedberg, J. S.; Ju, Y. Biofunctionalization, Cytotoxicity, and Cell Uptake of Lanthanide Doped Hydrophobically Ligated $NaYF_4$ Upconversion Nanophosphors. *J. Appl. Phys.* **2008**, *104*. 094308-1-7.

(64) Kobayashi, H.; Kosaka, N.; Ogawa, M.; Morgan, N. Y.; Smith, P. D.; Murray, C. B.; Ye, X.; Collins, J.; Kumar, G. A.; Bell, H.; *et al.* In Vivo Multiple Color Lymphatic Imaging Using Upconverting Nanocrystals. *J. Mater. Chem.* **2009**, *19*, 6481-6484.

(65) Hilderbrand, S. A.; Shao, F.; Salthouse, C.; Mahmood, U.; Weissleder, R. Upconverting Luminescent Nanomaterials: Application to in Vivo Bioimaging. *Chem. Commun.* **2009**, 4188-4190.

(66) Wei, Z.; Sun, L.; Liu, J.; Zhang, J. Z.; Yang, H.; Yang, Y.; Shi, L. Cysteine Modified Rare-Earth up-Converting Nanoparticles for Invitro and Invivo Bioimaging. *Biomaterials* **2014**, *35*, 387–392.

(67) Dong, B.; Cao, B.; He, Y.; Liu, Z.; Li, Z.; Feng, Z. Temperature Sensing and in Vivo Imaging by Molybdenum Sensitized Visible Upconversion Luminescence of Rare-Earth Oxides. *Adv. Mater.* **2012**, *24*, 1987–1993.

(68) Yang, T.; Sun, Y.; Liu, Q.; Feng, W.; Yang, P.; Li, F. Cubic Sub-20 nm $NaLuF_4$-Based Upconversion Nanophosphors for High-Contrast Bioimaging in Different Animal Species. *Biomaterials* **2012**, *33*, 3733–3742.

(69) Zhao, J.; Jin, D.; Schartner, E. P.; Lu, Y.; Liu, Y.; Zvyagin, A. V; Zhang, L.; Dawes, J.

M.; Xi, P.; Piper, J. a; *et al*. Single-Nanocrystal Sensitivity Achieved by Enhanced Upconversion Luminescence. *Nat. Nanotechnol.* **2013**, *8*, 729–734.

(70) Deng, M.; Ma, Y.; Huang, S.; Hu, G.; Wang, L. Monodisperse Upconversion $NaYF_4$ Nanocrystals: Syntheses and Bioapplications. *Nano Res.* **2011**, *4*, 685–694.

(71) Sun, E.-Z.; Liu, A.-A.; Zhang, Z.-L.; Liu, S.-L.; Tian, Z.-Q.; Pang, D.-W. Real-Time Dissection of Distinct Dynamin-Dependent Endocytic Routes of Influenza A Virus by Quantum Dot-Based Single-Virus Tracking. *ACS Nano* **2017**, acsnano.6b07853.

(72) Idris, N. M.; Li, Z.; Ye, L.; Wei Sim, E. K.; Mahendran, R.; Ho, P. C. L.; Zhang, Y. Tracking Transplanted Cells in Live Animal Using Upconversion Fluorescent Nanoparticles. *Biomaterials* **2009**, *30*, 5104–5113.

(73) He, M.; Huang, P.; Zhang, C.; Hu, H.; Bao, C.; Gao, G.; He, R.; Cui, D. Dual Phase-Controlled Synthesis of Uniform Lanthanide-Doped $NaGdF_4$ Upconversion Nanocrystals via an OA/ionic Liquid Two-Phase System for in Vivo Dual-Modality Imaging. *Adv. Funct. Mater.* **2011**, *21*, 4470–4477.

(74) Wang, C.; Cheng, L.; Liu, Z. Upconversion Nanoparticles for Photodynamic Therapy and Other Cancer Therapeutics. *Theranostics* **2013**, *3*, 317–330.

(75) Chatterjee, D. K.; Fong, L. S.; Zhang, Y. Nanoparticles in Photodynamic Therapy: An Emerging Paradigm. *Adv. Drug Deliv. Rev.* **2008**, *60*, 1627–1637.

(76) Wang, M.; Mi, C.-C.; Wang, W.-X.; Liu, C.-H.; Wu, Y.-F.; Xu, Z.-R.; Mao, C.-B.; Xu, S.-K. Immunolabeling and NIR-Excited Fluorescent Imaging of HeLa Cells by Using $NaYF_4$: Yb, Er Upconversion Nanoparticles. *ACS Nano* **2009**, *3*, 1580–1586.

(77) Li, H. H.; Wu, X. L.; Sun, H. Z.; Wang, K.; Fan, C. Y.; Zhang, L. L.; Yang, F. M.; Zhang, J. P. Dual-Porosity SiO_2/C Nanocomposite with Enhanced Lithium Storage Performance. *J. Phys. Chem. C* **2015**, *119*, 3495–3501.

(78) Kumar, R.; Nyk, M.; Ohulchanskyy, T. Y.; Flask, C. A.; Prasad, P. N. Combined Optical and MR Bloimaging Using Rare Earth Ion Doped $NaYF_4$ Nanocrystals. *Adv. Funct. Mater.* **2009**, *19*, 853–859.

(79) Bogdan, N.; Rodríguez, E. M.; Sanz-Rodríguez, F.; Iglesias de la Cruz, M. C.; Juarranz, Á.; Jaque, D.; Solé, J. G.; Capobianco, J. A. Bio-Functionalization of Ligand-Free Upconverting Lanthanide Doped Nanoparticles for Bio-Imaging and Cell Targeting.

Nanoscale **2012**, *4*, 3647-3650.

(80) Ni, D.; Zhang, J.; Bu, W.; Xing, H.; Han, F.; Xiao, Q.; Yao, Z.; Chen, F.; He, Q.; Liu, J.; *et al.* Dual-Targeting Upconversion Nanoprobes across the Blood-Brain Barrier for Magnetic Resonance/fluorescence Imaging of Intracranial Glioblastoma. *ACS Nano* **2014**, *8*, 1231–1242.

(81) Xiong, L. Q.; Chen, Z. G.; Yu, M. X.; Li, F. Y.; Liu, C.; Huang, C. H. Synthesis, Characterization, and in Vivo Targeted Imaging of Amine-Functionalized Rare-Earth up-Converting Nanophosphors. *Biomaterials* **2009**, *30*, 5592–5600.

(82) Heer, S.; Kömpe, K.; Güdel, H. U.; Haase, M. Highly Efficient Multicolour Upconversion Emission in Transparent Colloids of Lanthanide-Doped $NaYF_4$ Nanocrystals. *Adv. Mater.* **2004**, *16*, 2102–2105.

(83) Zhang, S.-Z.; Sun, L.-D.; Tian, H.; Liu, Y.; Wang, J.-F.; Yan, C.-H. Reversible Luminescence Switching of $NaYF_4$: Yb, Er Nanoparticles with Controlled Assembly of Gold Nanoparticles. *Chem. Commun.* **2009**, 2547-2549.

(84) Wang, F.; Deng, R.; Wang, J.; Wang, Q.; Han, Y.; Zhu, H.; Chen, X.; Liu, X. Tuning Upconversion through Energy Migration in Core–shell Nanoparticles. *Nat. Mater.* **2011**, *10*, 968–973.

(85) Su, Q.; Han, S.; Xie, X.; Zhu, H.; Chen, H.; Chen, C. K.; Liu, R. S.; Chen, X.; Wang, F.; Liu, X. The Effect of Surface Coating on Energy Migration-Mediated Upconversion. *J. Am. Chem. Soc.* **2012**, *134*, 20849–20857.

(86) Zhong, Y.; Tian, G.; Gu, Z.; Yang, Y.; Gu, L.; Zhao, Y.; Ma, Y.; Yao, J. Elimination of Photon Quenching by a Transition Layer to Fabricate a Quenching-Shield Sandwich Structure for 800 nm Excited Upconversion Luminescence of Nd^{3+}-Sensitized Nanoparticles. *Adv. Mater.* **2014**, *26*, 2831–2837.

(87) Chen, Z.; Chen, H.; Hu, H.; Yu, M.; Li, F.; Zhang, Q.; Zhou, Z.; Yi, T.; Huang, C. Versatile Synthesis Strategy for Carboxylic Acid-Functionalized Upconverting Nanophosphors as Biological Labels. *J. Am. Chem. Soc.* **2008**, *130*, 3023–3029.

(88) Wang, X.; Kong, X.; Yu, Y.; Sun, Y.; Zhang, H. Effect of Annealing on Upconversion Luminescence of ZnO: Er^{3+} Nanocrystals and High Thermal Sensitivity. *J. Phys. Chem. C* **2007**, *111*, 15119–15124.

(89) Vetrone, F.; Naccache, R.; Zamarrón, A.; De La Fuente, A. J.; Sanz-Rodríguez, F.; Maestro, L. M.; Rodriguez, E. M.; Jaque, D.; Sole, J. G.; Capobianco, J. A. Temperature Sensing Using Fluorescent Nanothermometers. *ACS Nano* **2010**, *4*, 3254–3258.

(90) Chen, B.; Dong, B.; Wang, J.; Zhang, S.; Xu, L.; Yu, W.; Song, H. Amphiphilic Silane Modified $NaYF_4$: Yb, Er Loaded with $Eu(TTA)_3(TPPO)_2$ Nanoparticles and Their Multi-Functions: Dual Mode Temperature Sensing and Cell Imaging. *Nanoscale* **2013**, *5*, 8541–8549.

(91) Shan, J.; Kong, W.; Wei, R.; Yao, N.; Ju, Y. An Investigation of the Thermal Sensitivity and Stability of the β-$NaYF_4$: Yb, Er Upconversion Nanophosphors. *J. Appl. Phys.* **2010**, *107*.

(92) Ximendes, E. C.; Santos, W. Q.; Rocha, U.; Kagola, U. K.; Sanz-Rodriguez, F.; Fernandez, N.; Gouveia-Neto, A. D. S.; Bravo, D.; Domingo, A. M.; Del Rosal, B.; *et al.* Unveiling in Vivo Subcutaneous Thermal Dynamics by Infrared Luminescent Nanothermometers. *Nano Lett.* **2016**, *16*, 1695–1703.

(93) Li, D.; Wang, Y.; Zhang, X.; Yang, K.; Liu, L.; Song, Y. Optical Temperature Sensor through Infrared Excited Blue Upconversion Emission in Tm^{3+}/Yb^{3+} Codoped Y_2O_3. *Opt. Commun.* **2012**, *285*, 1925–1928.

(94) Sun, L.-N.; Peng, H.; Stich, M. I. J.; Achatz, D.; Wolfbeis, O. S. pH Sensor Based on Upconverting Luminescent Lanthanide Nanorods. *Chem. Commun. (Camb).* **2009**, 5000–5002.

(95) Thanh, N. T. K.; Maclean, N.; Mahiddine, S. Mechanisms of Nucleation and Growth of Nanoparticles in Solution. *Chem. Rev.* **2014**, *114*, 7610–7630.

(96) Markus, Y. (The H. U. of J. Thermodynamics of Solvation of Ions Part 5. - Gibbs Free Energy of Hydration at 298.15 K. *Faraday Trans* **1989**, *87*, 3819–3824.

(97) LaMer, V.; Dinegar, R. Theory, Production and Mechanism of Formation of Monodispersed Hydrosols. *J. Am. Chem. Soc.* **1950**, *72*, 4847–4854.

(98) Ostwald, W. Studien Über Die Bildung Und Umwandlung Fester Körper. *Z. Phys. Chem.* **1897**, *22*, 289–330.

(99) Wang, L.; Li, P.; Li, Y. Down- and up-Conversion Luminescent Nanorods. *Adv. Mater.* **2007**, *19*, 3304–3307.

(100) Sun, Y.; Liu, Q.; Peng, J.; Feng, W.; Zhang, Y.; Yang, P.; Li, F. Radioisotope Post-Labeling Upconversion Nanophosphors for in Vivo Quantitative Tracking. *Biomaterials* **2013**, *34*, 2289–2295.

(101) Peng, J.; Sun, Y.; Zhao, L.; Wu, Y.; Feng, W.; Gao, Y.; Li, F. Polyphosphoric Acid Capping Radioactive/upconverting $NaLuF_4$: Yb, Tm, ^{153}Sm Nanoparticles for Blood Pool Imaging Invivo. *Biomaterials* **2013**, *34*, 9535–9544.

(102) Stouwdam, J. W.; Van Veggel, F. C. J. M. Near-Infrared Emission of Redispersible Er^{3+}, Nd^{3+}, and Ho^{3+} Doped LaF_3 Nanoparticles. *Nano Lett.* **2002**, *2*, 733–737.

(103) Li, Z.; Zhang, Y. An Efficient and User-Friendly Method for the Synthesis of Hexagonal-Phase $NaYF_4$: Yb, Er/Tm Nanocrystals with Controllable Shape and Upconversion Fluorescence. *Nanotechnology* **2008**, *19*, 345606–345610.

(104) Zhang, Y.; Sun, X.; Si, R.; You, L.; Yan, C. Single-Crystalline and Monodisperse LaF_3 Triangular Nanoplates from a Single- Source Precursor. *Mercury* **2005**, *34*, 5–7.

(105) Mai, H.-X.; Zhang, Y.-W.; Si, R.; Yan, Z.-G.; Sun, L.; You, L.-P.; Yan, C.-H. High-Quality Sodium Rare-Earth Fluoride Nanocrystals: Controlled Synthesis and Optical Properties. *J. Am. Chem. Soc.* **2006**, *128*, 6426–6436.

(106) Mai, H. X.; Zhang, Y. W.; Sun, L. D.; Yan, C. H. Size- and Phase-Controlled Synthesis of Monodisperse $NaYF_4$: Yb, Er Nanocrystals from a Unique Delayed Nucleation Pathway Monitored with Upconversion Spectroscopy. *J. Phys. Chem. C* **2007**, *111*, 13730–13739.

(107) Ehlert, O.; Thomann, R.; Darbandi, M.; Nann, T. A Four-Color Colloidal Multiplexing Nanoparticle System. *ACS Nano* **2008**, *2*, 120–124.

(108) Du, Y. P.; Zhang, Y. W.; Yan, Z. G.; Sun, L. D.; Gao, S.; Yan, C. H. Single-Crystalline and near-Monodispersed $NaMF_3$ (M = Mn, Co, Ni, Mg) and $LiMAlF_6$ (M = Ca, Sr) Nanocrystals from Cothermolysis of Multiple Trifluoroacetates in Solution. *Chem.-An Asian J.* **2007**, *2*, 965–974.

(109) Shan, J.; Ju, Y. A Single-Step Synthesis and the Kinetic Mechanism for Monodisperse and Hexagonal-Phase $NaYF_4$: Yb, Er Upconversion Nanophosphors. *Nanotechnology* **2009**, *20*, 275603.

(110) Wei Yang; Lu Fengqi; Xinrong, Z.; Chen, D. Synthesis of Oil-Dispersible Hexagonal-

Phase and Hexagonal-Shaped $NaYF_4$: Yb,Er Nanoplates. *Chem. Mater* **2006**, 5733–5737.

(111) Shan, J.; Qin, X.; Yao, N.; Ju, Y. :Yb, Ln (Ln = Er, Ho and Tm) Upconversion Nanocrystals in TOPO. *Nanotechnology* **2007**, *18*, 445607.

(112) Liang, L.; Xu, H.; Su, Q.; Konishi, H.; Jiang, Y.; Wu, M.; Wang, Y.; Xia, D. Hydrothermal Synthesis of Prismatic $NaHoF_4$ Microtubes and $NaSmF_4$ Nanotubes. *Inorg. Chem.* **2004**, *43*, 1594–1596.

(113) Zeng, J. H.; Su, J.; Li, Z. H.; Yan, R. X.; Li, Y. D. Synthesis and Upconversion Luminescence of Hexagonal-Phase $NaYF_4$: Yb, Er^{3+} Phosphors of Controlled Size and Morphology. *Adv. Mater.* **2005**, *17*, 2119–2123.

(114) Zhang, F.; Wan, Y.; Yu, T.; Zhang, F.; Shi, Y.; Xie, S.; Li, Y.; Xu, L.; Tu, B.; Zhao, D. Uniform Nanostructured Arrays of Sodium Rare-Earth Fluorides for Highly Efficient Multicolor Upconversion Luminescence. *Angew. Chemie - Int. Ed.* **2007**, *46*, 7976–7979.

(115) Patra, A.; Friend, C. S.; Kapoor, R.; Prasad, P. N. Upconversion in Er^{3+}: ZrO_2 Nanocrystals. *J. Phys. Chem. B* **2002**, *106*, 1909–1912.

(116) Patra, A.; Friend, C. S.; Kapoor, R.; Prasad, P. N. Fluorescence Upconversion Properties of Er^{3+}-Doped TiO_2 and $BaTiO_3$ Nanocrystallites. *Chem. Mater.* **2003**, *15*, 3650–3655.

(117) Daldosso, M.; Falcomer, D.; Speghini, A.; Bettinelli, M.; Enzo, S.; Lasio, B.; Polizzi, S. Synthesis, Structural Investigation and Luminescence Spectroscopy of Nanocrystalline $Gd_3Ga_5O_{12}$ Doped with Lanthanide Ions. *J. Alloys Compd.* **2008**, *451*, 553–556.

(118) Mahalingam, V.; Mangiarini, F.; Vetrone, F.; Venkatramu, V.; Bettinelli, M.; Speghini, A.; Capobianco, J. A. Bright White Upconversion Emission from $Tm^{3+}/Yb^{3+}/Er^{3+}$-Doped $Lu_3Ga_5O_{12}$ Nanocrystals. *J. Phys. Chem. C* **2008**, *112*, 17745–17749.

(119) Liu, X.; Zhao, J.; Sun, Y.; Song, K.; Yu, Y.; Du, C.; Kong, X.; Zhang, H. Ionothermal Synthesis of Hexagonal-Phase $NaYF_4$: Yb^{3+}, Er^{3+}/Tm^{3+} Upconversion Nanophosphors. *Chem. Commun. (Camb).* **2009**, 6628–6630.

(120) Qin, X.; Yokomori, T.; Ju, Y. Flame Synthesis and Characterization of Rare-Earth (Er^{3+}, Ho^{3+}, and Tm^{3+}) Doped Upconversion Nanophosphors. *Appl. Phys. Lett.* **2007**, *90*, 1–4.

(121) Vetrone, F.; Boyer, J.-C.; Capobianco, J. a.; Speghini, A.; Bettinelli, M. Luminescence

Spectroscopy and Near-Infrared to Visible Upconversion of Nanocrystalline $Gd_3Ga_5O_{12}$: Er^{3+}. *J. Phys. Chem. B* **2003**, *107*, 10747–10752.

(122) Maciel, G. S.; Rakov, N.; Fokine, M.; Carvalho, I. C. S.; Pinheiro, C. B. Strong Upconversion from $Er_3Al_5O_{12}$ Ceramic Powders Prepared by Low Temperature Direct Combustion Synthesis. *Appl. Phys. Lett.* **2006**, *89*, 1–4.

(123) Ye, T.; Guiwen, Z.; Weiping, Z.; Shangda, X. Combustion Synthesis and Photoluminescence of Nanocrystalline Y_2O_3: Eu Phosphors. *Mater. Res. Bull.* **1997**, *32*, 501–506.

(124) Singh, S. K.; Kumar, K.; Rai, S. B. Multifunctional Er^{3+}-Yb^{3+} Codoped Gd_2O_3 Nanocrystalline Phosphor Synthesized through Optimized Combustion Route. *Appl. Phys. B Lasers Opt.* **2009**, *94*, 165–173.

(125) Kong, W.; Shan, J.; Ju, Y. Flame Synthesis and Effects of Host Materials on Yb^{3+}/Er^{3+} Co-Doped Upconversion Nanophosphors. *Mater. Lett.* **2010**, *64*, 688–691.

(126) Polte, J.; Ahner, T. T.; Delissen, F.; Sokolov, S.; Emmerling, F.; Thünemann, A. F.; Kraehnert, R. Mechanism of Gold Nanoparticle Formation in the Classical Citrate Synthesis Method Derived from Coupled in Situ XANES and SAXS Evaluation. *J. Am. Chem. Soc.* **2010**, *132*, 1296–1301.

(127) Gao, D.; Zhang, X.; Gao, W. Tuning Upconversion Emission by Controlling Particle Shape in $NaYF_4$: Yb^{3+}/Er^{3+} Nanocrystals. *J. Appl. Phys.* **2012**, *111*, 3–8.

(128) Rinkel, T.; Nordmann, J.; Raj, A. N.; Haase, M. Ostwald-Ripening and Particle Size Focussing of Sub-10nm $NaYF_4$ Upconversion Nanocrystals. *Nanoscale* **2014**, *6*, 14523–14530.

(129) Gao, D.; Zhang, X.; Gao, W. Formation of Bundle-Shaped β-$NaYF_4$ Upconversion Microtubes via Ostwald Ripening. *ACS Appl. Mater. Interfaces* **2013**, *5*, 9732–9739.

(130) Johnson, N. J. J.; Korinek, A.; Dong, C.; Van Veggel, F. C. J. M. Self-Focusing by Ostwald Ripening: A Strategy for Layer-by-Layer Epitaxial Growth on Upconverting Nanocrystals. *J. Am. Chem. Soc.* **2012**, *134*, 11068–11071.

(131) Suter, J. D.; Pekas, N.; Berry, M. T.; May, P. S. Real-Time-Monitoring of the Synthesis of β-$NaYF_4$: 17% Yb, 3% Er Nanocrystals Using NIR-to-Visible Upconversion Luminescence. *J. Phys. Chem. C* **2014**, 13238-13247.

(132) Mao, C.; Yang, X.; Zhao, L. Simultaneous Morphology Control and Upconversion Fluorescence Enhancement of $NaYF_4$: Yb, Er Crystals through Alkali Ions Doping. *Chem. Eng. J.* **2013**, *229*, 429–435.

(133) Shan, J.; Ju, Y. Controlled Synthesis of Lanthanide-Doped $NaYF_4$ Upconversion Nanocrystals via Ligand Induced Crystal Phase Transition and Silica Coating. *Appl. Phys. Lett.* **2007**, *91*.

(134) Shang, Y.; Hao, S.; Liu, J.; Tan, M.; Wang, N.; Yang, C.; Chen, G. Synthesis of Upconversion β-$NaYF_4$: Nd^{3+}/Yb^{3+}/Er^{3+} Particles with Enhanced Luminescent Intensity through Control of Morphology and Phase. *Nanomaterials* **2015**, 218–232.

(135) Ding, M.; Yin, S.; Ni, Y.; Lu, C.; Chen, D.; Zhong, J.; Ji, Z.; Xu, Z. Controlled Synthesis of β -$NaYF_4$: Yb^{3+}/Er^{3+} Microstructures with Morphology- and Size-Dependent Upconversion Luminescence. *Ceram. Int.* **2015**, *41*, 7411–7420.

(136) Na, H.; Woo, K.; Lim, K.; Jang, H. S. Rational Morphology Control of β-$NaYF_4$: Yb, Er/Tm Upconversion Nanophosphors Using a Ligand, an Additive, and Lanthanide Doping. *Nanoscale* **2013**, *5*, 4242–4251.

(137) Park, Y. Il; Kim, J. H.; Lee, K. T.; Jeon, K. S.; Na, H. Bin; Yu, J. H.; Kim, H. M.; Lee, N.; Choi, S. H.; Baik, S. Il; *et al.* Nonblinking and Nonbleaching Upconverting Nanoparticles as an Optical Imaging Nanoprobe and T1 Magnetic Resonance Imaging Contrast Agent. *Adv. Mater.* **2009**, *21*, 4467–4471.

(138) Chen, G.; Ohulchanskyy, T. Y.; Liu, S.; Law, W.-C.; Wu, F.; Swihart, M. T.; Ågren, H.; Prasad, P. N. Core/Shell $NaGdF_4$: Nd^{3+}/$NaGdF_4$ Nanocrystals with Efficient Near-Infrared to Near-Infrared Downconversion Photoluminescence for Bioimaging Applications. *ACS Nano* **2012**, *6*, 2969–2977.

(139) Li, X.; Wang, R.; Zhang, F.; Zhao, D. Engineering Homogeneous Doping in Single Nanoparticle to Enhance Upconversion Efficiency Engineering Homogeneous Doping in Single Nanoparticle to Enhance Upconversion Efficiency. *Nano Lett.* **2014**, *14*, 3634–3639.

(140) Li, C.; Liu, X.; Yang, P.; Zhang, C.; Lian, H.; Lin, J. LaF_3, CeF_3, CeF_3: Tb^{3+}, and CeF_3: Tb^{3+}@LaF_3 (Core-Shell) Nanoplates: Hydrothermal Synthesis and Luminescence Properties. *J. Phys. Chem. C* **2008**, *112*, 2904–2910.

(141) Lei, L.; Chen, D.; Zhu, W.; Xu, J.; Wang, Y. Impact of High ytterbium(III)

Concentration in the Shell on Upconversion Luminescence of Core-Shell Nanocrystals. *Chem. - An Asian J.* **2014**, *9*, 2765–2770.

(142) Lei, L.; Chen, D.; Huang, P.; Xu, J.; Zhang, R.; Wang, Y. Modifying the Size and Uniformity of Upconversion Yb/Er: $NaGdF_4$ Nanocrystals through Alkaline-Earth Doping. *Nanoscale* **2013**, *5*, 11298–11305.

(143) Kang, N.; Liu, Y.; Zhou, Y.; Wang, D.; Chen, C.; Ye, S.; Nie, L.; Ren, L. Phase and Size Control of Core Shell Upconversion Nanocrystals Light up Deep Dual Luminescence Imaging and CT In Vivo. *Adv. Healthc. Mater.* **2016**, *5*, 1356–1363.

(144) Chen, D.; Lei, L.; Xu, J.; Yang, A.; Wang, Y. Abnormal Size-Dependent Upconversion Emissions and Multi-Color Tuning in Er^{3+}-Doped CaF_2-YbF_3 Disordered Solid-Solution Nanocrystals. *Nanotechnology* **2013**, *24*, 85708.

(145) Ostrowski, A. D.; Chan, E. M.; Gargas, D. J.; Katz, E. M.; Han, G.; Schuck, P. J.; Milliron, D. J.; Cohen, B. E. Controlled Synthesis and Single-Particle Imaging of Bright , Sub-10 nm Lanthanide - Doped Upconverting Nanocrystals. **2012**, 2686–2692.

(146) Wang, S. G.; Schwarz, W. H. E. Lanthanide Diatomics and Lanthanide Contractions. *J. Phys. Chem.* **1995**, *99*, 11687–11695.

(147) Damasco, J. a; Chen, G.; Shao, W.; Ågren, H.; Huang, H.; Song, W. Size-Tunable and Monodisperse Tm^{3+}/Gd^{3+}-Doped Hexagonal $NaYbF_4$ Nanoparticles with Engineered Efficient Near Infrared-to-Near Infrared Upconversion for In Vivo Imaging. *ACS Appl. Mater. Interfaces* **2014**, *6*, 13884–13893.

(148) Mai, H. X.; Zhang, Y. W.; Sun, L. D.; Yan, C. H. Highly Efficient Multicolor up-Conversion Emissions and Their Mechanisms of Monodisperse $NaYF_4$: Yb, Er Core and Core/shell-Structured Nanocrystals. *J. Phys. Chem. C* **2007**, *111*, 13721–13729.

(149) Qian, H. S.; Zhang, Y. Synthesis of Hexagonal-Phase Core-Shell $NaYF_4$ Nanocrystals with Tunable Upconversion Fluorescence. *Langmuir* **2008**, *24*, 12123–12125.

(150) Zhang, C.; Lee, J. Y. Prevalence of Anisotropic Shell Growth in Rare Earth Core-Shell Upconversion Nanocrystals. *ACS Nano* **2013**, *7*, 4393–4402.

(151) Wang, F.; Deng, R.; Liu, X. Preparation of Core-Shell $NaGdF_4$ Nanoparticles Doped with Luminescent Lanthanide Ions to be Used as Upconversion-Based Probes. *Nat. Protoc.* **2014**, *9*, 1634–1644.

(152) Abel, K. A.; Boyer, J.-C.; Andrei, C. M.; van Veggel, F. C. J. M. Analysis of the Shell Thickness Distribution on $NaYF_4$/$NaGdF_4$ Core/Shell Nanocrystals by EELS and EDS. *J. Phys. Chem. Lett.* **2011**, *2*, 185–189.

(153) Huang, J.; Sun, Y.; Huang, S.; Yu, K.; Zhao, Q.; Peng, F.; Yu, H.; Wang, H.; Yang, J. Crystal Engineering and SERS Properties of Ag-Fe_3O_4 Nanohybrids: From Heterodimer to Core–shell Nanostructures. *J. Mater. Chem.* **2011**, *21*, 17930-17937.

(154) Li, X.; Shen, D.; Yang, J.; Yao, C.; Che, R.; Zhang, F.; Zhao, D. Successive Layer-by-Layer Strategy for Multi-Shell Epitaxial Growth: Shell Thickness and Doping Position Dependence in Upconverting Optical Properties. *Chem. Mater.* **2013**, *25*, 106–112.

(155) Wen, H.; Zhu, H.; Chen, X.; Hung, T. F.; Wang, B.; Zhu, G.; Yu, S. F.; Wang, F. Upconverting near-Infrared Light through Energy Management in Core-Shell-Shell Nanoparticles. *Angew. Chemie - Int. Ed.* **2013**, *52*, 13419–13423.

(156) Wang, R.; Li, X.; Zhou, L.; Zhang, F. Epitaxial Seeded Growth of Rare-Earth Nanocrystals with Efficient 800 nm Near-Infrared to 1525 nm Short-Wavelength Infrared Downconversion Photoluminescence for in Vivo Bioimaging. *Angew. Chemie - Int. Ed.* **2014**, *53*, 12086–12090.

(157) Liu, D.; Xu, X.; Du, Y.; Qin, X.; Zhang, Y.; Ma, C.; Wen, S.; Ren, W.; Goldys, E. M.; Piper, J. A.; *et al*. Three-Dimensional Controlled Growth of Monodisperse Sub-50 nm Heterogeneous Nanocrystals. *Nat. Commun.* **2016**, *7*, 10254.

(158) Zhang, F.; Che, R.; Li, X.; Yao, C.; Yang, J.; Shen, D.; Hu, P.; Li, W.; Zhao, D. Direct Imaging the Upconversion Nanocrystal Core/shell Structure at the Subnanometer Level: Shell Thickness Dependence in Upconverting Optical Properties. *Nano Lett.* **2012**, *12*, 2852–2858.

(159) Haldar, K. K.; Pradhan, N.; Patra, A. Formation of Heteroepitaxy in Different Shapes of Au-CdSe Metal-Semiconductor Hybrid Nanostructures. *Small* **2013**, *9*, 3424–3432.

(160) Lee, J. S.; Shevchenko, E. V.; Talapin, D. V. Au-PbS Core-Shell Nanocrystals: Plasmonic Absorption Enhancement and Electrical Doping via Intra-Particle Charge Transfer. *J. Am. Chem. Soc.* **2008**, *130*, 9673–9675.

(161) Son, J. S.; Lee, J.; Shevchenko, E. V; Talapin, D. V. Magnet-in-the-Semiconductor Nanomaterials : High Electron Mobility. *J. Phys. Chem. Lett.* **2013**, *4*, 1918–1923.

(162) Guardia, P.; Korobchevskaya, K.; Casu, A.; Genovese, A.; Manna, L.; Comin, A. Plasmon Dynamics in Colloidal Au_2Cd Alloy-CdSe Core/shell Nanocrystals. *ACS Nano* **2013**, *7*, 1045–1053.

(163) Jiang, J.; Gu, H.; Shao, H.; Devlin, E.; Papaefthymiou, G. C.; Ying, J. Y. Bifunctional Fe_3O_4-Ag Heterodimer Nanoparticles for Two-Photon Fluorescence Imaging and Magnetic Manipulation. *Adv. Mater.* **2008**, *20*, 4403–4407.

(164) Zhou, B.; Shi, B.; Jin, D.; Liu, X. Controlling Upconversion Nanocrystals for Emerging Applications. *Nat. Publ. Gr.* **2015**, *10*, 924–936.

(165) Yin, M.; Wu, L.; Li, Z.; Ren, J.; Qu, X. Facile in Situ Fabrication of Graphene-Upconversion Hybrid Materials with Amplified Electrogenerated Chemiluminescence. *Nanoscale* **2012**, *4*, 400–404.

(166) Liu, N.; Qin, W.; Qin, G.; Jiang, T.; Zhao, D. Highly Plasmon-Enhanced Upconversion Emissions from Au@β-$NaYF_4$: Yb, Tm Hybrid Nanostructures. *Chem. Commun. (Camb).* **2011**, *47*, 7671–7673.

(167) Xing, H.; Bu, W.; Zhang, S.; Zheng, X.; Li, M.; Chen, F.; He, Q.; Zhou, L.; Peng, W.; Hua, Y.; *et al.* Multifunctional Nanoprobes for Upconversion Fluorescence, MR and CT Trimodal Imaging. *Biomaterials* **2012**, *33*, 1079–1089.

(168) Yan, C.; Dadvand, A.; Rosei, F.; Perepichka, D. F. Near-IR Photoresponse in New Up-Converting CdSe/$NaYF_4$: Yb, Er Nanoheterostructures. *J. Am. Chem. Soc.* **2010**, *132*, 8868–8869.

(169) Song, Y.; Liu, G.; Dong, X.; Wang, J.; Yu, W.; Li, J. Au Nanorods@$NaGdF_4$/Yb^{3+}, Er^{3+} Multifunctional Hybrid Nanocomposites with Upconversion Luminescence, Magnetism, and Photothermal Property. *J. Phys. Chem. C* **2015**, *119*, 18527–18536.

(170) Sudheendra, L.; Ortalan, V.; Dey, S.; Browning, N. D.; Kennedy, I. M. Plasmonic Enhanced Emissions from Cubic $NaYF_4$: Yb: Er/Tm Nanophosphors. *Chem. Mater.* **2011**, *23*, 2987–2993.

(171) SOM, S.; DAS, S.; YANG, C.-Y.; LU, C.-H. Phosphors Prepared Via the Rapid Microwave- Assisted Hydrothermal Route At Low Temperature: Phase and Morphology Control. **2016**, *41*, 464–467.

(172) Zhou, J.; Liu, Q.; Feng, W.; Sun, Y.; Li, F. Upconversion Luminescent Materials:

Advances and Applications. *Chem. Rev.* **2015**, *115*, 395–465.

(173) Lezhnina, M. M.; Justel, T.; Katker, H.; Wiechert, D. U.; Kynast, U. H. Efficient Luminescence from Rare-Earth Fluoride Nanoparticles with Optically Functional Shells. *Adv. Funct. Mater.* **2006**, *16*, 935–942.

(174) Boyer, J.-C.; Vetrone, F.; Cuccia, L. A.; Capobianco, J. A. Synthesis of Colloidal Upconverting $NaYF_4$ Nanocrystals Doped with Er^{3+}, Yb^{3+} and Tm^{3+}, Yb^{3+} via Thermal Decomposition of Lanthanide Trifluoroacetate Precursors. *J. Am. Chem. Soc.* **2006**, *128*, 7444–7445.

(175) Liu, G. K.; Zhuang, H. Z.; Chen, X. Y. Restricted Phonon Relaxation and Anomalous Thermalization of Rare Earth Ions in Nanocrystals. *Nano Lett.* **2002**, *2*, 535–539.

(176) Yi, G.; Peng, Y.; Gao, Z. Strong Red-Emitting near-Infrared-to-Visible Upconversion Fluorescent Nanoparticles. *Chem. Mater.* **2011**, *23*, 2729–2734.

(177) Xie, X.; Gao, N.; Deng, R.; Sun, Q.; Xu, Q.; Liu, X. Mechanistic Investigation of Photon Upconversion in Nd^{3+}-Sensitized Core–Shell Nanoparticles. *J. Am. Chem. Soc.* **2013**, *135*, 12608–12611.

(178) Wang, Z. L.; Quan, Z. W.; Jia, P. Y.; Lin, C. K.; Luo, Y.; Chen, Y.; Fang, J.; Zhou, W.; Connor, C. J. O.; Lin, J. Article A Facile Synthesis and Photoluminescent Properties of Redispersible CeF, CeF: Tb, and CeF: Tb/LaF (Core/Shell) Nanoparticles A Facile Synthesis and Photoluminescent Properties of Redispersible CeF_3, CeF_3 : Tb^{3+}, and CeF_3: Tb^{3+}. **2006**, *3*, 2030–2037.

(179) Zhou, B.; Tao, L.; Tsang, Y. H.; Jin, W. Core-Shell Nanoarchitecture: A Strategy to Significantly Enhance White-Light Upconversion of Lanthanide-Doped Nanoparticles. *J. Mater. Chem. C* **2013**, *1*, 4313–4318.

(180) Wang, Y. F.; Sun, L. D.; Xiao, J. W.; Feng, W.; Zhou, J. C.; Shen, J.; Yan, C. H. Rare-Earth Nanoparticles with Enhanced Upconversion Emission and Suppressed Rare-Earth-Ion Leakage. *Chem. - A Eur. J.* **2012**, *18*, 5558–5564.

(181) Dyck, N. C.; Van Veggel, F. C. J. M.; Demopoulos, G. P. Size-Dependent Maximization of Upconversion Efficiency of Citrate-Stabilized β-Phase $NaYF_4$: Yb^{3+}, Er^{3+} Crystals via Annealing. *ACS Appl. Mater. Interfaces* **2013**, *5*, 11661–11667.

(182) C, R. K.; Lambert, K.; Dorfs, D.; Frederic, P.; Poelman, D.; Eychmu, A.; Hens, Z.; Smet,

P. F. Synthesis of Extremely Small CdSe and Bright Blue Luminescent CdSe/ZnS Nanoparticles by a Prefocused Hot-Injection Approach Synthesis of Extremely Small CdSe and Bright Blue Luminescent CdSe/ZnS Nanoparticles by a Prefocused Hot-Injection Approach. **2009**, 1743–1749.

(183) Zhang, F.; Li, J.; Shan, J.; Xu, L.; Zhao, D. Shape, Size, and Phase-Controlled Rare-Earth Fluoride Nanocrystals with Optical up-Conversion Properties. *Chem.-A Eur. J.* **2009**, *15*, 11010–11019.

(184) Li, D.; Shao, Q.; Dong, Y.; Jiang, J. Thermal Sensitivity and Stability of $NaYF_4$: Yb^{3+}, Er^{3+} Upconversion Nanowires, Nanorods and Nanoplates. *Mater. Lett.* **2013**, *110*, 233–236.

(185) Liu, C.; Wang, H.; Li, X.; Chen, D. Monodisperse, Size-Tunable and Highly Efficient β-$NaYF_4$: Yb, Er(Tm) up-Conversion Luminescent Nanospheres: Controllable Synthesis and Their Surface Modifications. *J. Mater. Chem.* **2009**, *19*, 3546-3553.

(186) Zhao, N.; Qi, L. Low-Temperature Synthesis of Star-Shaped PbS Nanocrystals in Aqueous Solutions of Mixed Cationic/anionic Surfactants. *Adv. Mater.* **2006**, *18*, 359–362.

(187) Xu, B.; Zhang, X.; Huang, W.; Yang, Y.; Ma, Y.; Gu, Z.; Zhai, T.; Zhao, Y. Nd^{3+} Sensitized Dumbbell-like Upconversion Nanoparticles for Photodynamic Therapy Application. *J. Mater. Chem. B* **2016**, *4*, 2776–2784.

(188) Patra, A.; Ghosh, P.; Chowdhury, P. S.; Alencar, M. A. R. C.; Whualkuer, L. B.; Rakov, N.; Maciel, G. S. Red to Blue Tunable Upconversion in Tm^{3+}-Doped ZrO_2 Nanocrystals. *J. Phys. Chem. B* **2005**, *109*, 10142–10146.

(189) Wang, F.; Liu, X. Upconversion Multicolor Fine-Tuning: Visible to near-Infrared Emission from Lanthanide-Doped $NaYF_4$ Nanoparticles. *J. Am. Chem. Soc.* **2008**, *130*, 5642–5643.

(190) Mahalingam, V.; Hazra, C.; Naccache, R.; Vetrone, F.; Capobianco, J. A. Enhancing the Color Purity of the Green Upconversion Emission from Er^{3+}/Yb^{3+}-Doped $GdVO_4$ Nanocrystals via Tuning of the Sensitizer Concentration. *J. Mater. Chem. C* **2013**, *1*, 6536–6540.

(191) Xiang, G.; Zhang, J.; Hao, Z.; Zhang, X.; Pan, G.; Luo, Y.; Lü, S.; Zhao, H. The Energy Transfer Mechanism in Pr^{3+} and Yb^{3+} Codoped β-$NaLuF_4$ Nanocrystals. *Phys. Chem.*

Chem. Phys. **2014**, *16*, 9289–9293.

(192) Ding, Y.; Zhang, X.; Gao, H.; Xu, S.; Wei, C.; Zhao, Y. Enhancement on Concentration Quenching Threshold and Upconversion Luminescence of β-$NaYF_4$: Er^{3+}/Yb^{3+} Codoping with Li^+ Ions. *J. Alloys Compd.* **2014**, *599*, 60–64.

(193) Chen, G.; Ohulchanskyy, T. Y.; Kumar, R.; Ågren, H.; Prasad, P. N. Ultrasmall Monodisperse $NaYF_4$: Yb^{3+}/Tm^{3+} Nanocrystals with Enhanced Near-Infrared to Near-Infrared Upconversion Photoluminescence. *ACS Nano* **2010**, *4*, 3163–3168.

(194) Hao, S.; Shao, W.; Qiu, H.; Shang, Y.; Fan, R.; Guo, X.; Zhao, L.; Chen, G.; Yang, C. Tuning the Size and Upconversion Emission of $NaYF_4$: Yb^{3+}/Pr^{3+} Nanoparticles through Yb^{3+} Doping. *RSC Adv.* **2014**, *4*, 56302–56306.

(195) Solis, D.; De La Rosa, E.; Meza, O.; Diaz-Torres, L. A.; Salas, P.; Angeles-Chavez, C. Role of Yb^{3+} and Er^{3+} Concentration on the Tunability of Green-Yellow-Red Upconversion Emission of Codoped ZrO_2: Yb^{3+}-Er^{3+} Nanocrystals. *J. Appl. Phys.* **2010**, *108*, 023103.

(196) Pires, A. M.; Heer, S.; Güdel, H. U.; Serra, O. A. Er, Yb Doped Yttrium Based Nanosized Phosphors: Particle Size, "host Lattice" and Doping Ion Concentration Effects on Upconversion Efficiency. *J. Fluoresc.* **2006**, *16*, 461–468.

(197) Liu, X.; Kong, X.; Zhang, Y.; Tu, L.; Wang, Y.; Zeng, Q.; Li, C.; Shi, Z.; Zhang, H. Breakthrough in Concentration Quenching Threshold of Upconversion Luminescence via Spatial Separation of the Emitter Doping Area for Bio-Applications. *Chem. Comm.* **2011**, *47*, 11957–11959.

(198) Schietinger, S.; Aichele, T.; Wang, H. Q.; Nann, T.; Benson, O. Plasmon-Enhanced Upconversion in Single $NaYF_4$: Yb^{3+}/Er^{3+} Codoped Nanocrystals. *Nano Lett.* **2010**, *10*, 134–138.

(199) Schneider, G.; Decher, G.; Nerambourg, N.; Praho, R.; Werts, M. H. V; Blanchard-Desce, M. Distance-Dependent Fluorescence Quenching on Gold Nanoparticles Ensheathed with Layer-by-Layer Assembled Polyelectrolytes. *Nano Lett.* **2006**, *6*, 530–536.

(200) Saboktakin, M.; Ye, X.; Oh, S. J.; Hong, S. H.; Fafarman, A. T.; Chettiar, U. K.; Engheta, N.; Murray, C. B.; Kagan, C. R. Metal-Enhanced Upconversion Luminescence Tunable through Metal Nanoparticle-Nanophosphor Separation. *ACS Nano* **2012**, *6*,

8758–8766.

(201) Zhang, W.; Ding, F.; Chou, S. Y. Large Enhancement of Upconversion Luminescence of $NaYF_4$: Yb^{3+}/Er^{3+} Nanocrystal by 3D Plasmonic Nano-Antennas. *Adv. Mater.* **2012**, *24*, 1–6.

(202) Verhagen, E.; Kuipers, L.; Polman, A. Enhanced Nonlinear Optical Effects with a Tapered Plasmonic Waveguide. *Nano Lett.* **2007**, *7*, 334–337.

(203) Zhang, F.; Braun, G. B.; Shi, Y.; Zhang, Y.; Sun, X.; Reich, N. O.; Zhao, D.; Stucky, G. Fabrication of $Ag@SiO_2@Y_2O_3$: Er Nanostructures for Bioimaging: Tuning of the Upconversion Fluorescence with Silver Nanoparticles. *J. Am. Chem. Soc.* **2010**, *132*, 2850–2851.

(204) Saboktakin, M.; Ye, X.; Chettiar, U. K.; Engheta, N.; Murray, C. B.; Kagan, C. R. Plasmonic Enhancement of Nanophosphor Upconversion Luminescence in Au Nanohole Arrays. *ACS Nano* **2013**, *7*, 7186–7192.

(205) Liu, N.; Prall, B. S.; Klimov, V. I. Hybrid Gold/silica/nanocrystal-Quantum-Dot Superstructures: Synthesis and Analysis of Semiconductor-Metal Interactions. *J. Am. Chem. Soc.* **2006**, *128*, 15362–15363.

(206) Nabika, H.; Deki, S. Enhancing and Quenching Functions of Silver Nanoparticles on the Luminescent Properties of Europium Complex in the Solution Phase. *J. Phys. Chem. B* **2003**, *107*, 9161–9164.

(207) Auzel, F. E. Materials and Devices Using Double-Pumped Phosphors with Energy Transfer. *Proc. IEEE* **1973**, *61*, 758–786.

(208) Tu, L.; Liu, X.; Wu, F.; Zhang, H. Excitation Energy Migration Dynamics in Upconversion Nanomaterials. *Chem. Soc. Rev.* **2015**, *44*, 1331–1345.

(209) Wang, F.; Deng, R.; Wang, J.; Wang, Q.; Han, Y.; Zhu, H.; Chen, X.; Liu, X. Tuning Upconversion through Energy Migration in Core–shell Nanoparticles. *Nat. Mater.* **2011**, *10*, 968–973.

CHAPTER 3

Probing the Interior Crystal Quality in the Development of More Efficient and Smaller Upconversion Nanoparticles

The research in this chapter was initially developed to study the crystal quality of UCNCs. It had been postulated that upconversion luminescence could be enhanced by increasing a number of sensitizer ions, increasing the nanocrystal size, and/or increasing excitation power[1–4]. I postulated that decreasing the number of defects could enhance upconversion in nanocrystals, and found that both external defects and internal defects influence the upconversion luminescence. By studying the material synthesis I found that the heating profile during synthesis of nanocrystals can both result in more morphologically and well monodispersed small nanocrystals and can also improve the interior crystal quality. With the co-authors listed below developed a unique quantitative method for the optical characterization of single nanocrystals upconversion. This not only confirmed that the synthesis method taken produced highly uniform nanocrystals, but also that the internal quality greatly influenced the efficiency of particle emission. This work is presented in the form of a journal publication from ***The Journal of Physical Chemistry Letters***.

3.1 Contribution to Paper 1

The author contribution for paper "Probing the interior crystal quality in the development of more efficient and smaller upconversion nanoparticles" are shown in **Table 3.1**.

Table 3.1 Author contribution summary for paper 1

Name	Experiment Design	Material Synthesis	Data Collection	Analysis	Figures and Tables	Manuscript
Chenshuo Ma	√	√	√	√	√	√
Xiaoxue Xu						√
Fan Wang				√		
Zhiguang Zhou				√		
Shihui Wen				√		
Deming Liu				√		
Jinghua Fang				√		
Candace I Lang						√
Dayong Jin				√		√

This work was supervised by my supervisors, Dayong Jin and Candace I Lang, during my first year of Ph.D. I carried out the majority of experimental work, including sample measurements and data collection. Fan Wang and Zhiguang Zhou set up the optical system; Xiaoxue Xu and Jinghua Fang assisted with some of the material measurement. Analysis of results was carried out in collaboration with the co-authors listed above. I prepared all the figures and tables and the manuscript draft; Dayong Jin, Candace I Lang and Xiaoxue Xu then made modifications. I prepared the final manuscript for publication.

3.2 Paper 1

Chenshuo Ma, Xiaoxue Xu, Fan Wang, Zhiguang Zhou, Shihui Wen, Deming Liu, Jinghua Fang, Candace I Lang, and Dayong Jin. "Probing the interior crystal quality in the development of more efficient and smaller upconversion nanoparticles", ***The Journal of Physical Chemistry Letters***, 2016, 7(16): 3252-3258.

THE JOURNAL OF PHYSICAL CHEMISTRY Letters

Letter

pubs.acs.org/JPCL

Probing the Interior Crystal Quality in the Development of More Efficient and Smaller Upconversion Nanoparticles

Chenshuo Ma,[†,‡] Xiaoxue Xu,[*,‡,§,∥] Fan Wang,[‡,§,∥] Zhiguang Zhou,[§,∥] Shihui Wen,[§,∥] Deming Liu,[‡,§,∥] Jinghua Fang,[§,∥] Candace I. Lang,[†] and Dayong Jin[*,‡,§,∥]

[†]Department of Engineering, Faculty of Science and Engineering, Macquarie University, Sydney, New South Wales 2109, Australia

[‡]Advanced Cytometry Laboratories, ARC Centre of Excellence for Nanoscale BioPhotonics, Macquarie University, Sydney, New South Wales 2109, Australia

[§]Institute for Biomedical Materials and Devices, Faculty of Science, University of Technology, Sydney, New South Wales 2007, Australia

[∥]ARC Research Hub for Integrated Device for End-user Analysis at Low-levels (IDEAL), Faculty of Science, University of Technology, Sydney, New South Wales 2007, Australia

S *Supporting Information*

ABSTRACT: Optical biomedical imaging using luminescent nanoparticles as contrast agents prefers small size, as they can be used at high dosages and efficiently cleared from body. Reducing nanoparticle size is critical for the stability and specificity for the fluorescence nanoparticles probes for in vitro diagnostics and subcellular imaging. The development of smaller and brighter upconversion nanoparticles (UCNPs) is accordingly a goal for complex imaging in bioenvironments. At present, however, small UCNPs are reported to exhibit less emission intensity due to increased surface deactivation and decreased number of dopants. Here we show that smaller and more efficient UCNPs can be made by improving the interior crystal quality via controlling heating rate during synthesis. We further developed a unique quantitative method for optical characterizations on the single UCNPs with varied sizes and the corresponding shell passivated UCNPs, confirming that the internal crystal quality dominates the relative emission efficiency of the UCNPs.

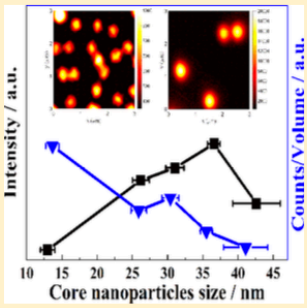

Upconversion nanoparticles (UCNPs), which convert low-energy infrared photons into high-energy visible and ultraviolet photons, are becoming sought-after for advanced biomedical and photonics applications.[1−8] The new generation lanthanide ion (Ln)-doped UCNPs, with enhanced optical and morphological properties, have been demonstrated to be robust multifunctional contrast agents for deep-tissue optical bioimaging[7−12] and to combine multiple imaging modalities[13−16] to guide high precision surgery. They are also useful as nanoscale light transducers for on-demand delivery and release of drugs for nanomedicine applications, to enhance the efficiency of photothermal therapy (PTT),[17−20] photodynamic therapy (PDT),[21,22] bio reductive chemotherapy[23,24] and synergetic therapy for tumor hypoxia.[25]

Most of the aforementioned reports concern UCNPs greater than ten nanometers in size. At this size, however, nanoparticles are not transported efficiently through subcellular membranes, or cannot be easily cleared from the body.[10,26] Even for in vitro diagnostics applications, smaller UCNPs would be more useful as these are expected to avoid nonspecific binding issues. Smaller UCNPs can be synthesized, but to date this has come at the expense of emission strength. This is partly due to the fact that many of them, for example, α-$NaYF_4$:Yb^{3+}, Er^{3+} (5−6 nm)[27] and α-$NaYF_4$:Yb^{3+}, Tm^{3+} (7−10 nm)[28] are cubic phase nanocrystals with low upconversion efficiency. A small particle size also results in a relative upconversion efficiency drop as the number of dopants per particle reduces, and the impact of surface quenching is expected to increase with the increased surface-to-volume ratio. Consequently, for upconversion nanotechnology to gain widespread biomedical and clinical application, a major objective must be the production of small (round or smaller than 10 nm) and brighter (high luminescence upconversion efficiency) UCNPs.

Photon luminescence upconversion efficiency can be optimized by intrinsic or extrinsic methods. Intrinsic methods include designing and synthesizing better crystalline hosts and selecting optimized dopants. Extrinsic methods include externally engineering core−shell architectures.

Intrinsic enhancement of relative upconversion efficiency has been reported for hexagonal sodium yttrium fluoride (β-$NaYF_4$): β-$NaYF_4$ nanocrystals, codoped with Yb^{3+} and/or Nd^{3+} as sensitizers and Er^{3+} or Ho^{3+} or Tm^{3+} as activators, are regarded as the most efficient upconversion system, with photon relative upconversion efficiency up-to-2 orders of magnitude higher than

Received: June 29, 2016
Accepted: August 4, 2016
Published: August 4, 2016

DOI: 10.1021/acs.jpclett.6b01434
J. Phys. Chem. Lett. 2016, 7, 3252−3258

the comparable α-$NaYF_4$.[29−31] A further intrinsic enhancement strategy has been achieved by manipulating the local crystal field of Ln^{3+} sites through codoping nonluminescent cations of Li^+,[31−33] Sc^{3+},[34] or Ca^{2+}[35] into the host nanocrystal. Other intrinsic strategies include high dopant levels of sensitizers and activators provided that superhigh power excitation is used,[2,36] and forming energy clustering at the sublattice.[37]

Extrinsic enhancement of relative upconversion efficiency has been reported by engineering inert shells to passivate UCNPs from surface quenching,[38−40] for instance, by coating 2.5 nm inert $NaGdF_4$ shells onto small β-$NaGdF_4$ UCNPs. This enhances the relative upconversion efficiency of β-$NaGdF_4$: 20%Yb^{3+}, 0.3% Tm^{3+} nanoparticles in the size range 10 nm -25 nm, by a factor of up to 460.[38] When the appropriate amount of oleylamine (OM) was used as cosurfactant, ultrasmall β-$NaYF_4$ UCNPs[41,42] from 4.5 to 15 nm were fabricated, and the relative upconversion efficiency of core−shell UCNPs after coating the inert shell with final size of 9 nm was found comparable with the 25 nm UCNPs. Other extrinsic approaches to enhancing photon upconversion include harnessing the effect of surface plasmon resonance by incorporating noble metal shell,[43−45] and sensitization amplification through the use of synthetic infrared dyes.[46,47]

Generally speaking, to achieve UCNPs which are both smaller and more efficient, intrinsic approaches are preferable as most of extrinsic strategies come at the expense of larger overall size and surface complexity,[48,49] not suitable for real world biological and biomedical applications.

The reported relative upconversion efficiency of UCNPs shows considerable variation, even for the same size, shape, and composition, when the photon luminescent properties are measured for the ensemble UCNPs. Our investigation on the relative upconversion efficiency of UCNPs has adopted a customized characterization system for single UCNPs. Our synthesis process control has shown that the heating profile during synthesis can not only result in more morphologically monodispersed small UCNPs but can also improve the interior crystal quality which affects the upconversion luminescence efficiency. Moreover, when each individual UCNPs and single inert shell coated UCNPs are characterized and compared, we further confirmed that the surface quenching caused by the interaction of UCNPs surfaces with the surrounding deactivations in ensemble phase can be diminished due to the dry condition preventing the access of surface quenching.

To understand why slowing down the heating up rate during the crystal synthesis helps to form smaller β-$NaYF_4$ UCNPs, we carefully monitored the crystal nucleation and crystal growth processes, shown in Scheme 1. This result suggests that every β-$NaYF_4$ nanocrystals are formed in a consequential process via the mediate phase of α-$NaYF_4$ nanocrystals which start to form at relatively low temperature around 260 °C. At 300 °C, the thermodynamically less stable α-$NaYF_4$ nanocrystals dissolve and release monomers to source the nucleation of larger β-$NaYF_4$ nanocrystals.[50] Therefore, delicate control over the transitional stage of α-$NaYF_4$ nanoparticles formation from 260 to 300 °C could play important role in the final formation of β-$NaYF_4$ nanocrystals. The more α-$NaYF_4$ nanocrystals can be formed at lower temperature by prolonging the heating up speed, the more β-$NaYF_4$ nucleus will be formed and fewer amounts of α-$NaYF_4$ nanocrystals will be available for the crystal growth of the formed β-$NaYF_4$ nucleus, and then the formed β-$NaYF_4$ nanocrystals are small. Hence, controlling more transit of α-$NaYF_4$ nanocrystals into β-$NaYF_4$ nanocrystals

Scheme 1. Progress of the β-$NaYF_4$ UCNPs Formation Process[a]

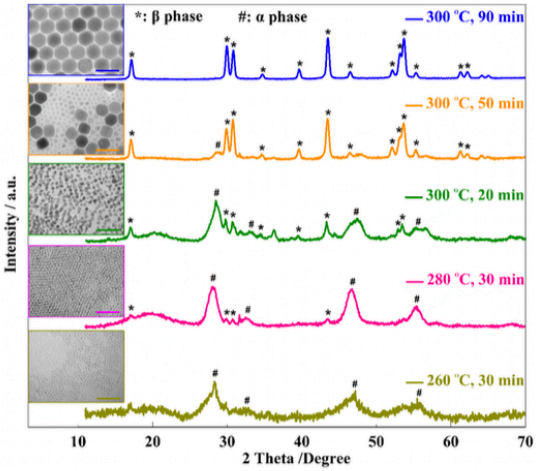

[a]XRD patterns characterized the compositions and TEM images of the UCNPs samples from different stages of synthesis temperatures for different holding reaction time durations. At a temperature of 260 °C and holding for 30 min, pure α-$NaYF_4$ nanocrystals were formed and the broaden diffraction peaks suggest the small size (~3 nm) of the $NaYF_4$ nanocrystals which is further confirmed by the TEM image. When held at 280 °C for 30 min, the dominant phase is still α-$NaYF_4$ nanocrystals with sharp diffraction peaks corresponding to the bigger nanocrystals (~5 nm) in TEM image and a small amount of β-$NaYF_4$ nanocrystals appeared. At the reaction temperature of 300 °C for 20 min, more β-$NaYF_4$ nanocrystals were formed together with the dominant α-$NaYF_4$ nanocrystals and the sizes of both increased to ~10 nm. β-$NaYF_4$ nanocrystals was the main product when prolonged the reaction time at 300 °C to 50 min, but α-$NaYF_4$ nanocrystals were still existed as shown in the XRD patterns and TEM image. Uniform and pure β-$NaYF_4$ nanocrystals were the final product around 30 nm. The scale bar is 50 nm.

before 300 °C is critical to ensure smaller and more monodisperse β-$NaYF_4$ nanocrystals.

To further verify our hypothesis, we conducted a series of experiments by varying the heating up time when rising the reaction solution temperature from 150 to 300 °C. Figure 1 shows the size of β-$NaYF_4$: 20% Yb^{3+}, 4% Tm^{3+} UCNPs increase from 13.0 to 42.6 nm when the heating up time is shorted from 21 to 8 min. The fastest heating up profile (8 min) produces the largest β-$NaYF_4$ UCNPs with size of 42.6 nm, though these β-$NaYF_4$ UCNPs all show very good size distributions (Supporting Information Figure S1) and the composition purity (see the XRD patterns in Supporting Information Figure S2). To test the reproducibility of this trend, Supporting Information Figure S3−S5 further shows the size of the synthesized β-$NaYF_4$: 20% Yb^{3+}, 8% Tm^{3+} UCNPs increase from 12.5 to 41.2 nm when the heating up time is shorted from 23 to 8.3 min.

To quantify and compare the upconversion emission intensity of each batches of UCNPs, we prepared the dispersion samples of the as-synthesized β-$NaYF_4$: 20% Yb^{3+}, 4% Tm^{3+} UCNPs with different sizes in cyclohexane with the same mass concentration and compared the integrated luminescence emission intensities using Fluorolog spectrometer. Interestingly, we found the intensity increased when the size of the UCNPs increased from 13.0 to 36.6 nm but the intensity then dropped for the

DOI: 10.1021/acs.jpclett.6b01434
J. Phys. Chem. Lett. 2016, 7, 3252−3258

The Journal of Physical Chemistry Letters Letter

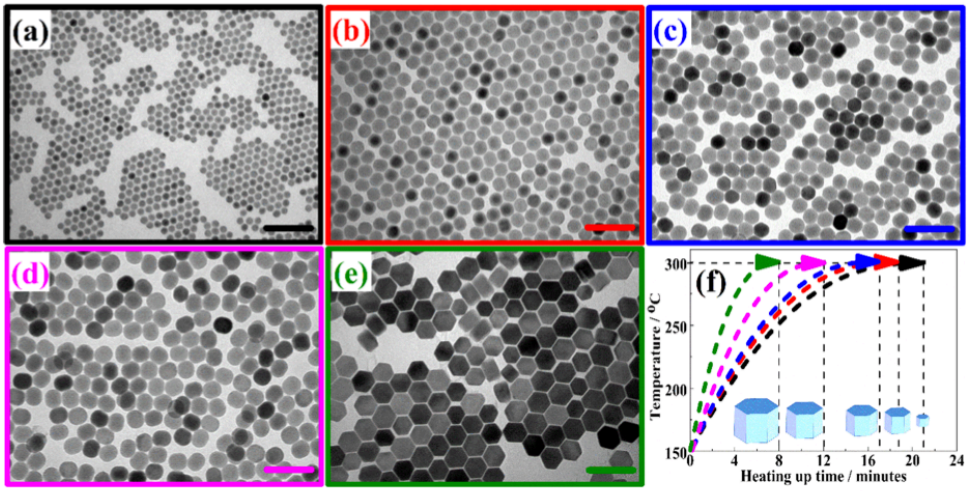

Figure 1. TEM images of different sized β-$NaYF_4$: 20%Yb^{3+}, 4%Tm^{3+} nanocrystals synthesized via controlling the heating up time from 150 to 300 °C for (a) 21 min, (b) 17 min, (c) 12 min, (d) 9.3 min, (e) 8 min, corresponding to tunable sizes of 13.0 nm, 26.2 nm, 31.1 nm, 36.6 and 42.6 nm respectively, and (f) schematic illustration of the different heating up profiles for controlling the nanocrystals size. The scale bar is 100 nm.

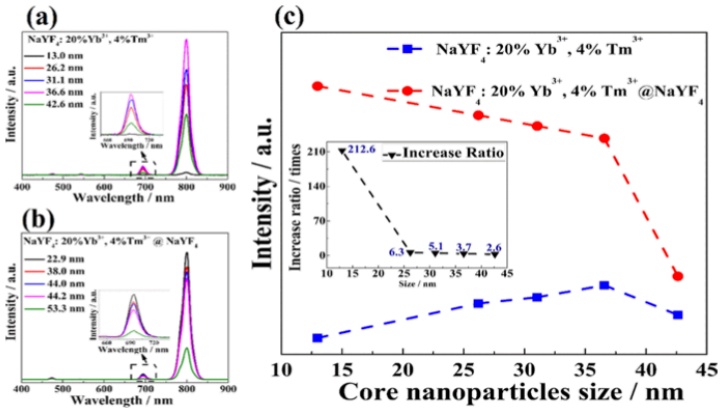

Figure 2. Fluorolog spectrometer measurement of (a) different sized β-$NaYF_4$: 20%Yb^{3+}, 4%Tm^{3+} UCNPsand (b) inert shell passivated β-$NaYF_4$: 20%Yb^{3+}, 4%Tm^{3+} UCNPs; (c) comparison of the relative upconversion efficiency of UCNPs and inert shell passivated UCNPs with different core nanocrystal sizes. Inset figure: The increase ratio between UCNPs and inert shell passivated UCNPs with different core nanocrystal sizes.

UCNPs of 42.6 nm, shown in Figure 2a and Figure 2c in blue. The similar phenomenon was also observed for the $NaYF_4$: 20%Yb^{3+}, 8%Tm^{3+} nanoparticles with different sizes from 12.5 to 41.2 nm and the emission spectra were shown in Supporting Information Figure S6. Comparing with smaller UCNPs, the decreased emission intensity of both the larger UCNPs doped with 4% and 8% Tm^{3+} respectively indicates that faster heating up profile probably introduces more internal defects, including point defects, line defects or even stacking faults during the crystal growth process. For crystal quality analysis, we chose three samples with different sizes (13.0, 31.3, and 42.6 nm, respectively) to do the high-resolution TEM (HRTEM) imaging. As shown in the Figure S10, all these samples revealed an interplanar lattice spacing of 0.52 nm, which is corresponding to the (100) crystal plane of β-phase $NaYF_4$: Yb/Tm crystals and the high qualities of single crystal structures. However, the HRTEM characterizations on the defects of the UCNPs with different sizes do not show any difference within three different sizes. Therefore, in this case, the crystal quality difference revealed in the optical properties could not be detected in the HRTEM analysis. Also, the TEM energy-dispersive X-ray spectroscopy (EDS) elemental mapping of the UCNPs in Figure S11 shows elemental Y, Yb, and F are homogeneous distributed within the whole nanoparticle. As the concentration of Tm is only 4%, it is hard to detect. However, with TEM EDS Line scan (Figure S12), which also indicated that the distribution of the doping ions within the upconversion nanoparticles is uniform, particularly the low dose of Tm distribution is shown uniform along the line scan. These results suggest that the distribution of the doping ions within the upconversion nanoparticles is not the factor causing the luminescence variation with the particle size changing.

To further probe the relationship between heating up rate during the synthesis and the interior crystalline quality affected

DOI: 10.1021/acs.jpclett.6b01434
J. Phys. Chem. Lett. 2016, 7, 3252−3258

The Journal of Physical Chemistry Letters Letter

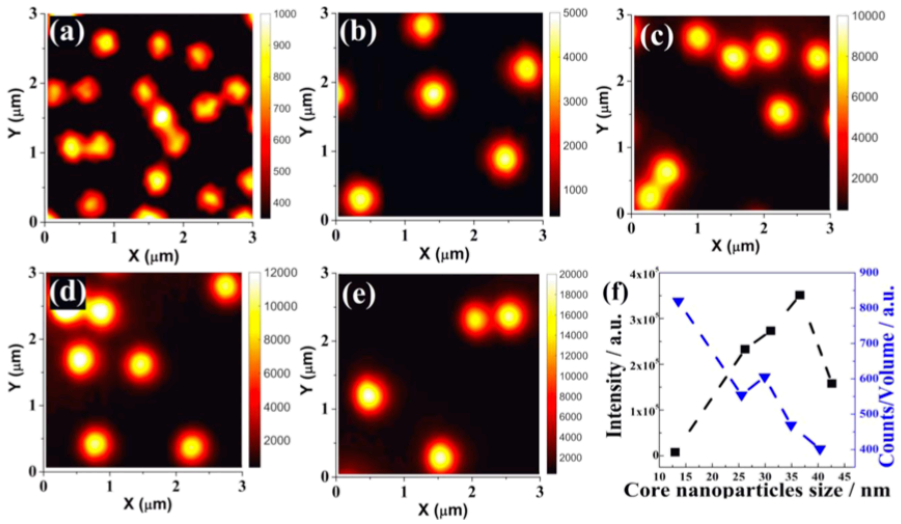

Figure 3. Confocal microscopy quantitative measurement of single $NaYF_4$: 20%Yb^{3+}, 4%Tm^{3+} UCNPs with different sizes: (a) 13.0 nm, (b) 26.2 nm, (c) 31.1 nm, (d) 36.6 nm, (e) 42.6 nm, respectively. (f) Emission intensity of different sized single UCNPs and the comparison of relative upconversion efficiency of different sized single UCNPs by normalizing the brightness with same amount of dopants.

by the internal defects that quench the luminescent emission intensity, we grew inert shells onto the as-synthesized β-$NaYF_4$: 20% Yb^{3+}, 4% Tm^{3+} UCNPs. This experiment is to minimize the influence from surface defects. The TEM images of the core−shell UCNPs were shown in Supporting Information Figure S7 and the increased nanoparticles size confirmed the shell coating in Supporting Information Figure S8. The inert shells for all UCNPs were uniformly coated at least for 3 nm in thickness for minimizing the surface deactivation effects on the luminescence emission.[51] As shown in Figure 2b, the relative upconversion efficiency of UCNPs has been enhanced by passivating the UCNPs from surface quenchers and the smaller ones benefit the most significant enhancement by a factor of 217. This result is consistent to previous literature report.[38] More interestingly, when we compare the relative upconversion efficiency of inert shell passivated UCNPs (the initial amount of β-$NaYF_4$: 20% Yb^{3+}, 4% Tm^{3+} UCNPs were kept the same mass concentration), the smaller ones display highest relative upconversion efficiency. This result clearly shows the smaller UCNPs made by slowing down the heating up rate contain less (internal) defects.

To further confirm the above observations, we built a laser scanning confocal microscope (Supporting Information Figure S9) for the intensity measurement of single UCNPs.[52] Briefly, the excitation source is a 976 nm single mode diode laser which is focused onto the sample through a 100× objective lens (NA 1.4). The emission from sample is collected by the same objective lens then projected into an optical fiber which has a core size matching with system Airy disk. A Single Photon Counting Avalanche Diode (SPAD) detector is connected to the collection optical fiber to detect the emission intensity. The scanning is achieved by moving the 3D piezo stage.

Figure 3a−e shows the confocal images of single UCNPs with quantitative emission intensity counts. The emissions of each sized $NaYF_4$: 20%Yb^{3+}, 4%Tm^{3+} UCNPs are uniform with monodispersed intensity profile, indicating the quality synthesis of each experiment. The integrated emission intensity of larger UCNPs is higher than that of the smaller ones as shown in the Figure 3f (black line tested by Fluorolog). This is primarily due to that the total number of dopants increases along the increased volume of UCNPs. But after normalizing the intensity against particle volume to compare the relative upconversion efficiency at the same amount of dopants, as shown in Figure 3f (blue line tested by laser scanning confocal microscope), the luminescence intensity of single UCNPs displays a decline trend with the increase of particle size. This result further suggests that the smaller UCNPs with higher relative upconversion efficiency benefit from the high interior crystal quality.

We attributed the quenching of upconversion luminescence of different sized UCNPs to the sum effect from both surface quenching and internal crystal defects. Because the single nanoparticle measurements were conducted in dry condition, the surface deactivation effects from ligands and solvents were alleviated and the internal defects within UCNPs dominate their emission efficiency. In comparison, the ensemble measurement in Fluorolog spectrometer, UCNPs are suspended in solvent and both internal defects and surface deactivations play roles in quenching the smaller UCNPs.

To provide evidence that the surface deactivation effects are primarily resulted from the interaction between surface ligands and solvents, we also quantify the intensity of single core−shell UCNPs under confocal microscopy, shown in Figure 4. As summarized by Figure 4f, after normalizing the brightness against particle volume to compare the relative upconversion efficiency at the same amount of dopants, the luminescence intensity of single core−shell UCNPs also clearly displays a decline trend with the increase of size. This result first suggests that the smallest upconversion nanoparticles (~13 nm) possess highest relative upconversion efficiency. When compared with Figure 3, measured under the confocal microscopy in dry condition, there is no obvious enhancement in intensity counts between the UCNPs and the UCNPs passivated by inert shells. This result further suggests that shell passivation effect is due to the prevention of the interactions between UCNP surface and solvent deactivations.[38] The crystalline

DOI: 10.1021/acs.jpclett.6b01434
J. Phys. Chem. Lett. 2016, 7, 3252−3258

The Journal of Physical Chemistry Letters Letter

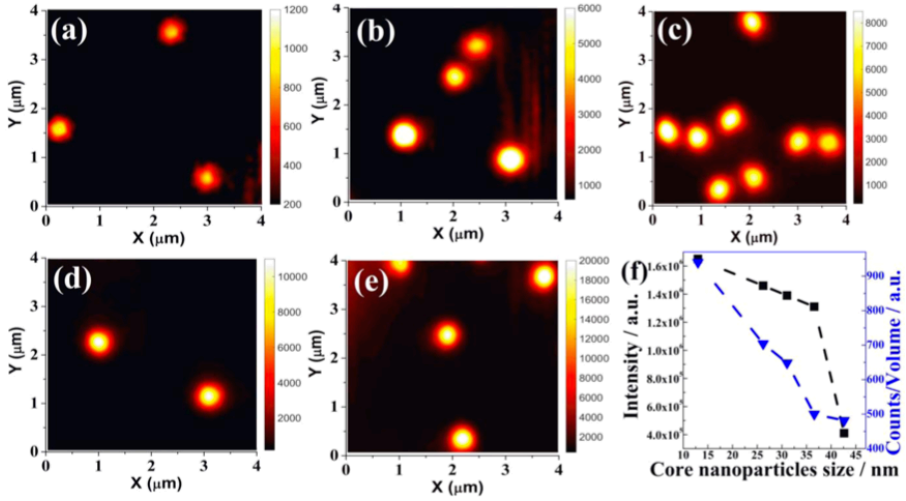

Figure 4. Confocal microscopy quantitative measurement of single inert-shell-passivated $NaYF_4$: 20%Yb^{3+}, 4%Tm^{3+} UCNPs with different core nanocrystal sizes: (a) 13.0 nm, (b) 26.2 nm, (c) 31.1 nm, (d) 36.6 nm, (e) 42.6 nm, respectively. (f) Emission intensity of single inert-shell-passivated single UCNPs with different core nanocrystal sizes and the comparison of relative upconversion efficiency by normalizing the brightness with same amount of emitters.

surface defects and surface ligands by themselves would not significantly quench the upconversion emission efficiency.

This work emphasizes the importance of controlling the transit stage of α-$NaYF_4$ nanoparticles into the formation of the β-$NaYF_4$ nanoparticles. Slowing down the heating up speed during the synthesis facilitates the formation of more β-$NaYF_4$ nuclei, this will not only help the control UCNPs size but also benefit the crystallinity by introducing less interior defects and optimizing the crystalline quality, which plays an important role in the relative upconversion efficiency of the UCNPs together with surface deactivations. By quantitative measurement of single UCNPs and inert shell-passivated UCNPs, this work also provides evidence that internal defects dominate the emission efficiency for the single UCNPs. As small as 13 nm UCNPs have been demonstrated by this work to exhibit highest emission efficiency. This work further suggests a general route to produce smaller and more efficient upconversion nanoparticles through proper monitoring of both internal defects and surface interaction with solvents.

■ EXPERIMENTAL METHODS

Synthesis of β-$NaYF_4$: 20%Yb^{3+}, 4%/8%Tm^{3+} Upconversion Nanoparticles (UCNPs). A modified synthesis method was adopted to prepare β-$NaYF_4$:20%Yb^{3+}, 4%/8%Tm^{3+} UCNPs.[53] Typically, a methanol solution of 0.04 (or 0.08) mmol $TmCl_3$, 0.2 mmol $YbCl_3$, 0.76 (or 0.72) mmol YCl_3 were mixed with 6 mL of OA and 15 mL of ODE in a 50 mL round-bottom flask. The mixed solution was degassed under Ar flow and slowly heated up to 150 °C and kept isothermally for 30 min to form a clear solution. Then, the solution was cooled down to room temperature, and then the 10 ml methanol solution dissolved with 4.0 mmol NH_4F and 2.5 mmol NaOH was added into the flask followed vigorous stirring for 30 min. Again in an argon atmosphere, the mixed solution was slowly heated up to 110 °C to evaporate all methanol and to 150 °C to evaporate all the residual water. Finally, the solution was heated up to 300 °C with different heating up profiles by controlling the heating time duration for 21 min, 17 min, 12 min, 9.3 min, and 8 min. Once reached to 300 °C, the reaction solution was kept at this temperature for another 90 min. Then the reaction was stopped and the solution was cooled down to room temperature. The colloidal solution was washed with cyclohexane/ethanol for four times and then redispersed in cyclohexane for characterization.

Synthesis of β-$NaYF_4$: 20%Yb^{3+}, 4%Tm^{3+}—$NaYF_4$ Core—Shell UCNPs. First, 0.12 mmol YCl_3 was added into the mixed solution of 3 mL of OA and 7.5 mL of ODE in a 50 mL round-bottom flask. The mixture solution was heated up to 150 °C with Ar flowing through and then was kept isothermally for 30 min to evaporate methanol and possible residual water. Then the clear solution was cooled down to room temperature followed by the addition of 5 ml method solution involving 0.48 mmol NH_4F and 0.3 mmol NaOH and stirring for 30 min. 0.1 mmol UCNPs was added into the solution too and then the whole mixture solution was heated up to 150 °C and held at 150 °C for 30 min. Then the reaction solution was heated up quickly to 300 °C and kept at this temperature for another 60 min. At room temperature, the colloidal solution was washed with cyclohexane/ethanol three times and then redispersed in cyclohexane for characterization.

■ ASSOCIATED CONTENT

Supporting Information

The Supporting Information is available free of charge on the ACS Publications website at DOI: 10.1021/acs.jpclett.6b01434.

Detailed experimental section, size distribution histograms, X-ray diffraction patterns, high resolution TEM, elemental mapping, fluorolog spectrometer measurement, as well as the schematic illustration of the system setup for customized scanning confocal microscope. (PDF)

■ AUTHOR INFORMATION

Corresponding Authors

*E-mail: xiaoxue.xu@mq.edu.au.

*E-mail: dayong.jin@uts.edu.au.

DOI: 10.1021/acs.jpclett.6b01434
J. Phys. Chem. Lett. 2016, 7, 3252−3258

Notes

The authors declare no competing financial interest.

■ ACKNOWLEDGMENTS

This project is primarily supported by the Australian Research Council (ARC) Future Fellowship Scheme (FT 130100517; DayongJin), ARC Centre of Excellence Scheme through Centre for Nanoscale BioPhotonics, Macquarie University Research Fellowship Scheme (Xiaoxue Xu), China Scholarship Council CSC scholarships (Chenshuo Ma: No.201408530049)

■ REFERENCES

(1) Zhou, B.; Shi, B.; Jin, D.; Liu, X. Controlling Upconversion Nanocrystals for Emerging Applications. *Nat. Nanotechnol.* **2015**, *10*, 924−936.

(2) Zhao, J.; Jin, D.; Schartner, E. P.; Lu, Y.; Liu, Y.; Zvyagin, A. V.; Zhang, L.; Dawes, J. M.; Xi, P.; Piper, J. A.; Goldys, E. M.; Monro, T. M. Single-Nanocrystal Sensitivity Achieved by Enhanced Upconversion Luminescence. *Nat. Nanotechnol.* **2013**, *8*, 729−734.

(3) Berry, M. T.; May, P. S. Disputed Mechanism for Nir-to-Red Upconversion Luminescence in Nayf4: Yb3+, Er3+. *J. Phys. Chem. A* **2015**, *119*, 9805−9811.

(4) Li, X.; Zhang, F.; Zhao, D. Lab on Upconversion Nanoparticles: Optical Properties and Applications Engineering Via Designed Nanostructure. *Chem. Soc. Rev.* **2015**, *44*, 1346−1378.

(5) Anderson, R. B.; Smith, S. J.; May, P. S.; Berry, M. T. Revisiting the NIR-to-Visible Upconversion Mechanism in B-Nayf4: Yb3+, Er3+. *J. Phys. Chem. Lett.* **2014**, *5*, 36−42.

(6) Zhao, J.; Lu, Z.; Yin, Y.; McRae, C.; Piper, J. A.; Dawes, J. M.; Jin, D.; Goldys, E. M. Upconversion Luminescence with Tunable Lifetime in Nayf 4: Yb, Er Nanocrystals: Role of Nanocrystal Size. *Nanoscale* **2013**, *5*, 944−952.

Nanocomposites: Integration of Upconversion Imaging and Photothermal Therapy. *J. Mater. Chem.* **2011**, *21*, 6193−6200.

(18) Cheng, L.; Yang, K.; Li, Y.; Zeng, X.; Shao, M.; Lee, S. T.; Liu, Z. Multifunctional Nanoparticles for Upconversion Luminescence/Mr Multimodal Imaging and Magnetically Targeted Photothermal Therapy. *Biomaterials* **2012**, *33*, 2215−22.

(19) Boyer, J.-C.; Manseau, M.-P.; Murray, J. I.; van Veggel, F. C. Surface Modification of Upconverting Nayf4 Nanoparticles with Peg−Phosphate Ligands for Nir (800 Nm) Biolabeling within the Biological Window. *Langmuir* **2010**, *26*, 1157−1164.

(20) Yang, P.; Quan, Z.; Lu, L.; Huang, S.; Lin, J. Luminescence Functionalization of Mesoporous Silica with Different Morphologies and Applications as Drug Delivery Systems. *Biomaterials* **2008**, *29*, 692−702.

(21) Lucky, S. S.; Muhammad Idris, N.; Li, Z.; Huang, K.; Soo, K. C.; Zhang, Y. Titania Coated Upconversion Nanoparticles for near-Infrared Light Triggered Photodynamic Therapy. *ACS Nano* **2015**, *9*, 191−205.

(22) Dou, Q. Q.; Rengaramchandran, A.; Selvan, S. T.; Paulmurugan, R.; Zhang, Y. Core-Shell Upconversion Nanoparticle - Semiconductor Heterostructures for Photodynamic Therapy. *Sci. Rep.* **2015**, *5*, 8252.

(23) Liu, J. N.; Bu, W. B.; Shi, J. L. Silica Coated Upconversion Nanoparticles: A Versatile Platform for the Development of Efficient Theranostics. *Acc. Chem. Res.* **2015**, *48*, 1797−805.

(24) Li, C.; Yang, D.; Ma, P.; Chen, Y.; Wu, Y.; Hou, Z.; Dai, Y.; Zhao, J.; Sui, C.; Lin, J. Multifunctional Upconversion Mesoporous Silica Nanostructures for Dual Modal Imaging and in Vivo Drug Delivery. *Small* **2013**, *9*, 4150−4159.

(25) Fan, W.; Bu, W.; Shi, J. On the Latest Three-Stage Development of Nanomedicines Based on Upconversion Nanoparticles. *Adv. Mater.* **2016**, *28*, 3987−4011.

(26) Zhang, F. *Photon Upconversion Nanomaterials*; Springer: New York, 2015; Vol. *416*.

(27) Schietinger, S.; Menezes, L. d. S.; Lauritzen, B. r.; Benson, O.

(36) Wu, S.; Han, G.; Milliron, D. J.; Aloni, S.; Altoe, V.; Talapin, D. V.; Cohen, B. E.; Schuck, P. J. Non-Blinking and Photostable Upconverted Luminescence from Single Lanthanide-Doped Nanocrystals. *Proc. Natl. Acad. Sci. U. S. A.* **2009**, *106*, 10917−10921.

(37) Wang, J.; Deng, R.; MacDonald, M. A.; Chen, B.; Yuan, J.; Wang, F.; Chi, D.; Hor, T. S. A.; Zhang, P.; Liu, G.; Han, Y.; Liu, X. Enhancing Multiphoton Upconversion through Energy Clustering at Sublattice Level. *Nat. Mater.* **2013**, *13*, 157−162.

(38) Wang, F.; Wang, J.; Liu, X. Direct Evidence of a Surface Quenching Effect on Size-Dependent Luminescence of Upconversion Nanoparticles. *Angew. Chem., Int. Ed.* **2010**, *49*, 7456−60.

(39) Zhang, F.; Che, R.; Li, X.; Yao, C.; Yang, J.; Shen, D.; Hu, P.; Li, W.; Zhao, D. Direct Imaging the Upconversion Nanocrystal Core/Shell Structure at the Subnanometer Level: Shell Thickness Dependence in Upconverting Optical Properties. *Nano Lett.* **2012**, *12*, 2852−2858.

(40) Li, X.; Wang, R.; Zhang, F.; Zhao, D. Engineering Homogeneous Doping in Single Nanoparticle to Enhance Upconversion Efficiency. *Nano Lett.* **2014**, *14*, 3634−3639.

(41) Gargas, D. J.; Chan, E. M.; Ostrowski, A. D.; Aloni, S.; Altoe, M. V.; Barnard, E. S.; Sanii, B.; Urban, J. J.; Milliron, D. J.; Cohen, B. E.; Schuck, P. J. Engineering Bright Sub-10-Nm Upconverting Nanocrystals for Single-Molecule Imaging. *Nat. Nanotechnol.* **2014**, *9*, 300−305.

(42) Ostrowski, A. D.; Chan, E. M.; Gargas, D. J.; Katz, E. M.; Han, G.; Schuck, P. J.; Milliron, D. J.; Cohen, B. E. Controlled Synthesis and Single-Particle Imaging of Bright, Sub-10 Nm Lanthanide-Doped Upconverting Nanocrystals. *ACS Nano* **2012**, *6*, 2686−2692.

(43) Schietinger, S.; Aichele, T.; Wang, H. Q.; Nann, T.; Benson, O. Plasmon-Enhanced Upconversion in Single Nayf4:Yb3+/Er3+ Codoped Nanocrystals. *Nano Lett.* **2010**, *10*, 134−8.

(44) Liao, J.; Yang, Z.; Lai, S.; Shao, B.; Li, J.; Qiu, J.; Song, Z.; Yang, Y. Upconversion Emission Enhancement of Nayf4:Yb,Er Nanoparticles by Coupling Silver Nanoparticle Plasmons and Photonic Crystal Effects. *J. Phys. Chem. C* **2014**, *118*, 17992−17999.

Supporting Information

Probing the Interior Crystal Quality in the Development of More Efficient and Smaller Upconversion Nanoparticles

Chenshuo Ma[§,‡], Xiaoxue Xu[‡,£,†*], Fan Wang[‡,£,†], Zhiguang Zhou[£,†], Shihui Wen[£,†], Deming Liu[‡,£,†], Jinghua Fang[£,†], Candace I Lang[§], and Dayong Jin[‡,£,†*]

[§] Department of Engineering, Faculty of Science and Engineering, Macquarie University, Sydney, NSW, 2109, Australia;

[‡]Advanced Cytometry Labs, ARC Centre of Excellence for Nanoscale BioPhotonics, Macquarie University, Sydney, NSW, 2109, Australia;

[£]Institute for Biomedical Materials and Devices, Faculty of Science, University of Technology Sydney, NSW, 2007, Australia;

[†]ARC Research Hub for Integrated Device for End-user Analysis at Low-levels (IDEAL), Faculty of Science, University of Technology Sydney, NSW, 2007, Australia;

Email: xiaoxue.xu@mq.edu.au; dayong.jin@uts.edu.au

Materials and Characterizations:

1. Reagents:

Yttrium chloride hexahydrate ($YCl_3 \cdot 6H_2O$, 99.99%), ytterbium chloride hexahydrate ($YbCl_3 \cdot 6H_2O$, 99.998%), thulium chloride hexahydrate ($TmCl_3 \cdot 6H_2O$, 99.9%), sodium hydroxide (NaOH, 98%), ammonium fluoride (NH_4F, 99.99%), oleic acid (OA, 90%), and 1-octadecene (ODE, 90%) were purchased from Sigma-Aldrich. Oleylamine (OM, 90%) was purchased from Pfaltz& Bauer. All reagents were used as received without further purification[1].

2. Characterizations

TEM Characterization:

The morphology of the synthesized UCNPs was characterized using transmission electron microscopy (TEM) (Philips CM10 TEM with Olympus Sis Megaview G2 Digital Camera) with an operating voltage of 100 kV. The samples were prepared by placing a drop of a dilute suspension of nanocrystals onto formvar-coated copper grids

(300 meshes) and letting it dry in a desiccator at room temperature. HRTEM and STEM elemental mapping were characterized using JEOL 2200FS TEM.

XRD Characterization:

Powder X-ray diffraction (XRD) patterns were obtained on a PANalyticalX'Pert Pro MPD X-ray diffractometer using Cu Kα1 radiation (40 kV, 40 mA, λ=0.15418 nm). The XRD samples were prepared by repeatedly dripping UCNPs dispersions in cyclohexane on a zero-background silicon wafer.

Photoluminescence characterization for UCNPs dispersions:

The upconversion luminescence spectra of colloidal solutions in quartz cuvettes with 10 mm path length were acquired using a Fluorolog-Tau3 spectrofluorometer (JobinYvon-Horiba) equipped with an external 980 nm CW diode laser with a pump power of 250mW. All the UCNPs samples were prepared with the same molar concentration of Tm^{3+} in the cyclohexane dispersions by weighing the same amount of the UCNPs.

Photoluminescence characterization for single UCNPs:

We built a laser scanning confocal microscope for the intensity measurement of single UCNPs as shown in Figure S9. The excitation source is a 976 nm single mode polarized laser (229 mW) which is focused onto the sample through a 100x objective lens (NA 1.4). The emission from sample is collecting by same objective lens then refocused into an optical fiber which has a core size matching with system Airy disk. A Single Photon Counting Avalanche Diode (SPAD) detector is connected to the collection optical fiber to detect the emission intensity. The scanning is achieved by moving the 3D piezo stage. The monodispersed single UCNPs samples were prepared using the following protocol:

1, Place a drop of 50 µl Poly-L-lysine solution (0.1% w/v in H_2O) on a cleaned cover-glass and leave it for 30 mins before rinse it using water and dry the surface at room temperature.

2. Prepare 0.1mg/ml UCNPs dispersion in cyclohexane, and place a drop of 20 µl UCNPs dispersion onto the cover-glass, then carefully rinse it using cyclohexane and let it dry naturally.

3. Make a drop of 20 µl Embedding Media on a glass slide, and then place the cover-glass onto the glass slide with Embedding media and squeeze out any air bubbles. Then dry the sample in an oven at 60 °C.

Supplementary Results

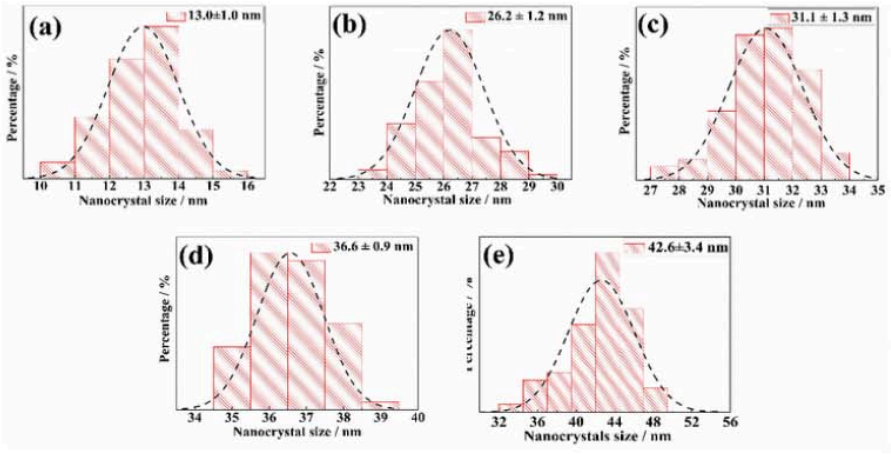

Figure S1. The size distribution histograms of β-$NaYF_4$: 20%Yb^{3+}, 4%Tm^{3+} UCNPs corresponding to TEM images in Figure 1. Histograms of the crystals sizes are drawn from analysis of >150 crystals for each sample.

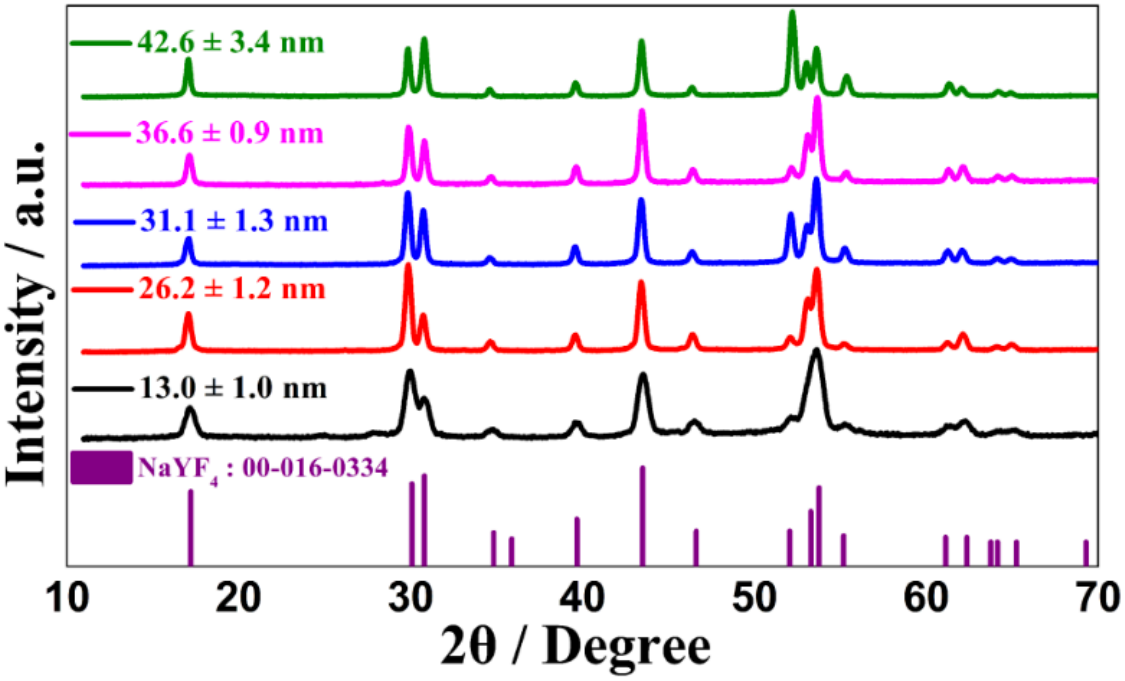

Figure S2. XRD patterns of different sized β-$NaYF_4$: 20% Yb^{3+}, 4%Tm^{3+}UCNPs.

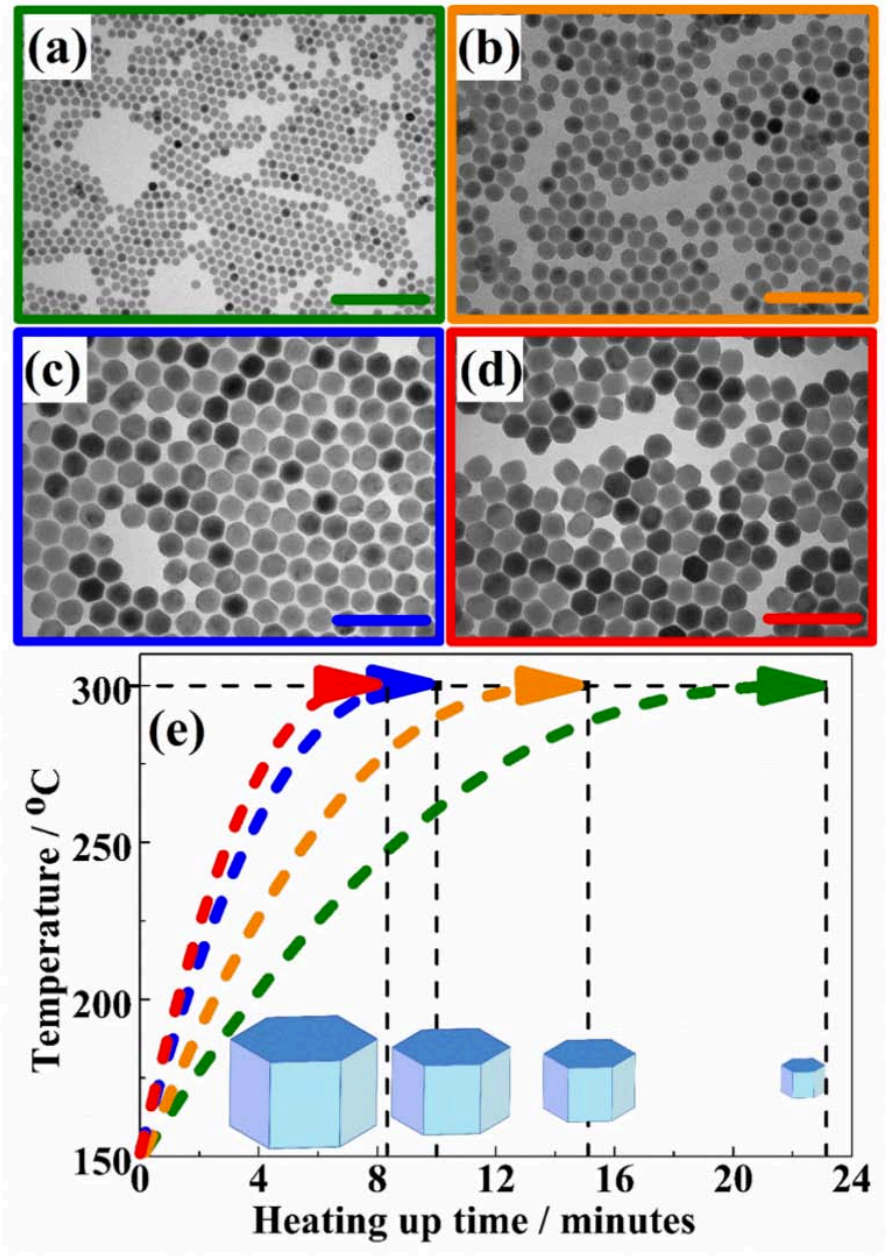

Figure S3.TEM images of different sized β-$NaYF_4$: 20%Yb^{3+}, 8%Tm^{3+} nanocrystals synthesized via controlling the heating up time from 150°C to 300°C for (a) 23 min, (b) 15 min, (c) 10 min, (d) 8.3 min, and scale bar is 100 nm. (e) Schematic illustration of the different heating up profiles for controlling the nanocrystals size.

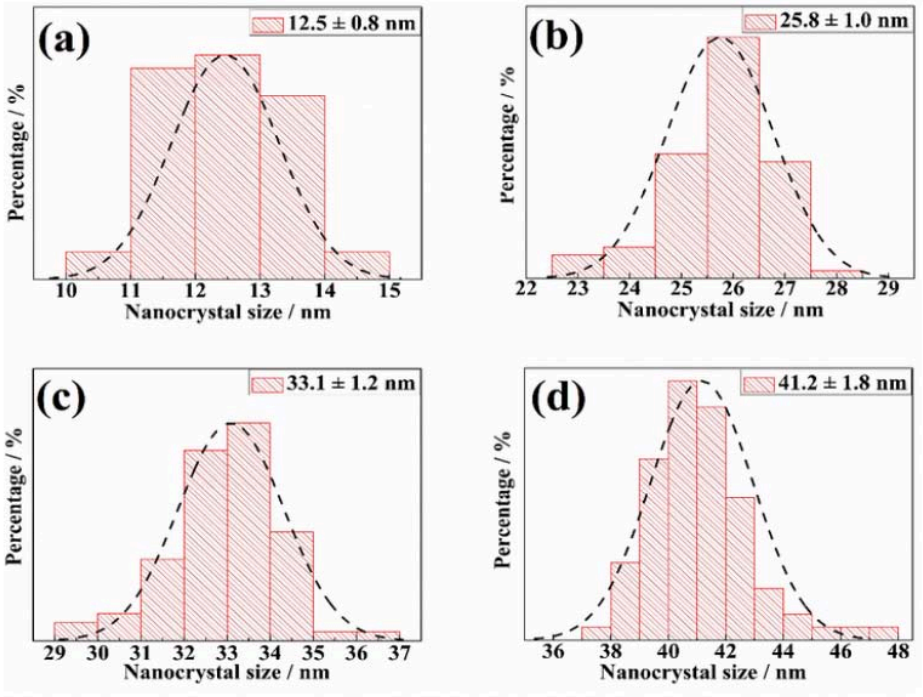

Figure S4. The size distribution histograms of β-$NaYF_4$: 20%Yb^{3+}, 8%Tm^{3+} UCNPs corresponding to TEM images in Figure S3. Histograms of the crystals sizes are drawn from analysis of >150 crystals for each sample.

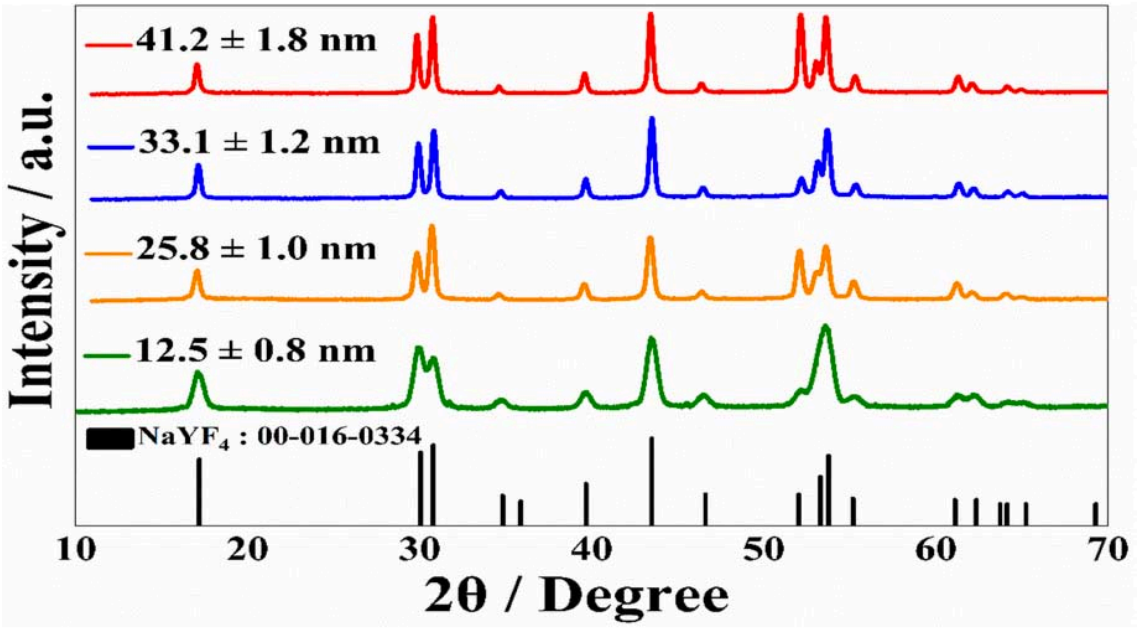

Figure S5. XRD patterns of different sized β-$NaYF_4$: 20% Yb^{3+}, 8%Tm^{3+} UCNPs.

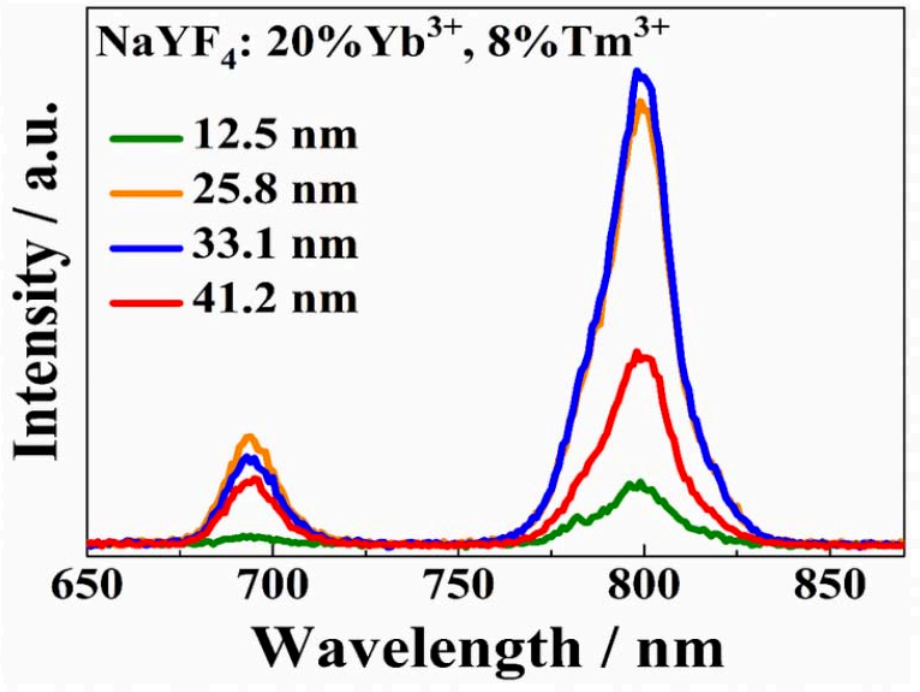

Figure S6. Fluorolog spectrometer measurement of different sized β-$NaYF_4$: 20%Yb^{3+}, 8%Tm^{3+} UCNPs.

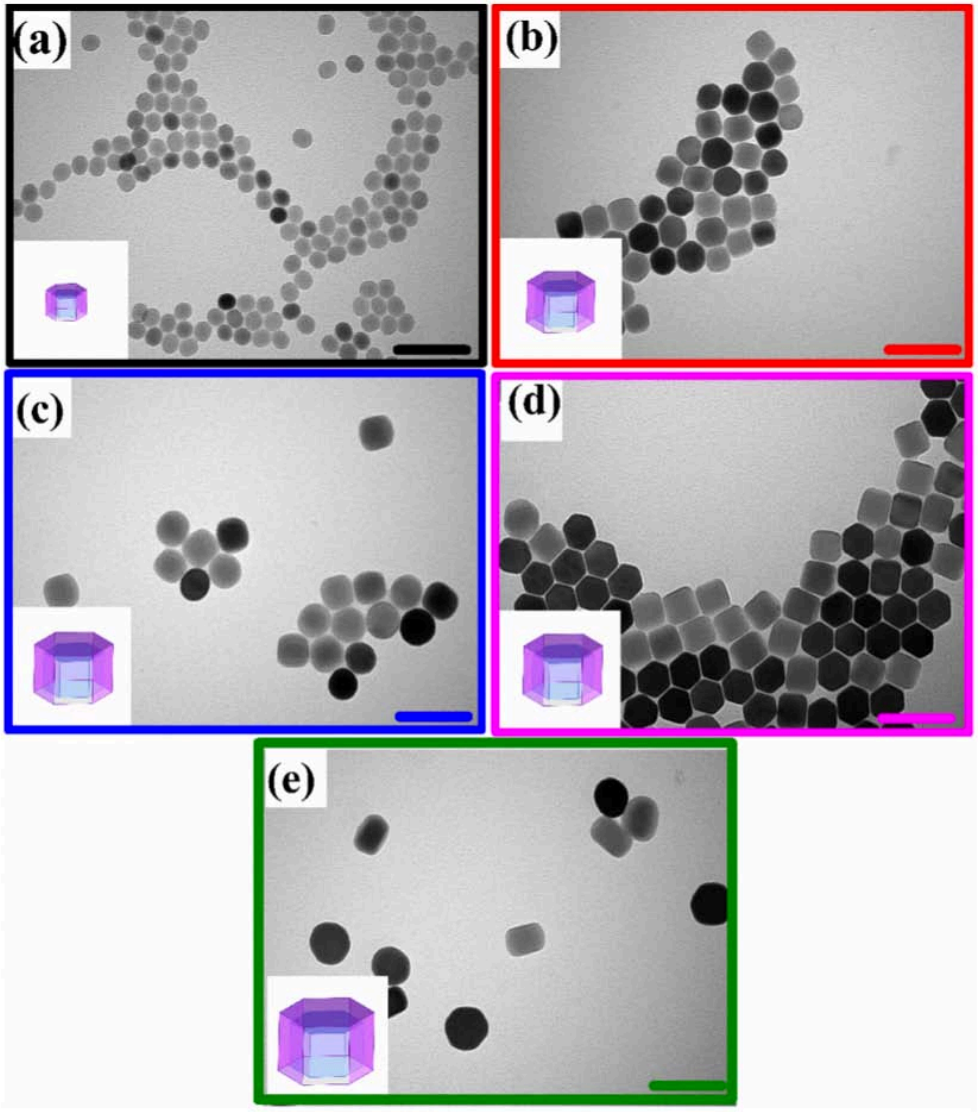

Figure S7.TEM images of different sized β-$NaYF_4$: 20%Yb^{3+}, 4%Tm^{3+} nanocrystals passivated with inert shell, scale bar is 100 nm.

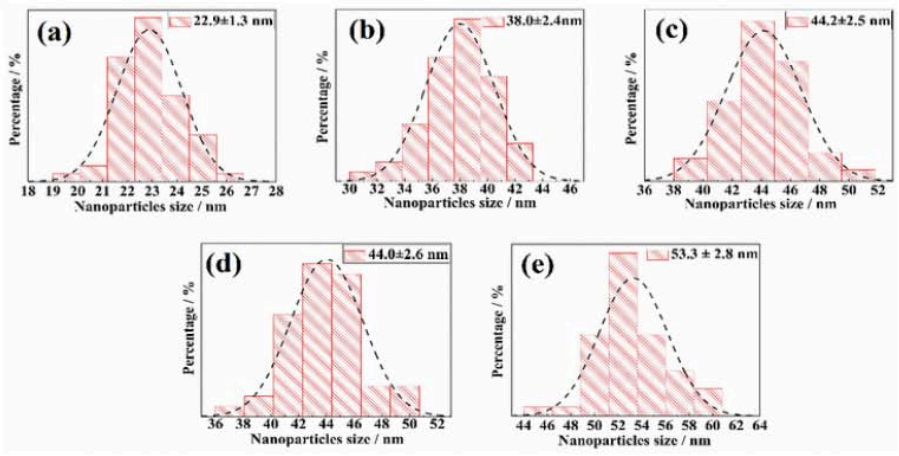

Figure S8. The size distribution histograms of different sized β-$NaYF_4$: 20%Yb^{3+}, 4%Tm^{3+} nanocrystals passivated with inert shell corresponding to TEM images in Figure S7. Histograms of the crystals sizes are drawn from analysis of >150 crystals for each sample.

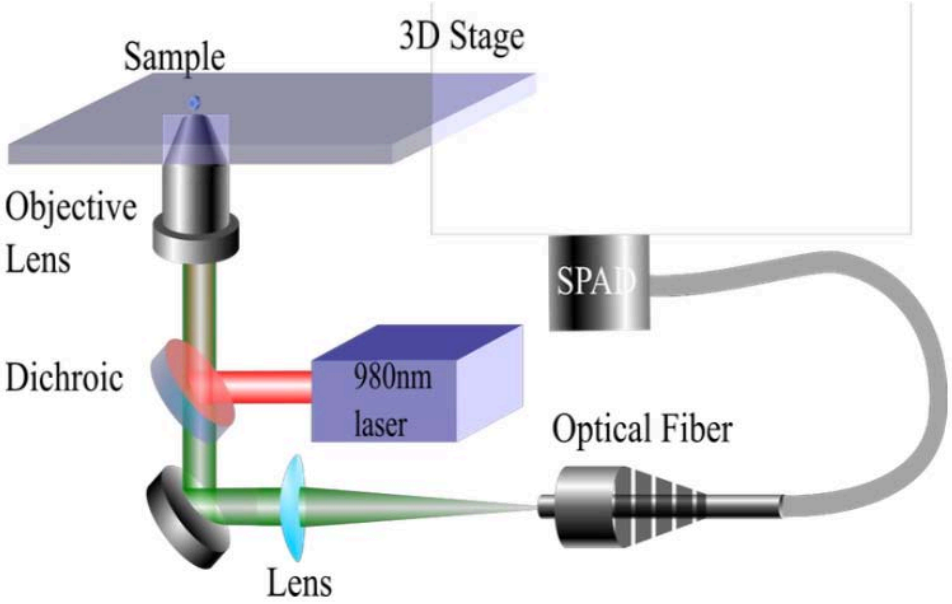

Figure S9. Schematic illustration of the system setup for customized scanning confocal microscope.

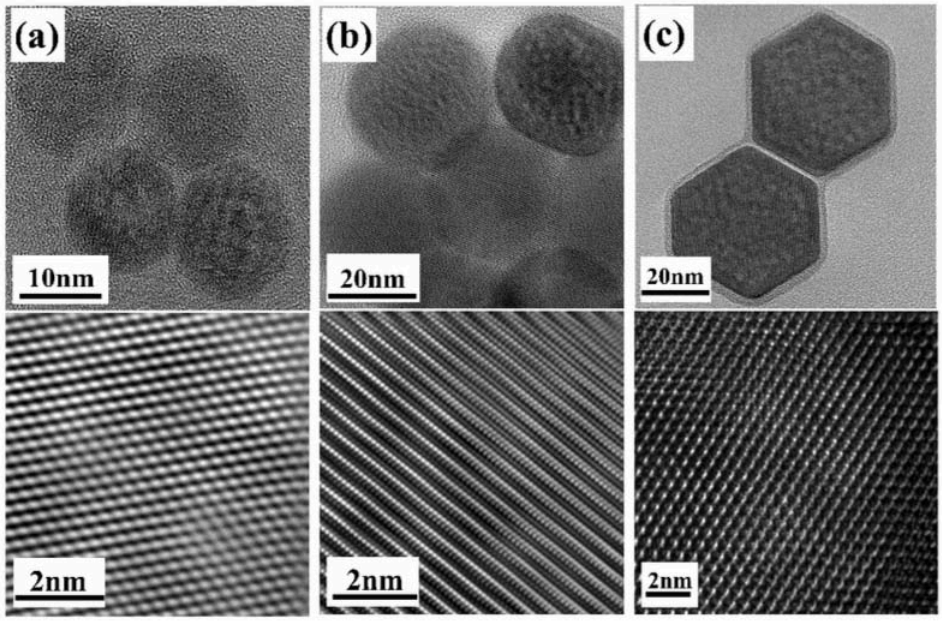

Figure S10. High Resolution TEM (HRTEM) images of β-$NaYF_4$: 20%Yb^{3+}, 4%Tm^{3+} nanocrystals with different size: (a) 13.0 nm, (b) 31.3 nm, (c) 42.6 nm.

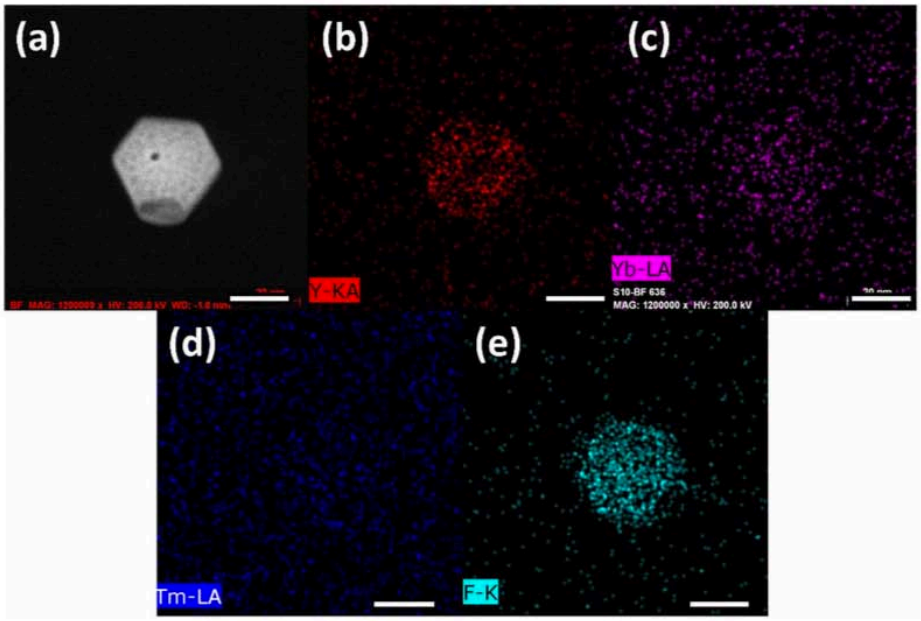

Figure S11. The TEM image (a) and TEM EDS elemental mapping of the Y (b), Yb (c), Tm (d), F (e) in β-$NaYF_4$: 20%Yb^{3+}, 4%Tm^{3+} nanocrystal (42.6 nm) , scale bar is 20 nm. The results show the homogenous distribution of elements Y, Yb and F. However it is hard to detect the Tm due to low doping concentration.

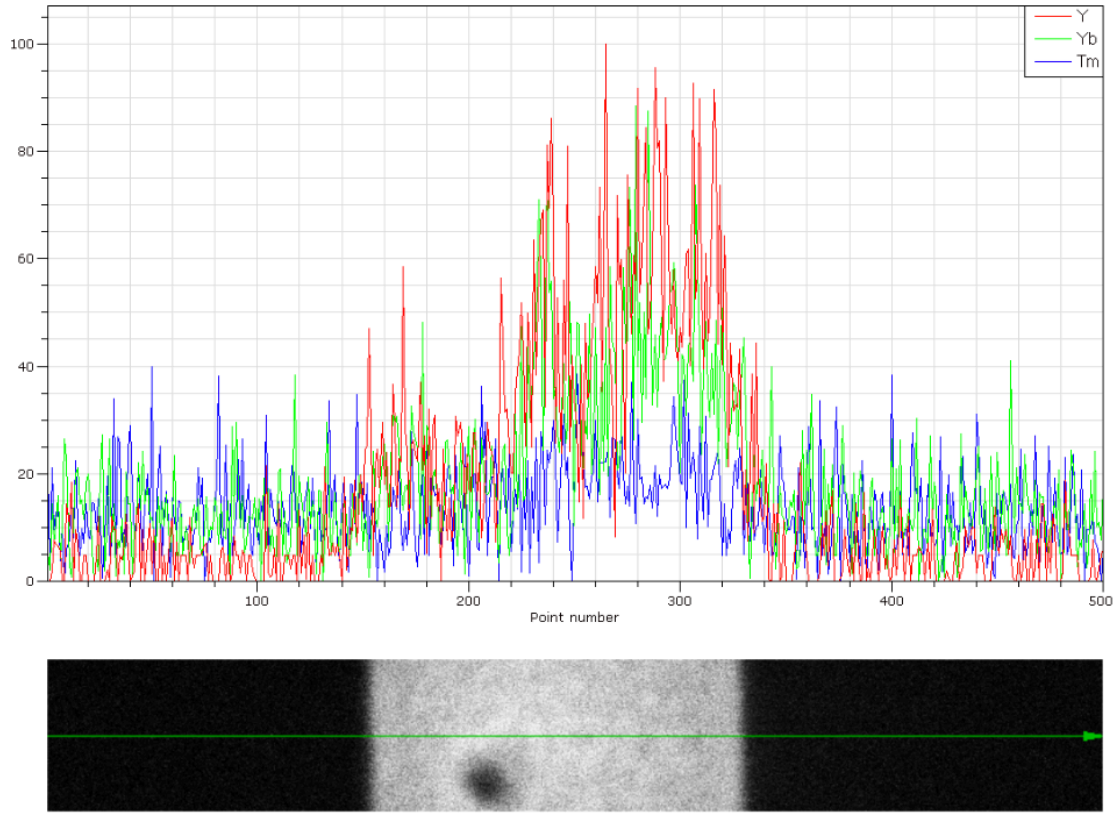

Figure S12. TEM EDS Line scan of single $NaYF_4$: 20%Yb^{3+}, 4%Tm^{3+} nanocrystal (42.6 nm), it showed the homogenous distribution of three different elements of Y, Yb, and Tm along the line. Particularly, it also shows the uniform distribution of Tm in the nanocrystal.

Reference

(1) Liu, D.; Xu, X.; Du, Y.; Qin, X.; Zhang, Y.; Ma, C.; Wen, S.; Ren, W.; Goldys, E. M.; Piper, J. A.; Dou, S.; Liu, X.; Jin, D.. Three-dimensional Controlled Growth of Monodisperse Sub-50 nm Heterogeneous Nanocrystals. *Nat*. *Commun*.**2016,***7*, 10254.

3.3 Remarks on Paper 1

This work reported the importance of controlling the synthesis conditions to optimize the nanocrystal size, which directly affects the upconversion luminescence. Good crystallinity that is crystals that are highly regular and contain few defects, plays an important role together with deactivations to its surface in the efficiency of its emission. The single nanocrystal luminescence measurement provides evidence that internal defects influenced the upconversion intensity for each single nanocrystal. This work further provided a route to produce nanocrystals which have both small size and efficient upconversion luminescence, by optimizing both internal defects and external defects.

REFERENCES

(1) Zhao, J.; Jin, D.; Schartner, E. P.; Lu, Y.; Liu, Y.; Zvyagin, A. V; Zhang, L.; Dawes, J. M.; Xi, P.; Piper, J. a; *et al.* Single-Nanocrystal Sensitivity Achieved by Enhanced Upconversion Luminescence. *Nat. Nanotechnol.* **2013**, *8*, 729–734.

(2) Ding, Y.; Zhang, X.; Gao, H.; Xu, S.; Wei, C.; Zhao, Y. Enhancement on Concentration Quenching Threshold and Upconversion Luminescence of β-$NaYF_4$: Er^{3+}/Yb^{3+} Codoping with Li^+ Ions. *J. Alloys Compd.* **2014**, *599*, 60–64.

(3) Chen, G.; Ohulchanskyy, T. Y.; Kumar, R.; Ågren, H.; Prasad, P. N. Ultrasmall Monodisperse $NaYF_4$: Yb^{3+}/Tm^{3+} Nanocrystals with Enhanced Near-Infrared to Near-Infrared Upconversion Photoluminescence. *ACS Nano* **2010**, *4*, 3163–3168.

(4) Hao, S.; Shao, W.; Qiu, H.; Shang, Y.; Fan, R.; Guo, X.; Zhao, L.; Chen, G.; Yang, C. Tuning the Size and Upconversion Emission of $NaYF_4$: Yb^{3+}/Pr^{3+} Nanoparticles through Yb^{3+} Doping. *RSC Adv.* **2014**, *4*, 56302–56306.

CHAPTER 4

Optimal Sensitizer Concentration in Single Upconversion Nanocrystals

The research in this chapter concerns development of a novel structure which can maximize the sensitizer doped in each single upconversion nanocrystal. Previously, 20 % of the sensitizer ions added was used to minimize the so-called "concentration quenching" effect[1,2]. It has recently been shown that the activator and sensitizer ions' effective luminescence can be increased by enhancing excitation power[3,4], but increasing sensitizer will increase nanocrystal size as well[5]. By studying the size of different kinds of rare earth ion doped UCNCs, I developed a method to synthesize sub-10 nanometre nanocrystals. I further developed a novel sandwich structure which has a small template core to allow an epitaxial growth of a size-tunable active shell enclosed by an inert shell to minimize surface quenching. This method can not only synthesize small nanocrystals but can dope a maximum amount of sensitizer ions. This work is presented in the form of a journal publication from ***Nano Letters***.

4.1 Contribution to Paper 2

The author contribution for paper "Optimal Sensitizer Concentration in Single Upconversion Nanocrystals" are shown in **Table 4.1**.

Table 4.1 Author contribution summary for paper 2

Name	Experiment Design	Material Synthesis	Data Collection	Analysis	Figures and Tables	Manuscript
Chenshuo Ma	√	√	√	√	√	√
Xiaoxue Xu						√
Fan Wang				√		
Zhiguang Zhou				√		
Deming Liu				√		
Jiangbo Zhao				√		
Ming Guan					√	
Candace I Lang						√
Dayong Jin				√		√

This work was supervised by my supervisors, Dayong Jin and Candace I Lang, during my second and half of third years of Ph.D. I carried out the majority of the experimental work, including sample synthesis and data collection. Fan Wang and Zhiguang Zhou set up the optical system. Analysis of results was carried out in collaboration with the co-authors listed above. I prepared all the figures and tables and the manuscript draft; Dayong Jin, Candace I Lang and Xiaoxue Xu then made some edits. I prepared the final manuscript for publication.

4.2 Paper 2

Chenshuo Ma, Xiaoxue Xu, Fan Wang, Zhiguang Zhou, Deming Liu, Jiangbo Zhao, Ming Guan, Candace I Lang, and Dayong Jin. "Optimal Sensitizer Concentration in Single Upconversion Nanocrystals", ***Nano Letters***, 2017, 17(5): 2858-2864.

NANO LETTERS
Letter
pubs.acs.org/NanoLett

Optimal Sensitizer Concentration in Single Upconversion Nanocrystals

Chenshuo Ma,[†,‡] Xiaoxue Xu,[*,‡,§] Fan Wang,[*,‡,§] Zhiguang Zhou,[§] Deming Liu,[§] Jiangbo Zhao,[∥] Ming Guan,[§] Candace I Lang,[†] and Dayong Jin[*,‡,§,⊥]

[†]Department of Engineering, Faculty of Science and Engineering, Macquarie University, Sydney, NSW 2109, Australia
[‡]Advanced Cytometry Laboratories, ARC Centre of Excellence for Nanoscale BioPhotonics, Macquarie University, Sydney, NSW 2109, Australia
[§]Institute for Biomedical Materials and Devices (IBMD), Faculty of Science, University of Technology Sydney, Sydney, NSW 2007, Australia
[∥]Institute for Photonics and Advanced Sensing (IPAS) and School of Physical Sciences, University of Adelaide, Adelaide, SA 5005, Australia
[⊥]ARC Research Hub for Integrated Device for End-user Analysis at Low-levels (IDEAL), Faculty of Science, University of Technology Sydney, Sydney, NSW 2007, Australia

S *Supporting Information*

ABSTRACT: Each single upconversion nanocrystal (UCNC) usually contains thousands of photon sensitizers and hundreds of photon activators to up-convert near-infrared photons into visible and ultraviolet emissions. Though in principle further increasing the sensitizers' concentration will enhance the absorption efficiency to produce brighter nanocrystals, typically 20% of Yb^{3+} ions has been used to avoid the so-called "concentration quenching" effect. Here we report that the concentration quenching effect does not limit the sensitizer concentration and $NaYbF_4$ is the most bright host matrix. Surface quenching and the large size of $NaYbF_4$ nanocrystals are the only factors limiting this optimal concentration. Therefore, we further designed sandwich nanostructures of $NaYbF_4$ between a small template core to allow an epitaxial growth of the size-tunable $NaYbF_4$ shell enclosed by an inert shell to minimize surface quenching. As a result, the suspension containing 25.2 nm sandwich structure UCNCs is 1.85 times brighter than the homogeneously doped ones, and the brightness of each single 25.2 nm heterogeneous UCNC is enhanced by nearly 3 times compared to the $NaYF_4$: 20% Yb^{3+}, 4% Tm^{3+} UCNCs in similar sizes. Particularly, the blue emission intensities of the UCNCs with the sandwich structure in the size of 13.6 and 25.2 nm are 1.36 times and 3.78 times higher than that of the monolithic UCNCs in the similar sizes. Maximizing the sensitizer concentration will accelerate the development of brighter and smaller UCNCs as more efficient biomolecule probes or photon energy converters.

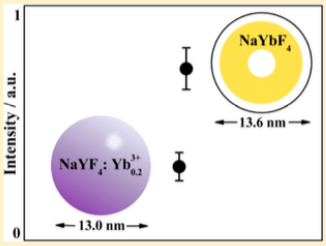

KEYWORDS: *Upconversion, single nanoparticle, core−shell, concentration quenching, lanthanide*

Rare-earth doped upconversion nanocrystals (UCNCs) are typically doped with ytterbium sensitizer ions (Yb^{3+}), which absorb infrared radiation and nonradiatively transfer their excitation to activator ions such as erbium (Er^{3+}), thulium (Tm^{3+}), or holmium (Ho^{3+}).[1−4] UCNCs capable of converting lower-energy infrared photons into high energy emissions, such as visible and ultraviolet light,[5−7] are promising for a broad range of applications spanning background-free biolabeling and biosensing,[8,9] light-triggered drug delivery,[10−13] multimodal bioimaging,[14] full-color 3D display,[15] solar energy harvesting, and light-emitting diodes (LEDs).[16−19] As upconversion luminescence is a multiphoton process, one of the long pursued goals in promoting UCNCs for crystal applications is to enhance upconversion efficiency and generate stronger upconversion brightness.[20,21] Thanks to decades of investigation in upconversion luminescence as well as the advancement of synthesis and instrumental characterization at nanoscale, various enhancement strategies to amplify upconversion luminescence have been proved, including optimizing crystal hosts and dopant concentrations, coating inert/active shells around nanocrystals,[12,22−26] tuning sizes of nanocrystals,[5,27−29] engineering sublattice arrangements,[30] and coupling with plasmonic noble metal nanostructures.[31,32]

Very recently, high- irradiance excitation was used to alleviate concentration quenching of upconversion luminescence for orders of magnitude brightness enhancement, where the optimal activator concentrations of Tm^{3+} and Er^{3+} in $NaYF_4$ increase from 0.5 mol % to 8 mol %, and from 2 mol % to more than 10 mol %, respectively.[9,33−35] However, the corresponding optimal sensitizer concentration, i.e., the typical trivalent Yb^{3+}

Received: December 23, 2016
Revised: April 12, 2017
Published: April 24, 2017

DOI: 10.1021/acs.nanolett.6b05331
Nano Lett. 2017, 17, 2858−2864

Nano Letters Letter

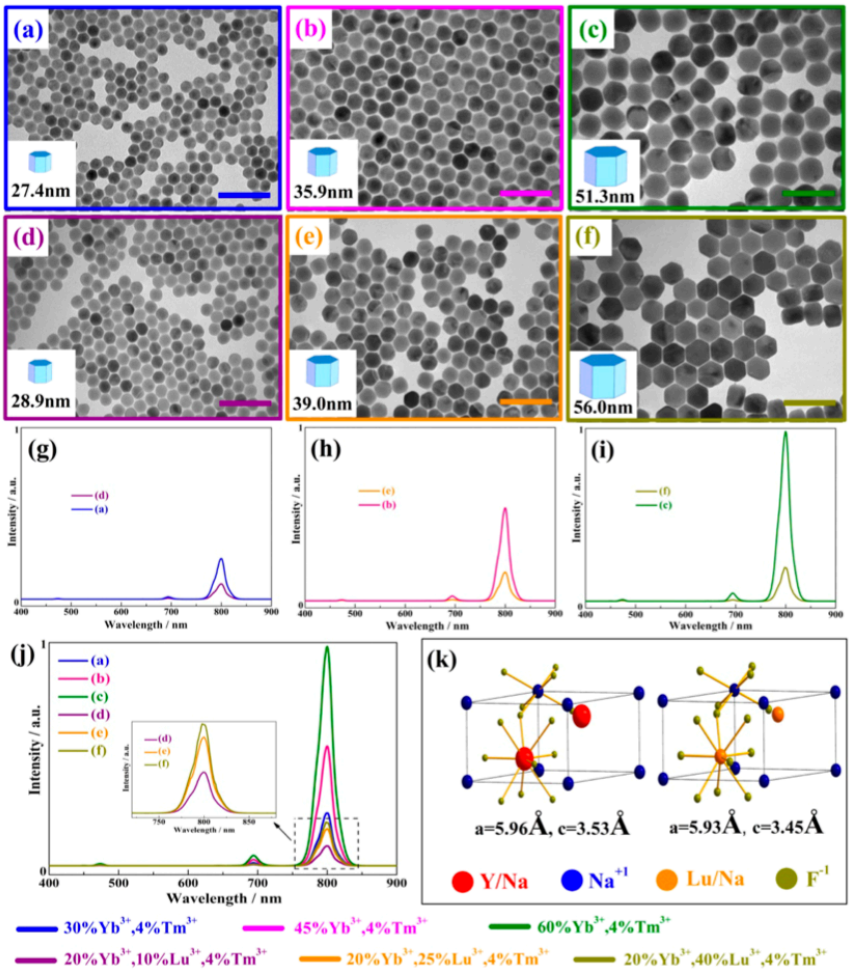

Figure 1. TEM images of $NaYF_4$: 4% Tm^{3+}, *x*% Yb^{3+}nanocrystals: (a) $x = 30$, (b) $x = 45$, (c) $x = 60$; and TEM images of $NaYF_4$: 4% Tm^{3+}, 20% Yb^{3+}, *y*% Lu^{3+} nanocrystals: (d) $y = 10$, (e) $y = 25$, (f) $y = 40$, scale bar is 100 nm; Luminescent emission spectra of the UCNCs dispersions measured using Fluorolog photospectrometer: (g) $NaYF_4$: 4% Tm^{3+}, 30% Yb^{3+}, and $NaYF_4$: 4% Tm^{3+}, 20% Yb^{3+}, 10% Lu^{3+}, (h) $NaYF_4$: 4% Tm^{3+}, 45% Yb^{3+}, and $NaYF_4$: 4% Tm^{3+}, 20% Yb^{3+}, 25% Lu^{3+}, (i) $NaYF_4$: 4% Tm^{3+}, 60% Yb^{3+}, and $NaYF_4$: 4% Tm^{3+}, 20% Yb^{3+}, 40% Lu^{3+}, (j) $NaYF_4$: 4% Tm^{3+}, *x*% Yb^{3+} ($x = 30, 45, 60$) and $NaYF_4$: 4% Tm^{3+}, 20% Yb^{3+}, *y*% Lu^{3+} ($y = 10, 25, 40$); (k) the size of unit cells of $NaYF_4$ and $NaLuF_4$ crystals.

ions, for the new level of activator concentration has not been updated yet. This gap is becoming pronounced when the UCNCs shrink smaller than 30 nm, where the upconversion brightness proportionally drops as the number of dopants per crystal reduces and the ratio of surface quenchers increases.

For biolabeling applications, both the excitation IR wavelength and 800 nm emission wavelength of Tm^{3+} doped UCNCs are attractive as they are within a "window of optical transparency" for imaging biological tissues.[36] Strategies to enhance the upconversion luminescence at 800 nm are accordingly of particular interest for in vivo bioimaging.[37,38] Nanocrystals optimally range from several nanometers to tens of nanometers in size.[39−41] Nanocrystals greater than 10 nm in size are not transported efficiently through subcellular membranes or cannot be easily cleared from the body, and for in vitro diagnostics applications, smaller fluorescent nanocrystals would be more useful as these are expected to avoid nonspecific binding issues. However, a small crystal size also results in a brightness drop as the number of dopants per crystal reduces, and the impact of surface quenching is expected to increase with the increased surface-to-volume ratio. Consequently, a major objective is to develop brighter and smaller UCNCs. Increasing the dopant concentration would be a straightforward strategy.

In this work, we find that the Yb^{3+} concentration is not limited by the concentration quenching effect and $NaYbF_4$ crystal is the best host for sensitizing more excitation photons to increase the brightness of UCNCs. We carefully look into this phenomenon by systematical design, synthesis, and characterization of β-$NaYF_4$ UCNCs with an incremental high concentration of sensitizer ions. By excluding the size and crystal structure effect, we directly confirm the sensitizer effect. To produce smaller UCNCs with optimal Yb^{3+} concentration, we first employ a Tb^{3+}-rich core as the template to allow

DOI: 10.1021/acs.nanolett.6b05331
Nano Lett. 2017, 17, 2858−2864

Nano Letters Letter

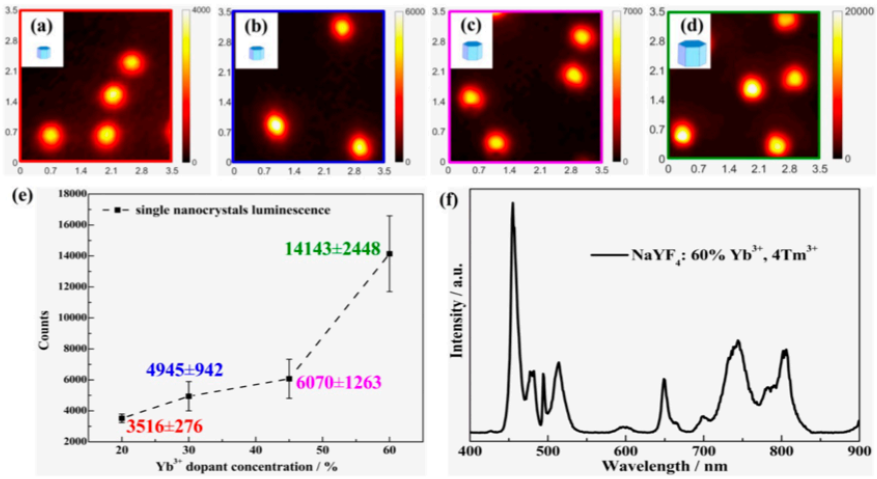

Figure 2. Confocal microscopy quantitative measurement of whole spectrum luminescence emission of single $NaYF_4$: x% Yb^{3+}, 4% Tm^{3+} UCNCs with different Yb^{3+} concentrations: (a) x = 20, (b) x = 30, (c) x = 45, (d) x = 60, respectively. (e) The emission intensity of single UCNCs vs Yb^{3+} concentration. (f) The whole spectrum emission of $NaYF_4$: 60% Yb^{3+}, 4% Tm^{3+} UCNC characterized using scanning confocal microscopy.

epitaxial growth of the size-controllable active layer of $NaYbF_4$. We further find the high concentration of Yb^{3+} ions on the relatively large surface of nanocrystals induce significant quenching. To passivate UCNCs from surface quenchers, an inert shell of $NaYF_4$ can be employed. Such a sandwich structure design has been proved useful to produce a range of brighter and size-tunable UCNCs.[42−44]

We confirm that a high dopant concentration of sensitizer ions Yb^{3+} will definitely benefit the overall brightness of UCNCs. Both the Fluorolog spectrophotometer and the upconversion confocal microscopy approach are used in this work to quantitatively characterize the emission counts of UCNCs dispersions and single UCNCs, which facilitates our investigation of the underpinning physics of photon upconversion process within the sensitizer-activator network of a single nanocrystal.

In our experiment, a series of $NaYF_4$: 4% Tm^{3+}, x% Yb^{3+} UCNCs (x = 0, 20, 30, 45, and 60) were synthesized under identical preparation conditions. As shown in the transmission electronic microscopy (TEM) images (Figure 1a−c and Figure S1a and b), the crystal size increases with the Yb^{3+} doping levels, from 19.6 ± 1.0 nm (0% Yb^{3+}) to 51.3 ± 1.8 nm (60% Yb^{3+}), which are shown in Figure S1e; the crystal size distribution histograms are shown in Figure S1c and d and Figure S2a−c. The X-ray powder diffraction (XRD) patterns of all the as-synthesized UCNCs are indexed to pure hexagonal phase ($NaYF_4$, JCPDS: 00-016-0334 and $NaYbF_4$, JCPDS: 00-027-1427; Figure S3). The XRD peaks shift toward higher angles as a function of Yb^{3+} concentration, this relates to a reduction of unit-cell volume due to the substitution of Y^{3+} ion (r = 1.075 Å) by the smaller Yb^{3+} ion (r = 1.042 Å). We normalized to the same Tm^{3+} concentration by the subtractive weighting method and inductively coupled plasma mass spectrometry (ICP-MS). Figure 1j shows that the luminescence intensity of the UCNCs dispersion is amplified as the Yb^{3+} concentration and crystal size increase, where the upconversion luminescence at 800 nm with 60% Yb^{3+} (~51.3 nm) is more than 4 times brighter than that of conventional 30% Yb^{3+} (~27.4 nm).

To differentiate the contribution of crystal size vs Yb^{3+} concentration to the enhanced upconversion luminescence, we grew $NaYF_4$: 4% Tm^{3+}, 20% Yb^{3+}, y% Lu^{3+} nanocrystals (y = 0, 10, 25, and 40) with varying sizes comparable to $NaYF_4$: 4% Tm^{3+}, 20−60% Yb^{3+} nanocrystals. To closely mimic the effect of Yb^{3+} dopants on $NaYF_4$ nanocrystals, an optically inert Lu^{3+} ion (r = 1.032 Å) was selected in the design, where 20% Yb^{3+} + 10% Lu^{3+}, 20% Yb^{3+} + 25% Lu^{3+}, and 20% Yb^{3+} + 40% Lu^{3+} correspond to 30% Yb^{3+}, 45% Yb^{3+}, and 60% Yb^{3+}, respectively. As Y^{3+} ions in $NaYF_4$ nanocrystals are substituted with the smaller ionic radii dopants, such as heavy Yb^{3+} and Lu^{3+} ions, larger nanocrystals tend to be formed owing to the higher crystal growth rate (Figure 1k).[18] Thus, the additional doping of Lu^{3+} ions in $NaYF_4$ nanocrystals can generate different sized nanocrystals, under identical reaction conditions as doping with Yb^{3+} ions did. Moreover, the similarity in ionic radii between Yb^{3+} and Lu^{3+} ensures a negligible effect of local crystallization distortion on upconversion intensity. As shown in TEM images Figure 1d−f, the additional doping of Lu^{3+} ions at 10%, to 25%, and 40% results in the crystal size increasing from ~24.6 nm ($NaYF_4$: 4% Tm^{3+}, 20% Yb^{3+} nanocrystals) to ~28.9 nm, ~39.0 nm, and ~56.0 nm, respectively (Figure 1d−f). The crystal size distribution histograms are shown in Figure S2d−f. Interestingly, when 60% Lu^{3+} is used, much larger nanocrystals are obtained (~148.4 nm) as shown in the Figure S4a−c. Importantly, smaller Lu^{3+} ions than Yb^{3+} ions leads to slightly larger hexagonal phase nanocrystals as indicated in TEM images and XRD analysis due to the reduced dipole polarizability of Lu^{3+} ions, which is convinced by the increased diffraction peak shift in XRD as a result of the decrease in unit-cell volume[18] (Figure S5).

Similarly, doping bigger lanthanide ion [Tb^{3+} ions with ionic radius (r = 1.095 Å)] induces the formation of smaller nanocrystals. Figure S6a−c shows TEM images of the $NaYF_4$: 4% Tm^{3+}, z% Tb^{3+} in which Tb^{3+} concentration increases from 20% to 45%. Clearly the size of nanocrystals decreases from 16.4, 12.7 to 10.6 nm. Figure S7a−d and Figure S8 further confirm the size measurement results and the XRD patterns for the $NaYF_4$: z% Tb^{3+}, 4% Tm^{3+} (z = 20, 30, and 45)

DOI: 10.1021/acs.nanolett.6b05331
Nano Lett. 2017, 17, 2858−2864

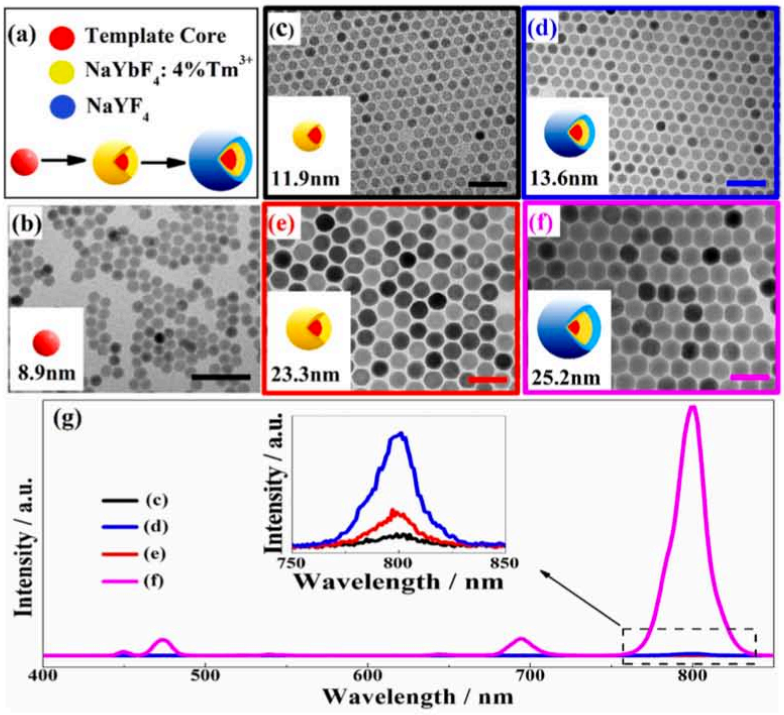

Figure 3. (a) Diagram of the sandwich nanostructure. TEM images of (b) template core nanocrystals of $NaYF_4$: 60% Tb^{3+}, 4% Tm^{3+} with a size of

Nano Letters Letter

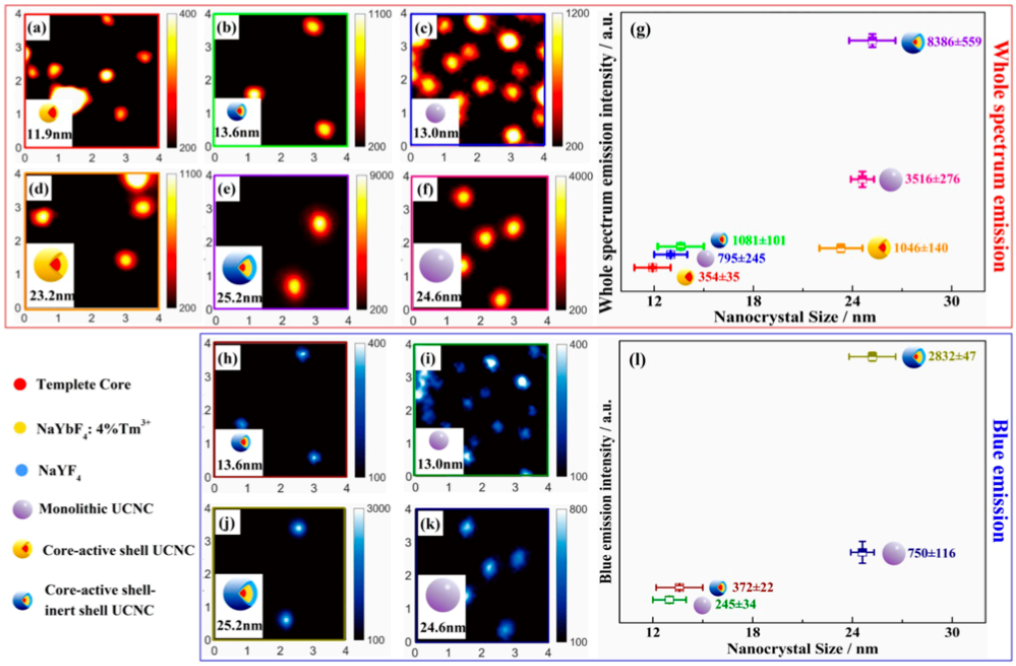

Figure 4. Confocal microscopy quantitative measurement of the whole spectrum emission for single UCNCs: (a) UCNCs of template core–active shell of $NaYbF_4$: 4% Tm^{3+} with a size of 11.9 nm, (b) UCNCs of template core–active shell–inert shell of $NaYF_4$ with a size of 13.6 nm, (c) monolithic UCNCs of $NaYF_4$: 20% Yb^{3+}, 4% Tm^{3+} with a size of 13.0 nm, (d) UCNCs of the template core–active shell with a size of 23.2 nm, (e)

To investigate whether the Tb-containing template core may quench the active $NaYbF_4$ host, small $NaYF_4$: 20% Gd^{3+}, 4% Tm^{3+} UCNCs (13.5 nm) are synthesized as the template core. The similar thickness of active shell ($NaYbF_4$: 4% Tm^{3+}; 3.35 nm) and the inert shell ($NaYF_4$; 1.55 nm thick) are used for a comparison experiment. Figure S12 shows the TEM images of template core, core−active shell, and template core−active shell−inert shell nanocrystals, with sizes of 13.5, 20.2, and 23.3 nm, respectively. As shown in Figure S13, the brightness of the single template core−active shell nanocrystals and the sandwich structured UCNCs have increased from 891 to 3730 counts. The similar sized monolithic UCNC (24.6 nm) shows emission intensity at 3516 counts. Compared to the Tb^{3+}-doped template cores, shown in Figure S14, the emission intensity increases with the volume of the active shell, i.e., the total number of Yb^{3+} ions in the active shell. This experiment confirms the Tb^{3+}-rich template core has a negligible influence on the upconversion emission of the $NaYbF_4$ active shell, as the size (volume) of the Tb^{3+} doped core nanocrystal (8.9 nm) is comparably small.

In conclusion, we find the optimal sensitizer concentration in single UCNCs is not limited by the "concentration quenching" effect as long as surface defects and interior defects can be minimized. Maximizing Yb^{3+} concentration to directly dope Tm^{3+} activator ions into the pure $NaYbF_4$ crystal host without the inert Y^{3+} ions can easily improve the brightness of UCNCs. Due to the smaller ionic radius and stronger electro negativity, the Yb^{3+} ions, having stronger binding energy to the F^- ions, result in the formation of larger nanocrystals. The high concentration of Yb^{3+} ions on the nanocrystal surface could significantly quench the overall brightness. To overcome both issues in the development of $NaYbF_4$-based UCNCs, a template

■ ACKNOWLEDGMENTS

We thank the Microscopy Unit at Macquarie University for the TEM characterization. This project is primarily supported by the Australian Research Council (ARC) Future Fellowship Scheme (FT 130100517; Dayong Jin), Macquarie University Research Fellowship Scheme (Xiaoxue Xu), China Scholarship Council CSC scholarships (Chenshuo Ma: No. 201408530049).

■ REFERENCES

(1) Chen, G.; Ågren, H.; Ohulchanskyy, T. Y.; Prasad, P. N. *Chem. Soc. Rev.* **2015**, *44*, 1680−1713.
(2) Chen, X.; Jin, L.; Kong, W.; Sun, T.; Zhang, W.; Liu, X.; Fan, J.; Yu, S. F.; Wang, F. *Nat. Commun.* **2016**, *7*, 10304.
(3) Haase, M.; Schäfer, H. *Angew. Chem., Int. Ed.* **2011**, *50*, 5808−5829.
(4) Zhou, B.; Shi, B.; Jin, D.; Liu, X. *Nat. Nanotechnol.* **2015**, *10*, 924−936.
(5) Anderson, R. B.; Smith, S. J.; May, P. S.; Berry, M. T. *J. Phys. Chem. Lett.* **2014**, *5*, 36−42.
(6) Zheng, W.; Huang, P.; Tu, D.; Ma, E.; Zhu, H.; Chen, X. *Chem. Soc. Rev.* **2015**, *44*, 1379−1415.
(7) Chen, G.; Shen, J.; Ohulchanskyy, T. Y.; Patel, N. J.; Kutikov, A.; Li, Z.; Song, J.; Pandey, R. K.; Ågren, H.; Prasad, P. N. *ACS Nano* **2012**, *6*, 8280−8287.
(8) Liu, Q.; Feng, W.; Li, F. *Coord. Chem. Rev.* **2014**, *273*−*274*, 100−110.
(9) Drees, C.; Raj, A. N.; Kurre, R.; Busch, K. B.; Haase, M.; Piehler, J. *Angew. Chem., Int. Ed.* **2016**, *55*, 11668−11672.
(10) He, S.; Krippes, K.; Ritz, S.; Chen, Z.; Best, A.; Butt, H.-J.; Mailänder, V.; Wu, S. *Chem. Commun.* **2015**, *51*, 431−434.
(11) Li, J.; Lee, W. Y.-W.; Wu, T.; Xu, J.; Zhang, K.; Wong, D. S. H.; Li, R.; Li, G.; Bian, L. *Biomaterials* **2016**, *110*, 1−10.

(29) Chen, G.; Ohulchanskyy, T. Y.; Kumar, R.; Ågren, H.; Prasad, P. N. *ACS Nano* **2010**, *4*, 3163−3168.
(30) Wang, J.; Deng, R.; MacDonald, M. A.; Chen, B.; Yuan, J.; Wang, F.; Chi, D.; Hor, T. S. A.; Zhang, P.; Liu, G. *Nat. Mater.* **2013**, *13*, 157−162.
(31) Chang, W.; Hölzer, P.; Travers, J.; Russell, P. S. J. *Opt. Lett.* **2013**, *38*, 2984−2987.
(32) Liu, Z.; Yang, B.; Chen, B.; He, M.; Hu, B. *Analyst* **2017**, *142*, 197−205.
(33) Zhao, J.; Lu, Z.; Yin, Y.; McRae, C.; Piper, J. A.; Dawes, J. M.; Jin, D.; Goldys, E. M. *Nanoscale* **2013**, *5*, 944−952.
(34) Misiak, M.; Prorok, K.; Cichy, B.; Bednarkiewicz, A.; STREK, W. *Opt. Mater.* **2013**, *35*, 1124−1128.
(35) MacDougall, S. K.; Ivaturi, A.; Marques-Hueso, J.; Krämer, K. W.; Richards, B. S. *Opt. Express* **2012**, *20*, A879−A887.
(36) Levy, E. S.; Tajon, C. A.; Bischof, T. S.; Iafrati, J.; Fernandez-Bravo, A.; Garfield, D. J.; Chamanzar, M.; Maharbiz, M. M.; Sohal, V. S.; Schuck, P. J. *ACS Nano* **2016**, *10*, 8423−8433.
(37) Chatterjee, D. K.; Rufaihah, A. J.; Zhang, Y. *Biomaterials* **2008**, *29*, 937−943.
(38) Patil, S.; Sandberg, A.; Heckert, E.; Self, W.; Seal, S. *Biomaterials* **2007**, *28*, 4600−4607.
(39) Damasco, J. A.; Chen, G.; Shao, W.; Agren, H.; Huang, H.; Song, W.; Lovell, J. F.; Prasad, P. N. *ACS Appl. Mater. Interfaces* **2014**, *6*, 13884−13893.
(40) Gargas, D. J.; Chan, E. M.; Ostrowski, A. D.; Aloni, S.; Altoe, M. V. P.; Barnard, E. S.; Sanii, B.; Urban, J. J.; Milliron, D. J.; Cohen, B. E. *Nat. Nanotechnol.* **2014**, *9*, 300−305.
(41) Ostrowski, A. D.; Chan, E. M.; Gargas, D. J.; Katz, E. M.; Han, G.; Schuck, P. J.; Milliron, D. J.; Cohen, B. E. *ACS Nano* **2012**, *6*, 2686−2692.
(42) Dou, Q.; Idris, N. M.; Zhang, Y. *Biomaterials* **2013**, *34*, 1722−1731.
(43) Shen, J.-W.; Wang, J.; Kong, D.; Yan, X.-P. *RSC Adv.* **2014**, *4*, 5088−5091.

Supporting information

Optimal Sensitizer Concentration in Single Upconversion Nanocrystals

Chenshuo Ma[†, ‡], Xiaoxue Xu[, ‡, §], Fan Wang,[*‡, §], Zhiguang Zhou[§], Deming Liu[§], Jiangbo Zhao[ǀ], Ming Guan[§], Candace I Lang[†], and Dayong Jin[*, ‡, §, ⊥]*

† Department of Engineering, Faculty of Science and Engineering, Macquarie University, Sydney, NSW, 2109, Australia

‡Advanced Cytometry Laboratories, ARC Centre of Excellence for Nanoscale BioPhotonics, Macquarie University, Sydney, NSW, 2109, Australia

§Institute for Biomedical Materials and Devices (IBMD), Faculty of Science, University of Technology Sydney, NSW, 2007, Australia

ǀInstitute for Photonics and Advanced Sensing (IPAS) and School of Physical Sciences, University of Adelaide, Adelaide, SA 5005, Australia

⊥ARC Research Hub for Integrated Device for End-user Analysis at Low-levels (IDEAL), Faculty of Science, University of Technology Sydney, NSW, 2007, Australia

*Email: dayong.jin@uts.edu.au.

*Email: fan.wang@uts.edu.au.

*Email: xiaoxue.xu@mq.edu.au.

EXPERIMENT:

1. Materials

$YCl_3 \cdot 6H_2O$ (99.99%), $YbCl_3 \cdot 6H_2O$ (99.99%), $TmCl_3 \cdot 6H_2O$ (99.99%), $GdCl_3 \cdot 6H_2O$ (99.99%), $TbCl_3 \cdot 6H_2O$ (99.99%), $LuCl_3 \cdot 6H_2O$ (99.99%), NH_4F (>98%), NaOH (>97%), oleic acid (OA, 90%), and 1-octadecene (ODE, 99%) were purchased from Sigma-Aldrich and used as received without further purification.

2. Synthesis of hexagonal-phase $NaYF_4$ nanocrystals:

$NaYF_4$ nanocrystals were synthesized using a typical method as previous work. Typically, methanol solution of 0.04 mmol $TmCl_3$, 0.96 mmol YCl_3 were mixed with 6 ml OA and 15 ml ODE in a 50 ml round bottom flask. The mixed solution was heated up to 150 ˚C for 30 min until it became clear. With gentle flow of argon gas through the reaction flask, the solution cooled slowly to room temperature. Methanol solution dissolved with 4 mmol NH_4F and 2.5 mmol NaOH was added into the flask with vigorous stirring for more than 30 min. Then, the mixed solution was heated up to 90 ˚C to evaporate methanol and to 150 ˚C to evaporate all the residual water. Finally, the solution was heated to 300 ˚C in an argon atmosphere and kept at this temperature for 90 min for complete reaction and crystal formation. After reaction and cooling down to room temperature, the synthesized nanocrystals were washed with cyclohexane/ethanol for several times and dispersed in cyclohexane for use. Other $NaYF_4$: 4% Tm^{3+}, *x*% Yb^{3+} (*x*= 20, 30, 45, 60), $NaYF_4$: 4% Tm^{3+}, 20% Yb^{3+}, *y*% Lu^{3+} (*y*= 10, 25, 40, 60), $NaYF_4$: 4% Tm^{3+}, *z*% Tb^{3+} (*z*= 20, 30, 45, 60), $NaYF_4$: 4% Tm^{3+}, 20% Gd^{3+} samples were synthesized as the same route using varied concentrations.

3. Synthesis of hexagonal phase core-shell structure and sandwich structure nanocrystals:

For the synthesis core-shell structure nanocrystals, typically, $NaYF_4$: 60% Tb^{3+}, 4% Tm^{3+} @ $NaYbF_4$: 4% Tm^{3+} nanocrystal. A modified hot-injection method was used for growing shells onto the core nanocrystals. 0.2 mmol $NaYF_4$: 60% Tb^{3+}, 4% Tm^{3+} nanocrystals were dispersed in cyclohexane and mixed with OA (3mL) and ODE (8mL) in a 50mL three-neck flask. The mixture was degassed under Ar flow and kept at 100 ˚C for 30 min to completely remove cyclohexane. Then heated up to 150 ˚C and kept at this temperature for 15 min to remove the any possible water. The mixture solution was quickly heated to 300˚C and $NaYbF_4$: 4% Tm^{3+} source solution was

injected to the core nanocrystals mixture solution using syringe. The injection rate is 0.05 ml/2 min. After the reaction, the precipitate was washed with cyclohexane/ethanol for several times and dispersed in cyclohexane for use. $NaYF_4$: 20% Gd^{3+}, 4% Tm^{3+} @ $NaYbF_4$: 4% Tm^{3+} nanocrystal samples were synthesized as the same route.

For the synthesis sandwich structure nanocrystals, typically, $NaYF_4$: 60% Tb^{3+}, 4% Tm^{3+} @ $NaYbF_4$: 4% Tm^{3+} @ $NaYF_4$ nanocrystal. The $NaYF_4$: 60% Tb^{3+}, 4% Tm^{3+} @ $NaYbF_4$: 4% Tm^{3+} nanocrystals were obtained, and further injection of more $NaYF_4$ source solution by using the same method. $NaYF_4$: 20% Gd^{3+}, 4% Tm^{3+} @ $NaYbF_4$: 4% Tm^{3+} @ $NaYF_4$ nanocrystal samples were synthesized as the same route.

4, Monodispersed single UCNPs samples

1, Place a drop of 50 µl Poly-L-lysine solution (0.1% w/v in H_2O) on a cleaned cover-glass and leave it for 30 mins before rinse it using water and dry the surface at room temperature.

2. Prepare 0.01 mg/ml UCNPs dispersion in cyclohexane, and place a drop of 20 µl UCNPs dispersion onto the cover-glass, then carefully rinse it using cyclohexane and let it dry naturally.

3. Make a drop of 20 µl Embedding Media on a glass slide, and then place the cover-glass onto the glass slide with Embedding media and squeeze out any air bubbles. Then dry the sample in an oven at 60 ˚C.

CHARACTERIZATIONS:

1. TEM Characterization:

The morphology of the synthesize nanocrystals was characterized using transmission electron microscopy (TEM) imaging (Philips CM10 TEM) with an operating voltage of 100 kV. The samples were prepared by placing a drop of a dilute suspension of nanocrystals onto the formvar-coated copper grids (300 meshes) and allowing it to dry in a desiccator at room temperature.

2. XRD Characterization:

Powder X-ray diffraction (XRD) patterns were obtained using a PANalyticalX'Pert Pro MPD X-ray diffractometer using Cu Kα1 radiation (40 kV, 40 mA, λ=0.15418 nm). The XRD samples were prepared by several drops of nanocrystal dispersions in cyclohexane cast on a zero-background silicon wafer.

3. Upconversion photoluminescence spectra by spectrofluorometer:

The upconversion luminescence spectra were obtained using of a Fluorolog-Tau3 spectrofluorometer (JobinYvon-Horiba) equipped with an external 980 nm CW diode laser with a pump power density of 500mW/cm^2. The upconversion nanocrystals were dispersed in the cyclohexane and were prepared to the concentration of 1 mg/ml normalized to the same Tm^{3+} concentration by the subtractive weighting method and inductively coupled plasma mass spectrometry (ICP-MS, Agilent 7500cx ICP-Quadrupole Mass Spectrometer) for the entire specimen. The dispersion was transferred to quartz cuvettes with 10 mm path length and three measurements were conducted for each sample.

4. Photoluminescence characterization of single UCNPs using Scanning Confocal Microscopy:

We built a stage-scan confocal microscope for the intensity measurement of single UCNPs as shown in Figure S9. The excitation source is a 980 nm single mode polarized laser (power density of 30MW/cm^2) which is focused onto the sample through a 100x objective lens (NA 1.4). The emission from sample is collected by the same objective lens and refocused into an optical fiber which has a core size matching with system Airy disk. A Single Photon Counting Avalanche Diode (SPAD) detector is connected to the collection optical fiber to detect the emission intensity. The scanning is achieved by moving the 3D piezo stage.

During the point by point scanning process, when the excitation laser beam moves closer to a single nanocrystal, the system will detect a brighter emission intensity. Therefore each of single nanocrystal will present a Gaussian spot in the confocal scanning microscope image. The maximum brightness value (photon count) of each Gaussian spot can be used to represent the brightness of that single particle. For each confocal image, we record all of the single nanocrystals' brightness values (photon counts). For each batch of samples, we average more than 15 single nanocrystals' values to give a mean brightness with standard deviation as error bars.

SUPPORTING RESULTS

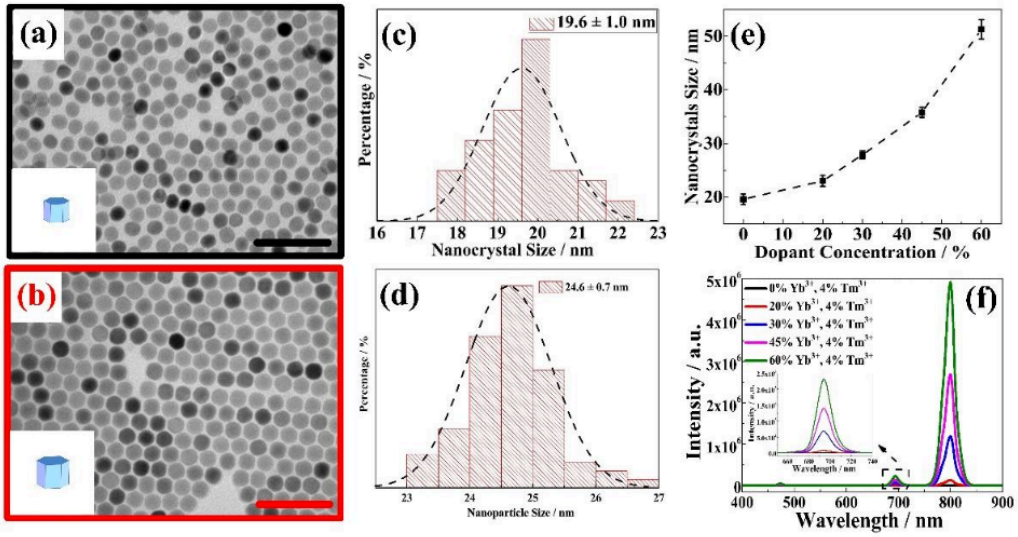

Figure S1.TEM images for $NaYF_4$: 4% Tm^{3+}, *x*% Yb^{3+} nanocrystals (a) *x*=0, (b) *x*=20 and crystal size distribution histograms corresponding to TEM images with (c) 19.6 ± 1.0 nm and (d) 24.6 ± 0.7 nm, respectively, the scale bar is 100 nm. Histograms of the crystals sizes are drawn from analysis of >150 crystals for each sample. (e) point-line curve about the relation between Yb^{3+} doping concentration and nanocrystals size, Yb^{3+}= 0%, 20%, 30%, 45%, 60%. (f) Fluorolog spectrometer measurement of $NaYF_4$: 4% Tm^{3+}, *x*% Yb^{3+} (*x*= 0, 20, 30, 45, 60).

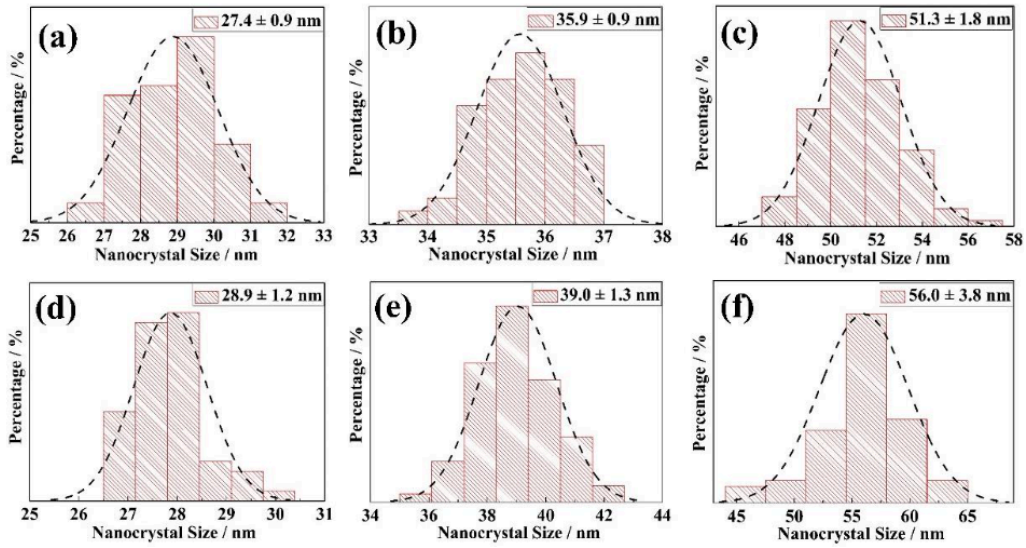

Figure S2. The nanocrystal size distribution histograms corresponding to TEM images in Figure 1a-f, respectively. Histograms of the crystals sizes are drawn from analysis of >150 crystals for each sample. The mean and standard deviation for each monocrystalline diameter are (a) 27.4 ± 0.9 nm; (b) 35.9 ± 0.9 nm; (c) 51.3 ± 1.8 nm; (d) 28.9 ± 1.2 nm; (e) 39.0 ± 1.3 nm; (f) 56.0 ± 3.8 nm, respectively.

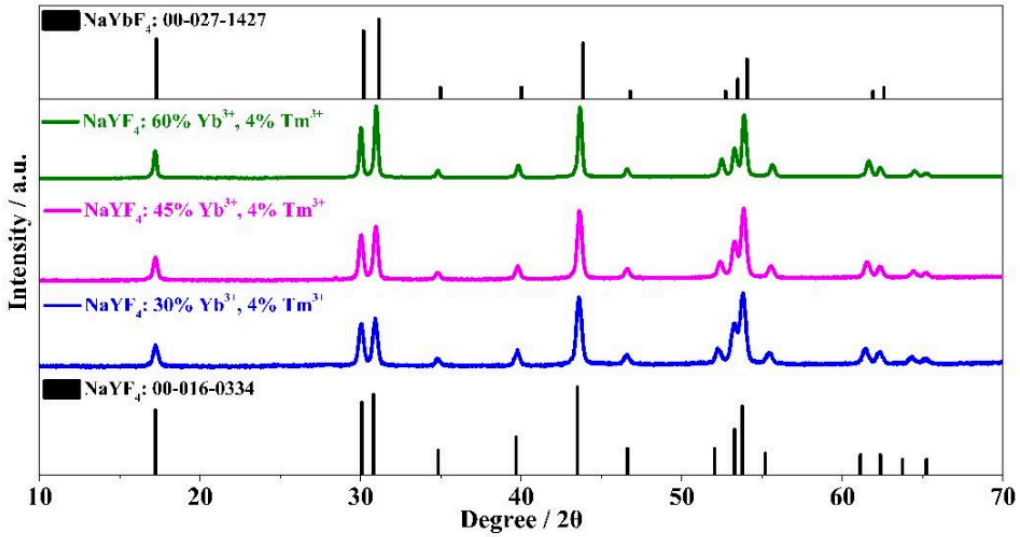

Figure S3. The XRD patterns of $NaYF_4$ nanocrystals co-doped with 4% Tm^{3+} and various concentration of Yb^{3+} ions of 30%, 45% and 60%, respectively, with the standard XRD patterns of hexagonal phase $NaYF_4$ (JCPDS: 00-016-0334) and $NaYbF_4$ (JCPDS: 00-027-1427).

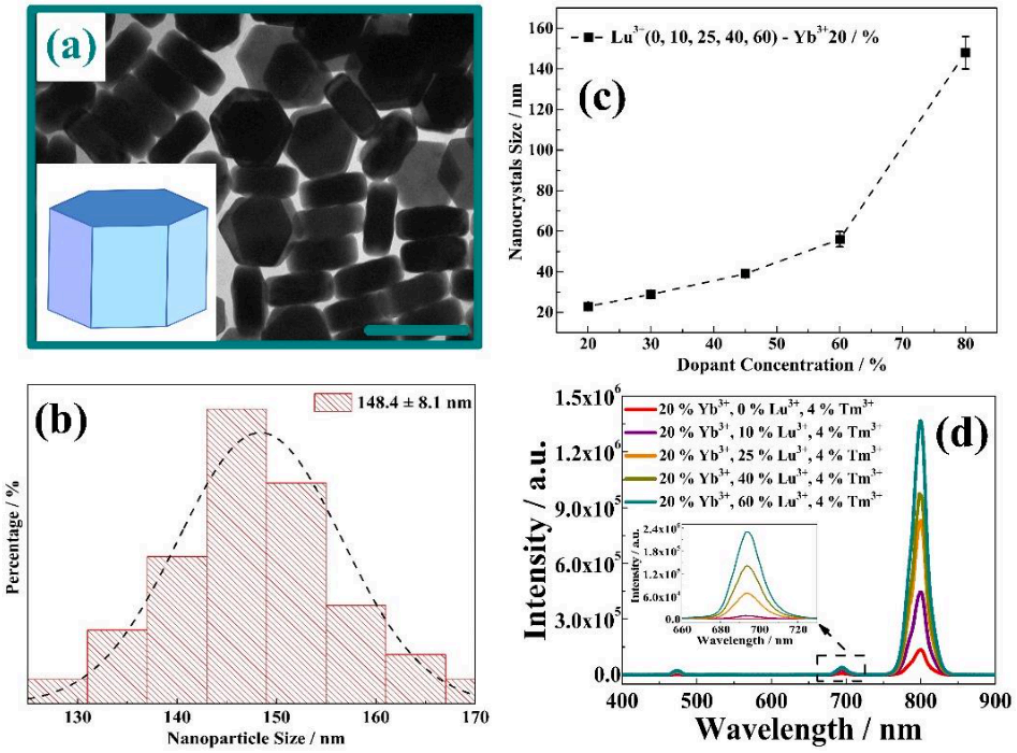

Figure S4. TEM images for (a) $NaYF_4$: 4% Tm^{3+}, 20% Yb^{3+}, 60% Lu^{3+} nanocrystals and crystal size distribution histograms corresponding to TEM images with (b) 148.4 ± 8.1 nm, scale bar is 200 nm. Histograms of the crystals sizes are drawn from analysis of >150 crystals for each sample. (c) point-line curve about the relation between Lu^{3+} doping concentration (Lu^{3+}= 0, 10, 25, 40, 60) and nanocrystals size. (d) Fluorolog spectrometer measurement of $NaYF_4$: 4% Tm^{3+}, 20% Yb^{3+}, *y*% Lu^{3+} (*y*=0, 10, 25, 40, 60).

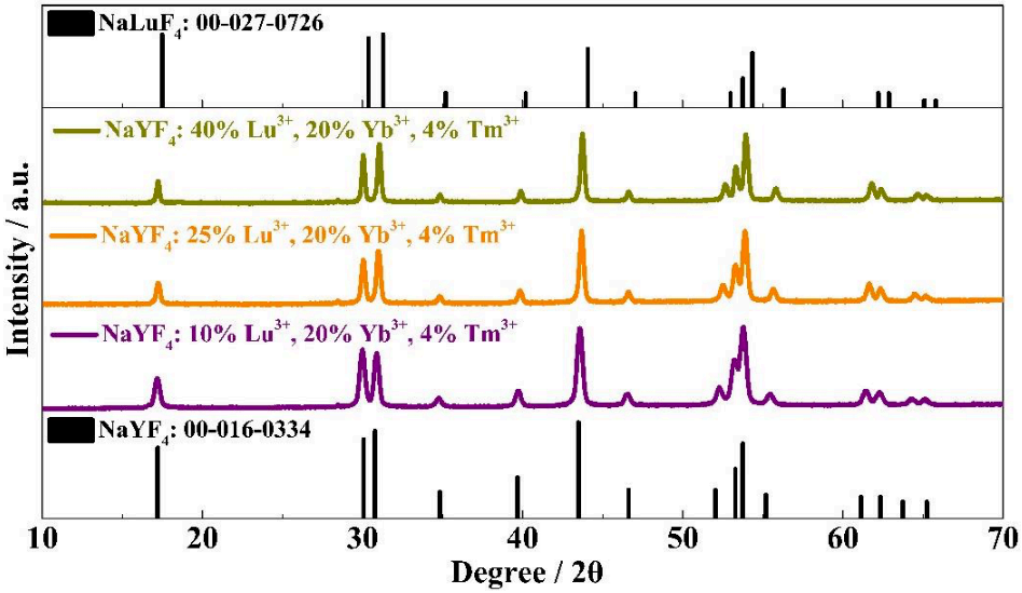

Figure S5. The XRD patterns of $NaYF_4$ nanocrystals co-doped with 4% Tm^{3+}, 20% Yb^{3+} and various concentration of Lu^{3+} ions of 10%, 25% and 40%, respectively, with the standard XRD patterns of hexagonal phase $NaYF_4$ (JCPDS: 00-016-0334) and $NaLuF_4$ (JCPDS: 00-027-0726).

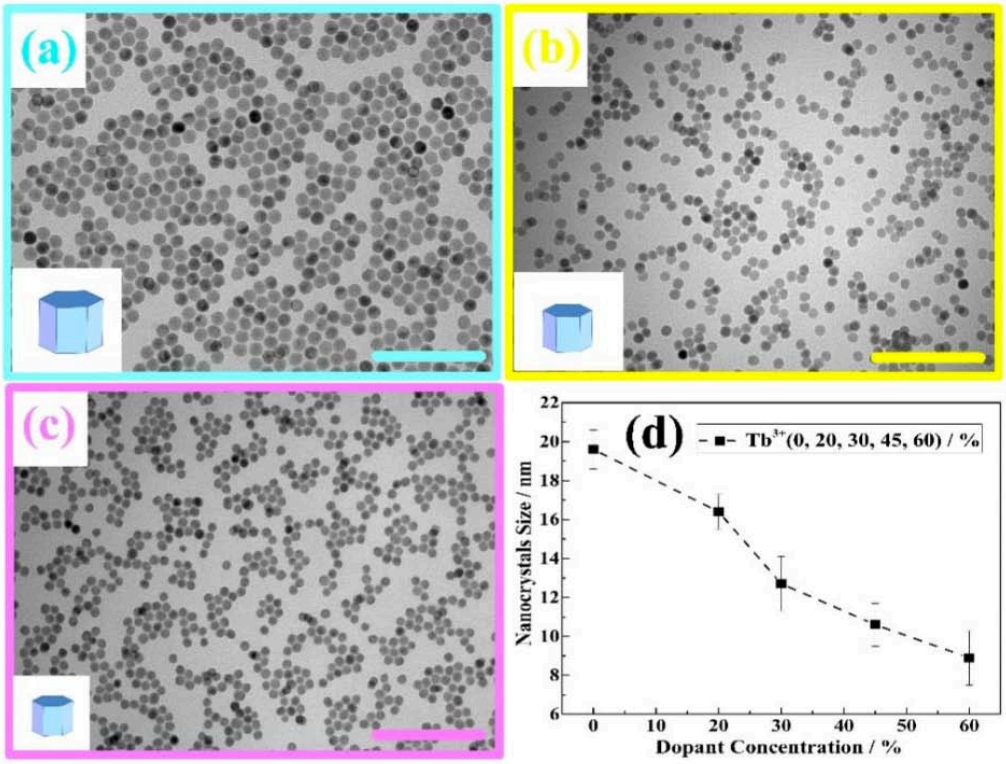

Figure S6. TEM images of different Tb^{3+} concentration β-$NaYF_4$: z% Tb^{3+}, 4% Tm^{3+} (z= 20, 30, 45) nanocrystals (a) x=20, (b) x=30, (c) x=45, scale bar is 100 nm, and (d) point-line curve about the relation between Tb^{3+} doping concentration (Tb^{3+}= 0%, 20%, 30%, 45%, 60%) and nanocrystals size.

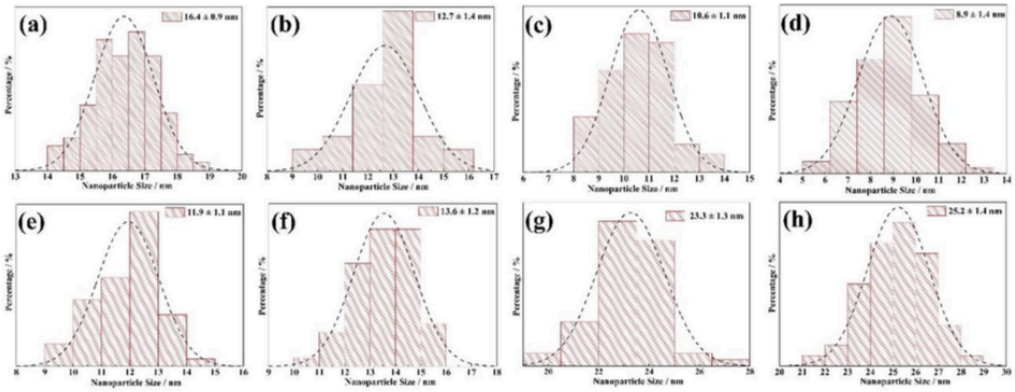

Figure S7. The size distribution histograms of β-$NaYF_4$: x% Tb^{3+}, 4% Tm^{3+} UCNPs corresponding to TEM images in Figure S6a-c for (a) 16.4 ± 0.9 nm; (b) 12.7 ± 1.4 nm; (c) 10.6 ± 1.1 nm, respectively, and Figure 3a for (d) 8.9 ± 1.4 nm. Figure 4b and c for (e) 11.9 ± 1.1 nm, (f) 13.6 ± 1.2 nm; Figure 4e and 4f for (g) 23.3 ± 1.3 nm and (h) 25.2 ± 1.4 nm, respectively. Histograms of the crystals sizes are drawn from analysis of >150 crystals for each sample.

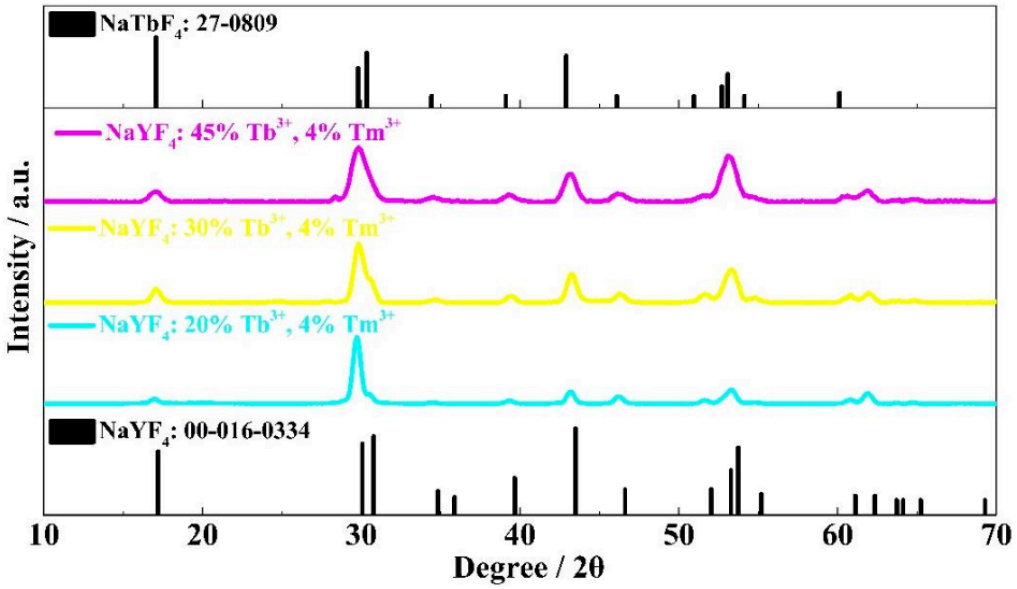

Figure S8. The XRD patterns of $NaYF_4$ nanocrystals co-doped with 4% $Tm^{3+}$and various concentration of Tb^{3+} ions of 20%, 30% and 45%, respectively, with the standard XRD patterns of hexagonal phase $NaYF_4$ (JCPDS: 00-016-0334) and $NaTbF_4$ (JCPDS: 27-0809).

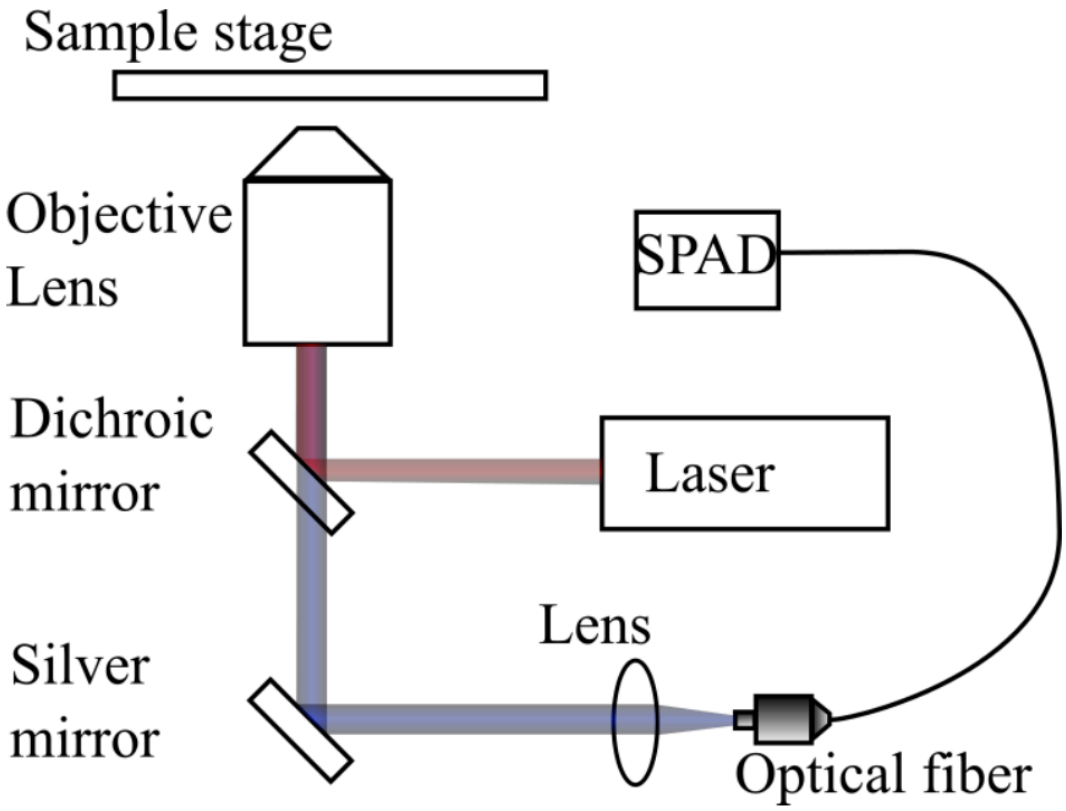

Figure S9. Schematic illustration of the system setup for customized scanning confocal microscope.

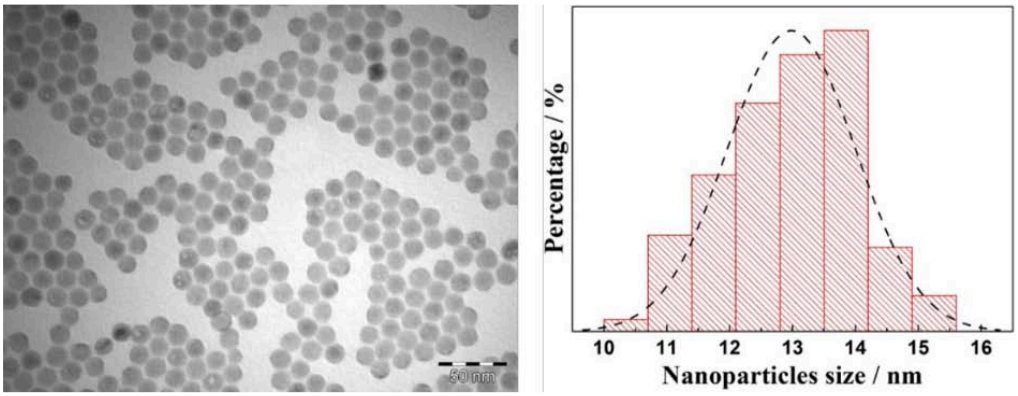

Figure S10. TEM images of β-$NaYF_4$: 20% Yb^{3+}, 4% Tm^{3+} and the size distribution histograms of it corresponding to TEM image, nanocrystals size is 13.0 ± 1.0 nm, scale bar is 50 nm. Histograms of the crystals sizes are drawn from analysis of >150 crystals for the sample.

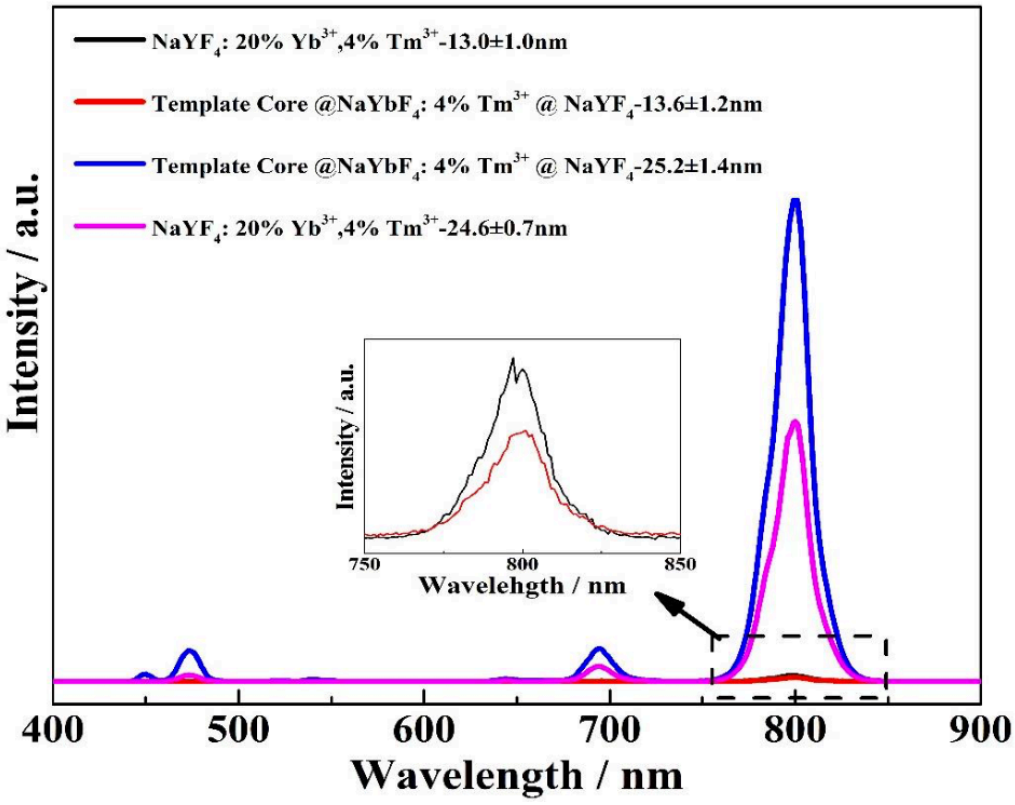

Figure S11. Fluorolog spectrometer measurement of nanocrystals template core @ $NaYbF_4$: 4% Tm^{3+} and template core @ $NaYbF_4$: 4% Tm^{3+} @ $NaYF_4$ structure with different size, and the similar size with $NaYF_4$: 20% Yb^{3+}, 4% Tm^{3+}, respectively.

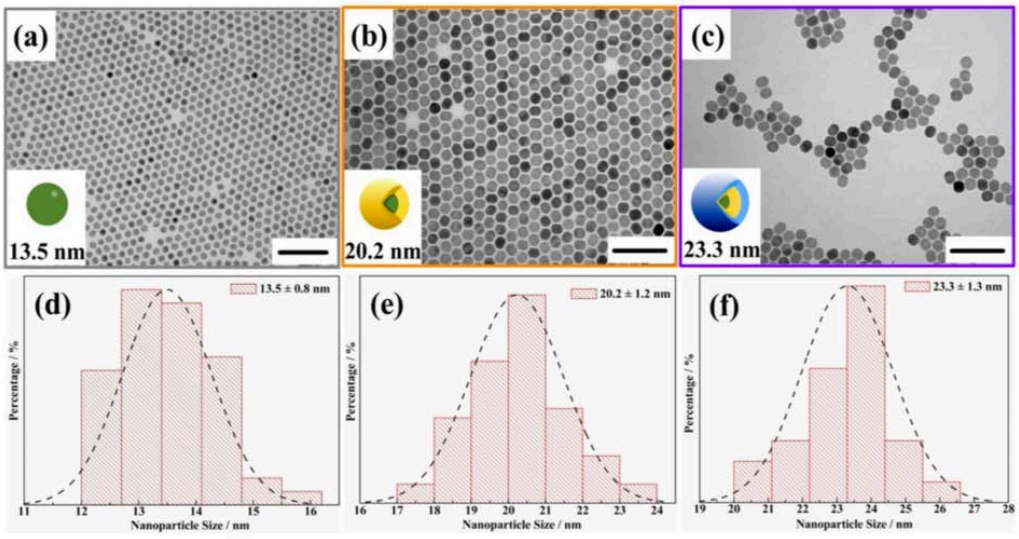

Figure S12. TEM images of (a) template core nanocrystals of $NaYF_4$: 20% Gd^{3+}, 4% Tm^{3+} with the size of 13.5 nm,(b) template core @ active shell nanostructure of $NaYF_4$: 20% Gd^{3+}, 4% Tm^{3+} @ $NaYbF_4$: 4% Tm^{3+} with size of 20.2 nm, (c) template core @ active shell @ inert shell nanostructure of $NaYF_4$: 20% Gd^{3+}, 4% Tm^{3+} @ $NaYbF_4$: 4% Tm^{3+} @ $NaYF_4$ with the size of 23.3 nm, scale bar is 100 nm. (d-f) are the size distribution histograms of their corresponding to TEM images (a-c), respectively. Histograms of the crystals sizes are drawn from analysis of >150 crystals for each sample.

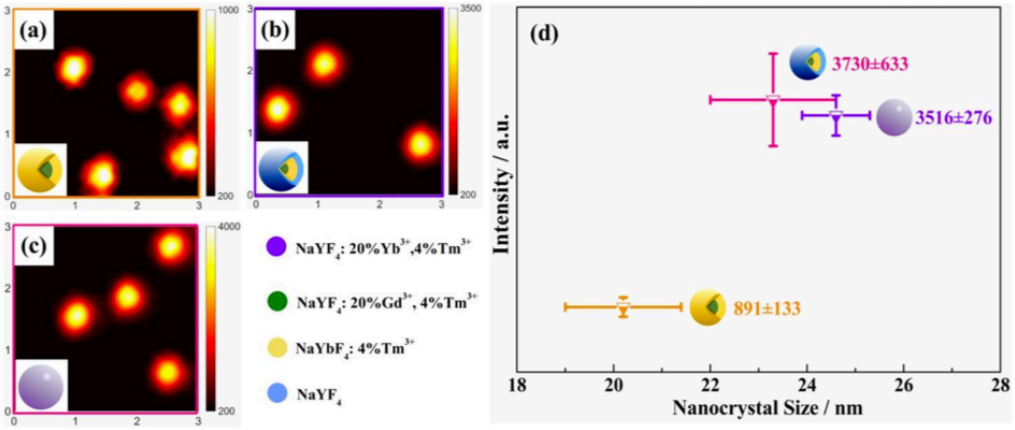

Figure S13. Confocal microscopy quantitative measurement of the whole spectrum emission for single UCNCs: (a) UCNCs of $NaYF_4$: 20% Gd^{3+}, 4% Tm^{3+} core @ active shell of $NaYbF_4$: 4% Tm^{3+} with the size of 20.2 nm, (b) UCNCs of $NaYF_4$: 20% Gd^{3+}, 4% Tm^{3+} core @ active shell of $NaYbF_4$: 4% Tm^{3+} @ inert shell of $NaYF_4$ with the size of 23.2 nm, (c) monolithic UCNCs of $NaYF_4$: 20% Yb^{3+}, 4% Tm^{3+} in size of 24.6 nm, (d) quantitative analysis of the whole spectrum emission intensities for single UCNCs corresponding to (a-c).

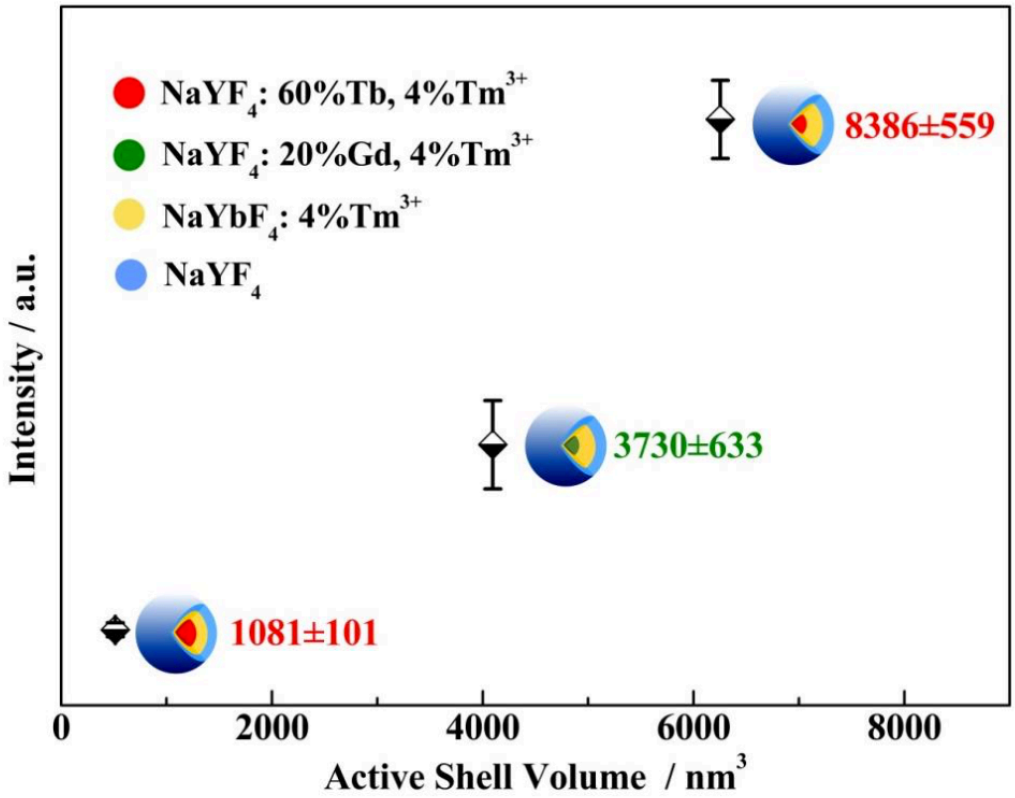

Figure S14. The whole spectrum emission intensities of single UCNCs with different design of sandwich nanostructures show a linear trend following the total volume of active shells.

4.3 Remarks on Paper 2

This work reported on the concentration quenching effect and demonstrated surprisingly that it was not limited by the concentration of the sensitizer under high excitation laser power. Novel sandwich nanostructure play an important role in synthesis nanocrystals which not only have small size but also have high upconversion luminescence. The single nanocrystal luminescence measurement provides evidence that maximizing the sensitizer concentration may accelerate the development of highly efficient probes or converters for application as biological probes and for use in photon energy conversion.

REFERENCE

(1) Mahalingam, V.; Hazra, C.; Naccache, R.; Vetrone, F.; Capobianco, J. A. Enhancing the Color Purity of the Green Upconversion Emission from Er^{3+}/Yb^{3+}-Doped $GdVO_4$ Nanocrystals via Tuning of the Sensitizer Concentration. *J. Mater. Chem. C* **2013**, *1*, 6536–6540.

(2) Xiang, G.; Zhang, J.; Hao, Z.; Zhang, X.; Pan, G.; Luo, Y.; Lü, S.; Zhao, H. The Energy Transfer Mechanism in Pr^{3+} and Yb^{3+} Codoped β-$NaLuF_4$ Nanocrystals. *Phys. Chem. Chem. Phys.* **2014**, *16*, 9289–9293.

(3) Zhao, J.; Jin, D.; Schartner, E. P.; Lu, Y.; Liu, Y.; Zvyagin, A. V; Zhang, L.; Dawes, J. M.; Xi, P.; Piper, J. a; *et al.* Single-Nanocrystal Sensitivity Achieved by Enhanced Upconversion Luminescence. *Nat. Nanotechnol.* **2013**, *8*, 729–734.

(4) Hao, S.; Shao, W.; Qiu, H.; Shang, Y.; Fan, R.; Guo, X.; Zhao, L.; Chen, G.; Yang, C. Tuning the Size and Upconversion Emission of $NaYF_4$: Yb^{3+}/Pr^{3+} Nanoparticles through Yb^{3+} Doping. *RSC Adv.* **2014**, *4*, 56302–56306.

(5) Wang, F.; Han, Y.; Lim, C. S.; Lu, Y.; Wang, J.; Xu, J.; Chen, H.; Zhang, C.; Hong, M.; Liu, X. Simultaneous Phase and Size Control of Upconversion Nanocrystals through Lanthanide Doping. *Nature* **2010**, *463*, 1061–1065.

CHAPTER 5

Uniformity and Application of UCNCs in Enhancing Super Resolution Nanoscopy

The research in this chapter was developed to study the uniformity of UCNCs and its application, typically on super resolution nanoscopy.

As shown in our previous research in chapter 4, doping is one of the keys to designing of UCNCs for higher luminescence (paper 2). No matter which dopant ratio of the emitter and sensitizer ions is used, it was often assumed that the dopants of sensitizer and activator ions were fabricated with a uniform distribution in their $NaREF_4$ host matrix[1–4]. But the actual distribution instead of the rare earth ions were found to not be clearly uniform. In paper 3, we employed both synchrotron-based XPS measurements and energy dispersive X-ray spectroscopy with electron microscopy to study the distribution of sensitizer ions within $NaYF_4$ nanocrystals. This work is presented in the form of a journal publication from ***Nanoscale***.

As our previous research in chapter 3 shows, defects within nanocrystals can influence the upconversion luminescence. Due to the sensitizer ions, distribution trends are the same under the same doping concentration no matter what the size is (paper 3), and I have shown that carefully controlling the synthesis conditions can minimize internal defects as well (paper 1). The smaller and brighter UCNCs can be used in super resolution nanoscopy. In paper 4, I use the same synthesis to achieve highly doped Tm^{3+} UCNCs; these exhibit good optical properties by using low power super resolution stimulated emission depletion microscopy, achieving nanoscale optical resolution of 28 nanometres. This work is presented in the form of a journal publication from ***Nature***.

5.1 Contribution to Paper 3

The author contribution for paper "Depth-profiling of Yb^{3+} sensitizer ions in $NaYF_4$ upconversion nanoparticles" are shown in **Table 5.1**.

Table 5.1 Author contribution summary for paper 3

Name	Experiment Design	Material Synthesis	Data Collection	Analysis	Figures and Tables	Manuscript
Xiaoxue Xu			√	√	√	√
Christian Clarke			√	√		
Chenshuo Ma	√	√	√			
Gilberto Casillas Garcia			√	√		
Minakshi Das				√		
Ming Guan			√	√	√	
Deming Liu				√		
Li Wang			√			
Anton Tadich			√			
Yi Du			√			
Cuong Ton-That						√
Dayong Jin						√

In this work, I carried out the majority of experimental work for experiment design and sample synthesis. I did some of the material measurement and part of the manuscript modification as well.

5.2 Paper 3

Xiaoxue Xu, Christian Clarke, **Chenshuo Ma**, Gilberto Casillas Garcia, Minakshi Das, Ming Guan, Deming Liu, Li Wang, Anton Tadich, Yi Du, Cuong Ton-That, and Dayong Jin, "Depth-profiling of Yb^{3+} sensitizer ions in $NaYF_4$ upconversion nanoparticles", ***Nanoscale***. 2017, 9, 7719-7726.

Nanoscale

COMMUNICATION

View Article Online
View Journal | View Issue

Cite this: *Nanoscale*, 2017, **9**, 7719

Received 28th February 2017,
Accepted 5th May 2017

DOI: 10.1039/c7nr01456b

rsc.li/nanoscale

Depth-profiling of Yb^{3+} sensitizer ions in $NaYF_4$ upconversion nanoparticles†

Xiaoxue Xu, *[a,b,c] Christian Clarke,[c] Chenshuo Ma,[b,d] Gilberto Casillas,[e] Minakshi Das,[a,b] Ming Guan,[c] Deming Liu,[b,c] Li Wang,[f] Anton Tadich,[g] Yi Du,[f] Cuong Ton-That*[c] and Dayong Jin [c,h]

Enhancing the efficiency of upconversion nanoparticles (UCNPs) and therefore their brightness is the critical goal for this emerging material to meet growing demands in many potential applications including sensing, imaging, solar energy conversion and photonics. The distribution of the photon sensitizer and activator ions that form a network of energy transfer systems within each single UCNP is vital for understanding and optimizing their optical properties. Here we employ synchrotron-based X-ray Photoelectron Spectroscopy (XPS) to characterize the depth distribution of Yb^{3+} sensitizer ions in host $NaYF_4$ nanoparticles and systematically correlate the structure with the optical properties for a range of UCNPs with different sizes and doping concentrations. We find a

1. Introduction

Doping is the key to the design of new materials to access untapped properties.[1,2] Lanthanide-doped upconversion nanoparticles (UCNPs), as a typical doped nanoparticle material, have attracted a great deal of attention in a wide range of applications,[3] such as sensing,[4–6] bio-imaging,[7,8] drug delivery,[9,10] cancer therapy,[11] anti-counterfeiting,[12,13] photovoltaic devices,[14] 3-D volumetric displays[15,16] and the recently discovered super resolution nanoscopy applications.[17] By introducing thousands of photon sensitizers (*i.e.*, Yb^{3+} ions) and activators ions (*i.e.*, Tm^{3+} and Er^{3+}) to form an energy-transfer

owing to the quenching of the emission by surface defects, impurities, ligands and solvents.[29–31] The decreased distance of the activators in the host nanoparticles due to increasing doping concentrations could induce self-quenching from cross-relaxation mechanisms[25,32,33] and amplified stimulated emissions.[17] It has also been reported that the heterogeneous distribution of Yb^{3+} within the host nanoparticles deteriorates the optical properties including the emission brightness and decay lifetime.[34]

It has often been assumed that the dopants of sensitizer and activator ions are uniformly distributed in the $NaREF_4$ host crystals mainly due to the similarity among the rare earth ions, but minor differences in the ionic radius and the electronic polarity could cause different local distributions across a single nanoparticle. van Veggel and co-workers have reported a non-uniform distribution of Y^{3+}, Nd^{3+} and Tb^{3+} in a $NaGdF_4$ matrix, due to the difference in the ionic radius of the dopants and that of Gd^{3+}.[35] Additionally, they were able to identify two distinct chemical environments of Y at the surface and interior of the $NaYF_4$ nanoparticles[36] and also provided evidence for the core–shell structure of $NaYF_4/NaGdF_4$ [37] and LaF_3/GdF_3 [38] using excitation energy-dependent X-ray photoelectron spectroscopy (XPS). Zhang *et al.*[34] confirmed the heterogeneous distribution of Yb^{3+} in $NaGdF_4$ nanoparticles using energy dispersive X-ray spectroscopy (EDX) and inductively coupled plasma mass/atomic emission spectrometry (ICP-MS/AES), whilst Yan and co-workers found that the lattice parameters as well as the coordination number and the local symmetry of rare earth ions within the $NaY/GdF_4:Yb^{3+},Er^{3+}$ nanoparticles

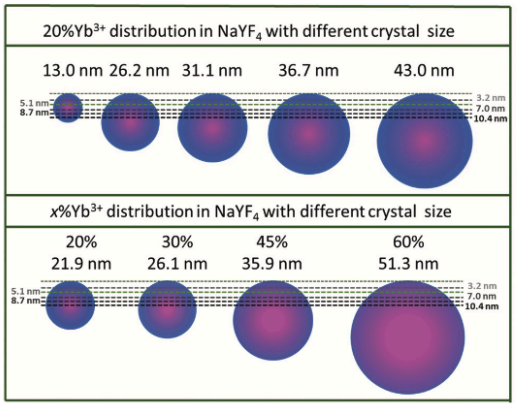

Fig. 1 Diagram of the proposed Yb^{3+} distribution within $NaYF_4$ nanoparticles as a function of nanoparticle size and doping concentration. The Yb^{3+} distribution within the $NaYF_4$ nanoparticle can be measured by the ratio of Yb^{3+}/Y^{3+} as a function of depth using the depth resolved XPS with an energy tuneable excitation synchrotron source. The dashed lines indicate the range of XPS sampling depths relative to the UCNP sizes used in this work.

shell-like nanostructure formed during the synthesis, the surface quenching effect would be minimized especially for the smaller nanoparticles. On the other hand, when the doping concentration of the Yb^{3+} ions increases in each UCNP, the Yb^{3+} ions would distribute in the same way of decreasing

hexahydrate ($TmCl_3 \cdot 6H_2O$, 99.9%), sodium hydroxide (NaOH, 98%), ammonium fluoride (NH_4F, 99.99%), oleic acid (OA, 90%), and 1-octadecene (ODE, 90%) were purchased from Sigma-Aldrich. All reagents were used as received without further purification.

2.2 Synthesis of $NaYF_4$:20%Yb^{3+},4%Tm^{3+} UCNPs with different sizes and UCNPs with different Yb^{3+} concentrations

A modified synthesis method was adopted to prepare β-$NaYF_4$:20%Yb^{3+},4%Tm^{3+} UCNPs.[41] The UCNPs with different sizes were synthesized *via* the following procedure. A methanol solution of 0.04 mmol $TmCl_3$, 0.2 mmol $YbCl_3$, and 0.76 mmol YCl_3 was mixed with 6 ml OA and 15 ml ODE in a 50 ml round bottom flask. The mixed solution was degassed under an Ar flow, slowly heated up to 150 °C and kept isothermally for 30 min to form a clear solution. Then the solution was cooled down to room temperature, the methanol solution was dissolved with 4.0 mmol NH_4F and 2.5 mmol NaOH was added into the flask followed by vigorous stirring for 30 min. Again under an argon atmosphere, the mixed solution was slowly heated up to 110 °C to evaporate all methanol and to 150 °C to evaporate all the residual water. Finally, the solution was heated up to 300 °C with different heating up profiles by controlling the heating time duration for 21 min, 17 min, 12 min, 9.3 min and 8 min. Once 300 °C was reached, the reaction solution was kept at this temperature for another 90 min. Then the reaction was stopped and the solution was cooled down to room temperature. The UCNPs with different sensitizer concentrations were synthesized with an adjusted $YbCl_3$ intensity was determined with the area ratio of Y and Yb plotted against photoelectron kinetic energy. The inelastic electron mean free path of the photoelectrons was calculated using the QUASES-IMFP-TPP2 M Ver.3.0 software.

2.5 Energy dispersive X-ray spectroscopy

Element mapping images were collected with an aberration-corrected analytical transmission electron microscope (TEM, JEOL ARM-200F) equipped with a Centurio SSD energy-dispersive X-ray spectroscopy (EDS) detector set at 77 K. The TEM was operated at 80 kV. The line profiles were processed with the LOWESS smoothing algorithm as implemented in OriginPro.

2.6 Inductively coupled plasma mass spectrometry

The doping concentrations were determined by inductively coupled plasma mass spectrometry (ICP1-MS) using an Agilent 7500cx ICP-Quadrupole Mass Spectrometer.

3. Results and discussion

Fig. 2 shows the morphology of the $NaYF_4$:Yb^{3+},Tm^{3+} nanoparticles with different sizes induced by controlling the heating rate for the formation of UCNPs[40] or by varying the doping concentration of Yb^{3+}.[24] The doping concentration of Tm^{3+} was kept the same at 4% for all the samples, so in this work the samples will be denoted as $NaYF_4$:Yb^{3+}. Fig. 2(a–e) show the $NaYF_4$:20%Yb^{3+} upconversion nanoparticles with

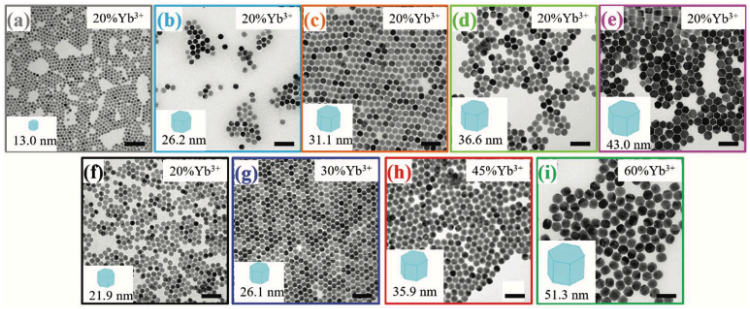

Fig. 2 TEM images of upconversion nanoparticles with different sizes and Yb^{3+} doping concentrations: (a–e) $NaYF_4$:20%Yb^{3+},4%Tm^{3+} upconversion nanoparticles with the sizes of 13.0 nm, 26.2 nm, 31.1 nm, 36.6 nm, and 43.0 nm respectively and (e–i) $NaYF_4$:*x*%Yb^{3+},4%Tm^{3+} upconversion nanoparticles with *x* = 20%, 30%, 45% and 60% and in the size of 21.9 nm, 26.1 nm, 35.9 nm and 51.3 nm respectively. The scale bar is 100 nm.

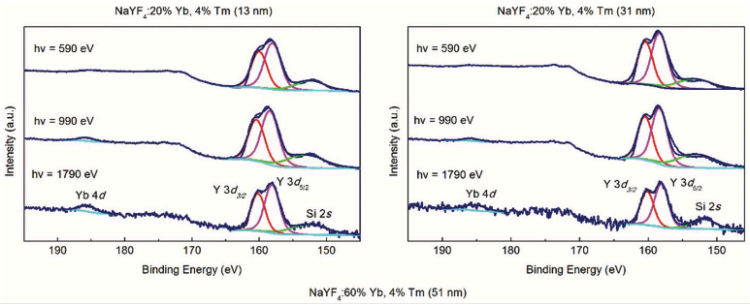

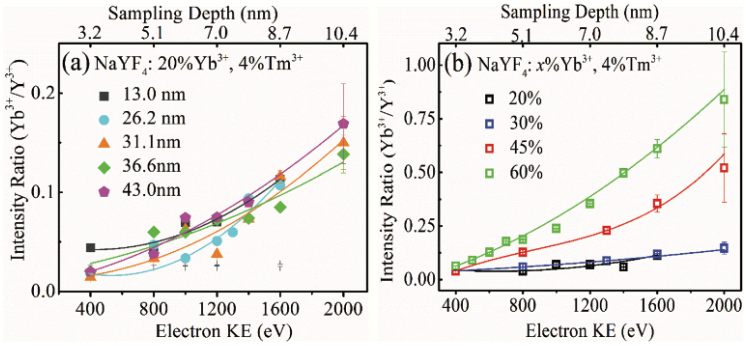

Fig. 4 Increasing Yb^{3+}/Y^{3+} atomic ratio within UCNPs with increasing photon energy/sampling depth is shown in (a) $NaYF_4$:20%Yb^{3+} nanoparticles with the sizes of 13.0 nm, 26.2 nm, 31.1 nm, 36.6 nm and 43.0 nm, and (b) $NaYF_4$ nanoparticles containing 20% Yb^{3+}, 30%Yb^{3+}, 45%Yb^{3+}, and 60%Yb^{3+} with the sizes of 21.9 nm, 26.1 nm, 35.9 nm and 51.3 nm, respectively.

Yb^{3+} doped $NaYF_4$ nanoparticles although the size varies from 13.0 nm to 43.0 nm, indicating that 20%Yb^{3+} is more concentrated in the crystal interior and gradually decreases from the centre to the surface. Since the uptrend slopes are similar, the distribution gradient from the centre to the surface should be the same for the nanoparticles with different sizes due to 20% Yb^{3+} being proportional to the volume of the nanoparticles. It is notable that the intensity ratio of Yb 4d and Y 3d at 3.2 nm sampling depth for the UNCPs of the size of 13.0 nm is higher than other sized nanoparticles. Because Yb^{3+} is more concentroscopy (ICP-MS) and STEM-EDS. ICP-MS was used to quantitatively characterize the composition of UCNPs. Table S1† lists the measured compositions of Y^{3+}, Yb^{3+}, and Tm^{3+} which are quite close to the designed values for all batches of UCNPs.

The constitution of UCNPs in terms of mainly Y^{3+} and Yb^{3+} was characterized using EDX as shown in Fig. 5, which shows the original HAADF image, the Y and Yb elemental map images, and the merged image of the three. Fig. 5(a and b) show the elemental maps of $NaYF_4$:20%Yb^{3+},4%Tm^{3+} with sizes of 31.1 nm and 43.0 nm. It can be seen that both Y and

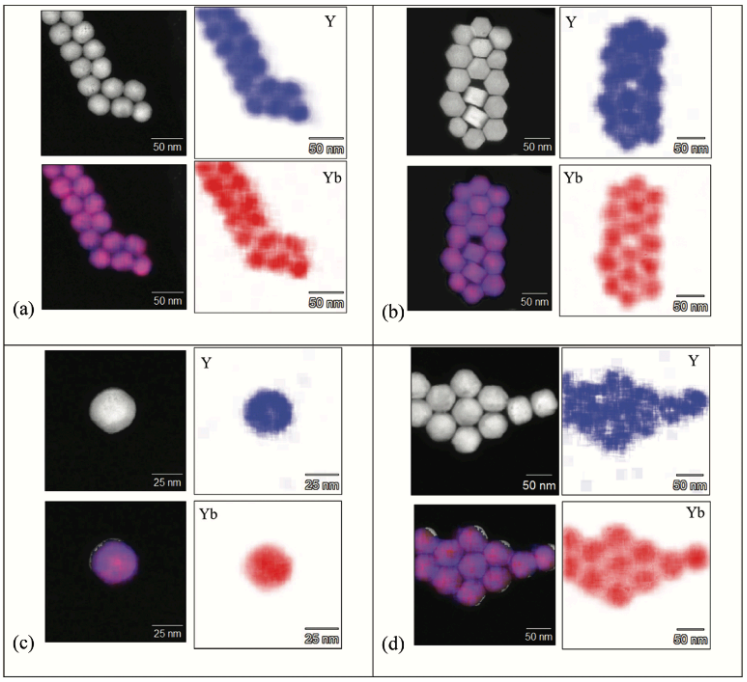

Fig. 5 Elemental maps of the (a) $NaYF_4$:20%Yb^{3+},4%Tm^{3+} with the size of 31.1 nm, (b) $NaYF_4$:20%Yb^{3+},4%Tm^{3+} with the size of 43.0 nm, (c) $NaYF_4$:45%Yb^{3+},4%Tm^{3+} with the size of 36.7 nm, and (d) $NaYF_4$:60%Yb^{3+},4%Tm^{3+} with the size of 51.3 nm.

dency of Yb^{3+} within the UCNPs. Compared to synchrotron based XPS with a varying photon energy, EDS possesses not only general accessibility, individual UCNP analysis, and less analysis time, but also less surface sensitivity and sample instability from the electron beam. Nevertheless, the consistent results from these two advanced characterization methods confirm the hypothesis we proposed in Fig. 1 for the sensitizer distribution within the UCNPs and it will deepen our understanding of the upconversion properties.

The highly concentrated distribution of sensitizer Yb^{3+} within the core of the host $NaYF_4$ nanoparticles could improve the upconversion luminescence properties. The optical intensities of single UCNPs from different batches of synthesis, measured by using a purpose-built confocal microscope, were compared in our previous work.[24,40] The emission intensity of the UCNPs increased with the nanoparticle size; however, the upconversion efficiency, which was normalized to the same activator number, was 820 counts, 554 counts, 605 counts, 469 counts and 401 counts for the UNCPs with 20%Yb^{3+} with the sizes of 13.0 nm, 26.2 nm, 31.1 nm, 36.6 nm and 43.0 nm, respectively. The Yb^{3+} distribution unravelled in the present work shows the formation of a Yb^{3+}-rich core and Yb^{3+}-depleted shell, which will minimize the surface quenching effect by reducing the energy loss from the interactions between sensitizer Yb^{3+} and surface defects, impurities, ligands and solvents.[29] This structure especially benefits the smaller UCNPs due to their high surface to volume ratio. UCNPs with the size of 13.0 nm exhibit higher emission efficiency (the intensity normalized to the number of activator ions) than tributed in a radial gradient manner from the centre to the surface of the UCNPs. As long as the doping concentration was kept the same, the Yb^{3+} distribution pattern for each nanoparticle was the same regardless of the nanoparticle size. As the doping concentration is increased, the Yb^{3+} concentrated centre area becomes larger. This heterogeneous distribution pattern does favour the emission intensity of UCNPs with a high concentration of Yb^{3+} sensitizer ions in the core region and less sensitizer ions on the surface to avoid the surface quenching effect.

Acknowledgements

This research was undertaken on the Soft X-ray Spectroscopy beamline at the Australian Synchrotron. We wish to acknowledge the technical assistance of Drs Bruce Cowie and Lars Thomsen. We thank the Microscopy Unit at Macquarie University and the Electron Microscopy Centre at the University of Wollongong. This project is primarily supported by the Australian Research Council (ARC) Future Fellowship Scheme (FT 130100517; Dayong Jin), the ARC Centre of Excellence for Nanoscale BioPhotonics (CE140100003), the Macquarie University Research Fellowship Scheme (Xiaoxue Xu), and the Australian Government Research Training Program Scholarship (Christian Clarke).

References

12 Y. Lu, J. Zhao, R. Zhao, Y. Lu, D. Liu, E. M. Goldys, X. Yang, P. Xi, A. Sunna, J. Lu, Y. Shi, R. C. Leif, Y. Huo, J. Shen, J. A. Piper, J. P. Robinson and D. Jin, *Nat. Photonics*, 2014, **8**, 32–36.

13 J. Zhao, D. Jin, E. P. Schartner, Y. Lu, Y. Liu, A. Z. Zvyagin, L. Zhang, J. M. Dawes, P. Xi, J. A. Piper, W. M. Goldys and T. M. Monro, *Nat. Nanotechnol.*, 2013, **8**, 729–734.

14 X. Liu, C. H. Yan and J. A. Capobianco, *Chem. Soc. Rev.*, 2015, **44**, 1299–1301.

15 F. Wang, Y. Han, C. S. Lim, Y. Lu, J. Wang, J. Xu, H. Chen, C. Zhang, M. Hong and X. Liu, *Nature*, 2010, **463**, 1061–1065.

16 R. Deng, F. Qin, R. Chen, W. Huang, M. Hong and X. Liu, *Nat. Nanotechnol.*, 2015, **10**, 237–242.

17 Y. Liu, Y. Lu, X. Yang, X. Zheng, S. Wen, F. Wang, X. Vidal, J. Zhao, D. Liu, Z. Zhou, C. Ma, J. Zhou, J. Piper, P. Xi and D. Jin, *Nature*, 2017, **543**, 229–233.

18 G. Chen, H. Qiu, P. N. Prasad and X. Chen, *Chem. Rev.*, 2014, **114**, 5161–5214.

19 S. Gai, C. Li, P. Yang and J. Lin, *Chem. Rev.*, 2014, **114**, 2343–2389.

20 X. Liu, X. Kong, Y. Zhang, L. Tu, Y. Wang, Q. Zeng, C. Li, Z. Shi and H. Zhang, *Chem. Commun.*, 2011, **47**, 11957–11959.

21 K. W. Krämer, D. Biner, G. Frei, H. U. Güdel, M. P. Hehlen and S. R. Lüthi, *Chem. Mater.*, 2004, **16**, 1244–1251.

22 J. C. Boyer and F. C. van Veggel, *Nanoscale*, 2010, **2**, 1417.

23 J. D. Suter, N. J. Pekas, M. T. Berry and P. S. May, *J. Phys. Chem. C*, 2014, **118**, 13238–13247.

24 C. Ma, X. Xu, F. Wang, Z. Zhou, D. Liu, J. Zhao, C. I. Lang and D. Jin, *Nano Lett.*, 2017, **17**, 2858–2864.

25 X. Chen, L. Jin, W. Kong, T. Sun, W. Zhang, X. Liu, J. Fan, S. F. Yu and F. Wang, *Nat. Commun.*, 2016, **7**, 10304.

26 B. Chen, Y. Liu, Y. Xiao, X. Chen, Y. Li, M. Li, X. Qiao, X. Fan and F. Wang, *J. Phys. Chem. Lett.*, 2016, **7**, 4916–4921.

27 B. Shen, S. Cheng, Y. Gu, D. Ni, Y. Gao, Q. Su, W. Feng and F. Li, *Nanoscale*, 2017, **9**, 1964–1971.

28 D. J. Gargas, E. M. Chan, A. D. Ostrowshik, S. Aloni, M. P. Altoe, E. S. Narnard, B. Sanii, J. J. Urban, D. J. Milliron, B. E. Cohen and P. J. Schuck, *Nat. Nanotechnol.*, 2014, **9**, 300–305.

29 F. Wang, J. Wang and X. Liu, *Angew. Chem., Int. Ed.*, 2010, **122**, 7618–7622.

30 D. Chen and P. Huang, *Dalton Trans.*, 2014, **43**, 11299–11304.

31 D. Chen, L. Liu, P. Huang, M. Ding, J. Zhong and Z. Ji, *J. Phys. Chem. Lett.*, 2015, **6**, 2833–2840.

32 H. Zhang, Y. Li, Y. Lin, Y. Huang and X. Duan, *Nanoscale*, 2011, **3**, 963–966.

33 F. Wang and X. Liu, *J. Am. Chem. Soc.*, 2008, **130**, 5642–5643.

34 X. Li, R. Wang, F. Zhang and D. Zhao, *Nano Lett.*, 2014, **14**, 3634–3639.

35 C. Dong, J. Pichaandi, T. Regier and F. C. J. M. van Veggel, *J. Phys. Chem. C*, 2011, **115**, 15950–15958.

36 J. Pichaandi, G. K. Das, N. J. J. Johnson, T. Regier and F. C. J. M. van Veggel, *J. Phys. Chem. C*, 2014, **118**, 21639–21646.

37 K. A. Abel, J. C. Boyer and F. C. J. M. van Veggel, *J. Am. Chem. Soc.*, 2009, **131**, 14644–14645.

38 C. Dong, J. Pichaandi, T. Regier and F. C. J. M. van Veggel, *Nanoscale*, 2011, **3**, 3376–3384.

39 H. Dong, L. D. Sun, Y. F. Wang, J. Ke, R. Si, J. W. Xiao, G. M. Lyu, S. Shi and C. H. Yan, *J. Am. Chem. Soc.*, 2015, **137**, 6569–6576.

40 C. Ma, X. Xu, F. Wang, Z. Zhou, S. Wen, D. Liu, J. Fang, C. I. Lang and D. Jin, *J. Phys. Chem. Lett.*, 2016, **7**, 3252–3258.

41 D. Liu, X. Xu, Y. Du, X. Qin, Y. Zhang, C. Ma, S. Wen, W. Ren, E. M. Goldys, J. A. Piper, S. Dou, X. Liu and D. Jin, *Nat. Commun.*, 2016, **7**, 10254–10258.

42 W. C. Lang, B. D. Padalia, L. M. Watson, D. J. Fabian and P. R. Norris, *Faraday Discuss. Chem. Soc.*, 1975, **60**, 37–43.

43 J. J. Yeh and I. Lindau, *At. Data Nucl. Data Tables*, 1985, **32**, 1–155.

Supplementary Information

Depth-profiling of Yb^{3+} sensitizer ions in $NaYF_4$ upconversion nanoparticles

Xiaoxue Xu‡, £,, Christian Clarke£, Chenshuo Ma§,‡, Gilberto Casillas¤, Minakshi Das‡, Ming Guan£, Deming Liu£, Li Wang¤, Anton Tadich∞, Yi Du¤, Cuong Ton-That£,*, and Dayong Jin£,†*

‡ Department of Chemistry and Biomolecular Science, Macquarie University, Sydney, NSW, 2109, Australia;

£ Institute for Biomedical Materials and Devices, Faculty of Science, University of Technology Sydney, NSW, 2007, Australia;

¤Institute for Superconducting and Electronic Materials, Innovation Campus, University of Wollongong, NSW, 2522, Australia

§ Department of Engineering, Macquarie University, Sydney, NSW, 2109, Australia;

† ARC Research Hub for Integrated Device for End-user Analysis at Low-levels (IDEAL), Faculty of Science, University of Technology Sydney, NSW, 2007, Australia;

∞ Australian Synchrotron, 800 Blackburn Road, Clayton, Victoria 3168, Australia

Corresponding Authors

Xiaoxue.xu@mq.edu.au

Cuong.Ton-That@uts.edu.au

SUPPORTING RESULTS:

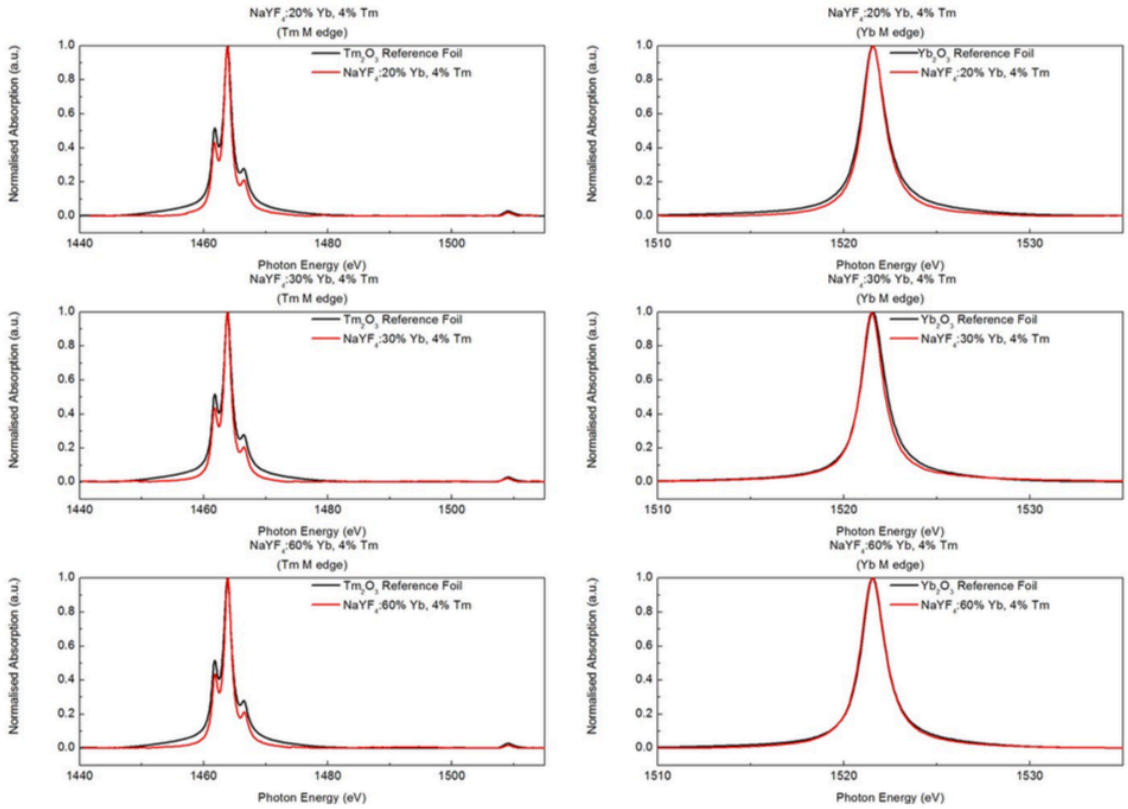

Figure S1. Normalised M-edge NEXAFS spectra of three UCNPs samples plotted together with respective Tm_2O_3 and Yb_2O_3 reference foils, confirming both Yb and Tm ions in the 3+ valence state, which is in the same state as that of host Y ions.

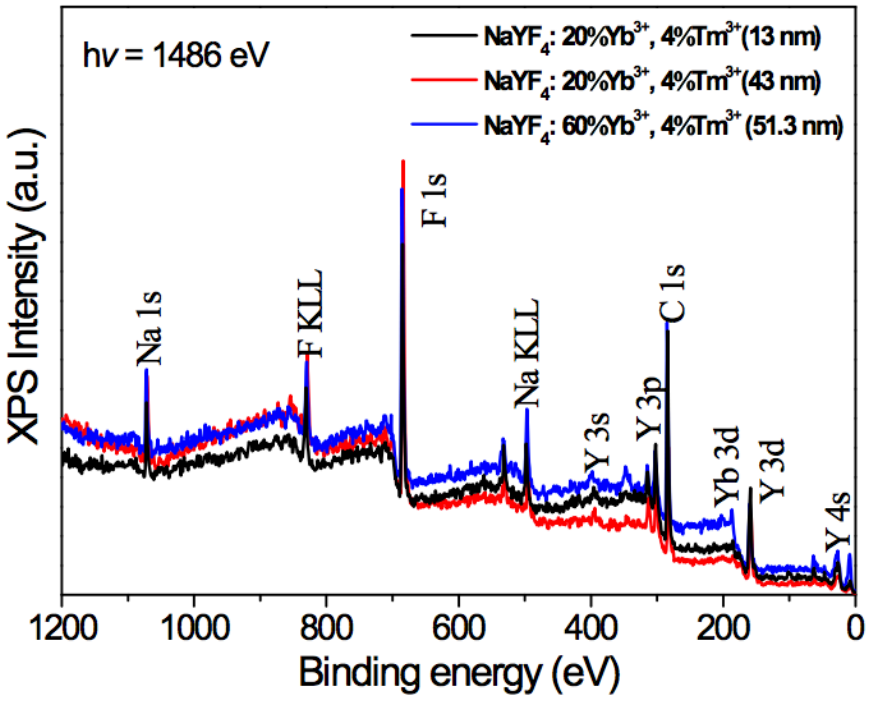

Figure S2. XPS survey spectra for the $NaYF_4$ UCNPs acquired at the photon energy of 1486 eV. All the peaks can be identified to the elements in the UCNP.

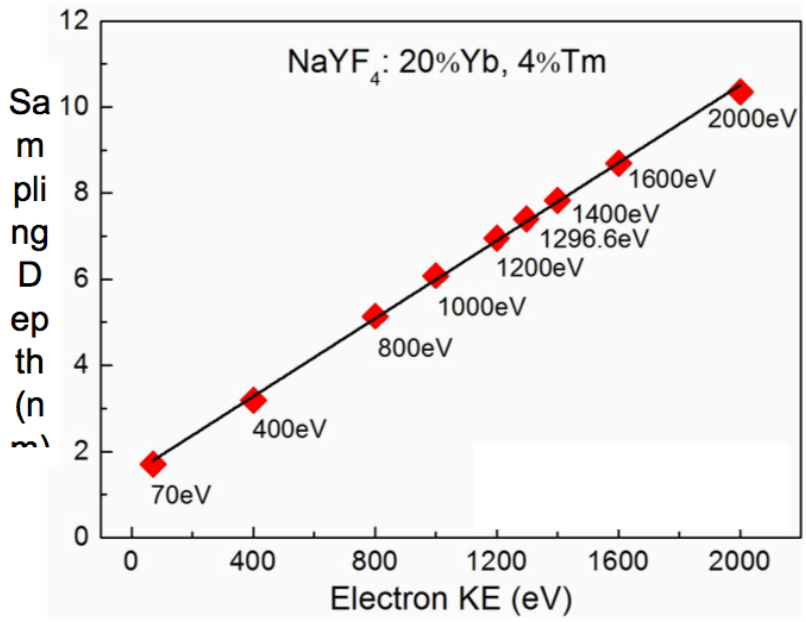

Figure S3. XPS sampling depth in $NaYF_4$ as a function of photoelectron kinetic energy (KE).

Table S1: Elemental composition of $NaYF_4$ UCNPs doped with Yb and Tm obtained from ICP-MS analysis.

Size	Designed Composition			Measured Composition		
(nm)	Y^{3+}	Yb^{3+}	Tm^{3+}	Y^{3+}	Yb^{3+}	Tm^{3+}
13.0	76%	20%	4%	76.03%	20.21%	3.75%
26.2				75.52%	20.94%	3.30%
31.1				77.87%	18.23%	3.54%
36.6				78.88%	17.42%	3.90%
43.0				79.62%	17.05%	3.70%
27.4	66%	30%		68.89%	27.60%	3.51%
35.9	51%	45%		53.05%	43.22%	3.74%
51.3	36%	60%		33.48%	63.24%	3.28%

5.3 Remarks on Paper 3

This work used synchrotron-based XPS and EDX to characterize the depth distribution of sensitizer ions in $NaYF_4$ nanocrystals. We found that in addition to the internal crystal quality and surface quenching, the sensitizer ions' distribution across the host nanocrystals also plays an important role. Our study shows sensitizer ions distributed in a radial gradient manner from the center to the surface within the UCNCs. Sensitizer ions show a preference for the center of the nanocrystal with increasing the concentration.

5.4 Contribution to Paper 4

The author contribution for paper "Amplified stimulated emission in upconversion nanoparticles for super resolution nanoscopy" are shown in **Table 5.2**.

Table 5.2 Author contribution summary for paper 4

Name	Experiment Design	Material Synthesis	System Build	Data Collection	Analysis	Figures and Tables	Manuscript
Yujia Liu	√		√	√	√	√	√
Yiqing Lu	√		√	√	√	√	√
Xusan Yang	√		√	√	√	√	√
Xianlin Zheng			√	√			
Shihui Wen		√		√			
Fan Wang			√	√			
Xavier Vidal			√	√			
Jiangbo Zhao		√					
Deming Liu		√					
Zhiguang Zhou			√	√			
Chenshuo Ma		√		√			
Jiajia Zhou		√					
James A. Piper							√
Peng Xi					√		√
Dayong Jin					√		√

In this work, I carried out part of the experimental work on sample synthesis and data collection. I prepared part of the optical measurement as well.

5.5 Paper 4

Yujia Liu, Yiqing Lu, Xusan Yang, Xianlin Zheng, Shihui Wen, Fan Wang, Xavier Vidal, Jiangbo Zhao, Deming Liu, Zhiguang Zhou, **Chenshuo Ma**, Jiajia Zhou, James A. Piper, Peng Xi, and Dayong Jin. "Amplified stimulated emission in upconversion nanoparticles for super resolution nanoscopy", ***Nature***, 2017, 543: 229-233.

LETTER

doi:10.1038/nature21366

Amplified stimulated emission in upconversion nanoparticles for super-resolution nanoscopy

Yujia Liu[1,2,3,4]*, Yiqing Lu[1,2]*, Xusan Yang[3]*, Xianlin Zheng[1,2], Shihui Wen[1,5], Fan Wang[1,2,5], Xavier Vidal[1,2], Jiangbo Zhao[1,2], Deming Liu[1,2], Zhiguang Zhou[1,5], Chenshuo Ma[1], Jiajia Zhou[5], James A. Piper[1,2], Peng Xi[1,3] & Dayong Jin[1,2,5]

Lanthanide-doped glasses and crystals are attractive for laser applications because the metastable energy levels of the trivalent lanthanide ions facilitate the establishment of population inversion and amplified stimulated emission at relatively low pump power[1–3]. At the nanometre scale, lanthanide-doped upconversion nanoparticles (UCNPs) can now be made with precisely controlled phase, dimension and doping level[4,5]. When excited in the near-infrared, these UCNPs emit stable, bright visible luminescence at a variety of selectable wavelengths[6–9], with single-nanoparticle sensitivity[10–13], which makes them suitable for advanced luminescence microscopy applications. Here we show that UCNPs doped with high concentrations of thulium ions (Tm^{3+}), excited at a wavelength of 980 nanometres, can readily establish a population inversion on their intermediate metastable $^3H_4$ level: the reduced inter-emitter distance at high Tm^{3+} doping concentration leads to intense cross-relaxation, inducing a photon-avalanche-like effect that rapidly populates the metastable $^3H_4$ level, resulting in population inversion relative to the $^3H_6$ ground level within a single nanoparticle. As a result, illumination by a laser at 808 nanometres, matching the upconversion band of the $^3H_4 \rightarrow {}^3H_6$ transition, can trigger amplified stimulated emission to discharge the $^3H_4$ intermediate level, so that the upconversion pathway to generate blue luminescence can be optically inhibited. We harness these properties to realize low-power super-resolution stimulated emission depletion (STED) microscopy and achieve nanometre-scale optical resolution (nanoscopy), imaging single UCNPs; the resolution is 28 nanometres, that is, 1/36th of the wavelength. These engineered nanocrystals offer saturation intensity two orders of magnitude lower than those of fluorescent probes currently employed in stimulated emission depletion microscopy, suggesting a new way of alleviating the square-root law that typically limits the resolution that can be practically achieved by such techniques.

To investigate conditions for amplified stimulated emission from single Yb/Tm co-doped $NaYF_4$ UCNPs, we built a dual-laser confocal microscope (Extended Data Fig. 1). As illustrated in Fig. 1a, the photon upconversion process comprises absorption of 980 nm excitation by the Yb^{3+} sensitizers, stepwise transfer of that energy onto the scaffold energy levels of the Tm^{3+} emitters, and eventually upconverted emission from the two-photon $^3H_4$, three-photon $^1G_4$ or four-photon $^1D_2$ levels of Tm^{3+}. In the presence of population inversion between the $^3H_4$ intermediate level and the $^3H_6$ ground level, a probe laser beam with wavelength corresponding to the energy gap (that is, 808 nm for $^3H_4 \rightarrow {}^3H_6$) will trigger stimulated emission to discharge the $^3H_4$ level, consequently inhibiting upconverted emission from higher excited levels (for example, $^1G_4$ and $^1D_2$).

Figure 1b shows confocal images of single UCNPs highly doped with 8% Tm^{3+} ions (and 20% Yb^{3+}). The upconversion emission under

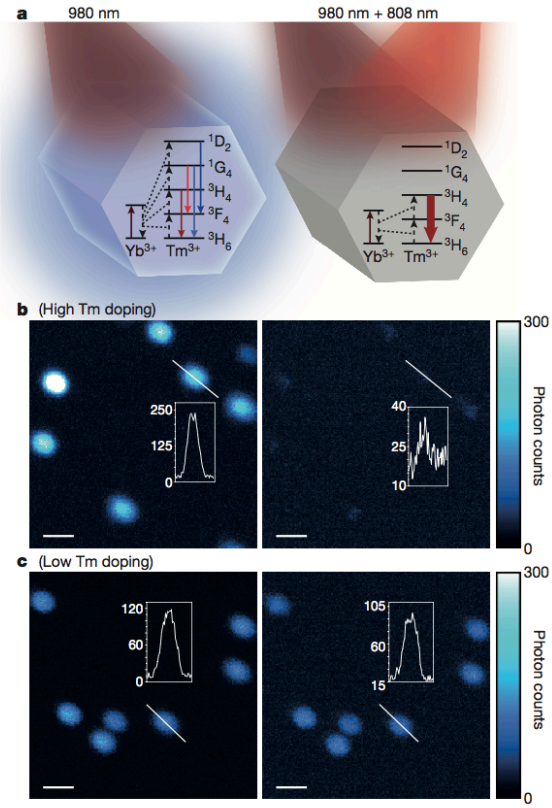

Figure 1 | Probing upconversion luminescence using dual-laser illumination. a, Energy level diagrams of Yb/Tm co-doped UCNPs under 980 nm illumination (left), and under both 980 nm and 808 nm illumination (right). See text for details. **b**, Confocal images in 455 nm upconversion emission of the 8% Tm-doped UCNPs under continuous-wave 980 nm laser (left) and under both 980 nm and 808 nm dual laser (right) illumination. **c**, As **b** but for 1% Tm-doped UCNPs. For **b** and **c**, the 980 nm and 808 nm laser powers measured at the objective back aperture were 1 mW and 5 mW, respectively. Each inset shows the luminescence signal profile along the diagonal white line in that panel across a typical nanocrystal. Pixel dwell time, 4 ms; scale bar, 500 nm.

[1]Advanced Cytometry Laboratories, ARC Centre of Excellence for Nanoscale BioPhotonics (CNBP), Macquarie University, Sydney, New South Wales 2109, Australia. [2]Department of Physics and Astronomy, Macquarie University, Sydney, New South Wales 2109, Australia. [3]Department of Biomedical Engineering, College of Engineering, Peking University, Beijing 100871, China. [4]School of Life Sciences and Biotechnology, Shanghai Jiao Tong University, Shanghai 200241, China. [5]Institute for Biomedical Materials and Devices (IBMD), Faculty of Science, University of Technology Sydney, Sydney, New South Wales 2007, Australia.
*These authors contributed equally to this work.

RESEARCH LETTER

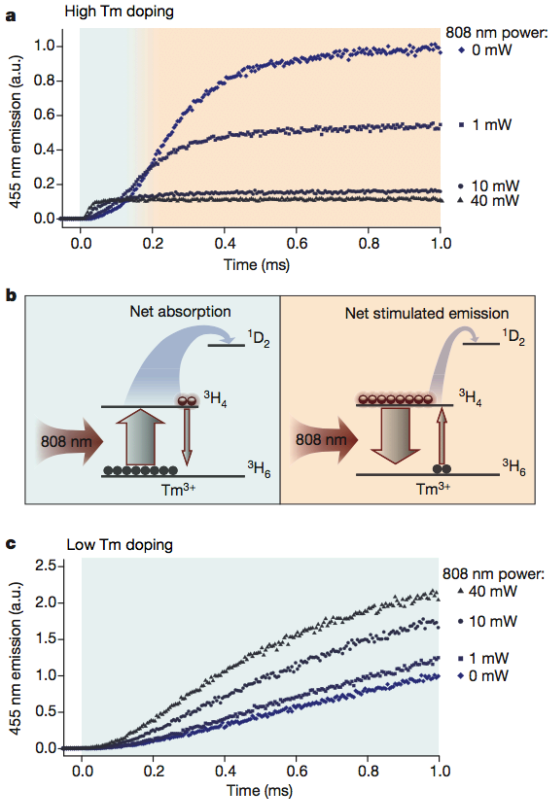

Figure 2 | Competition between absorption and stimulated emission. **a**, Transient response of the 455 nm emission from 8% Tm-doped UCNPs under synchronous 980 nm and 808 nm pulses (1 ms duration). The 980 nm laser power was fixed at 1 mW, while the 808 nm laser power was varied from 0 to 40 mW (both at the objective back aperture). **b**, Diagrams illustrating net absorption (left) and net stimulated emission (right) between $^3H_4$ and $^3H_6$ levels when the UCNPs under 980 nm excitation were probed with the 808 nm laser, which then led to either inhibition or enhancement of the further upconverted emission. See text for details. **c**, As **a** but for 1% Tm-doped UCNPs.

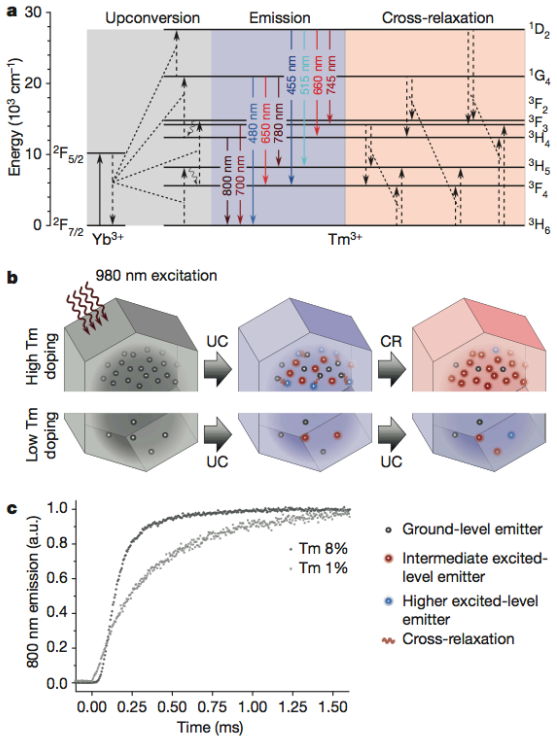

Figure 3 | The photon-avalanche-like process underlying enhanced population inversion. **a**, Energy level diagram of Yb/Tm co-doped UCNPs including typical cross-relaxation pathways among Tm^{3+} emitters. Solid arrows, excitation and emission; curved arrows, non-radiative relaxation; dashed arrows connected by dotted lines, energy transfer processes. **b**, Diagrams of the photon-avalanche-like process, which stems from the intense cross-relaxation among emitters in a highly doped nanocrystal only (sensitizers are not shown). UC, upconversion; CR, cross-relaxation. **c**, Transient response of the upconverted emission measured at 800 nm from 8% and 1% Tm-doped UCNPs after the 980 nm excitation was switched on at time = 0 ms (in the absence of the 808 nm probing beam). The 980 nm laser power was 1 mW at the objective back aperture.

continuous-wave (CW) 980 nm excitation was clearly inhibited once a CW 808 nm probe beam was applied. By contrast, under the same experiment conditions, the UCNPs with low doping concentration (conventionally 1% Tm^{3+} and 20% Yb^{3+}) showed negligible optical switching effects (Fig. 1c).

Since the 808 nm probe matches only the $^3H_4 \rightarrow {}^3H_6$ transition (no upconversion emission is observed under 808 nm excitation alone, Extended Data Fig. 2), inhibition of visible upconversion emission by the 808 nm probe is concrete evidence for population inversion and net stimulated emission on $^3H_4 \rightarrow {}^3H_6$; if this were not so, visible upconversion emission would be enhanced because of the increased optical pumping to $^3H_4$. To confirm this, we measured the transient response of the upconversion emission at 455 nm (Fig. 2) and at 650 nm (Extended Data Fig. 3) using synchronized 980 nm and 808 nm pulses. Initially, the emission from 8% Tm-doped UCNPs is indeed enhanced (Fig. 2a), indicating that the absorption of 808 nm dominates (cartoon shown in Fig. 2b left). The more intense the 808 nm beam, the more obvious the initial enhancement. However increase of the upconversion emission is rapidly truncated once sufficient 980 nm energy is transferred to Tm^{3+} ($^3H_4$) acceptors to establish a population inversion, whereupon stimulated emission on $^3H_4 \rightarrow {}^3H_6$ dominates and upconversion emissions from the three- and four-photon levels of $^1G_4$ and $^1D_2$ are short-circuited (cartoon shown in Fig. 2b right). By contrast, for 1% Tm-doped nanocrystals, the build-up of upconversion emission is accelerated by the probe 808 nm beam (that is, enhancement; corresponding to Fig. 2b left), showing no sign of population inversion over the same period of time (Fig. 2c).

The differences shown above between the two UCNPs of different Tm^{3+} concentrations indicate that the critical population inversion is driven by a key mechanism related to the doping concentration, which we ascribe to a photon-avalanche-like process. This refers to the intense cross-relaxation between emitters such that those in a higher excited energy level have high probability for transfer of energy to a nearby emitter in the ground or lower energy level instead of undergoing other relaxation pathways, forming a positive feedback process accelerating the accumulation of emitters in intermediate excited energy levels. Unlike ordinary photon avalanche, however, the condition of non-resonant ground-level absorption is not met with co-doped UCNPs containing sensitizers and emitters, so that the threshold behaviour of photon avalanche is absent[14–17] (see Methods and Extended Data Fig. 4 for discussion). For the Tm-doped UCNPs, the similarly spaced energy levels of Tm^{3+} provide abundant cross-relaxation pathways (Fig. 3a). The cross-relaxation coefficients are

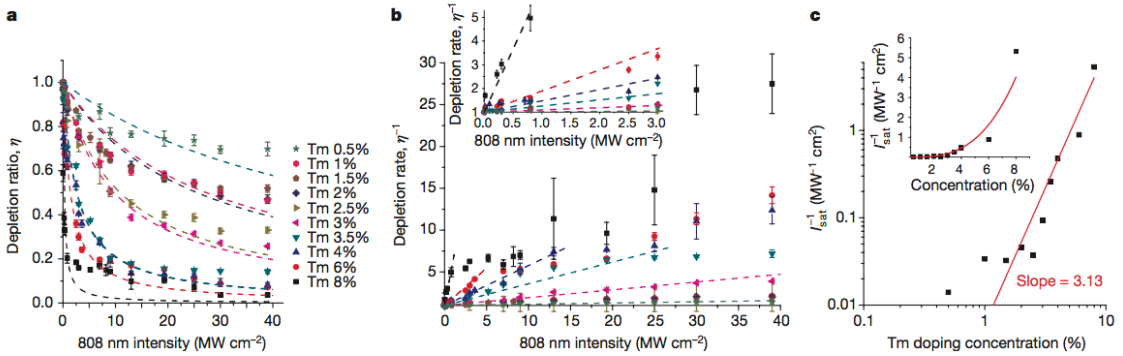

Figure 4 | Optical switching efficiency with respect to Tm doping concentration. a, Depletion ratio of the upconversion emission at 455 nm, as a result of intermediate-level stimulated emission, under continuous-wave 980 nm excitation at a fixed intensity of 0.66 MW cm^{-2} and 808 nm intensities up to 39 MW cm^{-2}, measured for a series of UCNPs with incremental Tm doping concentrations from 0.5 to 8 mol%. Dashed lines are fitted curves using the form $\eta = (1 + I_{808}/I_{sat})^{-1}$, where I_{sat} denotes the saturation intensity. **b**, The depletion ratio data in **a** are inverted to illustrate the linear relation $\eta^{-1} = 1 + I_{808}/I_{sat}$. In the inset, the dashed lines are fitted using all data points; in the main panel, linear curve fitting for Tm concentrations ≥3.5% uses only data points at low 808 nm intensity. At high 808 nm intensity, the reciprocals of depletion ratio start to deviate from linearity towards plateaus. Error bars in **a** and **b**, ±1 s.d. with $n = 5$ each. **c**, Inverse of the saturation intensity values obtained by linear curve fitting in **b** in relation to the Tm doping concentration, plotted on a log–log scale in the main panel and on a linear scale in the inset.

enhanced quadratically as the doping concentration increases (assuming that energy transfer between two ions is inversely proportional to the sixth power of their separation[18,19], and that the average separation distance is the cube root of the reciprocal of the doping concentration), so that cross-relaxation dominates when the emitters are close enough to each other (Fig. 3b).

The presence or absence of the photon-avalanche-like process was experimentally verified by measuring the transient response of the upconversion emission from the $^3H_4$ level under excitation by a single wavelength of 980 nm. The 800 nm upconversion emission of the 8% Tm-doped nanocrystals exhibited an 'S' shape over the build-up period (Fig. 3c), which is a signature of photon avalanche[14,15,17,20]. In contrast, for the 1% Tm-doped nanocrystals, the increase of 800 nm emission took place immediately upon 980 nm excitation. Theoretically, the precondition for photon avalanche is when the cross-relaxation coefficient surpasses the intrinsic decay rate from the higher excited level to the ground level, thereby producing positive feedback[14,16]. By fitting the transient responses of the 8% Tm-doped nanocrystals to rate equations, we show that the rate parameters obtained satisfy this requirement (Extended Data Fig. 5); in contrast, for 1% Tm-doped UCNPs where the cross-relaxation coefficients are reduced quadratically with the doping concentration (that is, dividing the coefficients by 64), the photon avalanche condition is not satisfied.

To determine the critical Tm^{3+} doping concentration for enhanced population inversion, a series of ten batches of 40-nm UCNPs were synthesized with incremental Tm concentrations from 0.5 mol% to 8 mol% (Extended Data Fig. 6). Under dual-laser CW illumination, the optical depletion ratio (that is, the ratio of the emission strength in the presence of the 808 nm depletion probe to that in the absence of that probe) of the 455 nm emission was measured as a function of the 808 nm intensity. As shown in Fig. 4a, within the available power range of the 808 nm laser, only UCNPs with Tm doping concentration >2% can have more than 50% of their emission switched off. For Tm doping concentrations above 4%, optimum depletion ratios above 90% can be achieved.

The saturation intensities, denoting the particular values of the probe intensity that halve the upconverted emission, were calculated from a plot of the inverse of the depletion ratio against the 808 nm intensity via linear curve fitting (Fig. 4b)[21,22]. The linearity found for UCNPs with Tm doping ≥3.5% holds only at low 808 nm intensity; at greater intensities, the fit becomes dual- or multi-segment, which suggests that the depletion efficiency for the highly-doped UCNPs is power dependent, and can be substantially amplified by the photon-avalanche-like effect. Those data points appearing with a linear fit in the low 808 nm intensity range show reduction of saturation intensities by more than two orders of magnitude (from 71.4 MW cm^{-2} to 0.19 MW cm^{-2}) as the Tm doping increases from 0.5% to 8%. Once the stimulated emission depletion at low intensity levels of the 808 nm illumination consumes the established population inversion, a balance is re-established between absorption and stimulated emission, and further inhibition of upconversion emission is diminished at higher 808 nm intensities (Extended Data Fig. 7).

The small saturation intensity of highly doped UCNPs suggests that the photon-avalanche-like effect in single UCNPs alleviates the square root law that all current super-resolution nanoscopy methods obey. Plotting the inverse of saturation intensity against the Tm doping concentration on a log–log scale shows a slope of 3.13 (Fig. 4c), suggesting that the saturation intensity is proportional to the average Tm–Tm distance to the ninth power. Both Fig. 4c and b confirm that the saturation intensities in upconversion materials are highly dependent on the doping concentration of emission centres, showing that the photon-avalanche-like effect plays the key role in bringing down the intensity requirement for stimulated emission depletion.

We further explored the use of highly doped UCNPs for optical super-resolution imaging; the 808 nm beam was spatially modulated to produce a doughnut-shaped point spread function (PSF) that overlapped with the Gaussian PSF of the 980 nm excitation beam at the focal plane (illustrated in Fig. 5a). The nanocrystals on the periphery of the 980 nm PSF would therefore be expected to be optically switched off by the 808 nm beam, leading to an effective excitation spot smaller than the optical diffraction limit, similar to the situation in STED microscopy[21]. To prove the concept, two samples of monodispersed UCNPs, both doped with 8% Tm and 20% Yb, were carefully characterized by transmission electron microscopy (TEM), showing average sizes of 39.8 and 12.9 nm, respectively (Fig. 5b and c). A region with a size comparable to the optical diffraction limit but containing three 40-nm UCNPs was selected, and a sequence of far-field optical super-resolution images that clearly resolve the adjacent UCNPs were recorded (Fig. 5d). Spot sizes of 48.3 nm were obtained by our upconversion-STED microscopy at an 808 nm intensity of 9.75 MW cm^{-2} (Fig. 5e and f). As the measured full-width at half-maximum (FWHM) is a convolution between the theoretical resolution and the physical size of the nanoparticle, this only gives the upper bound of the actual PSF size. Deconvolution based on the simple Pythagorean equation[23] shows this result corresponds

RESEARCH LETTER

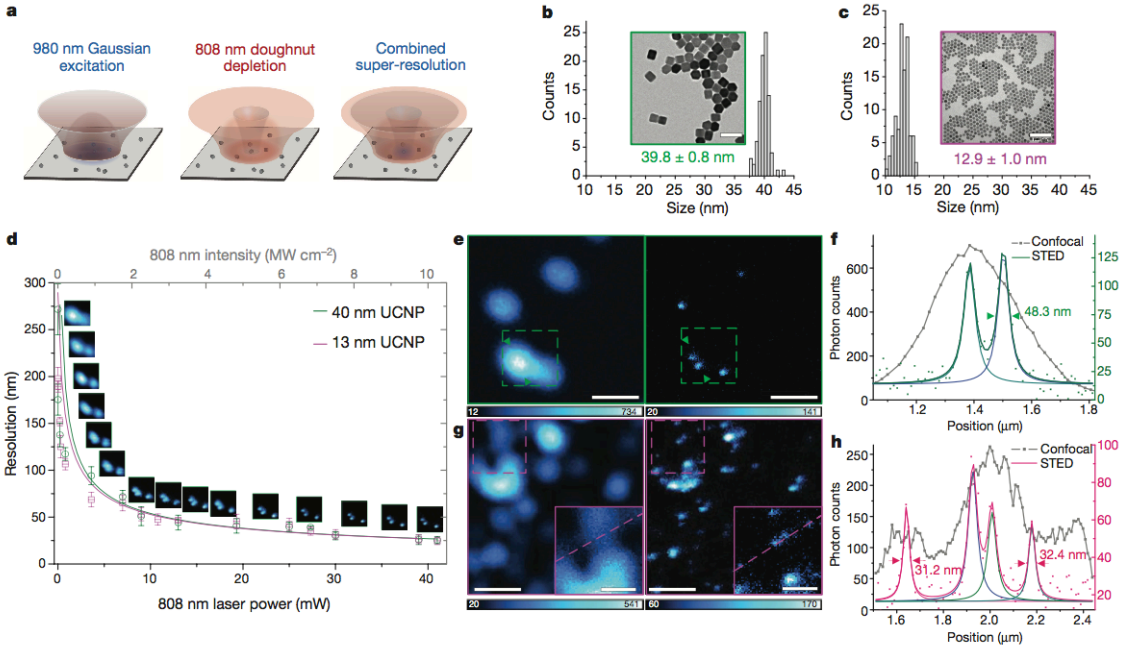

Figure 5 | Super-resolution imaging of the highly-doped UCNPs. **a**, Diagrams of the upconversion-STED super-resolution imaging, in which a Gaussian excitation profile (980 nm) and a Gauss–Laguerre mode 'doughnut' depletion profile (808 nm) at far field are employed. 9.75 MW cm^{-2}, respectively. Pixel dwell time, 4 ms; scale bars, 500 nm. Dashed boxes mark an area containing closely spaced 13-nm UCNPs that can be resolved in upconversion-STED but not in confocal imaging. **f**, Intensity profiles between the arrows across two UCNPs in **e**, showing

further reducing saturation intensity. The longer imaging acquisition times for STED based on UCNPs might also be circumvented by employing parallelized scanning with beam arrays in the future[29].

In conclusion, we note that a variety of bioconjugation methods have been developed that make $NaYF_4$ nanocrystals usable as molecular probes for bioimaging[30], and with improved protocols to avoid non-specific binding and aggregation, we believe that highly doped UCNPs together with the upconversion-STED technique reported here will be important in nanoscale biology investigations. The present results also suggest new approaches to developing nanoscale lasers[31] and other nanophotonics applications demanding amplification by simulated emission at the nanoscale[32,33].

Online Content Methods, along with any additional Extended Data display items and Source Data, are available in the online version of the paper; references unique to these sections appear only in the online paper.

Received 23 August 2016; accepted 4 January 2017.
Published online 22 February 2017.

1. Urquhart, P. Review of rare-earth doped fiber lasers and amplifiers. *IEE Proc. J. Optoelectron.* **135,** 385–402 (1988).
2. Stoneman, R. C. & Esterowitz, L. Efficient, broadly tunable, laser-pumped Tm-YAG and Tm-YSGG CW lasers. *Opt. Lett.* **15,** 486–488 (1990).
3. Jackson, S. D. Towards high-power mid-infrared emission from a fibre laser. *Nat. Photon.* **6,** 423–431 (2012).
4. Wang, F. *et al.* Simultaneous phase and size control of upconversion nanocrystals through lanthanide doping. *Nature* **463,** 1061–1065 (2010).
5. Liu, D. *et al.* Three-dimensional controlled growth of monodisperse sub-50 nm heterogeneous nanocrystals. *Nat. Commun.* **7,** 10254 (2016).
6. Mai, H.-X., Zhang, Y.-W., Sun, L.-D. & Yan, C.-H. Highly efficient multicolor up-conversion emissions and their mechanisms of monodisperse $NaYF_4$: Yb,Er core and core/shell-structured nanocrystals. *J. Phys. Chem. C* **111,** 13721–13729 (2007).
7. Chen, G., Ohulchanskyy, T. Y., Kumar, R., Agren, H. & Prasad, P. N. Ultrasmall monodisperse $NaYF_4$:Yb^{3+}/Tm^{3+} nanocrystals with enhanced near-infrared to near-infrared upconversion photoluminescence. *ACS Nano* **4,** 3163–3168 (2010).
8. Wang, F. *et al.* Tuning upconversion through energy migration in core-shell
18. Selvin, P. R. The renaissance of fluorescence resonance energy transfer. *Nat. Struct. Biol.* **7,** 730–734 (2000).
19. Rabouw, F. T., den Hartog, S. A., Senden, T. & Meijerink, A. Photonic effects on the Forster resonance energy transfer efficiency. *Nat. Commun.* **5,** 3610 (2014).
20. Auzel, F. Upconversion and anti-Stokes processes with f and d ions in solids. *Chem. Rev.* **104,** 139–174 (2004).
21. Willig, K. I., Harke, B., Medda, R. & Hell, S. W. STED microscopy with continuous wave beams. *Nat. Methods* **4,** 915–918 (2007).
22. Leutenegger, M., Eggeling, C. & Hell, S. W. Analytical description of STED microscopy performance. *Opt. Express* **18,** 26417–26429 (2010).
23. Donnert, G. *et al.* Macromolecular-scale resolution in biological fluorescence microscopy. *Proc. Natl Acad. Sci. USA* **103,** 11440–11445 (2006).
24. Kolesov, R. *et al.* Super-resolution upconversion microscopy of praseodymium-doped yttrium aluminum garnet nanoparticles. *Phys. Rev. B* **84,** 153413 (2011).
25. Han, K. Y. *et al.* Three-dimensional stimulated emission depletion microscopy of nitrogen-vacancy centers in diamond using continuous-wave light. *Nano Lett.* **9,** 3323–3329 (2009).
26. Hanne, J. *et al.* STED nanoscopy with fluorescent quantum dots. *Nat. Commun.* **6,** 7127 (2015).
27. Harke, B. *et al.* Resolution scaling in STED microscopy. *Opt. Express* **16,** 4154–4162 (2008).
28. Wu, R. *et al.* Optical depletion mechanism of upconverting luminescence and its potential for multi-photon STED-like microscopy. *Opt. Express* **23,** 32401–32412 (2015).
29. Chmyrov, A. *et al.* Nanoscopy with more than 100,000 'doughnuts'. *Nat. Methods* **10,** 737–740 (2013).
30. Sedlmeier, A. & Gorris, H. H. Surface modification and characterization of photon-upconverting nanoparticles for bioanalytical applications. *Chem. Soc. Rev.* **44,** 1526–1560 (2015).
31. He, L., Ozdemir, S. K., Zhu, J., Kim, W. & Yang, L. Detecting single viruses and nanoparticles using whispering gallery microlasers. *Nat. Nanotechnol.* **6,** 428–432 (2011).
32. Koenderink, A. F., Alù, A. & Polman, A. Nanophotonics: shrinking light-based technology. *Science* **348,** 516–521 (2015).
33. Buchegger, B. *et al.* Stimulated emission depletion lithography with mercapto-functional polymers. *ACS Nano* **10,** 1954–1959 (2016).

Acknowledgements This project was primarily supported by the Australian Research Council (ARC) Future Fellowship Scheme (D.J., FT 130100517), the ARC Centre of Excellence for Nanoscale BioPhotonics (CE140100003), the

RESEARCH LETTER

METHODS

Dual-laser confocal/super-resolution microscope. The optical system was built on a sample scanning configuration employing a 3-axis closed-loop piezo stage (stage body MAX311D/M, piezo controller BPC303; Thorlabs). Illustrated in Extended Data Fig. 1, a single-mode fibre-coupled 980 nm diode laser (LE-LS-980-300-FCS, LEO Photonics; maximum output power 300 mW) was used as the excitation source. After collimation, the excitation beam was transmitted through a long-pass dichroic mirror (ZT860lpxr, Chroma), then reflected by a second short-pass dichroic mirror (T750spxrxt, Chroma), and focused through an oil-immersion objective (UPlanAPO, Olympus; 100×, NA = 1.4) onto the sample slide. The first dichroic mirror also allowed the 808 nm probing beam from a polarization-maintaining fibre-coupled diode laser (LU0808M250-1C16F30A, Lumics; single mode, linear polarization, maximum output power 250 mW) to merge with the 980 nm beam. The luminescence signal from the sample was collected by the same objective, split from the excitation and probing beams by the second dichroic mirror, before being coupled into a multi-mode fibre (M24L01, Thorlabs). The other end of the fibre was connected to a single-photon avalanche diode (SPAD; SPCM-AQRH-13-FC, PerkinElmer) capable of being time-gated electronically. To select upconversion emission bands, different band-pass filters (FF01-448/20-25 and FF01-660/13-25, Semrock) were inserted in the detection path for both transient response measurement and confocal imaging. The distal end of the multi-mode fibre could also be switched to a miniature monochromator (MicroHR Auto, Horiba) equipped with a second SPAD for measuring upconversion emission spectra (Extended Data Fig. 2).

For measuring the 800 nm transient response under 980 nm excitation only (Fig. 3c), the distal end of the multi-mode fibre connected to the SPAD was substituted for the distal end of the polarization-maintaining fibre of the 808 nm laser, with a band-pass filter (FB800-10, Thorlabs) also inserted in the beam path.

For acquiring optical super-resolution images, a quarter-wave plate (WPQ10M-808, Thorlabs) was used to first transform the 808 nm beam from linear polarization to circular polarization. In practice a half-wave plate (WPH10M-808, Thorlabs) was also used to facilitate the adjustment towards quality circular polarization. Then, a vortex phase plate (VPP-1a, RPC Photonics) was inserted in the 808 nm beam path, so that a doughnut-shaped PSF was generated at the focal plane. In both cases of dual-laser confocal and super-resolution imaging, the two beams of 980 and 808 nm were carefully aligned to ensure precise overlapping of

Remaining in the argon atmosphere, the mixture was slowly heated up to 110 °C to evaporate methanol and then to 150 °C to evaporate residual water. After that, the solution was heated up to 300 °C in 23 min, and kept at that temperature for another 1.5 h. The reaction was then stopped, and the slurry was cooled down to room temperature. The nanocrystals were washed with cyclohexane/ethanol for four times, and finally re-dispersed in cyclohexane.

Preparation of sample slides. Sample slides carrying individual-distributed UCNPs were carefully prepared. To achieve the best imaging quality, an embedding medium with refractive index matching that of the immersion oil was made first. 2.4 g Mowiol 4-88 (Sigma-Aldrich) was mixed with 6 g glycerol in a 50 ml centrifuge tube. After stirring on a magnetic stirrer for 1 h, 6 ml Milli-Q water was added, and the stirring continued for another 2 h. Then, 12 ml tris(hydroxymethyl)aminomethane (Tris)-HCl buffer (0.2 M, pH 8.5) was added, and the solution was water-bathed at 50 °C under constant agitation until the Mowiol was largely dissolved. Any remaining solids were removed by centrifugation at 7,500*g* for 30 min.

To prepare a sample slide, a cover slip was washed with pure ethanol and then Milli-Q water under ultrasonication, and then treated with 50 μl polylysine solution (0.1% in H_2O w/v). After 30 min, the polylysine was washed off with Milli-Q water, and the cover slip was air-dried. 20 μl of the UCNPs (diluted to 0.01 mg ml^{-1} in cyclohexane) were dropped onto the treated surface, which was immediately washed with 500 μl cyclohexane twice. After being air-dried, the cover slip was put over a clean glass slide spread with 10 μl as-prepared embedding medium, and any air bubbles were squeezed out by gentle force. The sample was kept at room temperature for another 24 h to ensure complete dryness before measurement.

Analytical interpretation of the photon-avalanche-like process. The photon avalanche (PA) phenomenon was first discovered in 1979 in Pr-doped $LaCl_3$ and $LaBr_3$ crystals[34], followed by reconfirmations in crystals and glasses doped with other lanthanides including Sm^{3+}, Nd^{3+}, Tm^{3+}, Er^{3+} and Ho^{3+} (refs 17, 20, 35). Later in the 90s various models were proposed to interpret the PA process. Two aspects of PA, namely (1) the intrinsic requirement of upconversion material to enable PA, and (2) the pumping condition in order to observe a PA threshold, have been shown with clear mathematical derivation[14–16,36]. These approaches were adopted here to explain the results obtained in this work.

To investigate the underlying cause of enhanced population inversion in highly-

To solve equation (6) at the equilibrium state (that is, $dn_1/dt = dn_3/dt = 0$), eliminating n_1 and n_2 leads to

$$\begin{aligned} &An_3^2 + Bn_3 - R_1R_2 = 0 \\ &A = k(R_2 + W_3 + bW_3 - W_2) \\ &B = kW_2 - kR_2 + bW_3R_2 + R_1R_2 + R_1W_3 + W_2W_3 \end{aligned} \tag{7}$$

Therefore

$$n_3 = \frac{B}{2A}\left[\mathrm{sgn}(B)\left(1 + \frac{4AR_1R_2}{B^2}\right)^{1/2} - 1\right] \tag{8}$$

Note that the other root of the quadratic equation, which is negative, is omitted.

The analytical solution of equations (7) and (8) appears identical to that derived by Joubert *et al.*[14] when they modelled PA in $LiYF_4:Nd^{3+}$, except in their case R_1 and R_2 are constant (due to the sole dopant of Nd^{3+}) whereas here they are proportional to n_{S2}. However, the number of sensitizers in a single nanocrystal is limited; therefore under sufficient excitation intensity, it is reasonable to assume that the population of n_{S2} approaches its asymptotic limit, so that R_1 and R_2 can be treated as constants in equations (7) and (8). This allows the previous analyses to be adopted for the Yb-Tm upconversion system here.

To understand whether the upconversion material is capable of PA (the first aspect of PA mentioned above), assuming $AR_1R_2/B^2 \ll 1$, from equation (8) we have

$$n_3 \approx \begin{cases} R_1R_2/B & \text{when } B > 0 \\ -B/A & \text{when } B < 0 \end{cases} \tag{9}$$

It can be seen that, when $B > 0$, n_3 is inversely proportional to B; therefore any change in B has negligible impact on n_3. When $B < 0$, n_3 becomes proportional to B, so that the change in B will lead to an obvious difference in n_3. This $B < 0$ regime is where PA happens, allowing n_3 to increase dramatically towards population inversion.

According to the expression of B in equation (7), if an upconversion material offers $k < bW_3$, it always gives $B > 0$, therefore PA can never happen. On the other hand, only if $k > bW_3$, both regimes may exist for the material, and PA starts when

Since $k > bW_3$, this leads to the pumping threshold for PA

$$R_{2,\mathrm{th}} = \frac{(k + W_3)W_2}{k - bW_3} \tag{15}$$

So that for $R_2 \le R_{2,\mathrm{th}}$, $n_3 = 0$. Since the value of zero cannot be plotted on a log–log scale when we plot n_3 against R_2, the PA threshold is therefore distinct for the case of zero ground-level absorption[36].

When $R_1 > 0$, clear observation of the PA threshold depends on the deviation of n_3 from that in the case of zero ground-level absorption. This can be semi-quantified by the values of n_3 at the threshold $R_{2,\mathrm{th}}$. For $R_1 = 0$, $n_3(R_{2,\mathrm{th}}) = 0$; whereas for $R_1 > 0$, note that at $R_{2,\mathrm{th}}$ we have $B = R_1R_2 + R_1W_3$, and equation (8) becomes

$$\begin{aligned} n_3(R_{2,\mathrm{th}}) &= \frac{\sqrt{B^2 + 4AR_1R_2} - B}{2A} \\ &= \frac{\sqrt{(R_1R_2 + R_1W_3)^2 + 4R_1R_2k(R_2 + W_3 + bW_3 - W_2)} - (R_1R_2 + R_1W_3)}{2k(R_2 + W_3 + bW_3 - W_2)} \end{aligned} \tag{16}$$

Combining equations (15) and (16), $n_3(R_{2,\mathrm{th}})$ can be solved as

$$n_3(R_{2,\mathrm{th}}) = \frac{(kW_2 + kW_3 + W_2W_3 - bW_3{}^2)\left[\sqrt{1 + \frac{4kW_2W_3(1+b)(k - bW_3 + W_2)(k + W_3)}{(kW_2 + kW_3 + W_2W_3 - bW_3{}^2)^2}}R_1 - 1\right]}{2kW_3(1+b)(k - bW_3 + W_2)} \tag{17}$$

Taking a first-order approximation, we have

$$\begin{aligned} n_3(R_{2,\mathrm{th}}) &\approx \frac{(k + W_3)W_2}{kW_2 + kW_3 + W_2W_3 - bW_3{}^2}R_1 \\ &= \frac{(k + W_3)W_2}{(k + W_3)W_2 + (k - bW_3)W_3}R_1 \end{aligned} \tag{18}$$

Therefore, n_3 will be close to zero at the threshold only if R_1 is very small, so that the threshold will distinctly appear. This aspect of PA, first explained by Goldner

RESEARCH LETTER

$$\begin{aligned}\frac{dn_3}{dt} &= P_{808}(n_1 - n_3) + c_2 n_{S2} n_2 - c_3 n_{S2} n_3 - W_3 n_3 + b_{43} W_4 n_4 \\ &\quad + b_{53} W_5 n_5 - k_{31} n_1 n_3 + k_{41} n_1 n_4 + 2k_{51} n_1 n_5 \\ \frac{dn_4}{dt} &= c_3 n_{S2} n_3 - c_4 n_{S2} n_4 - W_4 n_4 + b_{54} W_5 n_5 - k_{41} n_1 n_4 \\ \frac{dn_5}{dt} &= c_4 n_{S2} n_4 - W_5 n_5 - k_{51} n_1 n_5\end{aligned} \tag{19}$$

where P_{980} is the absorption rate of Yb^{3+}; P_{808} is the absorption/stimulated emission rate of Tm^{3+} (so that the term of $P_{808}(n_1 - n_3)$ introduced into dn_3/dt represents the net effect of absorption and stimulated emission); W_S is the intrinsic decay rate of excited Yb^{3+}; c_i is the upconversion coefficient between excited Yb^{3+} and Tm^{3+} on level i; W_i is the intrinsic decay rate of Tm^{3+} on level i; b_{ij} is the branching ratio for Tm^{3+} decaying from level i to level j satisfying $\sum_{j=1}^{i-1} b_{ij} = 1$; k_{ij} is the cross-relaxation coefficient between Tm^{3+} on level i and level j; and n is the population of ions on an energy level satisfying

$$\begin{aligned} n_{S1} + n_{S2} &= 1 \\ n_1 + n_2 + n_3 + n_4 + n_5 &= 1 \end{aligned} \tag{20}$$

We use this rate-equations model of equations (19) and (20) to fit the transient response obtained from the 8% Tm-doped UCNPs under dual-laser excitation. The rate parameters yielded are summarized in Extended Data Fig. 5b, and the simulation results are plotted in Extended Data Fig. 5c, showing good consistency with the measurements.

The cross-relaxation coefficients are found to be orders of magnitude larger than the decay rates as well as the upconversion coefficients. In particular, it is seen that the precondition for PA for the lowest three energy levels (that is, $k_{31} > b_{31} W_3$) has been satisfied; whereas if k_{31} is reduced quadratically with the doping concentration, for 1% Tm-doped nanocrystals we have $k_{31}' = 2.3 \times 10^3$, so that $k_{31}' < b_{31} W_3$. These support the assertion that intense cross-relaxation in the PA-like process plays the key role in enhancing population inversion.

It should be noted that the modelling conducted here does not address all of the processes in the Yb–Tm upconversion system. On the one hand, Extended Data Fig. 2 indicates that both the blue peak at 480 nm and the red peak at 650 nm become negligible for high Tm^{3+} doping concentrations, suggesting substantial cross-relaxation involving the $^1G_4$ level. This may well include $(n_4, n_2) \rightarrow (n_3, n_3)$, $(n_4, n_3)/(n_3, n_4) \rightarrow (n_2, n_5)$ and $(n_4, n_4) \rightarrow (n_3, n_5)$, in addition to the sole $(n_4, n_1) \rightarrow (n_3, n_2)/(n_2, n_3)$ cross-relaxation process involving n_4 that has been considered in the rate equations of equation (19). On the other hand, our current system is not able to characterize Tm^{3+} emission bands outside the visible range, such as the one-photon emission at 1.8 μm and the five-photon emission at 350 nm. Nevertheless, the current modelling provides results reasonably close to the experimental data, which we believe is suited for illustrating the physical picture and forming a stepping stone for more precise investigation in the future.

Sample size. No statistical methods were used to predetermine sample size.

Data availability. The data that support the findings of this study are available from the corresponding authors upon reasonable request.

34. Chivian, J. S., Case, W. E. & Eden, D. D. The photon avalanche: a new phenomenon in Pr^{3+}-based infrared quantum counters. *Appl. Phys. Lett.* **35,** 124–125 (1979).
35. Joubert, M. F. Photon avalanche upconversion in rare earth laser materials. *Opt. Mater.* **11,** 181–203 (1999).
36. Goldner, P. & Pelle, F. Photon avalanche fluorescence and lasers. *Opt. Mater.* **5,** 239–249 (1996).

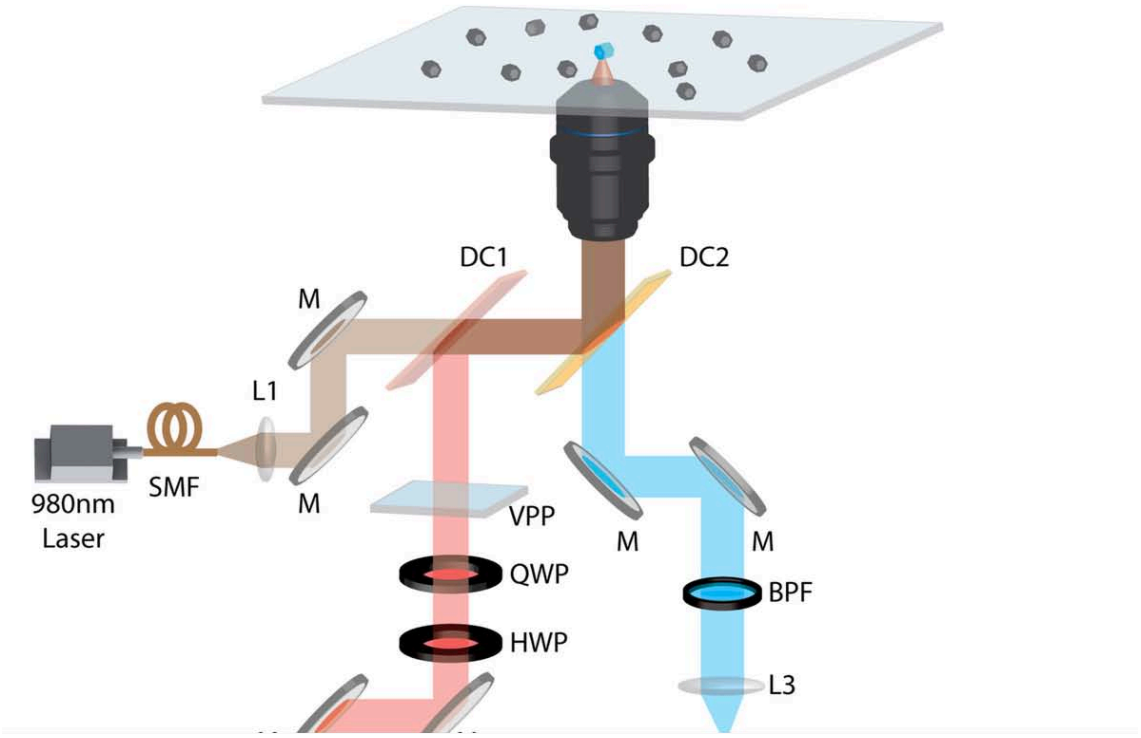

RESEARCH LETTER

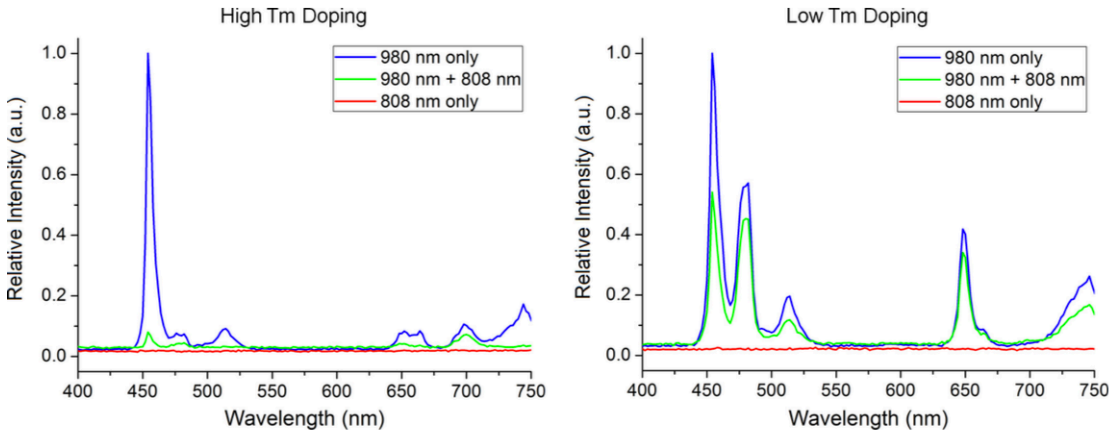

Extended Data Figure 2 | Upconversion emission spectra of 8% (left) and 1% (right) Tm-doped UCNPs. The 980 nm and 808 nm laser powers measured at the objective back aperture were 1 and 10 mW, respectively.

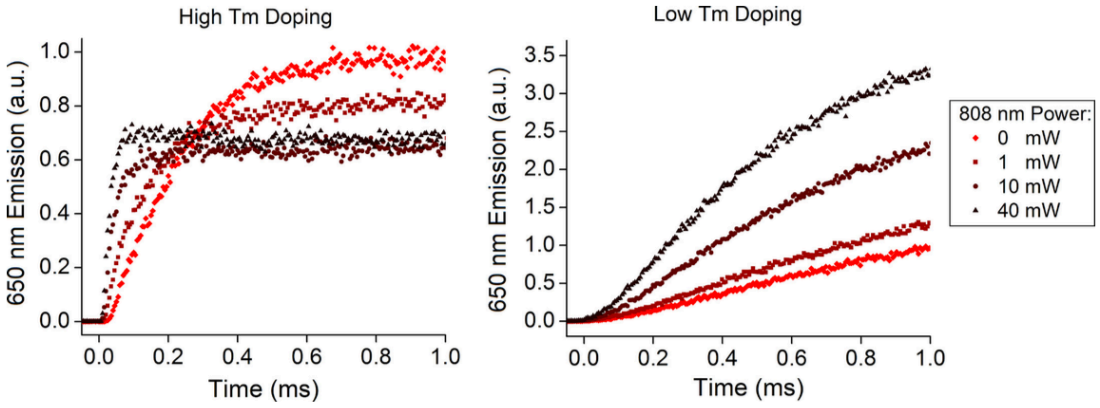

Extended Data Figure 3 | Transient responses of 650 nm upconversion emission under synchronous 980 nm and 808 nm pulses. Left, 8% Tm-doped UCNPs; right, 1% Tm-doped UCNPs. The 980 nm laser power was fixed at 1 mW, while the 808 nm laser power was varied from 0 to 40 mW (both measured at the objective back aperture).

RESEARCH LETTER

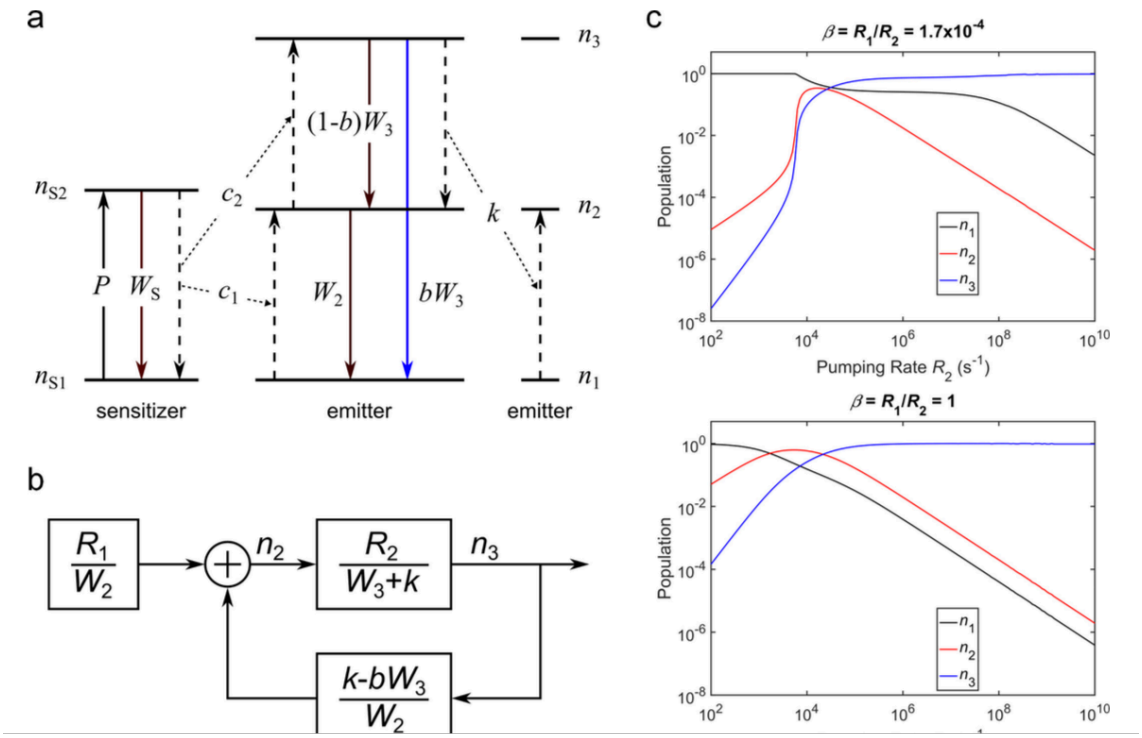

LETTER RESEARCH

a

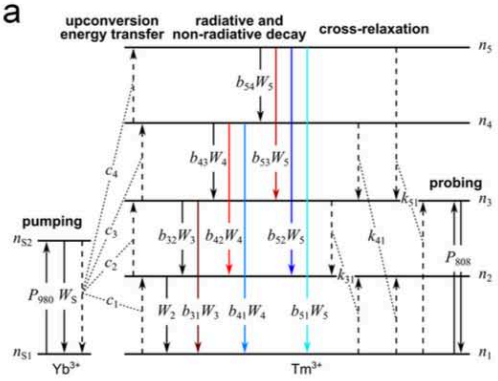

b

absorption rates (s^{-1})		decay rates (s^{-1})				
P_{980}	P_{808}	W_5	W_2	W_3	W_4	W_5
2.75×10^4	7.4×10^5	7.6×10^3	6.4×10^3	1.8×10^4	1.4×10^4	3.2×10^3

upconversion coefficients				cross-relaxation coefficients		
c_1	c_2	c_3	c_4	k_{31}	k_{41}	k_{51}
6.23×10^4	5.7×10^4	7.4×10^4	5.2×10^3	1.5×10^5	1.75×10^5	4.8×10^5

branching ratios								
b_{31}	b_{32}	b_{41}	b_{42}	b_{43}	b_{51}	b_{52}	b_{53}	b_{54}
0.27	0.73	0.18	0.24	0.58	0.24	0.23	0.20	0.33

c

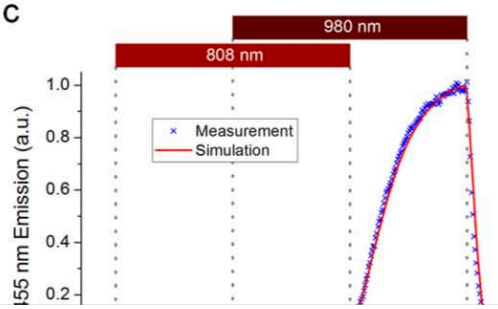

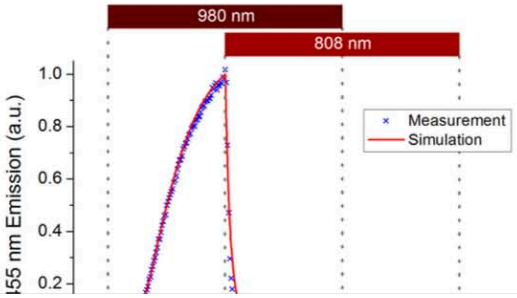

RESEARCH LETTER

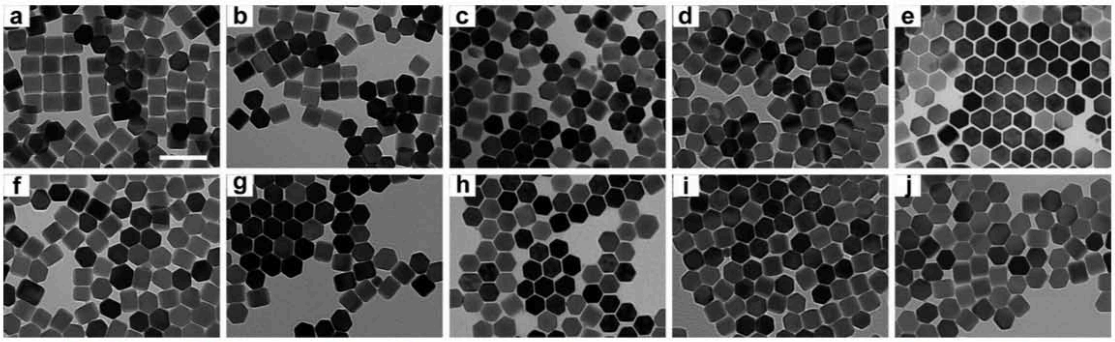

Extended Data Figure 6 | TEM images of the $NaYF_4$:Yb,Tm nanocrystals. The Yb doping concentration was fixed at 20 mol%, and **a**–**j**, the Tm doping concentrations are respectively 0.5, 1, 1.5, 2, 2.5, 3, 3.5, 4, 6 and 8 mol%. All nanocrystals have average sizes around 40 nm. Scale bar, 100 nm.

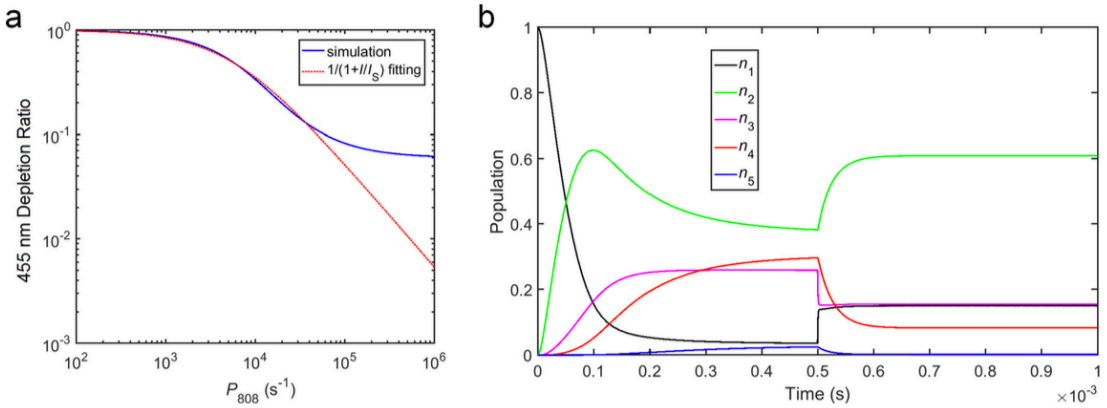

Extended Data Figure 7 | Simulation of the optical switching at 455 nm for 8% Tm-doped UCNPs. a, The 455 nm depletion ratio as a function of the 808 nm probing rate, which is simulated using the rate parameters listed in Extended Data Fig. 5b. The curve fits well to $1/(1+I/I_S)$ except for the high power range. **b**, Emitter populations as a function of time, again simulated using the rate parameters listed in Extended Data Fig. 5b. The 980 nm pumping is turned on at time = 0 s, while the 808 nm probing is turned on at time = 0.5 ms. Note the overlap between n_1 ($^3H_6$ ground level) and n_3 ($^3H_4$ intermediate level) once the 808 nm probing is turned on.

RESEARCH LETTER

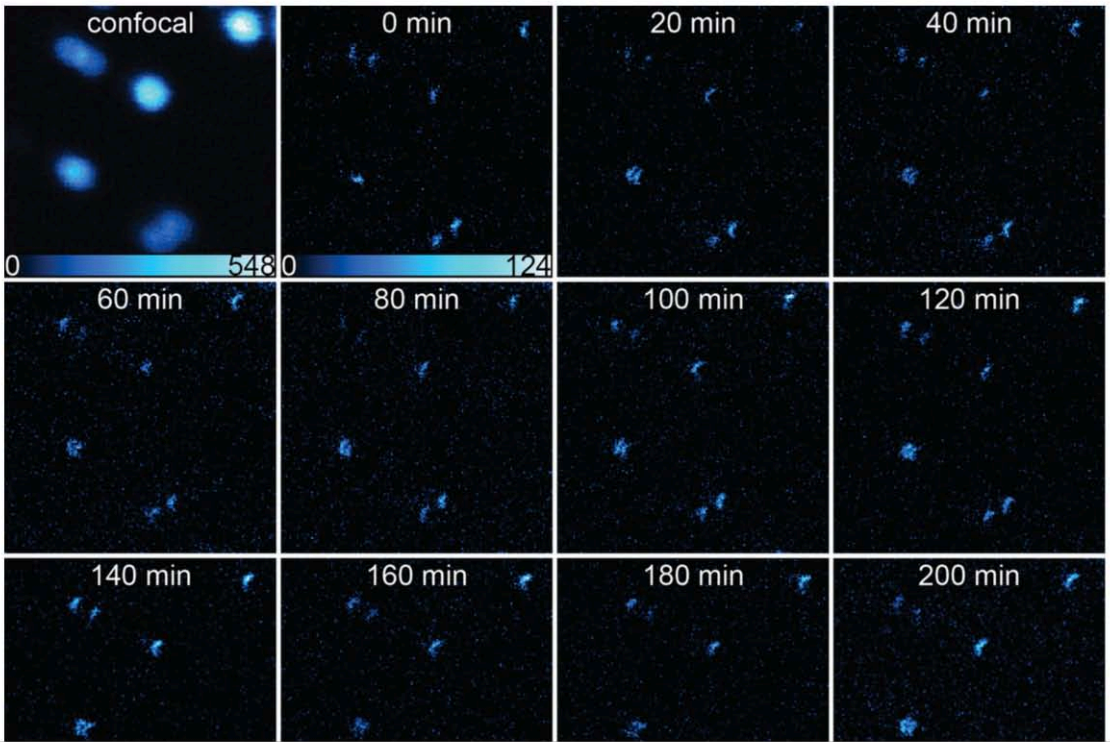

5.6 Remarks on Paper 4

This work uses low-power STED nanoscopy to achieve saturation intensity two orders of magnitude lower than other nanoscopy by using $NaYF_4$ UCNCs. Highly doped UCNCs offer efficient optical switching with saturation intensity as low as 0.19 MW/cm^2. UCNCs, highly doped with emitter ions, having good crystal quality and smaller size - together with the reported STED technique - provide a new way of developing molecular probes for bioimaging.

REFERENCES

(1) Xu, M.; Fei, L.; Zhang, W.; Li, T.; Lu, W.; Zhang, N.; Lai, Y.; Zhang, Z.; Fang, J.; Zhang, K.; *et al.* Tailoring Anisotropic Li-Ion Transport Tunnels on Orthogonally Arranged Li-Rich Layered Oxide Nanoplates Toward High-Performance Li-Ion Batteries. *Nano Lett.* **2017**, *17*, 1670–1677.

(2) Dong, C.; Pichaandi, J.; Regier, T.; Van Veggel, F. C. J. M. Nonstatistical Dopant Distribution of Ln^{3+}-Doped $NaGdF_4$ Nanoparticles. *J. Phys. Chem. C* **2011**, *115*, 15950–15958.

(3) Dong, C.; Pichaandi, J.; Regier, T.; van Veggel, F. C. J. M. The Unexpected Structures of "core–shell" and "alloy" LnF_3 Nanoparticles as Examined by Variable Energy X-Ray Photo-Electron Spectroscopy. *Nanoscale* **2011**, *3*, 3376.

(4) Abel, K. A.; Boyer, J.-C.; Veggel, F. C. J. M. van. Hard Proof of the $NaYF_4$/$NaGdF_4$ Nanocrystal Core/Shell Structure. *J. Am. Chem. Soc.* **2009**, *131*, 14644–14645.

CHAPTER 6

Summary and Future work

6.1 Summary of the Thesis

UCNCs are sought-after for advanced biomedical and photonics applications because of their ability to convert low-energy infrared photons into high-energy visible and ultraviolet photons. Lanthanide ion-doped UCNCs can be useful for applications including deep-tissue optical imaging, light transducer, drug delivery and photothermal therapy. Two of the key problems for UCNCs applications is the need to size-tune and enhance luminescence. This thesis develops efficient routes to solve these problems. The key results of this thesis are summarized below:

1. A type of UCNCs that had a smaller size with a high luminescence efficiency was fabricated by improving the interior crystal quality via controlling the rate of its heating during its synthesis.
2. A unique quantitative method for optical characterization of single UCNCs fabricated to various sizes and with shell passivated crystals was performed and confirmed that internal crystal quality dominated the relative emission efficiency of these nanocrystals.
3. An effective method to control UCNCs size has been developed. The size could range from sub-10nm to over 100nm by varying the kind/amount of rare earth ions dopant.
4. A novel UCNCs sandwich structure was fabricated that had an active interlayer formed within a small template core. This allowed epitaxial growth of the size-tunable interlayer shell that was enclosed with an inert shell and was found to minimize emission quenching on the surface of each particle.
5. The optical sensitizer concentration in single UCNCs is not limited by the concentration quenching effect as long as interior and exterior defects can be minimized.
6. Sensitizer ions were found to have a radial gradient distribution from the core to the surface within each nanocrystals. This distribution, with high sensitizer

concentration in the core region and fewer at the surface, favored increasing the emission intensity of the nanocrystals by minimizing quenching at the particle's surface.

These work further suggests several routes produce smaller and more efficient UCNCs to profound implications for the upconversion optical property variations.

6.2 Future work on UCNCs Enhancement

Future work, combining the research on size-tunable and luminescence enhanced UCNCs, encompasses three possible directions of research in UCNCs, as follows.

6.2.1 UCNCs Tracking of Living Single Cells using Low Excitation Power

Tumor diagnosis and therapy by tumor-targeted imaging[1–3] is one part of UCNCs' application. Usually, upconversion targeted imaging uses UCNCs conjugated with folic acid[4,5,3,6], antibodies[7–9] and peptides[10–13]. If crystal tracking can be included in biomedical diagnosis and therapy, this would clarify the drug delivery routes, cellular dynamics, and transport phenomena[14–16] within the living cells. Some tracking applications have been proposed by using QDs[17] and carbon nanotubes[17]. Because of the advantage of nontoxic and specific optical properties, UCNCs offer potential as tracking tools among cells[18,19,20]. From this, single UCNCs tracking in living cells could become more useful for further biomedical applications. To realize this aim, new single UCNCs tracking microscopy system could be developed to carry out measurements, fabricate new upconversion nanomaterials which can be emitted at low excitation power but have relatively high luminescence and identify good modification methods on crystals to realize the specific targeting effect within the cells.

6.2.2 UCNCs photo catalytic hybrids using metal-free materials

Semiconductor photocatalysis plays an important role in environmental remedy and solar energy conversion. The most commonly used composite photocatalysts are UCNCs with TiO_2 under 980 nm excitation laser because TiO_2 is non-toxic, low cost, and chemically stable[21–24]. Nowadays, another material, C_3N_4, has become a more

efficient photocatalyst material[26]. A facile method is required to integrate UCNCs into C_3N_4 nanosheets and display improved photocatalytic activity under a Xe lamp. Since the carbon nitride can be synthesized in several morphologies and its abundance, stability, and chemical tunableness[27–29]. I am looking forward to trying other methods about these two materials incorporation such as foist the smaller UCNCs into C_3N_4 nanotube to realize more efficient photocatalysis. This kind of combination can valid make C_3N_4 excitable by near-infrared light via energy transfer from UCNCs with the ingenious energy gap match.

6.2.3 Hybrid-UCNCs material displaying epitaxial growth

The hybrid growth of core-shell structures is a novel method that can combine different materials with different compositions and structures. In other words, two or more materials which have different properties and functions can be synthesized together and play more effective roles. A range of hybrid nanostructures could be fabricated by bringing together the rare earth fluorides, semiconductor nanocrystals, and noble metal structures. The hybrid core-shell nanostructure has been researched in a variety of areas such as metals and semiconductors[30, 31], alloys semiconductors[32, 33], metallic oxide and metals[34–37]. These hybrid core-shell structures are formed by fusing the two kinds of nanocrystals at a matched facet, subsequent nucleation, and further growth onto the second component on the core nanocrystal. The key challenge in synthesizing these hybrid materials via epitaxial growth approach lies in the matched crystalline facets between $NaReF_4$ and other materials. I plan to grow a layer of bridge shell to realize the crystal lattice match.

6.2.4 Plasmonic enhancement of upconversion luminescence

Researchers have found that for metal and UCNPs, the upconversion luminescence is not always enhanced but is sometimes quenched[38]. This is the result of different distances between the luminescent material and the metal surface. If the UCNPs is brought into contact with the metal surface, the luminescence will be quenched. Control of the distance between the metallic surface and luminescent nanocrystals such as organic dyes[39], quantum dots[40], organic molecules[41] and silica[34] have accordingly become a hot topic in recent years.

For controlling the fit distance between metal and luminescent material to realize plasmatic enhancement, the most commonly used structure is a metal film coverage UCNPs layer and the metal particles coated with each single UCNPs[43,44]. However, the plasmon enhancement of upconversion luminescence is still in infancy. Their underlying mechanisms remain debatable, and claims of improved efficacy need to be verified and much more scientific research is needed in this area.

REFERENCE

(1) Zako, T.; Nagata, H.; Terada, N.; Utsumi, A.; Sakono, M.; Yohda, M.; Ueda, H.; Soga, K.; Maeda, M. Cyclic RGD Peptide-Labeled Upconversion Nanophosphors for Tumor Cell-Targeted Imaging. *Biochem. Biophys. Res. Commun.* **2009**, *381*, 54–58.

(2) Chen, F.; Zhang, S.; Bu, W.; Liu, X.; Chen, Y.; He, Q.; Zhu, M.; Zhang, L.; Zhou, L.; Peng, W.; *et al.* A "Neck-Formation" strategy for an Antiquenching Magnetic/upconversion Fluorescent Bimodal Cancer Probe. *Chem. - A Eur. J.* **2010**, *16*, 11254–11260.

(3) Hu, H.; Xiong, L.; Zhou, J.; Li, F.; Cao, T.; Huang, C. Multimodal-Luminescence Core-Shell Nanocomposites for Targeted Imaging of Tumor Cells. *Chem. - A Eur. J.* **2009**, *15*, 3577–3584.

(4) Chatterjee, D. K.; Rufaihah, A. J.; Zhang, Y. Upconversion Fluorescence Imaging of Cells and Small Animals Using Lanthanide Doped Nanocrystals. *Biomaterials* **2008**, *29*, 937–943.

(5) Xiong, L. Q.; Chen, Z. G.; Yu, M. X.; Li, F. Y.; Liu, C.; Huang, C. H. Synthesis, Characterization, and in Vivo Targeted Imaging of Amine-Functionalized Rare-Earth up-Converting Nanophosphors. *Biomaterials* **2009**, *30*, 5592–5600.

(6) Batteries, L. À. S. Graphene/Single-Walled Carbon Nanotube HybridsOne -Step Catalytic Growth and Applications for High-Rate. *ACS Nano* **2012**, *6*, 10759–10769.

(7) Wang, M.; Mi, C.-C.; Wang, W.-X.; Liu, C.-H.; Wu, Y.-F.; Xu, Z.-R.; Mao, C.-B.; Xu, S.-K. Immunolabeling and NIR-Excited Fluorescent Imaging of HeLa Cells by Using $NaYF_4$: Yb, Er Upconversion Nanoparticles. *ACS Nano* **2009**, *3*, 1580–1586.

(8) Li, H. H.; Wu, X. L.; Sun, H. Z.; Wang, K.; Fan, C. Y.; Zhang, L. L.; Yang, F. M.; Zhang, J. P. Dual-Porosity SiO_2/C Nanocomposite with Enhanced Lithium Storage Performance. *J. Phys. Chem. C* **2015**, *119*, 3495–3501.

(9) Kumar, R.; Nyk, M.; Ohulchanskyy, T. Y.; Flask, C. A.; Prasad, P. N. Combined Optical and MR Bloimaging Using Rare Earth Ion Doped $NaYF_4$ Nanocrystals. *Adv. Funct. Mater.* **2009**, *19*, 853–859.

(10) Bogdan, N.; Rodríguez, E. M.; Sanz-Rodríguez, F.; Iglesias de la Cruz, M. C.; Juarranz, Á.; Jaque, D.; Solé, J. G.; Capobianco, J. A. Bio-Functionalization of Ligand-Free

Upconverting Lanthanide Doped Nanoparticles for Bio-Imaging and Cell Targeting. *Nanoscale* **2012**, *4*, 3647–3650.

(11) Ni, D.; Zhang, J.; Bu, W.; Xing, H.; Han, F.; Xiao, Q.; Yao, Z.; Chen, F.; He, Q.; Liu, J.; *et al.* Dual-Targeting Upconversion Nanoprobes across the Blood-Brain Barrier for Magnetic Resonance/fluorescence Imaging of Intracranial Glioblastoma. *ACS Nano* **2014**, *8*, 1231–1242.

(12) Yu, X. F.; Sun, Z.; Li, M.; Xiang, Y.; Wang, Q. Q.; Tang, F.; Wu, Y.; Cao, Z.; Li, W. Neurotoxin-Conjugated Upconversion Nanoprobes for Direct Visualization of Tumors under near-Infrared Irradiation. *Biomaterials* **2010**, *31*, 8724–8731.

(13) Xiong, L.; Chen, Z.; Tian, Q.; Cao, T.; Xu, C.; Li, F. Targeted Imaging in Vivo Using Peptide-Labeled Nanophosphors. *Imaging* **2009**, *81*, 8687-8694.

(14) Zhao, J.; Jin, D.; Schartner, E. P.; Lu, Y.; Liu, Y.; Zvyagin, A. V; Zhang, L.; Dawes, J. M.; Xi, P.; Piper, J. a; *et al.* Single-Nanocrystal Sensitivity Achieved by Enhanced Upconversion Luminescence. *Nat. Nanotechnol.* **2013**, *8*, 729–734.

(15) Deng, M.; Ma, Y.; Huang, S.; Hu, G.; Wang, L. Monodisperse Upconversion $NaYF_4$ Nanocrystals: Syntheses and Bioapplications. *Nano Res.* **2011**, *4*, 685–694.

(16) Damasco, J. a; Chen, G.; Shao, W.; Ågren, H.; Huang, H.; Song, W. Size-Tunable and Monodisperse Tm^{3+}/Gd^{3+}-Doped Hexagonal $NaYbF_4$ Nanoparticles with Engineered E fficient Near Infrared-to-Near Infrared Upconversion for In Vivo Imaging. *ACS Appl. Mater. Interfaces* **2014**, *6*, 13884–13893.

(17) Sun, E.-Z.; Liu, A.-A.; Zhang, Z.-L.; Liu, S.-L.; Tian, Z.-Q.; Pang, D.-W. Real-Time Dissection of Distinct Dynamin-Dependent Endocytic Routes of Influenza A Virus by Quantum Dot-Based Single-Virus Tracking. *ACS Nano* **2017**, acsnano.6b07853.

(18) Idris, N. M.; Li, Z.; Ye, L.; Wei Sim, E. K.; Mahendran, R.; Ho, P. C. L.; Zhang, Y. Tracking Transplanted Cells in Live Animal Using Upconversion Fluorescent Nanoparticles. *Biomaterials* **2009**, *30*, 5104–5113.

(19) Idris, N. M.; Li, Z.; Ye, L.; Wei Sim, E. K.; Mahendran, R.; Ho, P. C. L.; Zhang, Y. Tracking Transplanted Cells in Live Animal Using Upconversion Fluorescent Nanoparticles. *Biomaterials* **2009**, *30*, 5104–5113.

(20) Xiang, J.; Xu, L.; Gong, H.; Zhu, W.; Wang, C.; Xu, J.; Feng, L.; Cheng, L.; Peng, R.;

Liu, Z. Antigen-Loaded Upconversion Nanoparticles for Dendritic Cell Stimulation, Tracking, and Vaccination in Dendritic Cell-Based Immunotherapy. *ACS Nano* **2015**, *9*, 6401–6411.

(21) Fujishima, A.; Rao, T. N.; Tryk, D. A. TiO_2 Photocatalysts and Diamond Electrodes. *Electrochim. Acta* **2000**, *45*, 4683–4690.

(22) FUJISHIMA, A.; HONDA, K. Electrochemical Photolysis of Water at a Semiconductor Electrode. *Nature* **1972**, *238*, 37–38.

(23) Park, J. S.; Choi, W. Enhanced Remote Photocatalytic Oxidation on Surface-Fluorinated TiO_2. *Langmuir* **2004**, *20*, 11523–11527.

(24) Wang, W.; Li, Y.; Kang, Z.; Wang, F.; Yu, J. C. A NIR-Driven Photocatalyst Based on α-$NaYF_4$: Yb, Tm@TiO_2 Core–shell Structure Supported on Reduced Graphene Oxide. *Appl. Catal. B Environ.* **2016**, *182*, 184–192.

(25) Cheng, E.; Yin, W.; Bai, S.; Qiao, R.; Zhong, Y.; Li, Z. Synthesis of vis/NIR-Driven Hybrid Photocatalysts by Electrostatic Assembly of $NaYF_4$: Yb, Tm Nanocrystals on G-C3N4 Nanosheets. *Mater. Lett.* **2015**, *146*, 87–90.

(26) Li, X.; Ren, H.; Zou, Z.; Sun, J.; Wang, J.; Liu, Z. Energy Gap Engineering of Polymeric Carbon Nitride Nanosheets for Matching with $NaYF_4$: Yb, Tm: Enhanced Visible-near Infrared Photocatalytic Activity. *Chem. Commun.* **2016**, *52*, 453–456.

(27) Cao, S.; Low, J.; Yu, J.; Jaroniec, M. Polymeric Photocatalysts Based on Graphitic Carbon Nitride. *Adv. Mater.* **2015**, *27*, 2150–2176.

(28) Wang, X.; Maeda, K.; Chen, X.; Takanabe, K.; Domen, K.; Hou, Y.; Fu, X.; Antonietti, M. Polymer Semiconductors for Artificial Photosynthesis: Hydrogen Evolution by Mesoporous Graphitic Carbon Nitride with Visible Light. *J. Am. Chem. Soc.* **2009**, *131*, 1680–1681.

(29) Mao, J.; Peng, T.; Zhang, X.; Li, K.; Ye, L.; Zan, L. Effect of Graphitic Carbon Nitride Microstructures on the Activity and Selectivity of Photocatalytic CO_2 Reduction under Visible Light. *Catal. Sci. Technol.* **2013**, *3*, 1253.

(30) Haldar, K. K.; Pradhan, N.; Patra, A. Formation of Heteroepitaxy in Different Shapes of Au-CdSe Metal-Semiconductor Hybrid Nanostructures. *Small* **2013**, *9*, 3424–3432.

(31) Lee, J. S.; Shevchenko, E. V.; Talapin, D. V. Au-PbS Core-Shell Nanocrystals: Plasmonic Absorption Enhancement and Electrical Doping via Intra-Particle Charge Transfer. *J. Am. Chem. Soc.* **2008**, *130*, 9673–9675.

(32) Son, J. S.; Lee, J.; Shevchenko, E. V; Talapin, D. V. Magnet-in-the-Semiconductor Nanomaterials : High Electron Mobility. *J. Phys. Chem. Lett.* **2013**, *4*, 1918–1923.

(33) Guardia, P.; Korobchevskaya, K.; Casu, A.; Genovese, A.; Manna, L.; Comin, A. Plasmon Dynamics in Colloidal Au_2Cd Alloy-CdSe Core/shell Nanocrystals. *ACS Nano* **2013**, *7*, 1045–1053.

(34) Huang, J.; Sun, Y.; Huang, S.; Yu, K.; Zhao, Q.; Peng, F.; Yu, H.; Wang, H.; Yang, J. Crystal Engineering and SERS Properties of Ag-Fe_3O_4 Nanohybrids: From Heterodimer to Core–shell Nanostructures. *J. Mater. Chem.* **2011**, *21*, 17930–17937.

(35) Jiang, J.; Gu, H.; Shao, H.; Devlin, E.; Papaefthymiou, G. C.; Ying, J. Y. Bifunctional Fe_3O_4-Ag Heterodimer Nanoparticles for Two-Photon Fluorescence Imaging and Magnetic Manipulation. *Adv. Mater.* **2008**, *20*, 4403–4407.

(36) Mao, Y.; Yi, P.; Deng, Z.; Ge, J. Fe_3O_4-Ag Heterostructure Nanocrystals with Tunable Ag Domains and Magnetic Properties. *CrystEngComm* **2013**, *15*, 3575.

(37) Muraca, D.; Odio, O. F.; Reguera, E.; Pirota, K. R. One Step Chemical Synthesis of Ag-Fe_3O_4 Heterodimer Nanoparticles: Optical, Structure, and Magnetic Properties. *IEEE Trans. Magn.* **2013**, *49*, 4606–4609.

(38) Schietinger, S.; Aichele, T.; Wang, H. Q.; Nann, T.; Benson, O. Plasmon-Enhanced Upconversion in Single $NaYF_4$: Yb^{3+}/Er^{3+} Codoped Nanocrystals. *Nano Lett.* **2010**, *10*, 134–138.

(39) Schneider, G.; Decher, G.; Nerambourg, N.; Praho, R.; Werts, M. H. V; Blanchard-Desce, M. Distance-Dependent Fluorescence Quenching on Gold Nanoparticles Ensheathed with Layer-by-Layer Assembled Polyelectrolytes. *Nano Lett.* **2006**, *6*, 530–536.

(40) Liu, N.; Prall, B. S.; Klimov, V. I. Hybrid Gold/silica/nanocrystal-Quantum-Dot Superstructures: Synthesis and Analysis of Semiconductor-Metal Interactions. *J. Am. Chem. Soc.* **2006**, *128*, 15362–15363.

(41) Nabika, H.; Deki, S. Enhancing and Quenching Functions of Silver Nanoparticles on the

Luminescent Properties of Europium Complex in the Solution Phase. *J. Phys. Chem. B* **2003**, *107*, 9161–9164.

(42) Zhang, F.; Braun, G. B.; Shi, Y.; Zhang, Y.; Sun, X.; Reich, N. O.; Zhao, D.; Stucky, G. Fabrication of $Ag@SiO_2@Y_2O_3$: Er Nanostructures for Bioimaging: Tuning of the Upconversion Fluorescence with Silver Nanoparticles. *J. Am. Chem. Soc.* **2010**, *132*, 2850–2851.

(43) Li, G. C.; Zhang, Y. L.; Jiang, J.; Luo, Y.; Lei, D. Y. Metal-Substrate-Mediated Plasmon Hybridization in a Nanoparticle Dimer for Photoluminescence Line-Width Shrinking and Intensity Enhancement. *ACS Nano* **2017**, *11*, 3067–3080.

(44) Wawrzynczyk, D.; Bednarkiewicz, A.; Nyk, M.; Gordel, M.; Strek, W.; Samoc, M. Modulation of up-Conversion Luminescence of lanthanide(III) Ion Co-Doped $NaYF_4$ Nanoparticles Using Gold Nanorods. *Opt. Mater. (Amst).* **2012**, *34*, 1708–1712.